Towards Electrically Injected Semiconductor Nanowire Lasers

Nikita Gagrani

July 2022

A thesis submitted for the Degree of Doctor of Philosophy of

The Australian National University

Department of Electronic Materials Engineering

Research School of Physics

College of Science

This thesis, to the best of my knowledge and belief, does not contain any results previously published by another person or submitted for a degree or diploma at any university except where due reference is made in the text.

Nikita Gagrani

July 2022

Acknowledgements

This thesis would not be possible without the help and support of many people. I would like to acknowledge them here.

Firstly, I would also like to express my sincere gratitude to my primary supervisor Prof. Hoe Tan, for his constant guidance throughout this Ph.D. I am really grateful for his readiness to help, mentorship, give valuable advice and constructive feedback, especially for experiments, simulations and writing research papers.

I would also like to express my gratitude to Prof. Chennupati Jagadish for providing me with this wonderful opportunity. It is a privilege to be a member of his group. Without his motivation, insightful feedback and support, it would be extremely challenging to carry on my Ph.D. during hard times. I am honoured to work under his supervision where, I learnt not only the scientific research but also many valuable lessons of life such as humbleness, kindness, hardworking and compassion. I will always remember and practice these lessons throughout my life.

I would especially like to thank Dr. Mykhaylo Lysevych for training me on the MOCVD system and his guidance, especially for the fruitful in-depth discussion on lasers and how to address some of the challenges. His expertise on lasers is really insightful and helped me throughout my Ph.D.

I also thank Prof. Lan Fu for her supervision and critical feedback on my work as well as on my research papers. Her expertise of device fabrication proved quite helpful during my Ph.D.

I am extremely grateful to Dr. Kaushal Vora for constantly supporting and helping me with both technical and non-technical problems. I really enjoyed working with him and thank him for making my Ph.D. journey easier and memorable.

During this thesis, I was fortunate to collaborate with Ms. Zahra Azimi, Dr. Tuomas Haggren, Dr. Inseok Yang and Mr. Khosro Z. Kamali from the Australian National University, Prof. Fang-Fang Ren from Nanjing University, China and Dr. Xutao Zhang from Northwestern Polytechnical University, China. It was a great learning experience. Thank you so much for believing in me and providing me this opportunity.

I would like to acknowledge Australian National Fabrication Facilities (ANFF)-ACT node for providing access to cutting edge facilities. I would like to thank ANFF staffs, namely Ms. Gayatri Vaidya, Dr. Li Li, Dr. Olivier Lee Cheong Lem, Dr. Mark Lockery, Dr. Fouad Karouta, Ms. Sue Berkeley and Dr. Naeem Shahid for training me on various tools and their readiness to help. I would also like to acknowledge financial support from Australian Research Council through the PhD scholarship and ANU for HDR Fee Remission Merit Scholarship.

I would like to thank the technical staff of the Department, Mr. Chris Kafer, Mr. Dane Kelly and Mr. Joshua Carr for providing technical assistance, Electronics Unit staff of the School, Mr. Dennis Gibson for fixing the tools and the School Computer Unit staff, Mr. Clarence Yew and Mr. Angus Kay for IT assistance. I also extend my thanks to Ms. Julie Arnold, Ms. Liudmila Mangos, Ms. Karen Nulty, Mrs. Siobhan Ryman and Ms. Liz Micallef for their dedicated work as departmental and school administrator and organising several social gatherings.

I would like to say special thanks to my colleagues Ahmed, Inseok, Dipankar, Rowena, Naiyin, Bijun, Reddy, Joshua, Vidur, Sonachand, Aswani, Wei Wen, Shiyu, Anha, Joshua, Bikesh, Aditya, Yuxin, Ziyuan, Yi, Asim, Zhicheng, Sukanta and Julie for encouraging me during my hard times and making this journey memorable. I am very fortunate to make some good friends like Fanlu, Huyen, Shankar, and Richa Awasthy. I cherish the moments I spend with you.

I express my sincere love to my sister, Ankita and my partner, Nishith for their care, support, mentorship, love and motivation. This thesis would not be possible without their support and encouragement. Finally, I would like express my humble obeisance to my family and friends, in particular my parents, grandparents and my brother for their unconditional love, and support.

Abstract

We are at a tipping point of the next industrial revolution, which will change the way we work, live and communicate. Especially, the augmentation of data storage and process will require communication networks that can handle around 175 zettabytes by the end of 2025. Optical interconnect technology is a promising candidate, as it can transmit data at lightning speeds within chips and boards in an energy efficient way. Laser is the backbone of such optical circuits and is often integrated with its electrical counterpart for power inputs. With the advances in fabrication techniques, micron-sized III-V semiconductor lasers are widely used, not only in data communication, but more widely in medicine, robotics, green energy, military etc. However, there is still a strong prerequisite to make these lasers even smaller and more energy efficient for optical interconnect technology. Nanowires are a suitable candidate for such devices due to their large surface area-to-volume ratio, high aspect ratio, confinement of photons in two dimensions and ease in integration with other substrates. However, research of III-V semiconductor nanowire Fabry-Pérot cavity lasers is still in the early stages and a lot more theoretical and experimental research need to be done to realise devices, in particular those that are electrically powered, that are manufacturable for practical applications.

In this thesis, in-depth theoretical and experimental studies to fabricate nanowire lasers are presented. First, numerical modelling to optimise the dimensions of nanowires are performed to achieve low threshold lasing. Following this, epitaxial growth optimisation is carried out to achieve the desired dimensions of nanowires. Subsequently, fabrication of two different types of device architecture featuring single nanowire and nanowire array devices are done. For single nanowire devices, an InP p-i-n axial structure is explored. The single nanowire laser devices display light

emitting diode (LED) characteristics, but unfortunately, they fail at higher injected current before lasing is observed. The potential causes of degradation of devices are high metal absorption, lower gain due to smaller active region and high free carrier absorption. To overcome high metal absorption and lower gain, radial p-n junction structures are investigated and significant improvement in the device performance is observed. However, the devices also fail at higher current injection levels prior to lasing threshold.

To overcome high free carrier absorption, transparent conducting oxides (TCOs) are used as a dopant layer forming a heterojunction with InP nanowire arrays as well as a contact layer. TCOs exhibit metal-like conductivity but with a high degree of transparency. Numerical analysis to compute the optimum nanowire dimensions to obtain lasing, such as diameter and length, are carried out. For n-type TCOs, ZnO and SnO_x are explored as potential materials, while for p-type TCOs, $Sn_xNi_yO_z$ is evaluated. Optical, compositional and electrical properties of the TCOs are investigated at various deposition conditions. Junction properties as well as band alignment at the TCO-InP interface are studied to have in-depth insight of carrier injection and transport across the heterojunction. Finally, electroluminescence characteristics are measured and all the devices show promising LED behaviour, but again, fail to lase due to excessive heating at higher current injection levels due to carrier crowding, non-uniformity and shifting of the recombination region. For ease of integration, cost effectiveness and minimising the shift of the recombination region, flexible nanowire array devices are also demonstrated, which provide LED characteristics, but still fail to lase. Potential reasons and steps towards improvement such as modified fabrication process to mitigate recombination inside the substrate, proper heat sinking and incorporation of quantum wells and quantum dots to enhance gain are investigated. Nevertheless, the knowledge and

understanding gained from devices fabricated in this thesis are promising steps towards realising electrically injected III-V semiconductor nanowire lasers.

List of Publications

[1] **N. Gagrani**, K. Vora, C. Jagadish, H. H. Tan, "Thin $Sn_xNi_yO_z$ Films as p-type Transparent Conducting Oxide and Their Application in Light Emitting Diodes", *ACS Applied Materials & Interfaces*, (under review).

[2] K. Z. Kamali, L. Xu, **N. Gagrani**, H. H. Tan, C. Jagadish, A. Miroshnichenko, D. Neshev, M. Rahmani, "Electrically-tunable solid-state metasurfaces via flash localised heating", Nature Photonics, (under review).

[3]. V. Khayrudinov , A. Sorokina, V. Raj, **N. Gagrani**, T. Koskinen, H. Jiang, I. Tittonen, C. Jagadish, H. H. Tan, H. Lipsanen, T. Haggren, "Direct GaAs nanowire growth and monolithic LED fabrication on flexible plastic substrates" *Advanced Electronics Materials*, pp- 2100311, 2022.

[4] **N. Gagrani**, K. Vora, S. Adhikari, Y. Jiang, C. Jagadish, H. H. Tan, *Advanced Optical Materials*, vol. 10, no. 11, pp-2102690, 2022.

[5] **N. Gagrani**, K. Vora, L. Fu, C. Jagadish, H. H. Tan, "Flexible InP-ZnO Nanowire Heterojunction Light Emitting Diodes", *Nanoscale Horizon,* vol. 7, no. 4, pp-446-454, 2022.

[6] Z. Azimi, **N. Gagrani**, J. Qu, O. LC Lem, S. Mokkapati, J. M Cairney, R. Zheng, H. H. Tan, C. Jagadish, J. Wong-Leung, "Understanding the role of facets and twin defects in the optical performance of GaAs nanowires for laser applications", *Nanoscale Horizon*, vol. 6, no. 7, pp-559-567, 2021.

[7] X. Zhang, R. Yi, **N. Gagrani**, Z. Li, F. Zhang, X. Gan, X. Yao, X. Yuan, N. Wang, J. Zhao, P. Chen, W. Lu, L. Fu, H. H. Tan, C. Jagadish "Ultralow Threshold, Single-Mode InGaAs/GaAs Multiquantum Disk Nanowire Lasers", *ACS nano*, vol.15, no.5, pp-9126, 9133, 2021.

[8] M.C. Luo, F.F. Ren, **N. Gagrani**, K. Qiu, Q. Wang, L. Yu, J. Ye, F. Yan, R. Zhang, H.H. Tan, C. Jagadish, X. Ji, "Polarization-Independent Indium Phosphide Nanowire Photodetectors", *Advanced Optical Materials*, vol. 8, no. 17, pp-2000514, 2020.

[9] I. Yang, Z. Li, J. Wong-Leung, Y. Zhu, Z. Li, **N. Gagrani**, L. Li, M. N. Lockrey, H. Nguyen, Y. Lu, H. H. Tan, C. Jagadish, L. Fu "Multiwavelength single nanowire InGaAs/InP quantum well light-emitting diodes", *Nanoletters*, v*ol.* 19, no.6, pp-3821-3829, 2019.

Table of Contents

List of Figures

List of Tables

List of Acronyms

a.u.	arbitrary unit
ALD	atomic layer deposition
ART	aspect ratio trapping
BE	binding energy
CAD	computer aided design
CB	conduction band
CBO	conduction band offset
DC	direct current
EBIC	electron beam-induced current
EBL	electron beam lithography
EDX	energy dispersive X-ray spectroscopy
EL	electroluminescence
F-P	Fabry-Pérot
FDE	finite difference eigenmode
FDTD	finite difference time domain
FEM	finite element method
FIB	focused ion beam
HH	heavy hole
I-V	current-voltage
ICP	inductively coupled plasma
IPA	isopropanol
ITO	indium tin oxide
KE	kinetic energy
L-I	light output power-current
LED	light emitting diode
LH	light hole
MOCVD	metal-organic chemical vapour deposition
NA	numerical aperture
OLED	organic light emitting diode

PDMS	polydimethylsiloxane
PECVD	plasma enhanced chemical vapour deposition
PL	photoluminescence
PMMA	polymethyl methacrylate
RC	resistor-capacitor
RF	radio-frequency
RIE	reactive ion etching
SAE	selective-area epitaxy
SECO	secondary electron cut-off
TCO	transparent conducting oxide
TMM	transverse matrix method
UPS	ultraviolet photoelectron spectroscopy
UV-Vis-NIR	ultraviolet-visible-near infrared
VBM	valence band maximum
VBO	valence band offset
VCSEL	vertical cavity surface emitting laser
VLS	vapour-liquid-solid
WZ	wurtzite
XPS	X-ray photoelectron spectroscopy
ZB	zinc blende

Chapter 1. Introduction

1.1 Motivation

Semiconductor lasers have remarkable impact on our society where they are extensively being used in diverse fields ranging from telecommunications, military, medical science, industry, graphics, sensors, information technology etc. Technological development has led to significant improvement in enhancing the efficiency and miniaturising the lasers down to the micrometre scale. The advantages of these small lasers are low operating power, ease of integration with other devices, low cost and high-volume manufacturing. Thanks to advanced fabrication techniques, apart from becoming the major component of consumer electronics, these lasers are now replacing their bigger counterpart (gas and solid-state lasers) in medical science, optical communications, photonics etc.

In biology and medical science, it is possible to implant biocompatible nanowire lasers in living cells. This will open up an opportunity to explore gene therapy and drug delivery, in vivo studies, bio-imaging/sensing, electrochemistry, and electrophysiology [1].

Every year, usage of data is increasing exponentially. Globally in 2018, 33 zettabytes of new data was generated and is expected to rise to 175 zettabytes by the end of 2025 [2]. To handle such a high volume of data, we need a high-performance computing device with low power consumption and high bandwidth. However, such devices are currently limited by resistive loss and RC delay in electrical interconnect. These issues could be addressed by replacing electrical interconnect with optical interconnect for short distance data communications. Primary element missing for such optical interconnect is nanoscale semiconductor lasers. Most of the leading chip manufacturing

companies have extensive research programs in chip-to-chip optical communications for future smart phones, Internet of Things and data-centres.

In Si-based electronics, Moore's law predicts that number and density of transistors doubles every two years in integrated circuits. Right now, transistors have already reached to the atomic scale such that further miniaturisation is extremely challenging, thereby putting a limit on the processing speed [3]. Furthermore, thin copper wires used to connect transistors on chip have RC delay. In addition, Ohmic losses lead to heat generation of the chip that affects their performance. Using optical signals to transmit data can avoid such issues and increase speed several folds [4]. Semiconductor laser is one of the key components in this optical data communication circuit. Unfortunately, the size of current semiconductor laser is much larger than the components in the electronic circuit. Hence decreasing its dimensions to sub-wavelength scale is required for high density integrated photonic circuits.

Due to the nanoscale one-dimensional wire like structure, semiconductor nanowires are promising solution for integrated photonic circuits. High aspect ratio, large surface-to-volume ratio, high crystalline quality and carrier/photon confinement in two dimensions make them different from other bulk structures. Compound semiconductor nanowires are promising solution for high density nanoscale lasers owing to their unique geometry which acts as a cavity/natural optical resonator and material which behave as a gain medium. High refractive index difference between the nanowire and the surrounding medium (air) leads to better confinement of optical modes [5]. Furthermore, due to sub-wavelength dimensions of nanowire, the end facets act as highly reflective mirror for optical feedback as compared to their bulk counterparts [6]. Additionally, by simply changing the composition of semiconductor, the output lasing wavelength can be altered for different applications that require different operational wavelengths.

Most of the research on semiconductor nanowire lasers focus on optically pumped nanowire lasers. However, for practical purposes, electrical injection is required. To date, there are very few demonstrations of electrically injected nanowire lasers primarily due to fabrication challenges, excessive heating, non-Ohmic contacts, non-uniform doping, metal absorption and non-uniform current injection [7].

1.2 Aim

The aim of this thesis is to provide a deeper insight of fabrication methods and challenges to achieve electrically injected nanowire lasers. This thesis mainly explores two different types of geometries to achieve lasing: first, single nanowire devices (p-i-n nanowires) and second, array nanowire devices (nanowires incorporating transparent conducting oxides (TCOs) to form both the p-n junction and the electrical contact). TCO and radial junction are used to reduce metal absorption losses, free carrier absorption and increase active region. In both the cases, simulation and experiments are performed and various challenges to achieve lasing along with possible solutions are discussed. Furthermore, detailed analysis of junction properties, band alignment, and TCO characterisation are performed to understand the origin of recombination in various InP-TCO nanowire structures. This thesis presents results of various nanowire devices such as single p-i-n InP nanowire, p-InP/n-ZnO core shell array device, p-InP/n-ZnO core shell flexible device, p-InP/n-SnO_x radial structure and n-InP/p-$Sn_xNi_yO_z$ core shell structure, their fabrication and characterisation.

1.3 Outline

The outline of this thesis is as follow:

Chapter 2: This chapter summarises the progress in nanowire lasers, nanowire LEDs and identify the potential issues to achieve electrically injected nanowire lasers. This chapter also explores some background knowledge and basic concepts used in the thesis.

Chapter 3: This chapter provides an overview of various numerical and experimental techniques used in this thesis. This chapter is mainly divided into 4 sections, namely experimental techniques, growth of nanowires, device fabrication, and numerical techniques used to simulate various nanowire structures to obtain low threshold lasing.

Chapter 4: This chapter investigates single nanowire device fabrication, device characterization and numerical techniques used to simulate single nanowire structures to obtain low threshold lasing. LaserMOD simulations are performed to determine the optimised dimensions of p-i-n nanowires. Experimental results of p-i-n InP single nanowire show that nanowire is burnt before reaching to threshold. To minimise metal absorption losses and increase gain, radial homojunction devices are investigated which show improvement in the device performance. However, the devices are degraded before reaching lasing suggesting incorporation of either TCO or quantum well.

Chapter 5: This chapter presents the simulations and fabrication of devices made from ensemble p-InP/n-ZnO core-shell structures. Simulations of ZnO are performed using LaserMOD and minimum threshold lower than an order is obtained. Several electrical properties like I-V (current-voltage) and electron bean induced current (EBIC) are studied to have deeper insight of junction. The devices show LEDs characteristics however, they burn when excessive current is passed through them. Detailed investigation of device degradation is done. Moreover, to overcome some of the issues, flexible LEDs are also fabricated and investigated at different operating temperatures.

Chapter 6: This chapter looks into the simulations of ensemble p-InP/n-SnO_x core shell nanowires. The advantages with SnO_x are that it is a low-cost material, and it exhibits higher chemical stability as compared to ZnO and ITO. Comprehensive study of SnO_x film at various deposition conditions is performed using Hall-effect measurements, ellipsometry, X-ray photoelectron spectroscopy (XPS) and UV-Vis-NIR spectrophotometry and trade-off between absorption and conductivity is observed. Band alignment at InP-SnO_x junction is also studied for various films. Electroluminescence (EL) measurements confirm that the structure works as an LED but degrades before reaching to the lasing. Extensive analysis of origin of various peaks as a function of temperature is performed for this structure.

Chapter 7: This chapter discusses n-InP/p-$Sn_xNi_yO_z$ core shell nanowire structures. Alloy of SnO_x and NiO_x is used to achieve stable p-doped layer. The advantages with p-doped TCO is that it solves the issues related to the shifting of the recombination region due to low hole mobility as well as reduces free carrier absorption since Zn dopants in InP have higher free carrier absorption than Si dopants in InP. Carrier transport properties and optical properties are investigated at various deposition conditions. Band alignment at the $Sn_xNi_yO_z$ /InP junction and core level of $Sn_xNi_yO_z$ film are studied to have deeper understanding of $Sn_xNi_yO_z$ film. Fabricated devices work as LEDs and burn when excessive current is passed to achieve lasing. To increase light output, core shell InP structures are also investigated to achieve lasing

Chapter 8: This chapter summarises the key results of thesis and provide directions to achieve low threshold electrically injected nanowire lasers.

Chapter 2. Background Knowledge and Literature Review

In this chapter, we provide some background knowledge on semiconductor lasers and review the relevant work done in nanowire lasers and LEDs. We also discuss the challenges to achieve lasing and the advantage of TCOs.

2.1 Background knowledge of semiconductor lasers

In this section, we provide insight on the basic concepts of semiconductor lasers, LEDs and p-n junction. First, we discuss the working principles and conditions required to achieve lasing. Then, we provide an overview of p-n junction and general concept on LEDs.

2.1.1 Type of electronic transitions

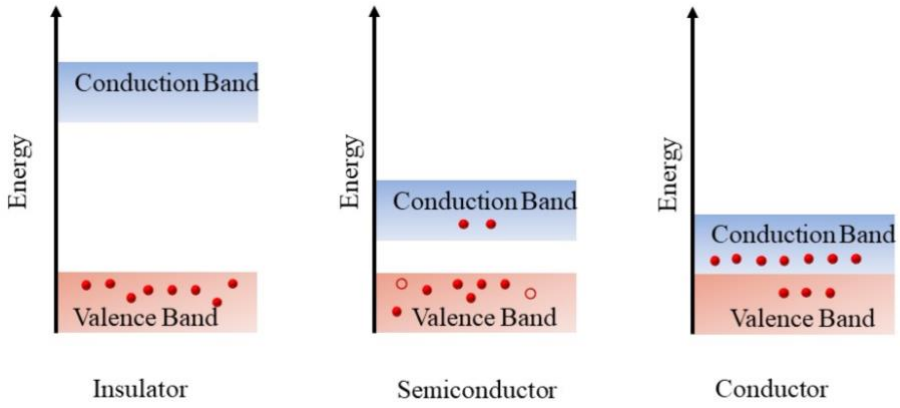

Figure 2-1 Schematic diagram showing difference between insulator, semiconductor and conductor.

A diode laser is made up of semiconductor materials. A semiconductor is a material whose conductivity is between metal and insulator (Figure 2-1). The conductivity of the semiconductors is due to the transition of the electrons from valence band to the conduction band. Valence band of a semiconductor is the outermost energy level where electrons are normally present at T = 0 K. On the other hand, conduction band is the lowest energy vacant level present at absolute zero. The

energy difference between the conduction and the valence band is the band gap of a semiconductor. Due to thermal or other external energy, electrons from valence band are excited to the conduction band leaving holes in the valence band, the probability of which is defined by the Fermi-Dirac distribution at thermal equilibrium. Transition of electrons between the valence band and conduction band leads to the optical properties of the semiconductor material. There are 4 basic types of possible transitions as indicated in Figure 2-2.

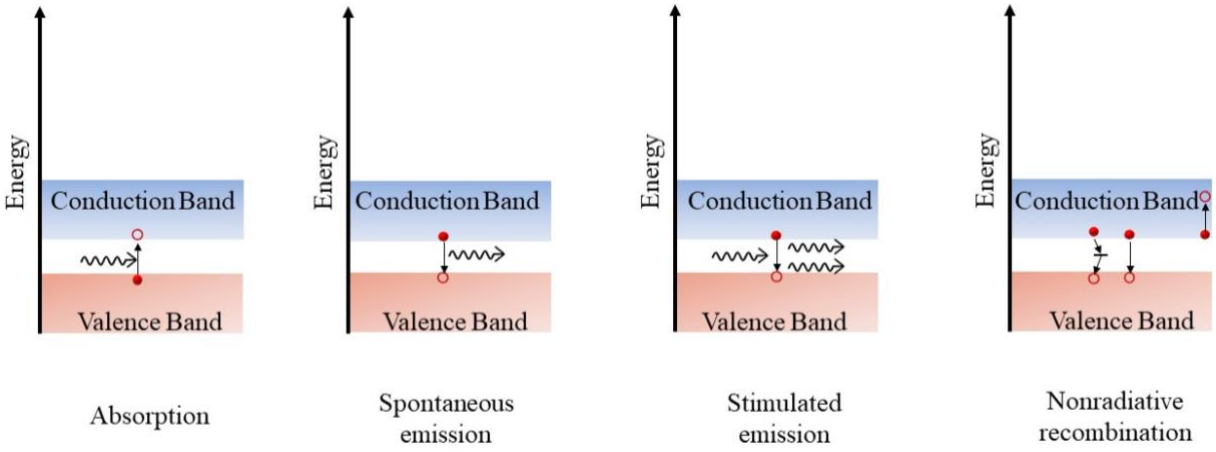

Figure 2-2 Different types of possible electronic transitions between conduction band and the valence band. Adapted from [8].

2.1.1.1 Absorption

Various types of absorptions can occur in semiconductors. In direct bandgap semiconductors (conduction band minimum and valence band maximum have same k-vector) such as GaAs, InP, GaN etc., an electron from valence band absorbs a photon and is excited to the conduction band. In indirect bandgap semiconductors (conduction band minimum and valence band maximum have different k-vectors) such as Si, Ge etc., phonon assisted transitions occur to conserve crystal momentum. In addition, inter-valence band transitions and free carrier transitions in both valence and conduction band can lead to absorption.

2.1.1.2 Spontaneous emission

Spontaneous emission occurs when an electron from conduction band recombines spontaneously, without any external stimulus and generates a photon. In such cases, the generated photon is incoherent in terms of phase, polarization and direction relative to other photons. This is the fundamental process within an LED where all the photons are random with respect to each other and there is no feedback mechanism. This kind of recombination requires an electron-hole pair, hence rate is proportional to square of excess carrier density.

2.1.1.3 Stimulated emission

Stimulated emission is the process when incident photon perturbs the system and leads to the radiative electron-hole recombination with same frequency, polarisation, direction and phase. This newly created photon also contributes to the existing field leading to the accumulation of a coherent field. When the number of stimulated recombination overcome the absorption and other losses, the condition of positive gain is achieved and the semiconductor device works as a laser.

2.1.1.4 Nonradiative recombination

Nonradiative recombination occurs when instead of emitting a photon, electron-hole recombination energy is dissipated in the form of either heat or lattice vibrations. There are mainly two types of nonradiative recombination: recombination at electron and hole traps, such as defects, surfaces, interfaces and Auger recombination. During the transitions, instead of transiting directly from conduction band to the valence band, if electron transit to levels in the mid-bands, the former transition occurs. Generally, these mid-bands are formed due to point defects, stacking faults or impurity atoms (dopants). Moreover, this kind of recombination is quite common at the surface of the semiconductor devices due to dangling bonds on the surface. Since only electron or hole is involved in the process, this recombination is proportional to excess carrier density.

Another type of non-radiative recombination is Auger recombination in which energy from the recombination of electron-hole pair is transferred to either another electron or another hole in the form of kinetic energy. Since, three carriers are involved in this process, this recombination is proportional to cube of excess carrier density. Nonradiative recombination causes absorption losses in the system and are undesirable.

2.1.2 Gain

When stimulated emission exceeds the total loss occurring in the cavity, the gain is positive and the device works as a laser. In the lasing regime, stimulated emission dominates spontaneous emission leading to the sudden rise in light output. However, some random photons from spontaneous emission will still be present, making it impossible to achieve a perfectly coherent emission. Two of the most common ways to pump the device to achieve positive gain are optical and electrical pumping. Optical pumping is usually accomplished by a more powerful optical source like lasers having higher photon energy than the bandgap of the device being pumped. In electrical pumping, a current is passed through the device, introducing excess electrons in the conduction band and holes in the valence band. When the number of electrons is higher in conduction band than valence band, it leads to population inversion i.e., optical amplification. Increase in pumping leads to enhancement in optical amplification, and finally the condition arises such that the total gain overcomes all the losses and lasing occurs. This condition is known as lasing threshold and the carrier density required to achieve this is known as the transparency carrier density. The losses in the system emerge mainly from mirror losses, intrinsic absorption, metal absorption from the electrical contacts and nonradiative recombination. In this thesis, we will mainly focus on electrical pumping. To pass current and generate photons in a semiconductor device, a p-n junction is required.

2.1.3 p-n junction

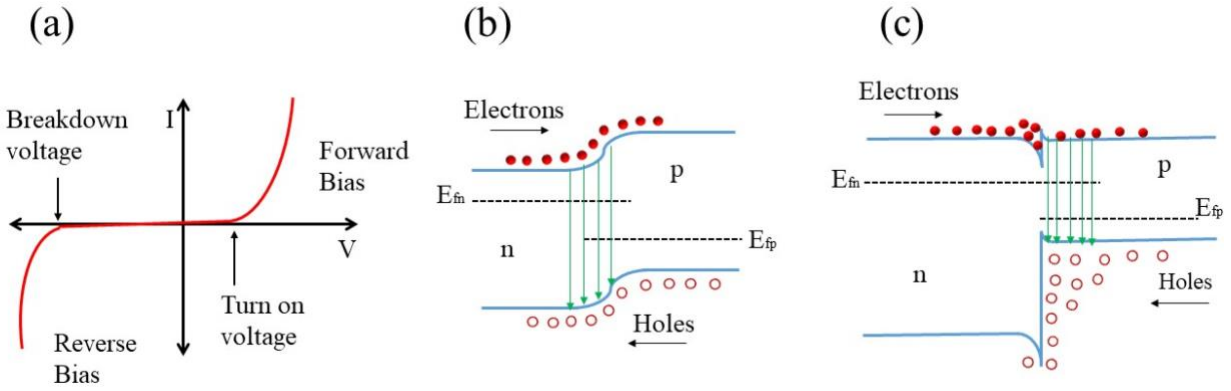

Figure 2-3 (a) I-V characteristics of a diode. Band diagram in forward bias (b) for homojunction (c) for heterojunction.

A p-n junction (diode) is formed at the interface of two semiconductors when a p-type material (excess holes) is brought in contact with an n-type material (excess electrons). The most important characteristic of p-n junctions is that, they are rectifying in nature i.e., they allow current to easily pass in one direction (forward bias) and restrict current in opposite direction (reverse bias). However, after certain voltage in reverse bias it is possible for a breakdown to occur, leading to excess current flow in the reverse direction. In general, all devices like LEDs and lasers work in the forward bias. Figure 2-3 (a) shows the I-V characteristics of a p-n junction. When current is passed through a diode for light emitting purposes, it is preferable that entire current generate electron and hole pairs. In reality, only a fraction of current generates electron and hole pairs and the rest of the current overflows from the junction. To increase this current fraction, a heterojunction, double heterojunction or quantum confinement can be employed in the structure. This introduces a barrier which confines the carriers in the active region which leads to efficient LED or laser. Comparison of current leakage between a homojunction and a heterojunction diode is depicted in Figure 2-3 (b) and Figure 2-3 (c).

2.1.4 Semiconductor lasers and LEDs

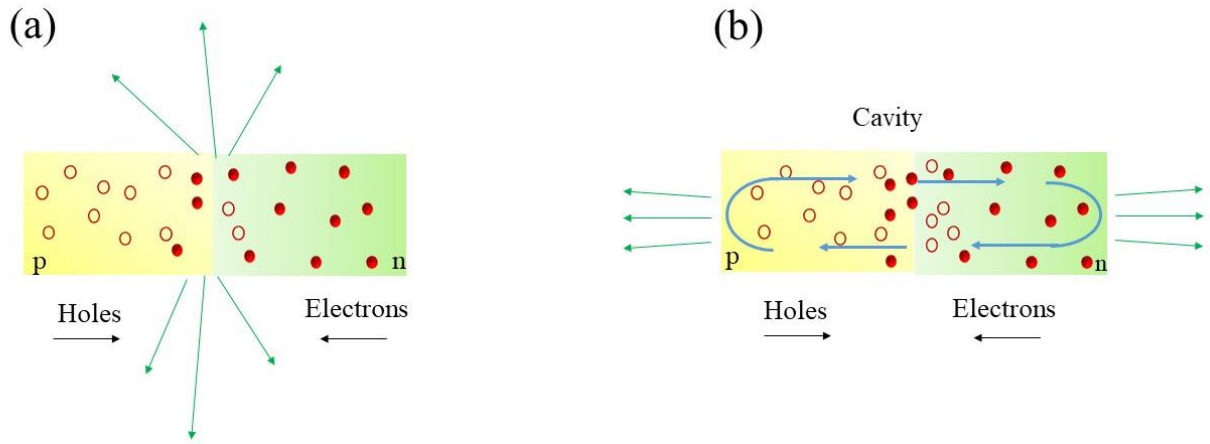

Figure 2-4 Schematic diagram of (a) an LED demonstrating incoherent output (b) a laser illustrating feedback mechanism inside cavity (blue arrows) and coherent output.

When current is injected in a diode, excess carriers are generated. Some of the generated carriers recombine non-radiatively, causing loss of carriers whereas some recombine radiatively and generate photons (spontaneous emission). Some current leaks in the process because of thermionic emission or lateral diffusion due to lack of confinement. This leakage current also contributes to the loss of carriers. When the generated photons are emitted from the device, it operates as an LED. Higher the current injection is, more the generated carriers are hence, more the light output.

To achieve lasing, a cavity is required to amplify the generated photons. As we keep injecting more current, threshold condition is reached when, the number of electrons are higher in conduction band than in the valence band. Now, the number of downward transitions are higher than upward transitions. The photon density gets amplified as stimulated electron hole pairs generate photons of same phase, direction and polarity. Once the amplified photon density offsets the total loss in the cavity, the device starts working as a laser. Figure 2-4 displays the difference between the working mechanism of a laser and an LED.

2.2 Review on semiconductor nanowire lasers

Intensive research has been going on in the 20 years or so to demonstrate nanowire lasers. The first nanowire laser was demonstrated in 2001 as optically pumped ZnO nanowire [9]. Since then, many studies have been carried out on various semiconductor nanowires to investigate lasing. Initially the majority of studies were on ZnO, CdS and GaN nanowires because they have large exciton binding energy at room temperature [10-13]. On the other hand, traditional III-V semiconductors such as GaAs and InP suffers issues with material quality and Auger recombination [14, 15].

Most of the studies on nanowire lasers are focused on optically pumped lasing as electrical injection has several challenges [16]. However, electrical injection is required to integrate nano-lasers with the photonic circuits and for practical applications. In this section we will review the different techniques used to achieve optically pumped lasing from nanowires and progress in the field of electrically injected nanowire lasers.

2.2.1 Optically pumped III-V semiconductor nanowire lasers

2.2.1.1 Nanowires transferred from the growth substrate

After extensive research in III-V nanowires, lasing was demonstrated by transferring the nanowire on another non-absorbing substrate. This reduces the optical losses due to the absorption from the growth substrate and increases mode confinement. Thick SiO_2 on Si was used as the transferred substrate due to the low refractive index. The nanowire acts as Fabry-Pérot (F-P) cavity for the modes propagating along the nanowire axis while its end facets act as mirrors due to high refractive index difference between nanowire and air [6, 17]. The first III-V semiconductor nanowire laser based on GaAs/GaAsP core shell nanowire was demonstrated at cryogenic temperatures due to poor material quality [15]. After several attempts and optimisations, room temperature lasing was

achieved on GaAs/AlGaAs nanowires using both metal organic chemical vapour deposition (MOCVD) and molecular beam epitaxy [18-20].

Initially most of the lasers were achieved using GaAs-based nanowires as defect-free GaAs nanowires can be realised using vapour-liquid-solid (VLS) growth mechanism. However, GaAs nanowires need passivation due to high surface recombination velocity which leads to complexities in device fabrication and increases cavity loss through absorption [19]. On the other end, InP nanowires have significantly lower surface recombination velocity [21]. Lasing from non-passivated InP nanowire was demonstrated by Gao et al. at room temperature [22].

To increase the efficiency of the lasers in terms of threshold current, differential gain, modulation bandwidth and temperature stability, quantum confinement of the active region is required [8]. Superior device performance can be achieved by discrete density of states using quantum confinement. Nanowire lasers with quantum confinement have been demonstrated using axial InGaAs quantum dots in GaAs/AlGaAs core-shell structure [23], GaAs/AlGaAs core-shell multi-quantum well structure [24-26], GaAs/InGaAs multi-quantum disk [27] and InP/InAs multiple axial quantum wells [28].

Apart from quantum confinement, several other techniques were used to achieve low threshold lasing. This includes a thin layer of crystalline silver to confine plasmonic modes in GaAs/AlGaAs core-shell nanowires [29], continuous wave lasing in GaAs/AlGaAs core-shell nanowires at 4K [30], p-doping to enhance radiative efficiency in un-passivated GaAs nanowires [31], enhancing quantum efficiency using antenna design in InP nanowires [32], hexagonal photonic cavity of array of GaAs/InGaAs/GaAs nanowires removed from substrate using polydimethylsiloxane (PDMS) [33] and thin metal layer for high thermal conductivity and enhanced confinement for quantum well structures of both core-shell GaAs/AlGaAs nanowires and axial InP/InAs nanowires[26, 28].

Takiguchi et al. used Si photonic crystal cavity, transferred InAsP/InP nanowire on it and demonstrated lasing [34, 35].

2.2.1.2 Ensemble nanowires

Several attempts have been made to demonstrate lasing of III-V compound semiconductor nanowires on Si. Monolithically integrated InGaAs/GaAs nanowire laser on Si, working at room temperature was first demonstrated by Chang-Hasnain's group [36]. Helical cavity modes instead of traditional F-P modes were observed in such geometry. They performed extensive study of this structure and concluded that InGaP shell is better passivating layer than GaAs [37]. They have also demonstrated lasing from needle shaped InP on Si [38], whisper gallery mode in InGaAs nano needles [39] and InP/InGaAs multiple quantum well laser using quantum confinement [40, 41]. Helical modes have also been reported while demonstrating room temperature lasing in polytypic InP nanowire on (001) Si using ART technique [42, 43].

Photonic crystal cavities can provide ultra-low threshold because they have strong optical confinement in small mode-volume and have high quality factor [44]. Room temperature lasing from InGaAs/InGaP nanowires, monolithically integrated on Si on insulator platform was demonstrated using photonic crystal cavity [45-48]. Photonic cavity was formed by nanowires and air holes which provide optical confinement by total internal reflection. In addition, single nanowire lasers grown on Si substrate with high spontaneous emission factor were demonstrated on GaAs/AlGaAs nanowire [49].

2.2.2 Electrically injected nanowire lasers

Miniaturisation of lasers is worthwhile if electrical pumping is possible for practical application of the devices. Electrical injection is one of the best features of semiconductor laser which is

advantageous over other lasers such as solid-state lasers, where optical pumping is the only option. For the last two decades, there has been immense global effort to demonstrate electrically injected nanowire lasers using innovative cavity designs and methods to overcome other requirements such as defect free nanowire, heavily doped p and n junction, high quality contacts, good thermal dissipation, integration with Si and mass production [16]. However, the progress in this area is still very slow and limited.

The first electrically injected nanowire laser was demonstrated in 2003 in n-doped CdS nanowires by transferring them onto heavily doped p-Si substrate. The devices could only work at low temperatures due to non-uniform current injection and poor optical quality [11]. After significant attempts, room temperature lasing was shown in ZnO nanowire arrays using electron-hole plasma mechanism. The devices were fabricated by growing p-doped ZnO nanowires on an n-doped ZnO thin film on sapphire substrate [12]. In addition to F-P cavity modes, several groups have reported random lasing from ZnO nanowire arrays [50-57]

Noteworthy progress has been made in group III-N nanowires to demonstrate lasing in ultraviolet regime. InGaN/GaN axial quantum well nanowire arrays grown on (001) Si were used for tunable, room temperature and continuous wave pumping. To enhance the reflectivity, SiO_2/TiO_2 Distributed Bragg refractor mirror was used [58-60]. Circular PMMA/air dielectric distributed mirrors were also used to achieve room temperature, low threshold lasing from InGaN/GaN triangular-shape nanowires formed via the top-down approach [61]. In addition, Anderson localisation was exploited to demonstrate room temperature, tunable wavelength random lasing from AlGaN/GaN core-shell nanowire arrays grown on Si [62-66].

In III-V semiconductors for near infrared wavelengths, pioneering work has been done in metal cavity lasers. A metal shell is used to tightly confine light within the sub-wavelength

semiconductor structure. Theoretically, the advantages of these metal cavity lasers are ultra-small physical volume, fast modulation and good heat dissipation at room temperature [67]. Hill et al. reported first metal cavity laser on InP/InGaAs/InP nano-pillars surrounded by a thin silicon nitride insulating layer and then coated with gold. High optical losses due to metal restrict lasing only at low temperatures [68]. Several attempts have been made to achieve room temperature and continuous wave lasing in metal cavity lasers including optimising insulating layer thickness [67], using rectangular geometry instead of circular to control dimension individually which helps in mode selection [69, 70], using aluminium oxide or SiO_2 instead of silicon nitride for better thermal management and passivation [71, 72], using tunnel junction for better current injection [73-75].

However, for practical applications several challenges such as complex device fabrication, low device lifetime, significant heating, efficient coupling in free space or waveguide structure need to be addressed [7, 69]. All the metal cavity lasers use top-down approach to obtain the nanostructures. Device lifetime is low due to damage at the surface caused by etching [7]. Moreover, insulating layer used to form a semiconductor-dielectric-metal core-shell structure can cause heating problem [76]. To address the majority of these problems, one of the feasible solutions is F-P cavity lasers using bottom-up approach. Although there are several reports on III-V LEDs however, electrically injected F-P cavity lasing in III-V nanowires is yet to be reported.

2.3 Review on III-V nanowire LEDs

Several structures have been investigated to study the EL properties from nanowires. Nanowires can be grown in 2 different configurations; axial and radial (core-shell). Radial structure has an advantage over axial structure due to the larger recombination region owing to a higher surface area-to-volume ratio. However, radial structures suffer with non-uniform current injection. The first axial nanowire array LED was reported in 1992 with tapered GaAs nanowires [77]. Following

this, studies on axial GaAs nanowires with improved morphology [78, 79] as well as radial heterojunction structure such as n-GaAs/InGaP/p-GaAs [80] and GaAs/InGaP [81] have been reported. To enhance light output, quantum well and quantum dots in the GaAs nano-LEDs have also been investigated [82-86].

The first InP nanowire LED was demonstrated by Lieber's group using axial single nanowires [87, 88]. Subsequently, more studies of doping profiles, far field properties and current injection properties were performed for axial homojunction InP nano-LEDs [89-92]. To achieve telecommunication wavelengths, quantum well and quantum disks were incorporated in InP nanowires and LED properties were investigated [93-97]. Modulation frequency of up to 3 GHz was also explored in InP/InAs quantum dot single nano-LEDs [98]. In addition to this, LEDs from InP-InAsP single quantum dot, AlGaInP core−shell nanowires and GaInP/AlGaInP quantum well nanowires have also been studied [99-101].

2.4 Challenges to realise III-V nanowire electrically injected F-P cavity lasers

2.4.1 Lower gain medium

Compared to the traditional bulk lasers, nanowire lasers have smaller active gain medium as the volume of nanowires is significantly lower. Due to its small size, mirror losses in the nanowire laser are higher. Furthermore, nonradiative recombination at the surface due to higher surface- to-volume ratio and scattering losses is also higher. To compensate the losses, higher gain is required which is obtained by injecting higher current. However, high current injection leads to significant heating of device which reduces gain [8]. Higher gain is the reason why the majority of optically pumped lasers requires strong pumping [7, 19, 36]. In optically pumped lasers, the entire active medium contributes to the gain. However, gain is limited to electron and hole diffusion length scales in

electrically injected nanowire lasers and remaining active medium act as an absorbing medium. As a consequence, electrically injected nanowire lasers require optimised design and is more challenging to achieve than optically pumped lasers.

2.4.2 Doping challenges

Incorporation of precise and high doping levels still remain elusive in III-V semiconductor nanowires, which makes it difficult to inject high current in the device without generating significant heat. The most prevalent method to grow nanowire is VLS where a metal nanoparticle such as gold is used as a catalyst. Controlled and uniform doping with gold catalyst is difficult because surface doping on the nanowire sidewalls occurs by the vapour-solid mechanism, which causes non-uniform distribution of dopants. This happens because nanowire sidewalls remain in contact with the dopants for a longer time than the core of the nanowire, so more dopants are incorporated there, causing a radially non-uniform distribution of dopants [102, 103]. Moreover, the use of excessive dopants can affect nanowire morphology [31] and can cause non-uniform axial doping due to incorporation and subsequently precipitation of dopants from nanoparticles [103]. To achieve uniform doping, selective area epitaxy (SAE) is a more promising method. Additionally, with SAE, larger diameter nanowires can be obtained without any defects such as twinning, and polytypism, which is another limitation of the VLS technique [22]. However, getting high p-doping in InP nanowires as well as defect-free structure in GaAs nanowires using SAE is still a challenge [20, 104]. Additionally, incorporation of dopants reduces carrier lifetime which may be detrimental for some device applications [105]. Furthermore, lower mobility of carriers in nanowires as compared to its bulk counterparts further reduces device performance [21].

2.4.3 Excessive heating

Excessive heating can significantly deteriorate the performance of device. The thermal conductivity of III-V nanowire is much lower than that of the bulk [106, 107]. Increase in surface-to-volume ratio leads to increased scattering of long wavelength phonons which are the dominant heat carriers at the nanowire surface [108]. Therefore, heat sinking is a serious issue in nanowire devices. Additionally, as mentioned in 2.2.1.1, most of the optically pumped lasers reported are those transferred onto a low refractive index substrate like SiO_2/Si. Lower thermal conductivity of SiO_2 and surrounding medium (air) as well as small contact area of vertical nanowires still attached to their growth substrates lead to local heat generation. This is why the majority of optically pumped lasers have been demonstrated under pulsed laser excitation. In the case of electrical injection, additional heat is generated due to the resistance in the device. Moreover, due to fabrication limitations and low doping concentrations, it is difficult to make high quality Ohmic contacts, which also contribute to localised heating near the contacts.

2.4.4 Challenges in fabrication process

Due to the small size of the nanowire cavity (usually a few μm's in length and a few 100's nm in diameter), the precise dimensions are very critical for operation. In SAE, although the morphology of all nanowires in an array is similar, not all of them have exactly same length and diameter [96, 109, 110], leading to challenges in contact fabrication, particularly in an axial p-n junction.

Due to its very small size, the traditional contact fabrication technique like photolithography is not much useful in case of single nanowire devices. Generally, electron beam lithography (EBL) is used to make contact to the nanowires which is time consuming and complicated in terms of alignment. Contact fabrication for axial structure is relatively easier than for radial structure. The positioning of metal contact is also very important for a good working device as they can result in

high absorption. In the case of a planar device, metal contact is made far from the active region to avoid metal absorption. However, for nanowire devices, metal contact is usually made near the active region, which introduces additional loss. Hence, an appropriate nanowire device design is required to realise F-P cavity lasers. Recently, with the advancement in TCOs, metal absorption could be substantially reduced by replacing metals with ITO [58, 60], albeit at the cost of increased contact resistance. Naturally, there is a trade-off between conductivity and absorption.

2.5 Transparent conducting oxides (TCOs)

There is a growing interest in replacing conventional metal contacts with TCOs, mainly because of significantly lower absorption and conductivity close to that of metals [111]. TCOs are traditionally wider band gap materials (>3.1 eV) which result in lower absorption in visible and infrared region making them an ideal candidate for III-V optical devices [112]. The electrical conductivity of TCOs can vary from insulating to nearly metallic, depending on the stoichiometric ratio. Moreover, they can act as a dopant layer (either p or n) with higher carrier concentration which alleviate the process of optimising doping levels during growth of the nanowires. The electrical conductivity of TCOs is due to the vacancies generated either due to deficiency of metal or oxides. Oxygen deficient TCOs are generally n-type as each oxygen vacancy contributes to two electrons [113]. Similarly, metal deficient TCOs are usually p-type. Doping of TCOs is also prevalent to enhance the conductivity [114].

A wide range of commercially available n-type TCOs such as ZnO, SnO_2, In_2O_3, CdO, Sb-doped SnO_2, F-doped SnO_2, ITO, Al-doped ZnO and Ga-doped ZnO have been investigated for practical use [115]. A myriad of dopants such as Cr, B, Sc, Y, In, Mg, Ga in copper-based oxides, Li, Al, Ga, In and N in tin oxide, NiO and $SrCu_2O_2$ have been investigated to achieve high mobility, high carrier concentration and low absorption in p-type TCOs [116, 117]. However, reports on using p-type

TCOs in devices are scant. The reason behind this is the strongly localised O 2*p*-derived orbital in the valence band [118, 119]. Therefore, modification in the valence band is required to reduce localisation to achieve p-doped TCOs.

2.6 Conclusions

In summary, this chapter covered the concepts and relevant information used in this thesis. First, it described the working principle of semiconductor lasers and LEDs. Following which, progress in optically pumped nanowire lasers was reviewed. For practical applications, electrically injected nanowire lasers are required. Therefore, advancement in the electrically injected nanowire lasers with potential challenges was discussed. Finally, the importance of TCOs as a replacement for metal contacts was highlighted.

Chapter 3. Experimental and Numerical Techniques

In this chapter, we describe both the numerical techniques used for laser design as well as the experimental methods from growth to the fabrication. For fabrication, we provide in-depth detail of various deposition and etching tools used in this thesis. We also describe some of the key characterisation instruments used to study the optical, electrical and structural properties of different structures. This chapter is divided into four sections that cover experimental techniques, growth, and fabrication, followed by numerical techniques used in this thesis.

3.1 Experimental techniques

3.1.1 Plasma enhanced chemical vapour deposition (PECVD)

PECVD is one form of chemical vapour deposition where additional kinetic energy for chemical reaction to occur at the surface of substrate is provided by plasma. The reactant gas is introduced between two electrodes in a parallel plate configuration - a grounded electrode on bottom and an RF biased electrode at the top. The capacitive coupling between these two electrodes is required to transfer RF power to the precursors (gases) to form plasma. This makes it possible to deposit high quality film at relatively low temperatures [120]. Due to this feature, it is a very popular tool in the semiconductor industry and is mainly used for low melting point substrates and photoresist. Figure 3-1 shows a schematic of a typical PECVD system. Substrate temperature, chamber pressure, plasma power and gas composition play important role in the resulting film properties, both, electrical and optical. The table 3-1 shows the impact of increasing or decreasing these parameters. The refractive index can be easily controlled by changing the gas ratio.

Table 3-1 Effect of different parameters on the deposited SiO_x film

	Deposition rate	Refractive index	Deposition rate uniformity	Refractive index uniformity	Film stress	BHF Etch Rate
↑ SiH_4 flow	↑↑	↑	↓↓		↑↑ (more tensile)	↑↑
↑ N_2O:SiH_4 ratio	↓	↓	↓	↓		
↑ 13MHz power	↑	↓	↑↑		↓↓ (more compr.)	↓↓
↑ Pressure	↓		↑	↑		
↑ Temperature	↑	↑				↓↓↓

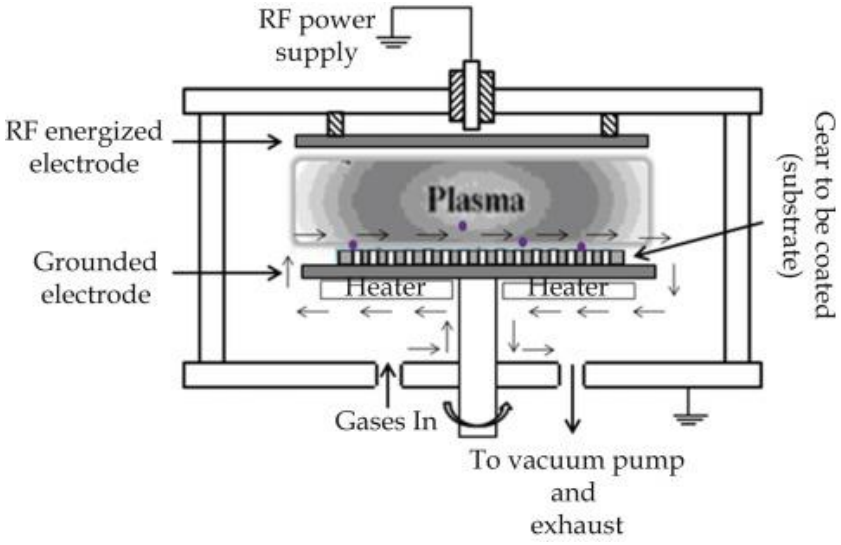

Figure 3-1 Schematic diagram of PECVD. Reproduced from [121].

In this thesis, Oxford Plasmalab 100 PECVD chamber was used to deposit SiO_2 at temperature of 300ºC. N_2, N_2O and SiH_4 were used with flow rate of 116, 710 and 9 sccm, respectively at 650 mTorr pressure. The deposition power was set to 20 W. During SiO_2 deposition, SiH_4 acts as the source of Si and N_2O that of oxygen. N_2 is used as a dilute gas to improve uniformity of the deposited SiO_2. 13.56 MHz RF power generator was used to generate the plasma.

The simplified reaction is as follows:

$SiH_4\,(g) + 2N_2O\,(g) \rightarrow SiO_2\,(s) + N_2\,(g) + H_2O\,(g)$

3.1.2 Electron beam lithography (EBL)

EBL was used for patterning the substrate for SAE and nanowire contact fabrication. EBL uses a focused beam of accelerated electrons to draw fine patterns on a substrate covered with electron sensitive resist. The incident electron beam interacts with the resist and changes its property such that the exposed part either dissolve in a developer (positive resist) or cross-link further so that unexposed part dissolve in a developer (negative resist). Since the wavelength of electron is much smaller than light, it provides remarkably high resolution as compared to photolithography [122]. Furthermore, arbitrary patterns can be directly written on the resist thereby, eliminating need of a mask. One disadvantage of EBL however is the patterning speed – it is much slower than other lithography techniques [122, 123].

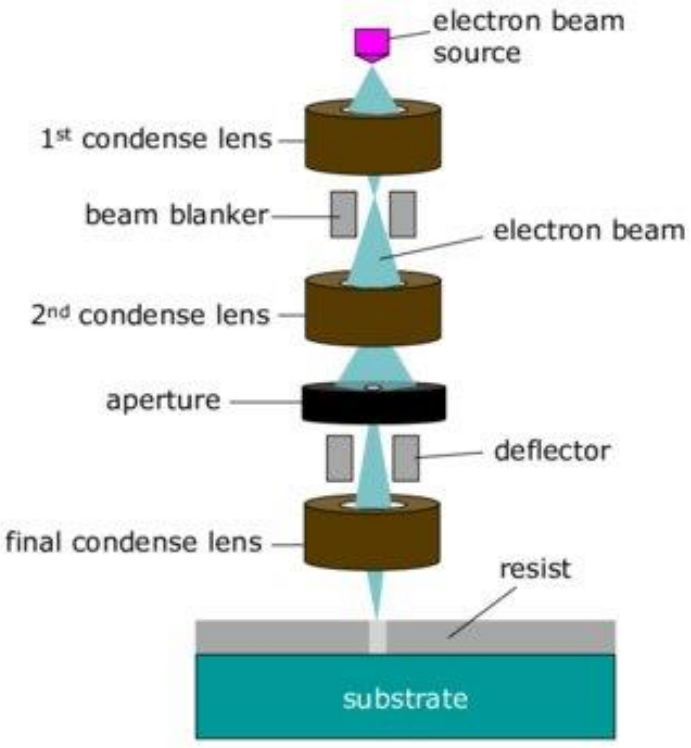

Figure 3-2 Schematic diagram of the EBL system. Reproduced from [124].

A Raith 150 system was used for all the EBL work reported in this thesis. Several key factors such as accelerating voltage, dose, and aperture were optimised to get desired outcomes. Dose is the number of electrons per unit area during writing. Resolution decreases with increasing dose as there will be more electron scattering in the resist and backscattering from the substrate (secondary dose). An aperture controls the amount of electrons incident on the substrate. Larger aperture means more electrons are striking on the substrate and hence writing time decreases. However, this degrades resolution too. Increasing the accelerating voltage can enhance the resolution, however, the required dose increases due to decrease in secondary dose from the substrate, resulting in longer writing times. While lower accelerating voltage requires a shorter time to write the pattern, resolution is compromised due to higher backscattering of electrons from substrate, resulting in patterns which are much wider than designed [125]. A way to work around to this problem is by using proximity correction software, incorporated in the EBL tool. Hence, it is a fine balance between these parameters to get the desired outcomes in terms of reasonable speed, high resolution and reliability.

In this work, mr-POS EBR resist was used for EBL patterning to grow nanowires. This resist was chosen because it exhibits better selectivity during dry etching as an etch mask when compared to traditional and more popular EBL resist – PMMA [126]. The acceleration voltage was 20 kV and doses were varied depending on the thickness of the resist. As the writing field size and the array pattern size were same – 100 µm x 100 µm, there was no need for stitching. To fabricate contacts on single nanowire, undiluted ZEP was used. Detailed information about contact fabrication is mentioned later on.

3.1.3 Metal-organic chemical vapour deposition (MOCVD)

MOCVD is a chemical vapour deposition technique used to grow mainly III-V and III-N semiconductors. In MOCVD epitaxial growth occurs on the substrate. The gaseous form of the reactants of the material to be grown are mixed at high temperature and chemical reaction occur forming the epitaxial layer of the material. The advantage of MOCVD is it does not require high vacuum and is suitable for mass production when compared to its counterpart molecular beam epitaxy [127].

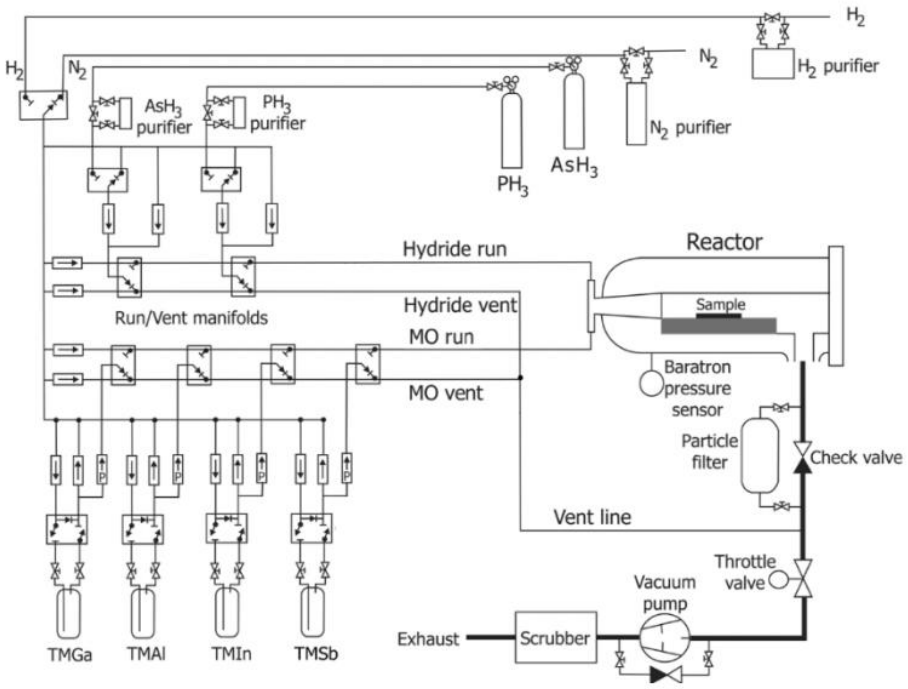

Figure 3-3 Schematic diagram of the MOCVD reactor used in this thesis.

In this thesis, an Aixtron 200/4 MOCVD system was used. The metal precursors in this MOCVD are trimethylgallium, trimethylindium, and trimethylaluminium and trimethylantimony and the non-metal hydride sources are AsH_3 and PH_3. For p doping diethylzinc and for n doping SiH_4 are used. The metal organic precursors are either solid or volatile liquid which have low vapour pressure that inhibits them from reaching the growth chamber. Hydrogen gas (H_2) is used as a

carrier gas to deliver them to the chamber. Ultra-high purity of H_2 is passed through the bubbler which stores the metal organic precursor to pick up a known amount of metal organic vapour and bring it to the growth chamber. The amount of metal organic material is controlled by controlling the temperature and pressure of the bubbler, and the flow rate of H_2 gas. The non-metal hydride sources are kept in high pressure cylinders. The key parameters for optimising the growth rate are the growth temperature, molar flow rate of the precursors and their stoichiometric ratio (V/III). Total flow rate of all the gases including carrier and pusher etc. are kept constant to achieve laminar flow and uniform growth. Generally high temperature is used during growth for efficient decomposition of precursors [128-130].

3.1.4 Reactive ion etching (RIE)

RIE is a dry etching method in which chemically reactive plasma is used to etch metals, dielectrics or semiconductors. RIE is widely used in micro- and nanofabrication due to its directionality over wet chemical etching [131]. In RIE, two plates inside a vacuum chamber are connected with a coupling capacitor and a radio frequency source. Using RF power, the gas between the plates is ionised which results in plasma consisting of electrons, ions and free radicals. The chemically reactive species in the plasma are accelerated towards the sample due to DC bias, react with the sample and etch away material by forming volatile products. This type of etching is more directional and have very less lateral etching regardless of the crystalline orientation due to the directional physical bombardment of the ions.

In this thesis, Oxford Plasmalab 80Plus RIE system was used to etch the SiO_2 layer which has been exposed after the removal of electron beam resist. To etch 150 nm of SiO_2 layer with hole opening of around 50 nm in the electron beam resist layer, CHF_3 flow of 50 sccm, pressure of 30 mTorr and RF power of 200 Watts were used for 16 mins.

3.1.5 Microwave plasma etching (Barrel Etcher)

In a barrel etcher, a plasma is used either for cleaning or etching. During cleaning, plasma is generated either from O_2 or Ar which removes all the organic particles from the substrate under reduced atmosphere pressure. Furthermore, the plasma leaves free radicals which enhance the adhesion of polymers on the substrate. For chemical etching, the material needs to react with the plasma and form volatile by-products [132].

In this thesis, PVA Tepla Gigabatch 310 M system was used to clean the substrate as well as to remove remnant layer of resist after developing.

3.1.6 Inductively coupled plasma reactive ion etching (ICP-RIE)

ICP-RIE etching is a plasma-based etching similar to RIE mentioned above, but with additional inductively coupled plasma source. High density plasma is generated in the chamber due to inductive coupling between the RF antenna and an inductive element. The RF antenna creates an alternating magnetic field and induce an electric field, which provides energy to the electrons to ionise the gas molecules. The plasma density is hundreds of times higher than that of RIE. This makes it possible to etch the sample at very low pressures and at higher etch rates. By separately controlling the ICP power and RF power (RIE), it is possible to optimise the etching process to obtain structures with lower surface roughness, high aspect-ratio and vertical sidewalls. The ICP source increases the etch selectivity and makes it possible to tune the etch window for chemical etching (high ICP and low RF powers), physical/chemical etching (moderate ICP and RF powers) or physical etching (low ICP and higher RF power) depending on the need [133, 134]. ICP-RIE is widely used for etching a variety of materials such as oxides, nitrides, metals and semiconductors based on silicon, III-Ns and III-Vs.

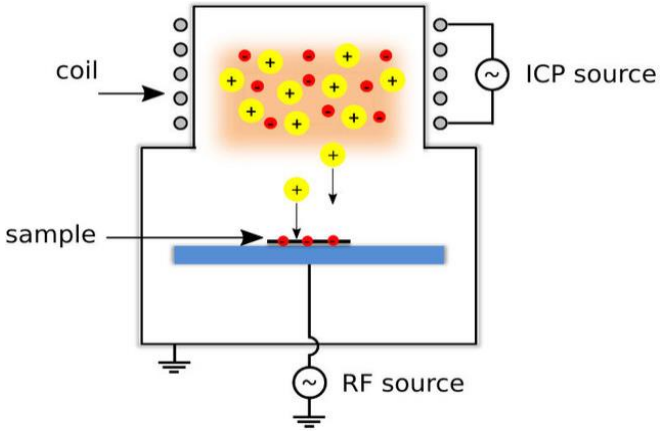

Figure 3-4 Schematic of an ICP-RIE system. Reproduced from [135].

In this thesis, a 200iP system from Samco Inc. was used to etch the SU-8 layer. Etching using oxygen and argon chemistry (argon is mainly used to sustain the plasma) resulted in the formation of micro-masking and damage to InP nanowires as shown in Figure 3-5(a). Micro-masking is a result of accumulation of antimony on the surface while etching and leads to high surface

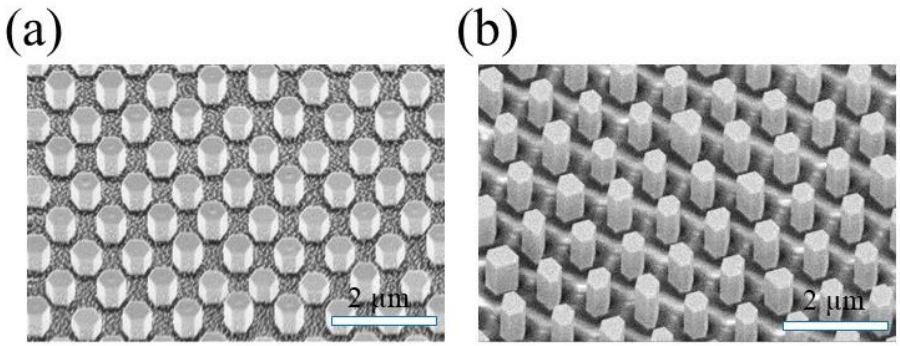

Figure 3-5 SEM images of the InP nanowire array after SU-8 etching at 15° tilted view with (a) Ar/O_2 and (b) $SF_6/O_2/Ar$ chemistry.

roughness [136]. To overcome these problems, etch optimisation studies were carried out by introducing SF_6 in addition to O_2 and Ar. We found that the chemistry of $SF_6/O_2/Ar$ (2/10/20 sccm) with ICP/RF power of 300/20 W at pressure of 1.33 hPa yields very smooth etching without any damage to nanowires as shown in Figure 3-5(b).

3.1.7 Sputter deposition

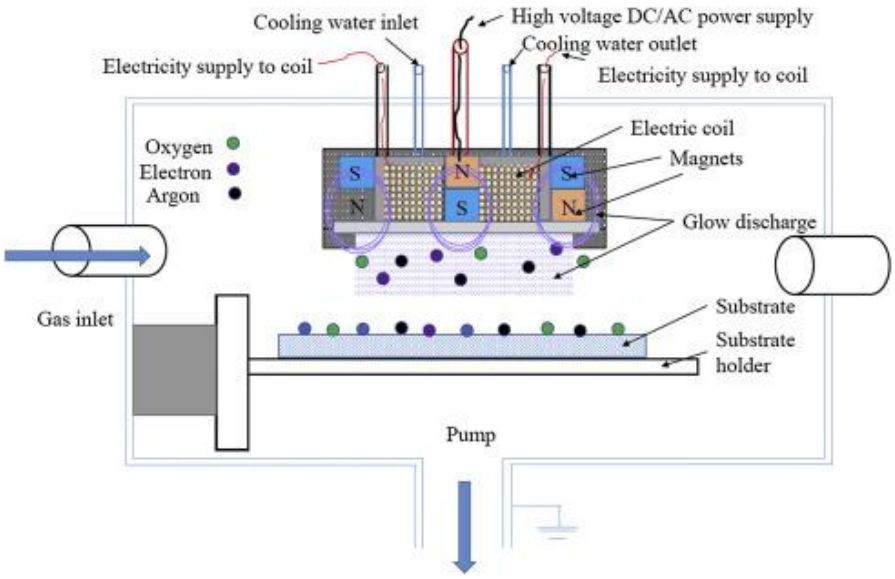

Figure 3-6 Schematic of deposition mechanism in a magnetron sputter system. Reproduced from [137].

Sputter deposition is a physical vapour deposition technique used to deposit thin films. It is a plasma system where the target (material to be deposited) is negatively biased and rest of the chamber including the substrate holder is grounded for DC sputtering and RF biased for RF sputtering. DC sputtering is used for conducting targets while RF sputtering can be used for any targets including dielectrics. For metals, DC sputtering is the preferred choice as it is faster. Prior to deposition, a gaseous plasma is formed using Ar^+ ions. Ar is used to generate plasma due to its low reactivity with the deposition material. These ions are accelerated towards negatively biased solid target composed of the material to be deposited. This physical bombardment of Ar^+ ions ejects particles from the target which then travels to the sample surface and condenses, thereby, forming a thin film of target material. The density of Ar^+ ions near the target can be increased by incorporating magnets in the gun configuration. This form of sputtering is called magnetron sputtering and is the most widely used form. Figure 3-6 shows the schematic of a magnetron sputter

deposition tool. Often, reactive gases such as oxygen and nitrogen are introduced in the chamber during metal sputtering to form oxides or nitrides of that metal at the sample surface. This is called reactive sputtering. A distinct advantage of reactive sputtering instead of using metal-oxide target is that the stoichiometry of these resulting oxides and nitrides can be controlled by varying the gas ratio of Ar and O_2/N_2 while it is fixed when using a metal-oxide target.In this thesis, an AJA ATC 2400 sputter deposition system was used. This system has five non- magnetic (metals and oxide) and one magnetic target guns which are separately powered. Nitrogen, oxygen, argon and mixture of these gases can be flown into the chamber and the desired flow is controlled by mass-flow controllers. Depositions of n-type SnO_x, p-type $Sn_xNi_yO_z$, ITO and Au were done using sputter.

3.1.8 Atomic layer deposition (ALD)

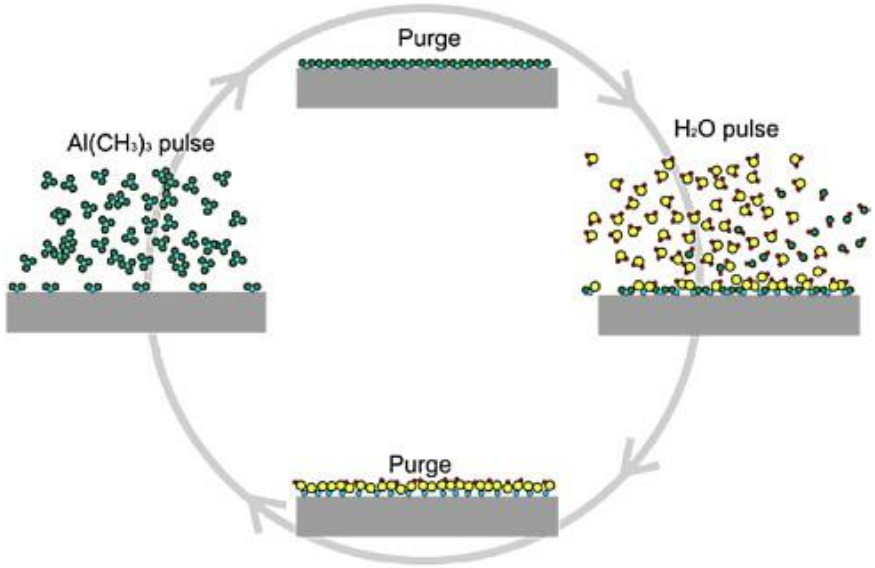

Figure 3-7 Schematic showing the various cycles in an ALD deposition of Al_2O_3. Reproduced from [138].

ALD is a chemical vapour deposition method that deposits thin films monolayer by monolayer. The advantage of ALD is it produces high quality conformal film with controllable thickness and

almost no pin-holes [139]. However, it is a time-consuming process [140]. For a binary material AB with precursor AD and BC, the deposition consists of 4 cycles.Adsorption of AD on the substrate

2. Removal of unreacted AD and by-products with a flow of N_2 or Ar gas at high pressure.
3. Adsorption of BC on the substrate and reaction between AD and BC.
4. Removal of unreacted BC and by-products with flow of N_2 or Ar gas at high pressure leaving layer AB on the substrate.

Usually, a metal-organic source is used as the metal precursor while either water, O_2 plasma or ozone (O_3) are used as a source for oxygen. It is also possible to deposit metal nitrides using NH_3 gas instead of oxygen source. Often, a plasma source is used instead for oxygen or nitrogen deposition cycle. As plasma radicals have higher kinetic energy, high quality deposition at lower temperature is possible. Precise thickness of the film (to monolayer accuracy) can be controlled by changing the number of cycles.

In this thesis, both Al_2O_3 and ZnO films were deposited using a Picosun SUNALE R-200 system. trimethylaluminium and diethylzinc were used as the metal-organic precursor for Al and Zn and water as a source for oxygen. The deposition was done at 150°C. Pulse time for trimethylaluminium and diethylzinc was 0.1 s followed by 4 s of N_2 purge in between pulses. Pulse time for water cycle was also 0.1 s followed by 4 s N_2 purge. The number of cycles were set to obtain the desired thickness of both the films.

3.1.9 Electron beam evaporation (E-beam evaporation)

Electron beam evaporation is a physical vapour deposition technique where the target material is evaporated using high energy electron beam emitted from a tungsten filament. The evaporated material precipitates on the substrate which is maintained at much lower temperature than the crucible (pocket where material to be deposited is placed). The entire process is done at high

vacuum. The high energy focused electron beam locally heats the source material which makes it possible to deposit high melting point metals. Furthermore, the deposited film is clean and without contamination due to this localized melting. It is a line of sight process and the most widely used technique for doing a lift-off process.

In this thesis, a Temescal BJD 2000 e-beam evaporator was used to deposit Ti and Au as a contact for all the devices. To control the precise thickness of the metal, a quartz crystal monitor is used for real time monitoring and once the targeted thickness is achieved, the shutter closes immediately and stops deposition. Uniformity of deposition is achieved by a rotating the wafer holder.

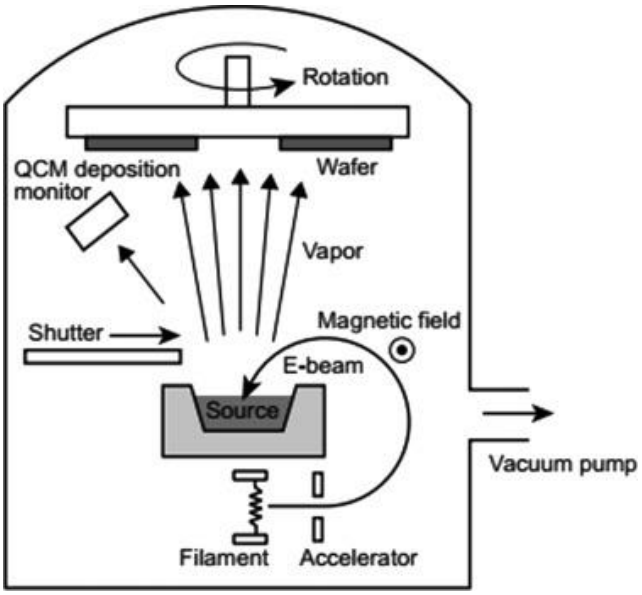

Figure 3-8 Schematic of an e-beam evaporation technique. Reproduced from [141].

3.1.10 Scanning electron microscopy (SEM)

SEM is a technique used to form image of very small structures of the order of nanometre with the help of backscattered electrons. The high magnification is due to wavelength of electron beam (de Broglie wavelength) which is much smaller than that of light. The beam of electron is produced by an electron gun and focused using magnetic lenses. This focused electron beam interacts with

the sample and generate various signals that are collected by different type of detectors. Figure 3-9 shows the different types of signals generated by electron-matter interaction. Apart from imaging, different detectors fitted inside the microscope can provide vital information about surface topology and composition of the specimen. Topological images are mainly formed by backscattered electrons. Inelastic scattering of incident electron beam by another material cause electrons to escape from the samples (secondary electrons). Backscattered electrons are the elastically scattered electrons by the nuclei of the atoms. These captured secondary and backscattered electrons formed a grey scale image. The number of backscattered electrons depends on atomic number of the atom, hence provide the information about the chemical composition of the sample [142]. The intensity of secondary electron provides information about topology of the sample. In this thesis, only secondary electrons were used to image sample surface to study the topology.

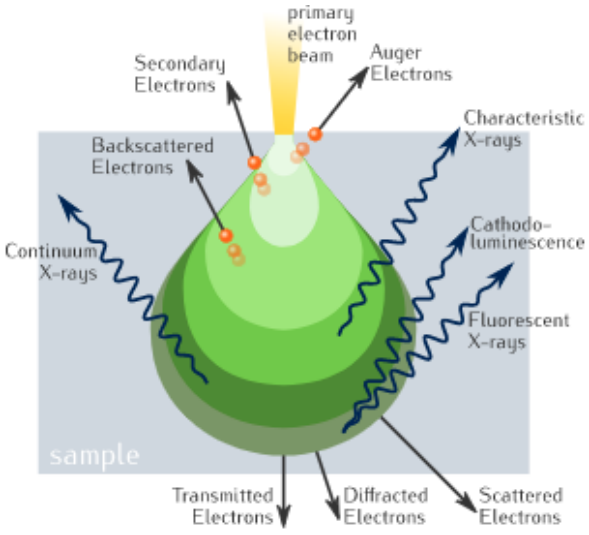

Figure 3-9 Possible signals generated by interaction of electrons with a sample.Reproduced from [143].

Reasonably conductive sample is required for SEM to avoid accumulation of electrostatic charge. For non-conductive samples like oxide or polymer, a thin layer of metal was first deposited to

prevent charging. The semiconductor used in thesis i.e. InP does not need an additional coating as it is fairly conductive. However, SU-8 requires a thin layer of gold coating which was done by sputter deposition. FEI Helios 600 Nanolab dual-beam FIB/SEM system and a FEI Verios 460 system were used for examining the dimensions of the nanowires and other features at different fabrication steps.

3.1.11 Micro-photoluminescence spectroscopy

Photoluminescence (PL) spectroscopy is a technique in which photons emitted from any material is captured when excited by an optical source. This technique is commonly used to analyse the

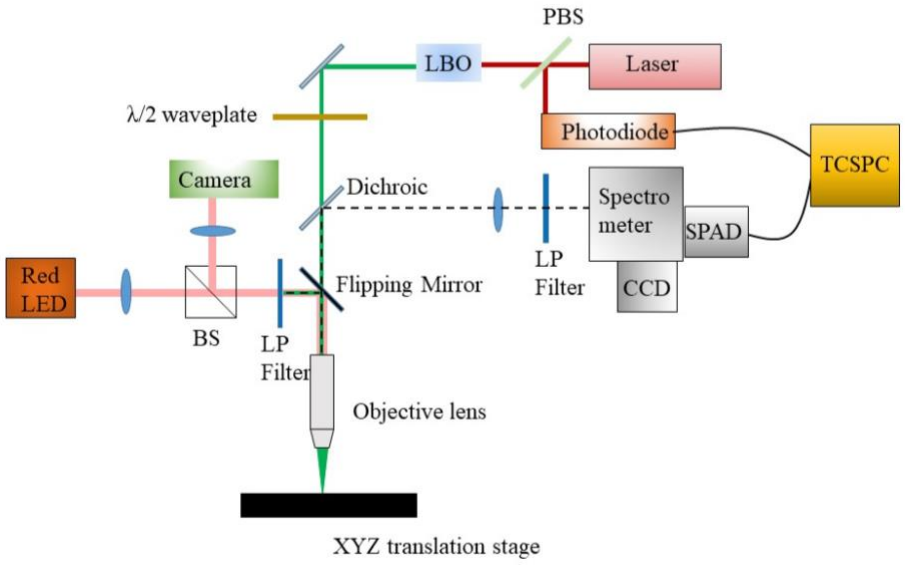

Figure 3-10 Schematic diagram of the micro-PL system.

optical properties of semiconductors. When a semiconductor material is pumped with higher energy than its bandgap, charge carriers (electrons and holes) are generated. These carriers can recombine by spontaneous emission and produce photons. The shape and peak position of the PL curve gives various information like bandgap of material, crystal structure, lattice temperature, impurities and thermal broadening [144, 145].

In this thesis, PL measurements were done using a home-made micro-PL system. To examine the properties of individual nanowires, spot size of the order of nanowires is required. This is done by integrating an optical microscope with PL measurements and this technique is known as micro-PL. For exciting the samples, a pulsed solid state laser (femtoTRAIN IC-Yb-2000, λ = 1044 nm, repetition rate 20.8 MHz, pulse length 400 fs) with a frequency doubler to 522 nm was used. The emitted light was focused onto the slit of a monochromator with a grating of 150 lines/mm (Acton, SpectraPro 2750) and detected by a Si-CCD (Princeton Instruments, PIXIS). A time correlated single photon counting (TCSPC) system is also connected to analyse the transient decay of the PL signal to extract the lifetime of the photo generated carriers.

3.1.12 Electroluminescence (EL)

Electroluminescence is an optoelectronic phenomenon in which current is passed through a p-n junction and photons are emitted by the recombination of excess electrons and holes. When current is applied through an external bias in a p-n junction device, electrons and holes enter from n- and p-type segment, respectively. These carriers diffused in the material, recombine and may emit photons, particularly in direct bandgap materials. The spectrum of these photons can then provide information about the device.

In this thesis, spectral measurements were done using a home-made micro-PL as described in section 3.1.11. Current was passed through the device using a Keysight B2902A source/measurement unit. For temperature dependent EL and I-V measurements, a Linkam stage was used which provide accurate temperature control from -195 to 350°C.

3.1.13 Electron beam induced current measurements (EBIC)

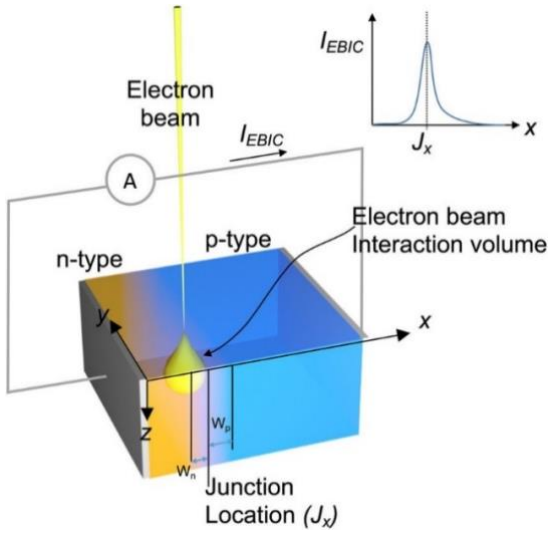

Figure 3-11 EBIC current generation process. Reproduced from [146].

EBIC is a characterisation technique that makes use of scanning electrons, typically in a SEM, to detect junctions in the device and to identify defects in the active region. The incident beam of electrons results in electron-hole pair generation at the p-n junction. The sample is connected to external power supply using special EBIC probes such that these electrons and holes drift by the internal electric field present in the depletion region resulting in a current flow to the probes. The beam is scanned along the sample and current is taken for each incident beam position. There will be very high current generated in the depletion region and is seen as a bright region in the EBIC image of the current map. This study gives information about the depletion region thickness as well as quality of the junction.

In this thesis, an FEI Helios 600 Nanolab focused ion beam (FIB) system equipped with Kleindiek NanoControl NC40 nano-manipulators was used to study the junction properties of n-ZnO/p-InP core-shell nanowires.

3.1.14 X-ray photoelectron spectroscopy (XPS)

XPS is a characterisation technique that uses X-rays to study the electronic structure and bonding in metals, semiconductors and dielectrics. Using soft X-rays, it is possible to limit the interaction to few nanometres (< 10 nm) and study the surface properties of the material. Hard X-rays, on the other hand, are used to study properties deeper from the near surface regions such as buried interfaces and bulk electronic structure as they can penetrate deeper into the material. Typically, a combination of soft and hard X-rays are used for in-depth study of a given material.

XPS is based on photoelectric effect. When an atom is irradiated with X-rays, the energy of the X-rays is transferred to electrons in the atoms which in turn may be excited to higher energy levels or even ejected from the atom. Depending on the irradiated energy and energy level of the atom, the emitted photoelectron will have kinetic energy according to the relation:

$$KE = h\nu - \Phi - BE \tag{3.1}$$

where Φ is the work function of the material, KE is the kinetic energy and BE is the binding energy of the photoelectron. By measuring the kinetic energy of the emitted electron, it is possible to calculate the binding energy of the material [147]. Since each element has a unique binding energy, it is thus possible to distinguish elements in the studied material. The experiments are conducted in vacuum so that the emitted electron reaches the detector without colliding with molecules in atmosphere. XPS can be used for solid, liquids and gases. The depth to which X-rays interacts with the material directly depends on their energy. By varying the energy of incident X-rays, it is thus possible to study the electronic structure as a function of depth.

In this thesis, XPS was done using an ESCALAB250Xi instrument from Thermo Scientific, UK at the University of New South Wales (UNSW) and the peak fitting was performed using the

CASAXPS software. XPS was used to study the atomic fraction, junction properties, core levels and oxidation states of SnO_x and $Sn_xNi_yO_z$ films.

3.1.15 Ultraviolet photoelectron spectroscopy (UPS)

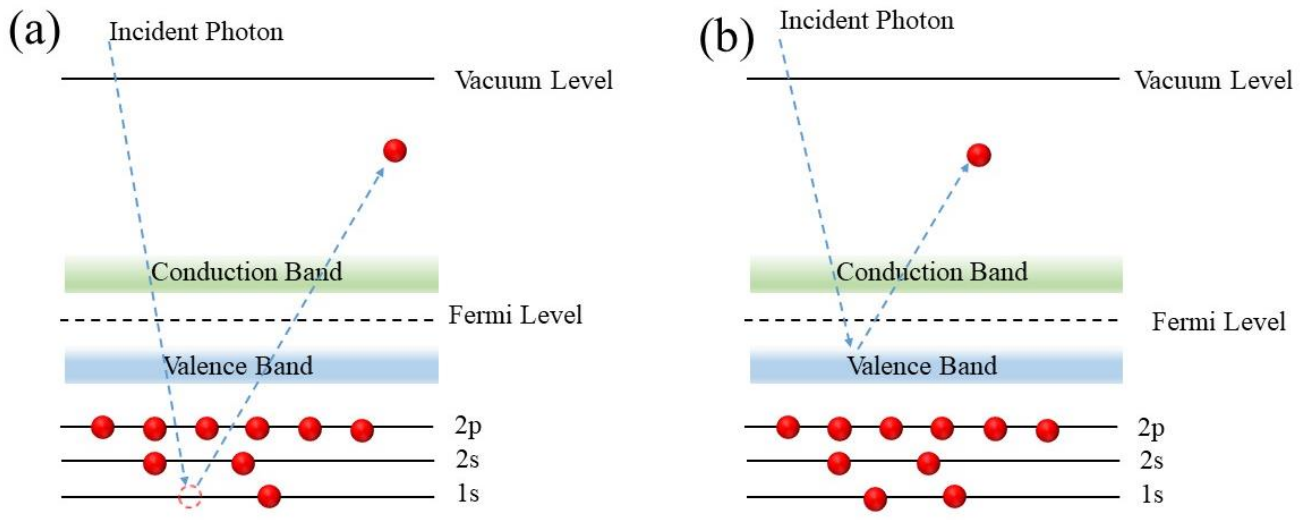

Figure 3-12 Schematic diagram comparing photoelectron ejection in (a) XPS and (b) UPS.

UPS is a sub-category of XPS wherein ultra-violet (UV) rays are used instead of X-rays as the incident energy to study valence bands of the specimen. Since incident UV light has very lower energies compared to X-rays, it is only able to affect electrons from the valence band of near surface atoms. As valence electrons are the only entity ejected in UPS, it provides a high-resolution measurement of the energy level of valence electrons as compared to XPS wherein the electrons are ejected from both the valence and core levels. Another useful result from the UPS is the extraction of work function of the sample material.

In this thesis, UPS was performed at UNSW to study the band alignment at the InP/SnO_x and InP/$Sn_xNi_yO_z$ interface using He-I line with an energy of 21.2 eV.

3.1.16 Hall-effect measurements

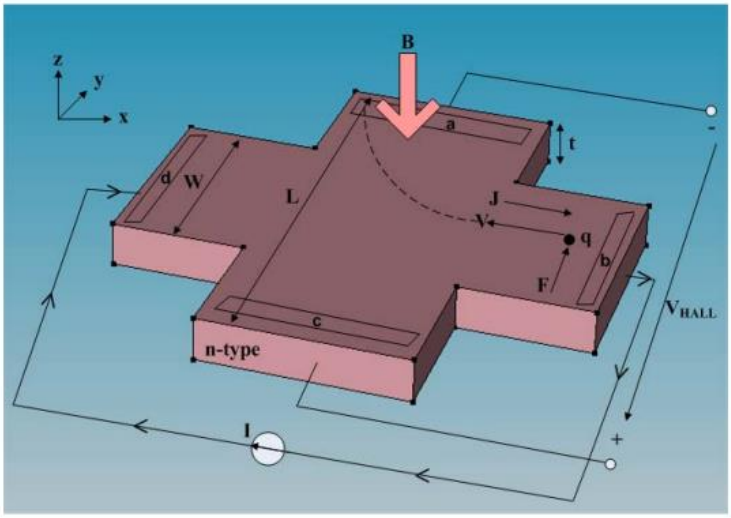

Figure 3-13 Operational principle of Hall-effect measurement using a Greek-cross geometry. Reproduced from [148].

Hall-effect measurements is a technique popularly employed in the field of semiconductors to determine the carrier concentration, mobility, resistivity and type of majority carriers. The Hall-effect measurements result in an electrical output in the form of voltage when a sample is exposed to a magnetic field perpendicular to electrical current passing through this layer. The sample consists of four or more electrical contacts arranged in either Van der Pauw (nearly square or circular) or Hall bar geometries (long and narrow). Hall bar geometries are better suited for resistance measurements but not for mobility as they are very sensitive to geometry of sample (width of sample and distance between contacts) and needs at least six contacts. This disadvantage is overcome by using Van der Pauw geometries as the accuracy of measurement is not too sensitive to sample geometry. However, Van der Pauw samples takes about twice as long to measure. A square sample having uniform thickness with electrical contacts at four edges is the most popular Van der Pauw configuration used due to ease of fabrication. However, measurement errors can as large as 10%. The Greek-cross Van der Pauw geometry can be used when high accuracy is required (errors less than 1%) [149]. Figure 3-13 shows the principle of Hall effect measurements in a Greek-

cross geometry. In this thesis, we used Greek-cross geometry for all Hall effect measurements with W = 1 mm. and L = 5 mm. Hall measurements were performed using a Lakeshore system.

3.1.17 Ellipsometry

Interaction of light with matter can reveal many interesting properties of a thin film such as complex dielectric constants, thickness, refractive index, surface roughness, bandgap, carrier concentration, resistivity and mobility [150]. Spectroscopic ellipsometry is one such tool and has become very popular for non-contact and non-invasive determination of these material properties by measuring the incident polarised light reflected from the sample [150-152]. The simplicity of sample preparation is another distinct advantage of ellipsometry as no additional fabrication steps are required post film deposition.

A schematic showing the working principle of ellipsometer is shown in Figure 3-14. In this technique, the sample is illuminated with a beam of polarised light that interacts with the sample and reflected from top surface and interfaces. The change in polarisation state of the reflected (or transmitted) beam is measured and is commonly characterised by two parameters named psi (ψ)and delta (Δ) as defined in equation below:

$$\tan(\psi)e^{(i\Delta)} = r_p/r_s \tag{3.2}$$

Here r_p and r_s are the reflectivity of p-polarised and s-polarised light. These two measured parameters, ψ and Δ are acquired as a function of wavelength and at different incident angles to improve the accuracy. The plot of these two measured parameters are fitted to an optical model to calculate various parameters described above.

A J.A. Wollam M2000 Ellipsometer was used for all the measurements done in this thesis. The wavelength range was 200-1700 nm. For each sample, data was taken at three angles – 55°, 65° and 75°.

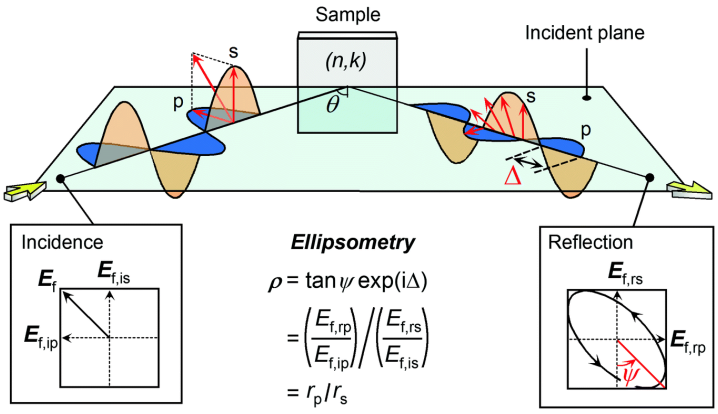

Figure 3-14 Operating principle of ellipsometry. Reproduced from [153].

3.2 Growth of nanowires by selective area epitaxy (SAE)

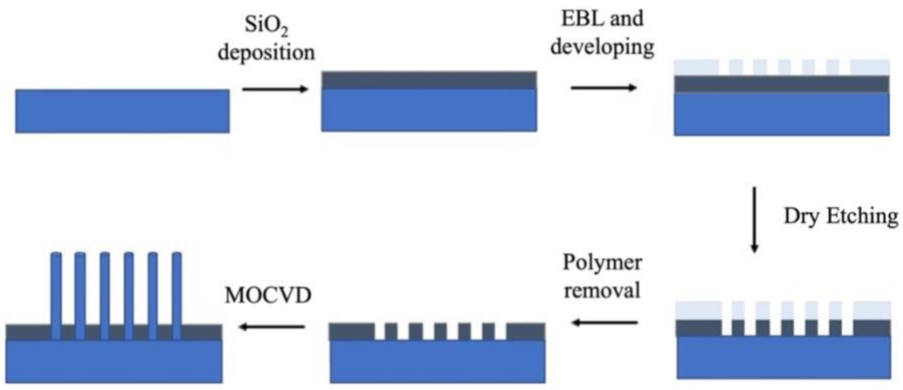

Figure 3-15 Schematic diagram of SAE.

SAE is a technique where growth takes place on a substrate which has been pre-deposited with a dielectric mask and patterned using EBL [22]. In the deposition chamber, nanowire growth will occur only in these patterns and not on the dielectric surface. The diameter and pitch of the grown nanowires are defined by the dimensions of the patterned holes while the length is dependent on

deposition time. In this thesis, we optimised our nanowire array design by varying the diameter and pitch.

A dielectric mask for the growth of nanowires was made by depositing 150 nm-thick SiO_2 using PECVD on InP (111)A wafers at 300°C. Then, a thin layer of undiluted positive electron beam resist (mrPOS-EBR) was spun on the substrate at 3000 rpm and baked for 2 mins at 150°C. Subsequently, EBL was used to create the desired pattern, which is typically predefined holes in hexagonal array of 100x100 μm^2. After EBL, the resist was developed in Mr-Dev-800 solvent for 60 sec, followed by plasma etching for 2 mins at 100 W power and 300 sccm O_2 flow. This short plasma step is essential to remove any residual resist at the base of the holes after developing. After this, RIE was done to transfer the holes from resist mask to the SiO_2 layer. The remaining resist was removed by soaking the wafer in acetone for one hour and then in ultrasonicated for 20 mins. It was then sprayed with isopropanol (IPA) to remove acetone and dried with N_2. The sample was cleaned again with oxygen plasma for 5 min to remove any residual resist. A trim etching was then performed to remove any damage on the InP surface underneath the openings. Trim etching was done by H_2O_2 and 10% H_3PO_4 in water solution [154] and immediately, the sample was transferred in the MOCVD chamber to avoid any oxidation of the InP surface. Figure 3-15 shows the schematic diagram of the SAE process. Axial and radial growth of nanowire was controlled by controlling temperature, V/III ratio and flow rates whereas the diameter was controlled by EBL design (hole diameter and pitch size).

3.3 Device fabrication

3.3.1 Single nanowires

Single nanowire devices were fabricated on 300 nm of SiO_2 layer deposited on silicon wafers. First, EBL was done to make alignment cross marks (Figure 3-16 (a)). After developing, 10 nm

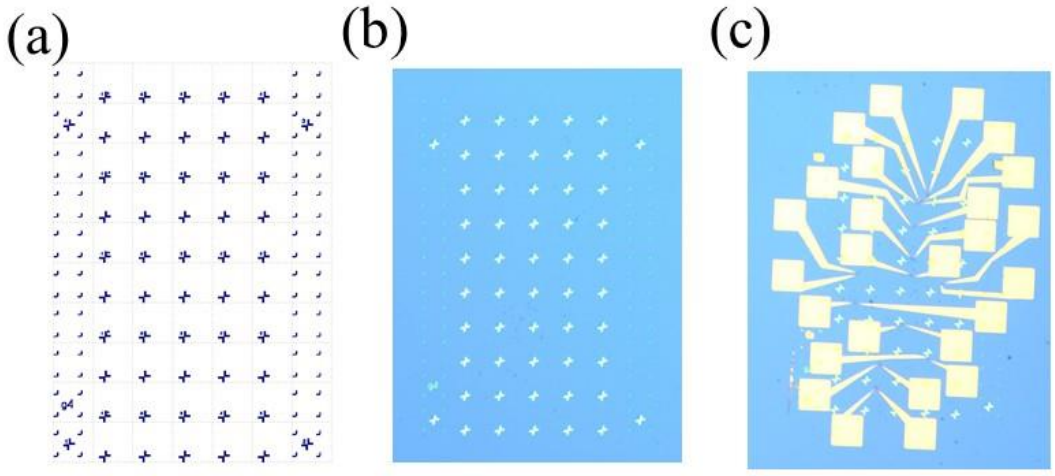

Figure 3-16 (a) EBL pattern where cross marks were made to align the nanowires and writing filed alignment marks were made on each side. Total size of pattern is 700 µm x 1000 µm. Optical microscope image (b) with marks and nanowires transferred inside the cross marks. (c) after contact formation.

Ti+70 nm of Au was deposited and lift off was done [155]. The sample was sonicated for 2 mins in acetone and IPA, respectively to remove the remaining resist as well as dust particles (Figure 3-16 (b)). Then, nanowires were mechanically transferred using a filter paper near the alignments marks. 2 nm of Al_2O_3 was deposited using ALD for passivation of the devices [156]. The optical image of each nanowire with alignment marks was taken and drawn in the Raith CAD interface. Two layers of undiluted ZEP were spun @ 500 rpm for 5 sec and 2000 rpm for 1 min followed by baking on a hot plate at 170^{o}C for 2 mins each time. This gives an overall thickness of ~ 1 µm. In general, the thickness of polymer should be more than double of metal thickness to achieve a clean lift off. Since the diameter of the nanowire was ~ 500 nm, hence at least 1 µm thick layer is required. Finally, EBL was done to make contact on the nanowires with 20 kV accelerating voltage, 30 µm aperture and the dose was varied depending on the dimensions required. For 80 nm line, a dose of 120 µJ/cm^{2}was used while for big pads and connecting line, a dose of 80 µJ/cm^2 was used. To get perfect alignment with the nanowires, writing field alignment was done in the proximity of the nanowires using alignment marks.

After EBL, the sample was developed in ZEP developer for 1 min 30 sec and then rinsed with IPA. A quick barrel etching was done to remove remnant resist in the openings. A quick dip for 10 sec in AZ726 MIF developer was carried out to remove Al_2O_3 from the resist opening. Just before depositing gold contact, a trim etching in HCl: H_2O was done for 2 min 30 sec to remove ~20 nm of the p-type shell from n-i-p InP nanowires. Finally, 10 nm Ti and 500 nm of Au was deposited using e-beam evaporator using a lift-off process (Figure 3-16 (c)). 10 nm of Ti was used as an adhesive layer whereas at least 500 nm of gold (same as diameter of nanowire) was required to avoid breakage of contact from the side facets of the nanowires [157]. Once lift off was done, the sample was cut into 2 mm x 2 mm size and mounted on a package. Finally, wire bonding was done to connect the pads to the external circuit.

3.3.2 Array nanowires

After SAE, the next step is to fabricate the device by making contacts to the p and n regions. In array devices, the InP substrate acts as one contact and TCO layer surrounding the nanowire as another. In order to separate the two contacts, we chose SU-8 photoresist due to its outstanding chemical and mechanical stability as well as excellent electrical insulating properties [158-161]. To fabricate array nanowire devices, first SU-8-5 was spin-coated at 3000 rpm and baked at 95°C for 2 min to planarise the wires. Subsequently, the sample was transferred into ICP-RIE and etching time was optimised so that remaining SU-8 is around 1-2 µm. After this, it was UV exposed for 1 min and hard baked at 150°C to make it thermally and chemically strong. Prior to deposition of TCO, the samples were dipped in 1% HF for 30 secs to remove any oxide formed on the surface of nanowires. Conformal n/p layer of TCO was deposited on the nanowires. n-ZnO was deposited using ALD and both p- and n-type SnO_x were deposited using sputter deposition. Then a 10 nm of

conformal layer of gold was deposited using sputter to decrease contact resistance and provide a uniform distribution of current along the nanowire array.

Finally, a 200 nm top gold pad was deposited near the nanowire array using a shadow mask by e-beam evaporator and a wire was soldered to connect the device to the external circuit. Figure 3-17 shows the fabrication of array nanowire devices. For bottom contact, indium-gallium alloy eutectic was applied at the bottom of the wafer and then, wafer was bonded on the copper sheet.

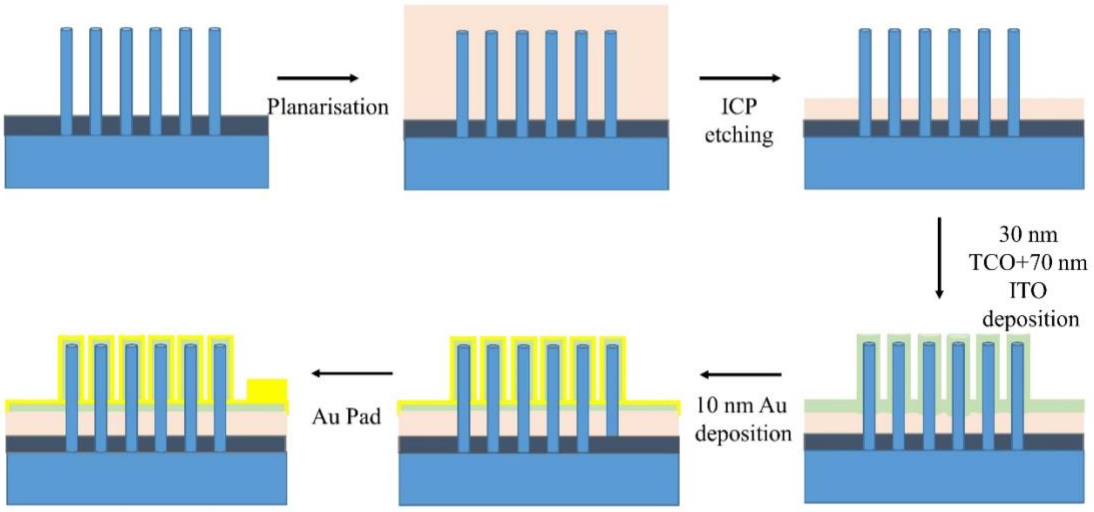

Figure 3-17 Schematic cross-sectional diagram of array nanowire LED fabrication.

3.3.3 Flexible array nanowire LED fabrication

To make flexible nanowire devices, first SU-8-5 was spin-coated at 2000 rpm and baked at 95°C for 5 min to achieve a film thickness of around 5 µm. After this, photolithography using MaN-1420 was done to open the area on the top of the nanowire array. This sample was transferred into the ICP-RIE chamber and etching time was optimised to obtain a final thickness of around 2 µm. The sample was then UV exposed for 1 min and hard baked at 150°C for 2 min to increase cross-linking of the SU-8 so that it becomes thermally and chemically strong. Then sample was dipped

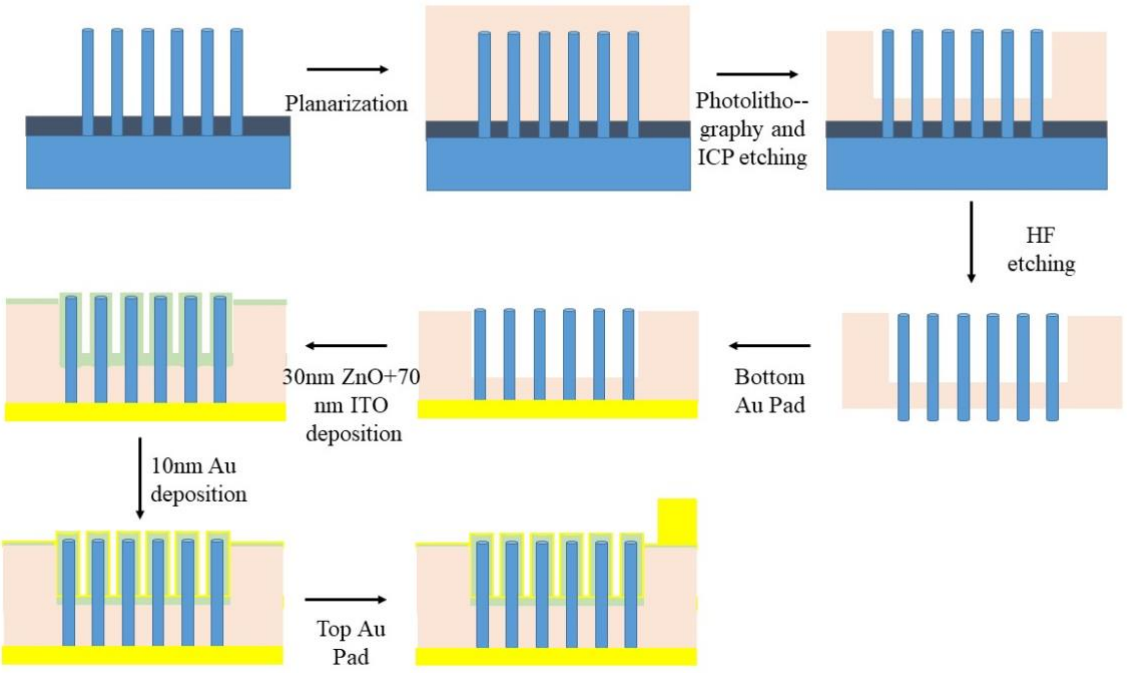

Figure 3-18 Schematic cross-sectional diagram of flexible array nanowire LED fabrication.

into acetone to remove the remaining MaN-1420. After this, the sample was put into 48% HF solution for 5 min, resulting in the underlying 150 nm of SiO_2 layer to be etched and the SU-8 film peeling off from the substrate with nanowires embedded into it. Finally, the released film was rinsed with DI water for 2 min and dried with nitrogen. Nanowire array in the film could be easily seen in an optical microscope. The film was flipped and the bottom 150 nm of Au contact was deposited along with a transparent acetate film (which housed the flexible film for measurements) using e-beam evaporator. The film was flipped back again, and the bottom Au pad was attached onto a gold-coated acetate film using silver paste. Finally, all the sides of the film were covered with Kapton tape and ZnO layer was deposited using ALD. After that, a conformal 10 nm of gold layer was deposited using sputter deposition and top contact pad was made by depositing 150 nm of Au using e-beam evaporator. Figure 3-18 demonstrates flexible LEDs fabrication process. Two

probes were used to connect the sample to an external circuit to measure I-V characteristics and EL properties.

3.4 Numerical techniques

3.4.1 Finite difference time domain (FDTD)

FDTD is a numerical analysis technique of solving partial differential equations using finite difference method. It can be used to solve Maxwell's equations written in partial differential equations by calculating the electric and magnetic fields at various points within the computational domain [162]. Maxwell's equations are solved across space and time over an independent spatial and temporal grid. In the time-domain, first the electric field is solved and, then the magnetic field is solved for the next interval of time, and the process repeats until the simulation converges. Since it is a time-domain method, a wide range of frequencies can be covered in a single simulation. Moreover, it can also be used to solve nonlinear material properties [163]. The results from FDTD simulation is also more intuitive compared to other numerical approaches as the simulated electric fields and magnetic fields can easily be visualized in space and time.

In this thesis, we used a commercially available software package Lumerical for FDTD simulations. We used this technique to simulate the reflection coefficients from end facets of nanowires.

3.4.2 Finite difference eigenmode (FDE)

FDE is a numerical technique used to calculate the spatial profile and frequency dependence of the optical modes. It solves Maxwell's equations using sparse matrix techniques to obtain guided mode profiles, effective index and loss across the cross-section of waveguides. By doing frequency sweep group delay, dispersion, group velocity and confinement factor can be calculated [164].

In this thesis, we used commercially available software package Lumerical for FDE simulations. FDE method was used to calculate guided modes supported in the nanowires as well as confinement factor of those modes.

3.4.3 LaserMOD

The basic principle of modelling in LaserMOD depends on the MINILASE II code [165]. Maxwell's equations are solved to determine light propagation properties inside any structure. Depending on the type of laser, different methods are used to solve these equations. For edge emitting lasers, modes are separated into longitudinal and transverse modes. Scalar Helmholtz equation is used to solve the transverse modes. Longitudinal modes are calculated by cavity length, effective index and wavelength. The product of longitudinal and transverse modes are considered as total number of modes. Finally, rate equation is solved for each mode separately. For vertical cavity surface emitting lasers (VCSEL), transfer matrix method (TMM) is used to solve modes supported inside a cavity. The fields at all the interfaces are separated into forward and backward propagating waves by applying proper boundary conditions. The transfer matrix of individual layer is first calculated and then the transfer matrix of whole structure is defined as the product of individual matrices.

In this thesis, LaserMOD is used to simulate various nanowire structures to study their lasing behaviour. Since nanowires have cylindrical geometry, VCSEL-type structure was used for all the simulations. Both 1D and 2D simulations were performed to optimise the dimensions of nanowire cavity in order to achieve low threshold lasing.

3.5 Summary

In summary, this chapter described the main experimental and numerical techniques used in this dissertation for SAE growth, fabrication, characterisation and simulations. The equipment employed for growth are PECVD, EBL, RIE and barrel etcher for SAE mask preparation and MOCVD for the epitaxy of the nanowires. To fabricate both single nanowire and array nanowire devices, ALD, EBL, sputter, e-beam evaporator, ICP-RIE were used. For the purpose of characterisation, SEM was used for morphological and structural characterisation while micro-PL was used for optical characterisation of the nanowires. I-V, EBIC, Hall-effect measurements and EL were used for electrical and optoelectronic characterisation of the fabricated devices. To investigate the surface properties of SnO_x and $Sn_xNi_yO_z$ films, XPS/UPS were performed. Simulations using Lumerical FDTD, Lumerical MODE and LaserMOD were done to design the appropriate nanowire structures to achieve low threshold lasing.

Chapter 4. Homojunction InP nanowire devices

Cavity dimensions are one of the most important parameters for the optimum performance of any laser. In this chapter, we simulate the most basic structure of F-P cavity, an InP nanowire to achieve low threshold lasing. After optimising the dimensions, experiments using optimised dimensions are performed for both axial and radial homojunction InP nanowire devices.

4.1 Axial p-i-n InP nanowires

4.1.1 Simulations

We selected a p-i-n InP nanowire lying down horizontally on a low refractive index SiO_2 substrate and is surrounded by air for simulations (Figure 4-1(a)). In this configuration, the nanowire acts as an F-P cavity and modes propagate along its axis. Large refractive index difference between surrounding medium (SiO_2 substrate and air) and the InP increases the confinement of the mode while the end facets act as mirrors [5]. Although actual InP nanowires have hexagonal cross sections, we simplified our geometry and modelled for circular cross-section using a VCSEL geometry. Previous studies have illustrated that mode properties are quite similar between nanowires with hexagonal and circular cross-sections, provided their cross-section areas are equal [166].

To perform simulations, first in the global setting, VCSEL was chosen. Following this, in the CAD environment, entire diameter cross-section of the VCSEL was drawn by assuming cylindrical symmetry along x = 0. In this way, actual 3D calculations were done by revolving the object along y axis. To draw the structure in CAD, bulk semiconductor was chosen and drawn three times indicating p, i and n segment of InP nanowire. After this, the material descriptions, doping

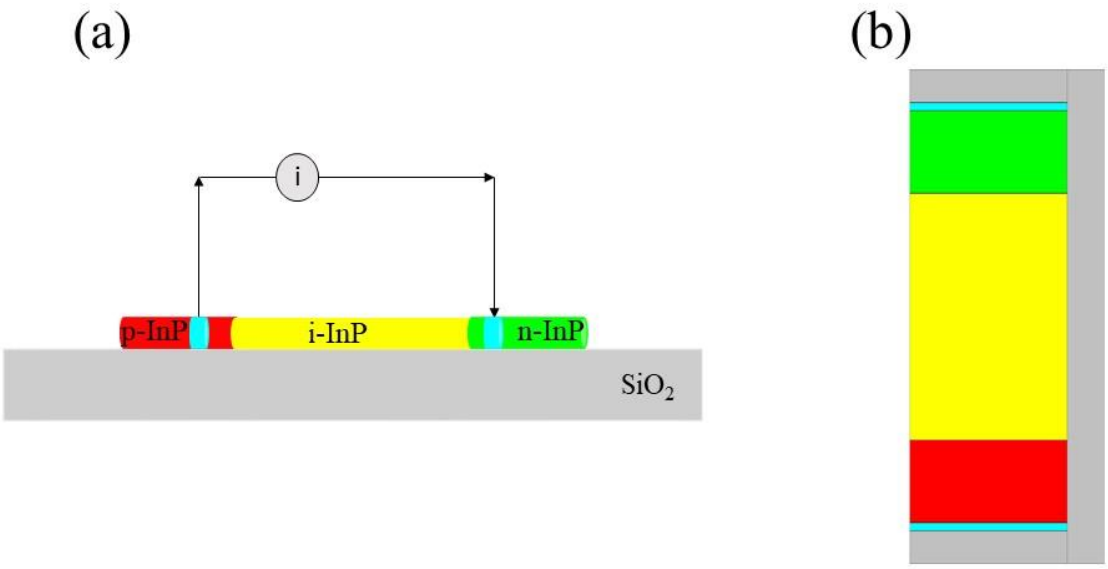

Figure 4-1 (a) Schematic diagram of a p-i-n nanowire (b) LaserMOD CAD interface showing the wire was covered with SiO_2 for better convergence (SiO_2 is only on right side as we revolve structure along x = 0).

concentration and dimensions were assigned for each segment. The entire structure was covered with SiO_2 for better convergence as indicated in Figure 4-1(b). All the segments were referred to each other so that each region tile automatically and boundaries could be resolved clearly. Then, the entire cross-section was transferred into a non-uniform mesh. Since gain is generated in the entire nanowire, all the segments were selected as an active region.

To optimise the laser dimensions , 1D was chosen with reflectivity of 0.99 at both the facets in the global settings. 1D simulations were performed to obtain the material gain spectrum and transmission spectrum of the cavity. Transmission spectrum gives an insight into the potential longitudinal modes inside the cavity. By adjusting the length of the cavity, gain peak and the main longitudinal mode was then aligned. This was required before running a full laser simulation in VCSEL. 1D VCSEL uses TMM to calculate cavity modes. TMM calculation works on uniform mesh hence, mesh size is controlled by defining number of grid points in x and y direction. Once the length was fixed, the global setting was changed from 1D to 2D and reflectivity was set to 0.

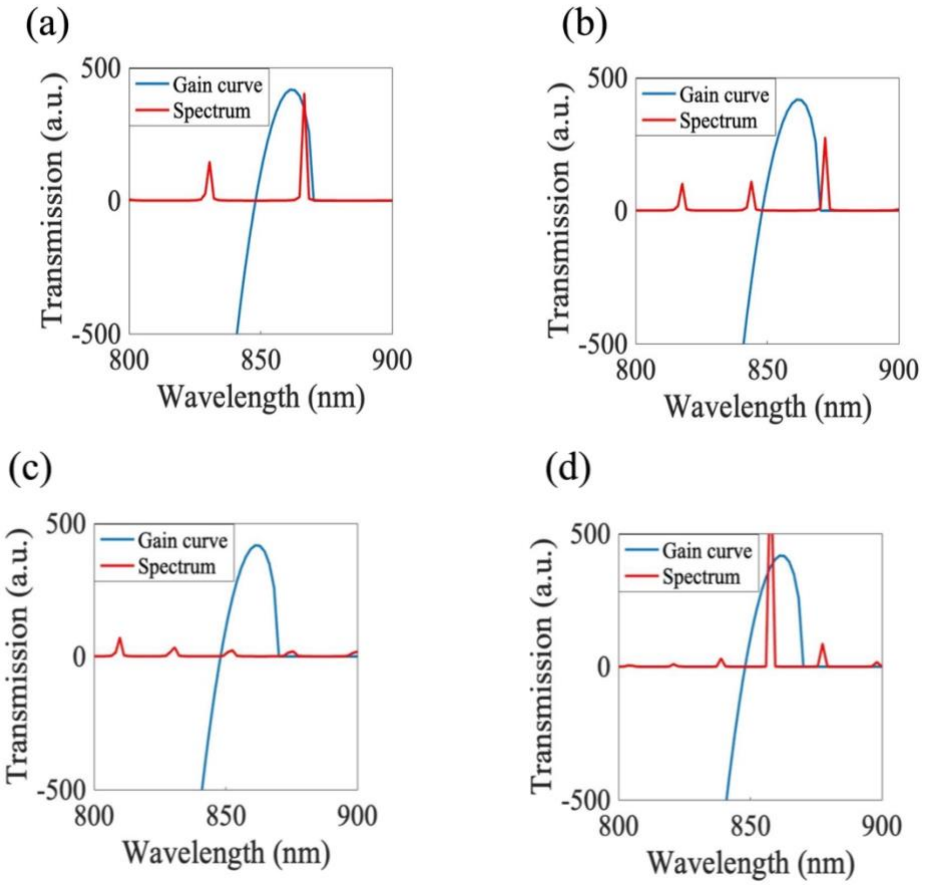

Figure 4-2 Room temperature gain curve at a carrier density of $2x10^{18}$ cm^{-3} plotted together with modes supported in axial InP nanowire of length (a) 3 µm (b) 4 µm (c) 5 µm (d) 6 µm.

In 2D, finite element method (FEM) solver was used to calculate cavity modes with the initial guess obtained from TMM solver. *Min div/layer* and *grid size in y* was used to control the resolution of FEM mesh. In FEM, reflectivity was calculated by the solver. In VCSEL, light output was measured at both the facets of the nanowire. Diameter of nanowire was varied such that transverse mode peak aligned with the gain peak. Once the peak was aligned, full laser simulations were performed.

The material data set used for simulations is in-built in the LaserMOD software. However, only data for zinc blende (ZB) InP is available in the data set. Since our InP nanowires have wurtzite (WZ) crystal structure, the material data set was slightly modified to simulate as close to the real

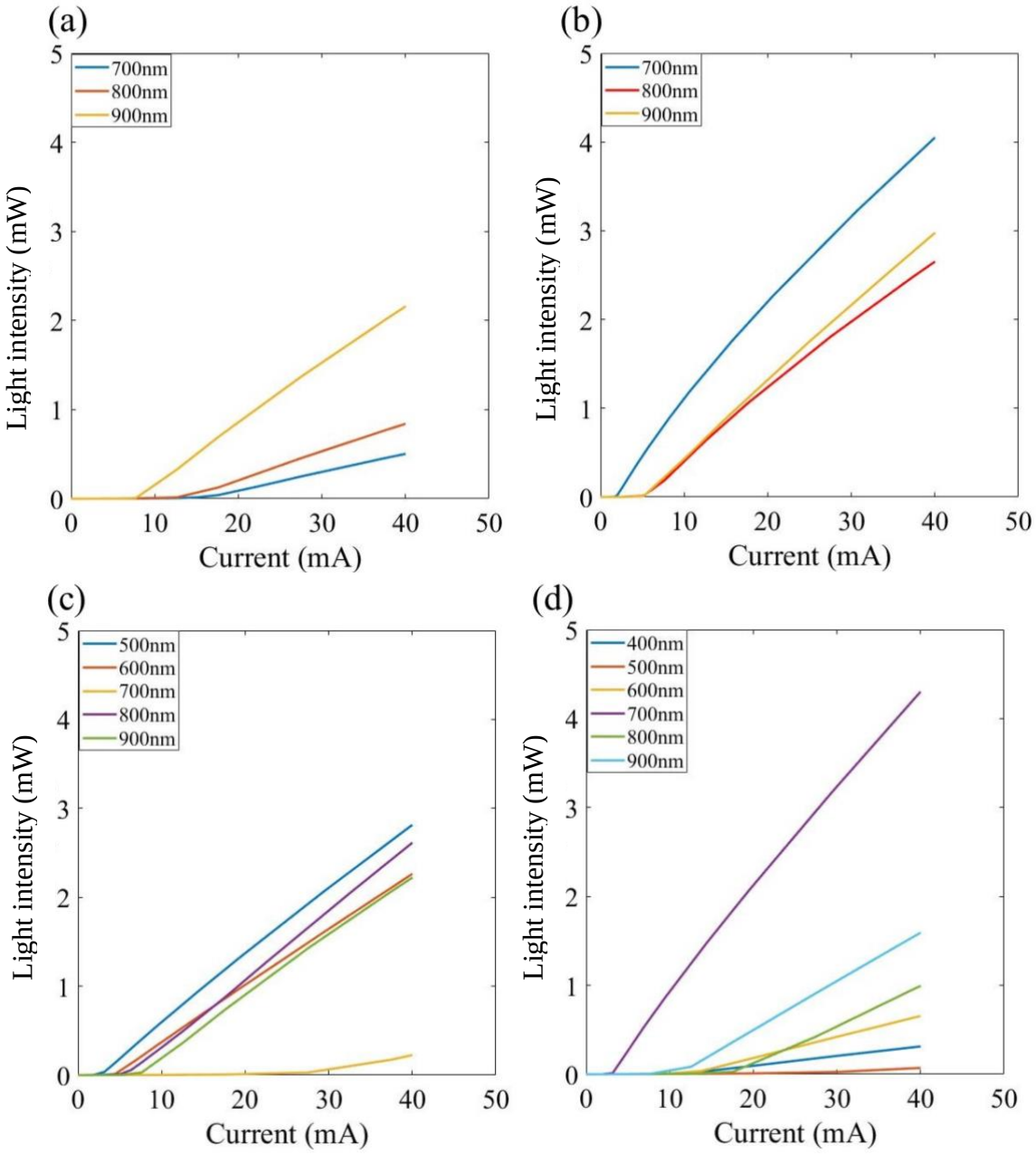

Figure 4-3 Room temperature L-I plots of axial p-i-n InP nanowire with a total length of (a) 3 µm (b) 4 µm (c) 5 µm (d) 6 µm with different diameters showing lasing.

structure as possible. The main parameters which affect simulations are band gap, mobility of electrons and holes and dielectric constants. The band gap of InP WZ structure has been studied extensively and reported at 1.42 eV [167]. The electron mobility of InP nanowire was taken as 700

$cm^2\ V^{-1}\ s^{-1}$ and hole mobility as 150 $cm^2\ V^{-1}\ s^{-1}$ [21]. Dielectric constants were kept same as the ZB structure.

To determine the optimum length of nanowire, length of the intrinsic section in the p-i-n InP nanowire was varied from 1– 4 µm. Overlap of the corresponding longitudinal modes and gain spectrum at a carrier concentration of $2x10^{18}$ cm^{-3} was observed. This provides information about the resonant peak for a particular length of the nanowire cavity. The length of p and n sections was set to 1 µm as a minimum of 1 µm was required for contact fabrication using EBL. The i-segment length of more than 4 µm (i.e. total length of 6 µm) was not considered for simulation due to experimental limitation of growing long nanowires using MOCVD reactors. Figure 4-2 displays the overlap of the gain spectrum with transmission spectrum at room temperature. From Figure 4-2, the resonant peaks at 0.8666 µm, 0.8525 µm, and 0.8578 µm can be observed for 3, 5 and 6 µm long InP nanowire cavities, respectively. For 4 µm long cavity, higher carrier concentration is required to overlap the longitudinal mode peak at 0.844 µm with the gain curve.

Once the resonant peak for a particular cavity was obtained, 2D simulations were performed to obtain the optimised diameter for the nanowire. The diameter was varied from 100 to 900 nm to align the longitudinal mode with the waveguide dimensions. Both n and p doping were kept constant at $5x10^{18}$ cm^{-3} and $2x10^{19}$ cm^{-3}, respectively. The lasing behaviour for different waveguide diameter and nanowire length are plotted in Figure 4-3. The minimum diameter required to achieve lasing with 3 and 4 µm long nanowire is 900 and 700 nm, respectively. Minimum diameter needed to obtain lasing decreases with increasing length because of the enhancement of the gain region. The minimum diameter required to achieve lasing in a 5 and a 6 µm long nanowire is 500 and 400 nm, respectively. The minimum threshold required to achieve lasing in a 3, 4, 5 and 6 µm long nanowire is 7.8, 1.98, 2.5 and 3.18 mA, respectively. Generally, high doping concentration is

Table 4-1 Variation of lasing threshold with doping concentration for an InP nanowire with a diameter of 900 nm and 3 μm in length.

p-doping / n-doping	$1x10^{18}$ cm^{-3}	$5.75x10^{18}$ cm^{-3}	$1x10^{19}$ cm^{-3}	$1.5x10^{19}$ cm^{-3}	$2x10^{19}$ cm^{-3}
$1x10^{18}$ cm^{-3}	No lasing	No lasing	No lasing	No lasing	No lasing
$2.5x10^{18}$ cm^{-3}	No lasing	No lasing	Soft threshold	15.2 mA	10.2 mA
$5x10^{18}$ cm^{-3}	No lasing	Soft threshold	15.1 mA	10 mA	7.8 mA

Table 4-2 Variation of lasing threshold with doping concentration for an InP nanowire with a diameter of 700 nm and 4 μm in length.

p-doping / n-doping	$1x10^{18}$ cm^{-3}	$5.75x10^{18}$ cm^{-3}	$1x10^{19}$ cm^{-3}	$1.5x10^{19}$ cm^{-3}	$2x10^{19}$ cm^{-3}
$1x10^{18}$ cm^{-3}	No lasing	Soft threshold	7.2 mA	4.55 mA	2.9 mA
$2.5x10^{18}$ cm^{-3}	No lasing	5.85 mA	3.6 mA	2.9 mA	2.7 mA
$5x10^{18}$ cm^{-3}	No lasing	4.15 mA	2.9 mA	2.3 mA	1.98 mA

Table 4-3 Variation of lasing threshold with doping concentration for an InP nanowire with a diameter 500 nm of and 5 μm in length

p-doping / n-doping	$1x10^{18}$ cm^{-3}	$5.75x10^{18}$ cm^{-3}	$1x10^{19}$ cm^{-3}	$1.5x10^{19}$ cm^{-3}	$2x10^{19}$ cm^{-3}
$1x10^{18}$ cm^{-3}	No lasing	No lasing	No lasing	Soft threshold	9.1 mA
$2.5x10^{18}$ cm^{-3}	No lasing	Soft threshold	6.15 mA	4 mA	3.8 mA
$5x10^{18}$ cm^{-3}	No lasing	6.9 mA	3.9 mA	2.9 mA	2.5 mA

Table 4-4 Variation of lasing threshold with doping concentration for an InP nanowire with a diameter of 400 nm and 6 µm in length

p-doping / n-doping	$1x10^{18}$ cm^{-3}	$5.75x10^{18}$ cm^{-3}	$1x10^{19}$ cm^{-3}	$1.5x10^{19}$ cm^{-3}	$2x10^{19}$ cm^{-3}
$1x10^{18}$ cm^{-3}	No lasing	No lasing	18.9 mA	9 mA	8.75 mA
$2.5x10^{18}$ cm^{-3}	No lasing	13.9 mA	6.4 mA	5 mA	4.35 mA
$5x10^{18}$ cm^{-3}	No lasing	6.25 mA	4.6 mA	3.6 mA	3.18 mA

required to form a good Ohmic contact to reduce the resistance of the device [168]. However, high doping levels increase optical losses significantly due to free carrier absorption [169] and Auger recombination [170]. To understand doping dependent behaviour, p-doping was varied from $1x10^{18}$ to $2x10^{19}$ cm^{-3} and n-doping was varied from $1x10^{18}$ to $5x10^{18}$ cm^{-3} for the minimum threshold conditions for nanowires of 3 to 6 µm in length (Table 4-1- 4-4). Here, length of both n and p section was kept to 1 µm each. The simulated threshold current required to achieve lasing for the doping ranges mentioned above is shown in following tables. It is evident that as we decrease the doping concentration, the minimum threshold current required to achieve lasing increases. This highlights the importance of forming good Ohmic contacts to the p- and n-segments to make an efficient device. The minimum threshold current obtained is 1.98 mA for 700 nm thick and 4 µm long nanowire. However, due to fabrication challenges related to EBL as discussed in section 3.3.1, we chose to check lasing from nanowires with a diameter of 500 nm and 5 and 6 µm in length.

4.1.2 Growth of nanowires

The diameter and pitch size of the SAE mask was varied from 200–600 nm and 1–3 µm, respectively, to get the nanowires with the right dimensions. As seen from Table 4-5 for the growth

Table 4-5 SEM images (45° tilted view) of InP nanowire arrays as a function of diameter and pitch. All scale bars are 2 μm.

Pitch / Diameter	0.5 μm	1 μm	2 μm	3 μm
200 nm	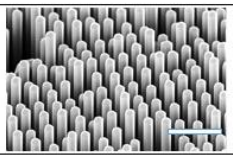		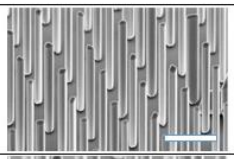	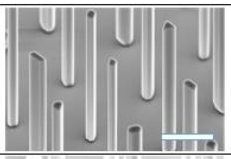
300 nm		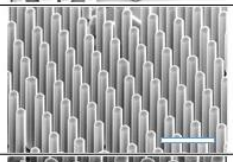	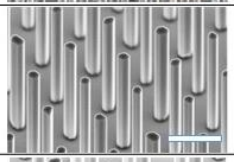	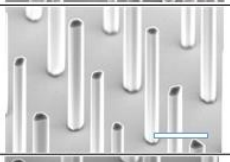
400 nm		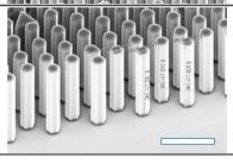	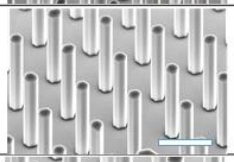	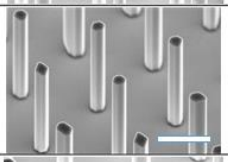
500 nm				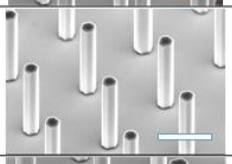
600 nm			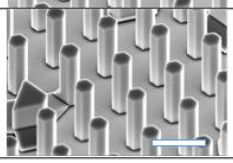	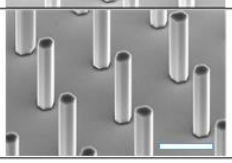

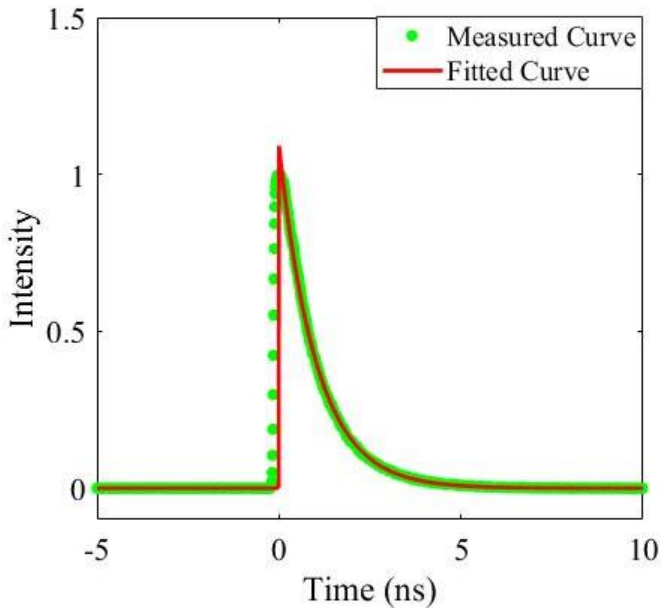

Figure 4-4 Time-resolved PL and fitting of undoped InP nanowire with a diameter ~500 nm and length of 5 μm.

of i-InP nanowires, in order to have better morphology, the opening diameter needs to be increased

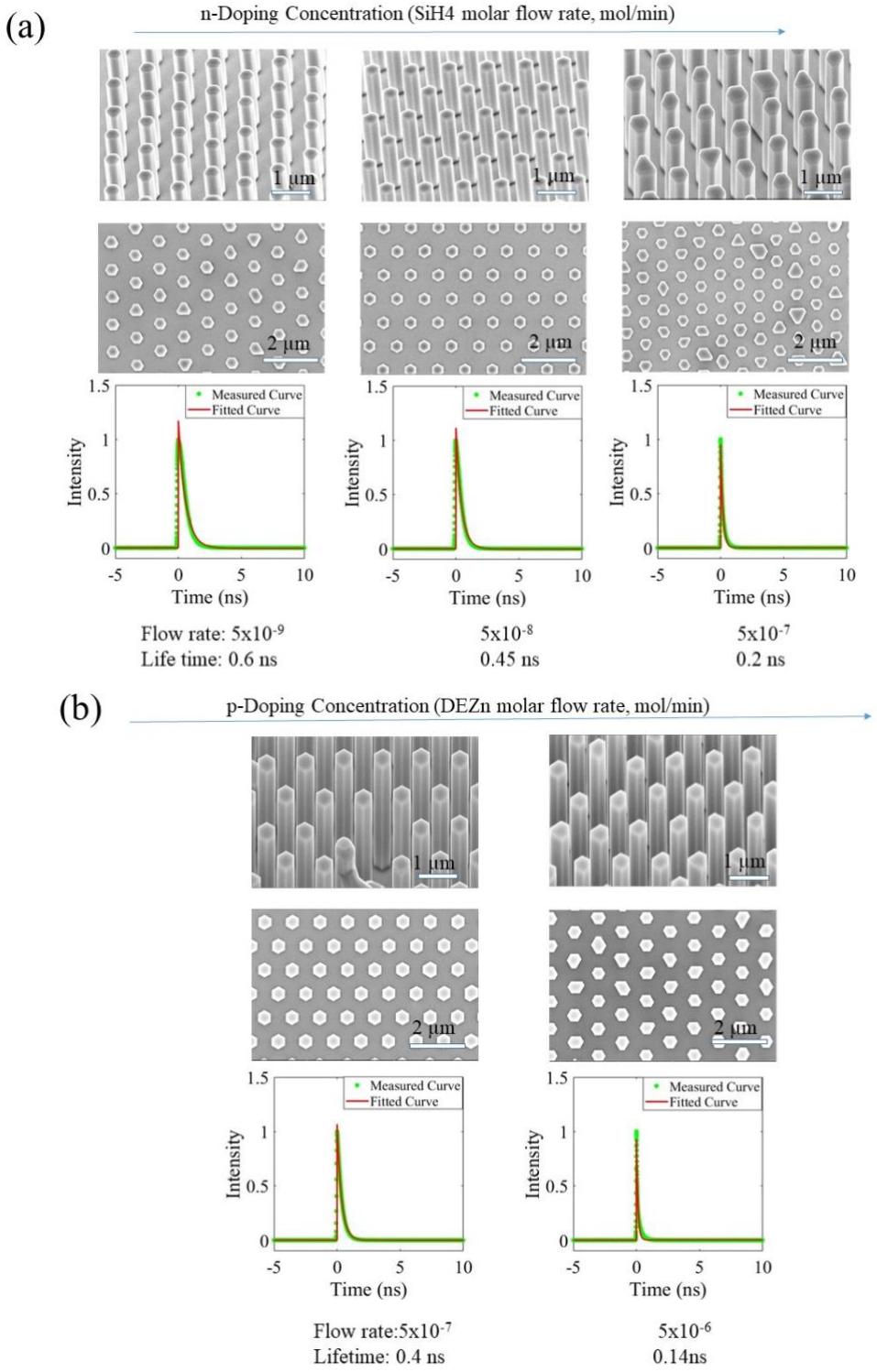

Figure 4-5 SEM images at 45° tilted view (top), top view (middle) and time-resolved PL and fitting of (a) n-doped and (b) p-doped InP nanowire arrays.

with increasing pitch size. Moreover, to obtain a diameter of around 500 nm, a pitch size of 1 µm

with hole opening of 400 nm is required which gives lifetime of ~1 ns (Figure 4-4). Once the mask pattern for undoped nanowires was fixed, doping studies were performed. Flow rates of the Zn (p-dopant) precursor were varied from $5x10^{-7}$ to $5x10^{-6}$ mol/min and Si (n dopant) precursor were varied from $5x10^{-9}$ to $5x10^{-7}$ mol/min. We found that morphology of the nanowires was not significantly affected by the variation in the dopant flow rates (Figure 4-5). However, the lifetime of the nanowires was found to decrease as the dopant flow rate was increased, indicating a rise in free carrier absorption [105]. It is evident from Tables 4-1 to 4-4 that higher doping concentration is required to achieve lasing hence, maximum dopants flow rates were used. The growth time for individual p, i and n section was optimised to achieve the desired length. A slight variation in height from 4- 6 µm in a 100 x 100 μm^2 array was observed from the centre to the edge of the array.

4.1.3 EL measurements

Following growth, devices were fabricated using the process described in section 3.3.1. Figure 4-6(a) shows a fabricated single nanowire device on SiO_2 substrate indicating perfect alignment to the electrical connections. The width of the electrical contact was ~ 300 nm. This was the minimum dimension that could be obtained using EBL on thick resist. Since the diameter of nanowire was 500 nm, at least 1 µm ZEP is needed for clean lift off. Resolution of EBL pattern decreases with resist thickness. Considering significantly high absorption from metals, it is important to reduce overlap of the metal contact with the active region [171]. Therefore, EBL conditions were optimised to achieve minimum contact width. Moreover, the end facets of the nanowire were kept free from the electrical contacts so that absorption of the emitted light could be minimised.

Simulated and measured I-V curves depicted in Figure 4-6(b) show a typical rectifying behaviour of the p-n junction. Higher turn-on voltage for experimentally measured I-V indicates high series

resistance at the contacts. This might be due to low doping level in nanowires and/or non-ideal Ohmic contact formation. Figure 4-6(c) shows the room temperature spectral characteristics of the device where luminescence increases with increasing current injection. However, at a current of more than 4 µA, the device was burnt. Degradation of device performance might be due to local

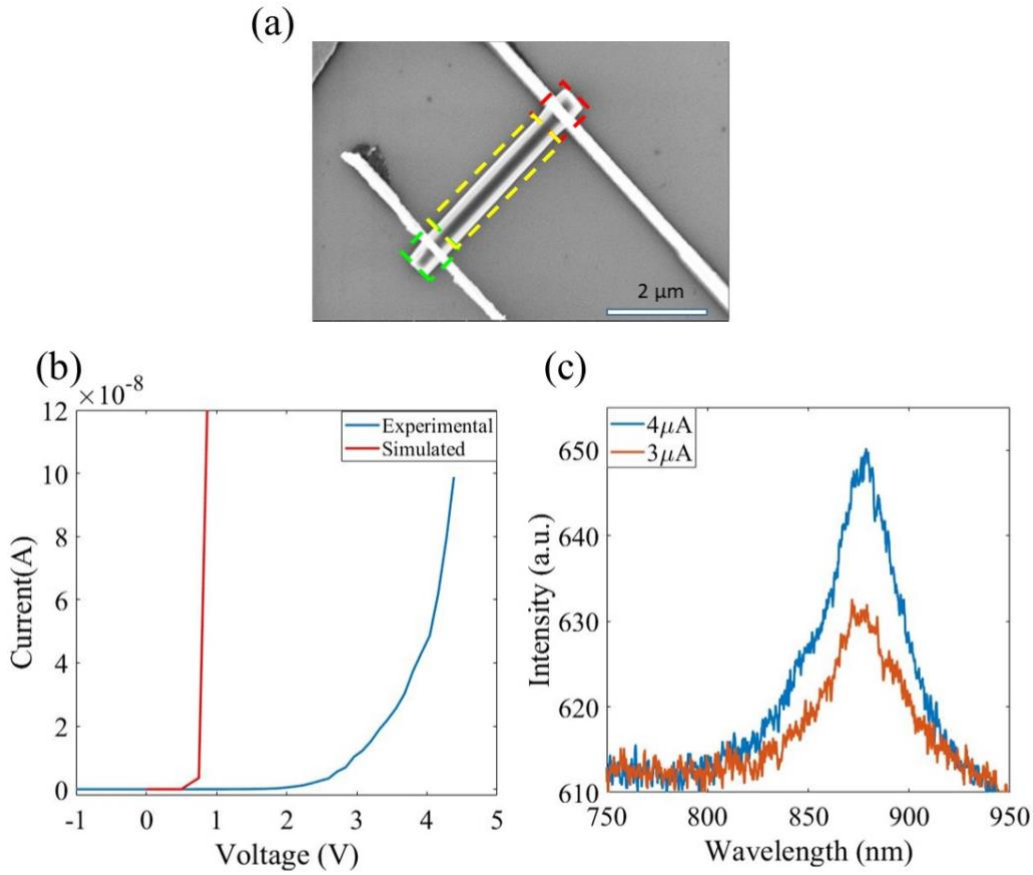

Figure 4-6 (a) SEM image of a single nanowire device with contacts fabricated, where green, yellow and red dashed rectangle represents n-doped region, undoped region and p-doped region, respectively. (b) Comparison of simulated and measured I-V characteristics at room temperature. (c) EL spectra of single nanowire device at different injection levels.

heat generation, non-ideal contacts, high free carrier absorption due to dopants and significant metal absorption as the metal contact is in direct contact with the nanowire. To minimise heating issues, further measurements were performed at low temperature (78 K). When temperature of a laser diode decreases, the gain generated increases [8]. Higher gain can be helpful in reducing

threshold current without generating excessive heat. This is because as temperature increases, gain decreases which leads to increase in transparency carrier density [8]. Spreading of carriers due to thermal energy is the main cause for this. Additionally, higher Auger recombination and carrier leakage due to thermal energy also contribute to the increase in threshold current [8].

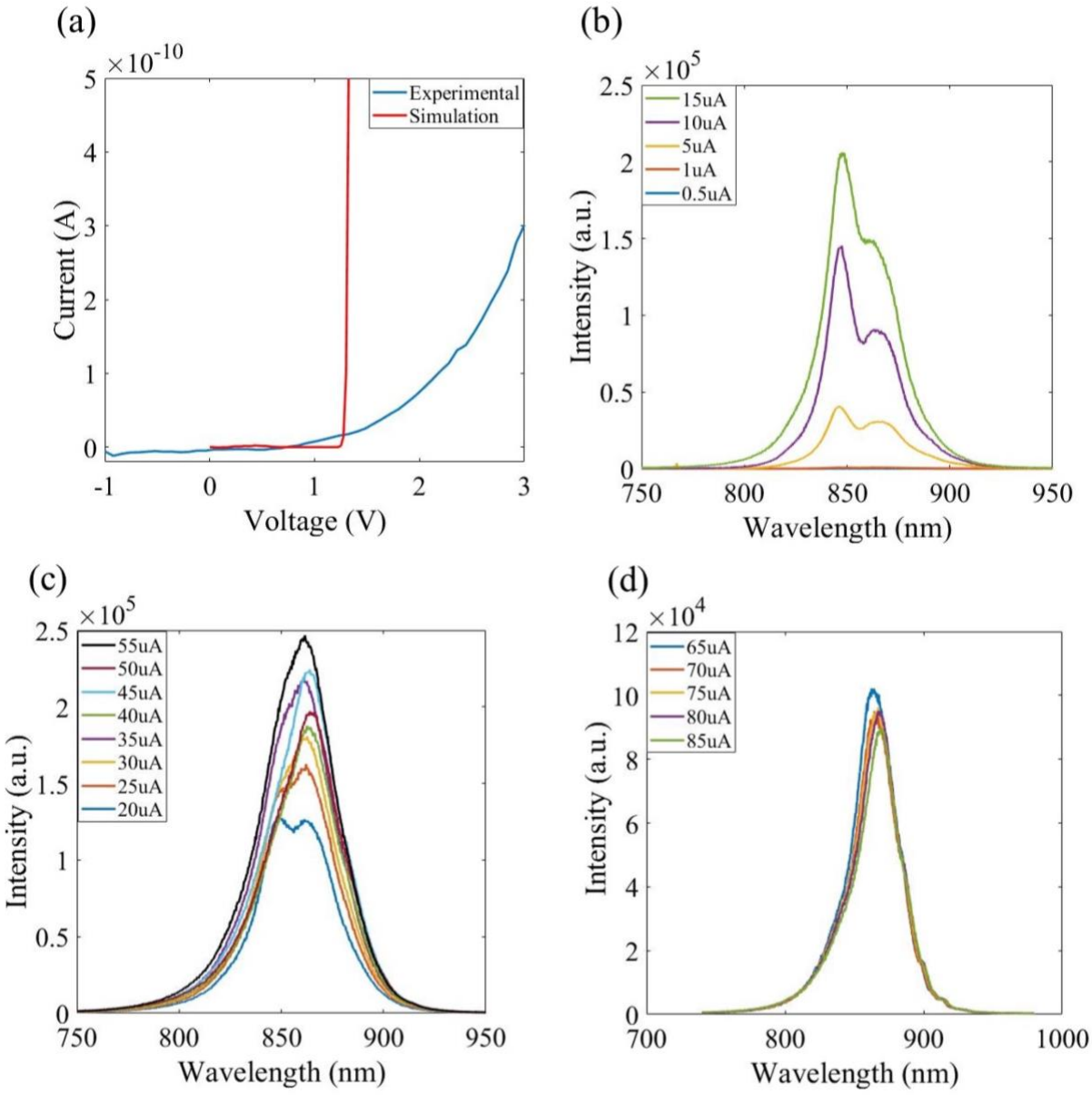

Figure 4-7 (a) Comparison of simulated and measured I-V characteristics. (b-d) EL spectra of single nanowire device at different current injection levels.

Fig. 4-7 (a) shows the comparison of the simulated and measured I-V curves for a nanowire with a diameter of 500 nm and 5 μm in length. For experimentally measured device, higher turn on voltage was observed as compared to simulated device indicating the above-mentioned issues. Figure 4-7 (b-d) shows the usual LED behaviour where EL intensity increases with increasing current injection. In contrast to room temperature measurements, two distinct peaks were observed at low temperature. The highest energy peak corresponds to band-to-band transition whereas the lowest energy peak is related to Zn acceptor levels. Detailed analysis of this peak is discussed in section 5.4.2. At higher current injection, both peaks merge and shift towards higher wavelength indicating significant heating of the device. The maximum current the nanowire could survive without burning is 85 μA. The peak position at 85 μA is 870 nm, indicating the local temperature is ~ 298 K [167]. Additionally, the minimum threshold required to achieve lasing is of the order of mA, as shown by the simulation results. This result clearly indicates that the p-i-n InP axial nanowire will burn before reaching lasing threshold, due to excessive heating.

4.2 Radial p-n InP nanowires

Another possible configuration for nanowires is the radial structure. The advantage with radial structure is that it has a larger active region than axial nanowire with similar dimensions. However, making single nanowire device with such structures is challenging. Therefore, we decided to make array device. Each array device consists of 100 nanowires so that higher current can be passed through it. The only issue with this configuration is that there is no refractive index difference between the nanowires and the substrate. This will lead to leakage of the mode generated inside the nanowires to the substrate. Potential solutions of this problem are to decrease the hole opening of the nanowires, increase the SiO_2 thickness and promote lateral growth of nanowires over the SiO_2 such that effective index at the interface decreases. Due to experimental limitations on

minimum hole opening, we fixed the opening at 100 nm and performed optical simulations to understand the loss at the SiO_2/InP interface. These simulations were done using commercially available Lumerical software.

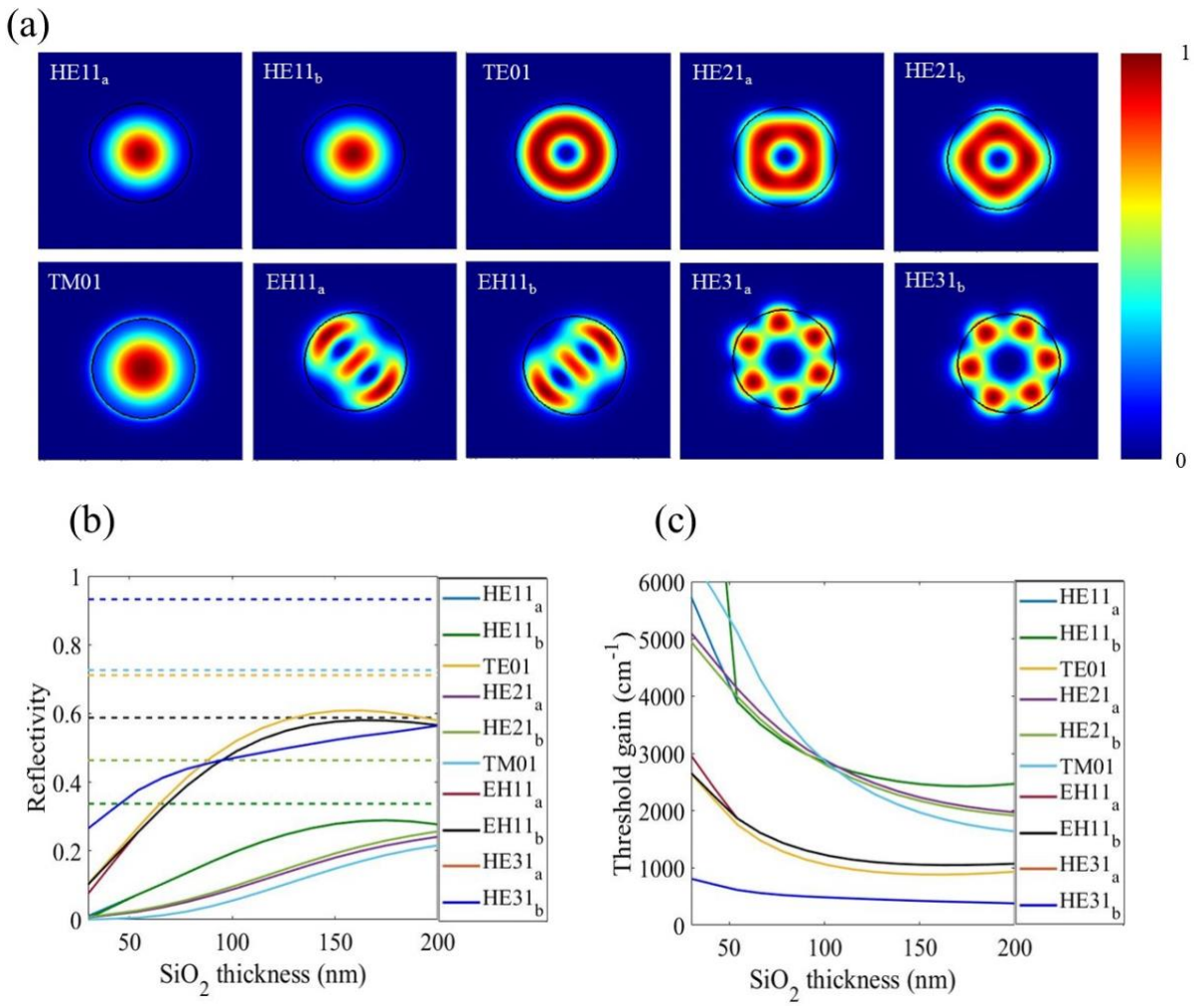

Figure 4-8 (a) Electric field intensity profile of the first 10 modes supported in 500 nm diameter InP nanowire at the wavelength of 870 nm. (b) Reflectivity for all the 10 modes at both ends of the nanowire as a function of SiO_2 thickness. Dashed line represents reflectivity at nanowire/air interface and bold line represent reflectivity at nanowire/SiO_2 interface for the same mode (c) Threshold gain as a function of SiO_2 thickness for the first 10 modes in 4 μm long InP nanowire.

To study the effect of SiO_2 thickness, the diameter of InP nanowire was fixed at 500 nm and reflectivity and confinement factor were calculated to find out the threshold gain. Saxena et al.

have reported the detailed calculations for the threshold gain [145]. First ten guided modes in a free standing InP nanowire were calculated using Lumerical MODE. Figure 4-8(a) shows the guided modes at the wavelength of 870 nm in an InP nanowire of 500 nm diameter. Wavelength of 870 nm corresponds to the bandgap of WZ InP nanowire at room temperature [167]. Once the possible modes in the nanowire were identified, the confinement factor (γ) was calculated using Lumerical MODE. Finally, reflectivity at air/InP facet (R_1) and SiO_2/InP facet (R_2) were calculated using Lumerical FDTD and threshold gain was measured using the following equation.

$$\gamma g_{th} \sim \frac{1}{L} \ln \frac{1}{R} \qquad (4.1)$$

Here, L is the nanowire length, g_{th} is the threshold gain, γ is the confinement factor and R is the geometric mean of the reflectance at both the facet ($\sqrt{R_1 R_2}$). Figure 4-8(b) shows the reflectivity at both the facets. It is quite evident that reflectivity for all the modes is lower at SiO_2 interface as compared to air interface indicating some mode leakage at the nanowire-substrate interface. Figure 4-8(c) displays the modelled threshold gain using equation 4.1 for the first ten modes. As the SiO_2 thickness increases from 30 to 150 nm, the threshold gain required to achieve lasing decreases. After this, change is quite small therefore, for all the ensemble devices, we used an SiO_2 thickness of ~ 150 nm as the SAE mask.

4.2.1 Simulations

Figure 4-9 displays the schematic diagram of radial InP nanowire where p-doped core with 50 nm of n-doped shell is considered. The donor concentration was set at $1x10^{18}$ cm^{-3} and the acceptor concentration was kept at $1x10^{17}$ cm^{-3}. A 20 nm of conformal ITO layer on n-doped shell was used to reduce series resistance and to act as a current spreading layer. The configuration of system was defined as WZ for the nanowire and ZB for the substrate with a doping concentration of $2x10^{18}$

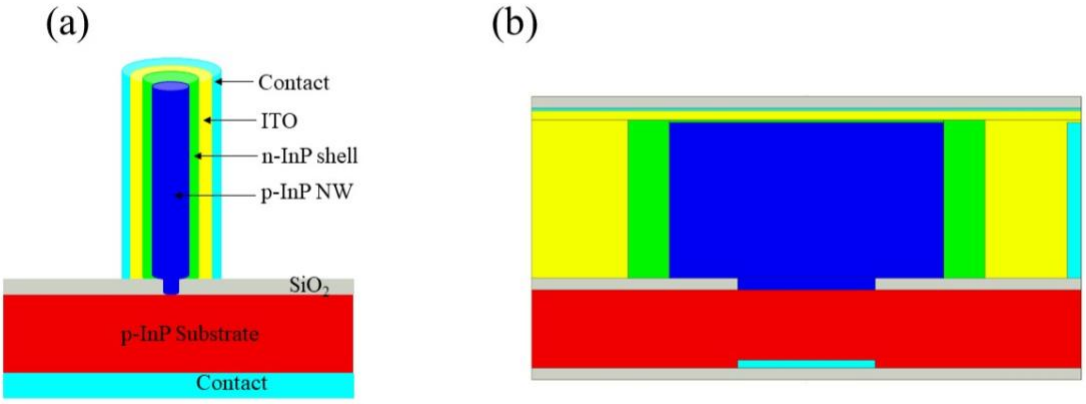

Figure 4-9 (a) Schematic diagram of core shell InP nanowire (b) LaserMOD CAD layout (not to the scale).

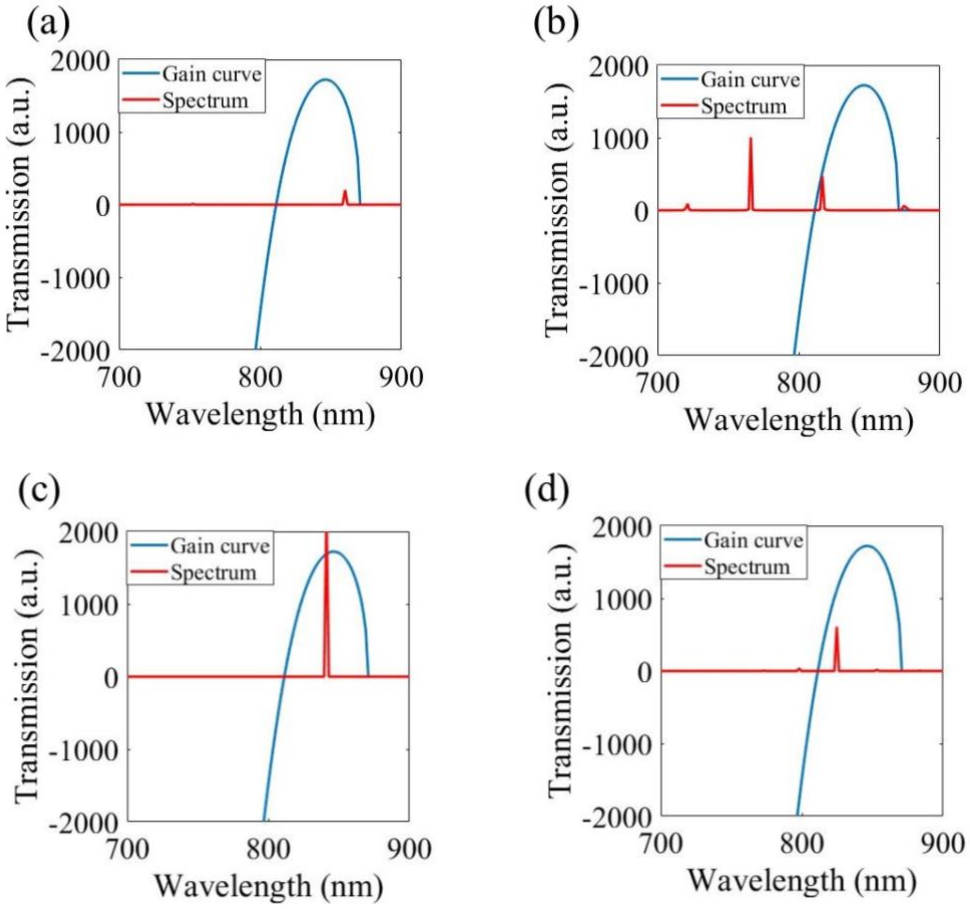

Figure 4-10 Room temperature gain curve at a carrier density of $4x10^{18}$ cm^{-3} plotted together with modes supported in radial InP nanowire of length (a) 1 µm (b) 2 µm (c) 3 µm (d) 4 µm.

cm^{-3}. While calculating the modes in 2D, *y min* was set to the bottom of the nanowire to study only

the modes supported inside the nanowire cavity. The rest of the steps were similar as discussed in section 4.1.1. The length of the nanowire was varied from 1– 4 µm and overlap of the corresponding longitudinal modes and gain spectrum at a carrier concentration of $4x10^{18}$ cm^{-3} was observed. Figure 4-10 shows the overlap of the gain spectrum with transmission spectrum at room temperature with the resonant peaks at 0.860, 0.816, 0.841 and 0.824 µm can be observed for 1, 2, 3 and 4 µm long radial InP nanowire cavities, respectively.

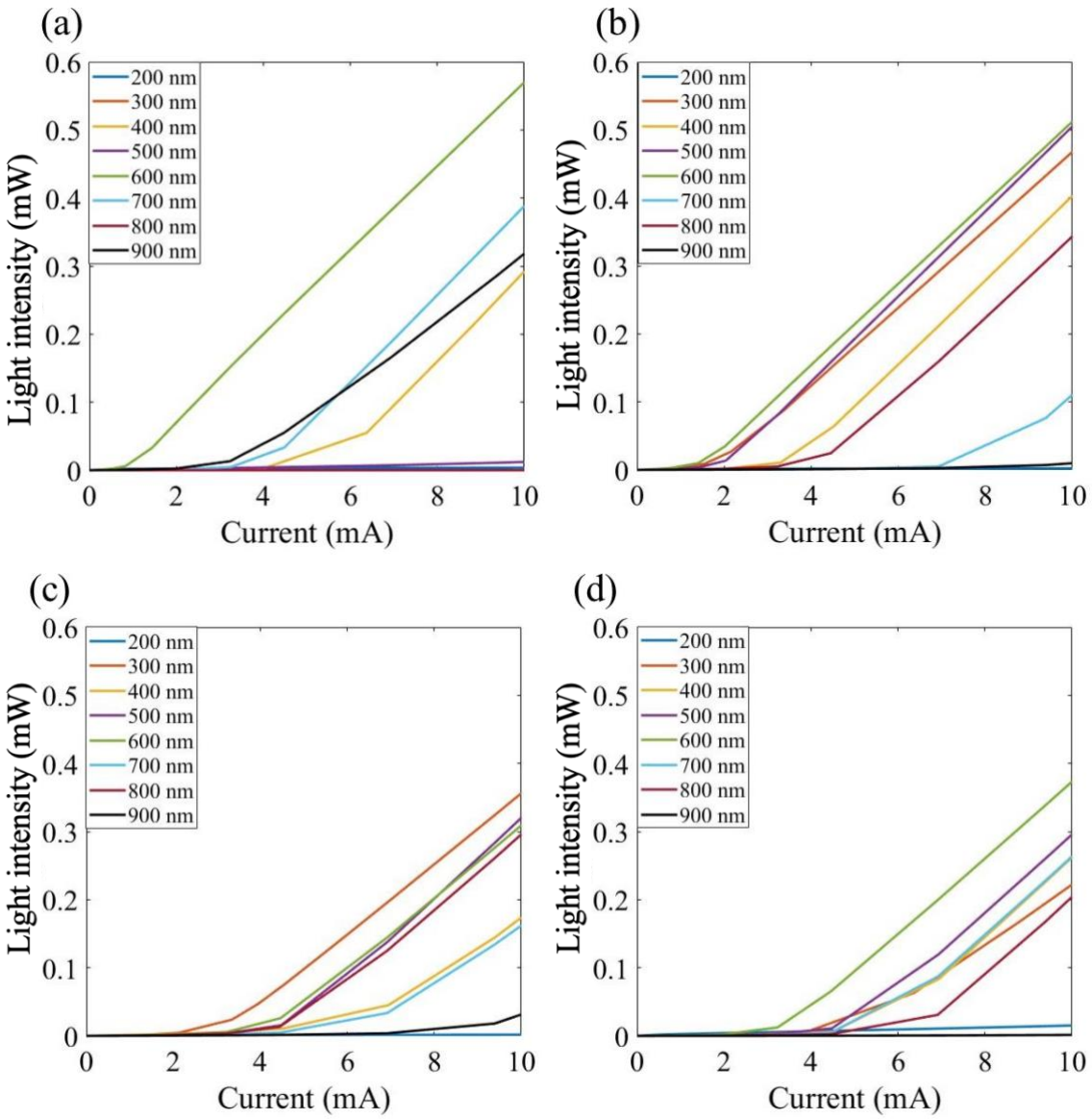

Figure 4-11 Room temperature L-I plots of radial InP nanowire with a total length of (a) 1 µm (b) 2 µm (c) 3 µm (d) 4 µm with different diameters showing lasing.

Following this, 2D simulations were performed where the diameter of core was varied from 100 to 900 nm to align the longitudinal mode with the waveguide dimensions. The lasing behaviour for different waveguide diameter and nanowire length are plotted in Figure 4-11. The minimum diameter required to achieve lasing is 600 nm for 1, 2 and, 4 µm long nanowire and 300 nm for 3 µm long wire. The minimum threshold required to achieve lasing in a 1, 2, 3 and 4 µm long nanowire is 0.83, 1.4, 2.13 and 3.23 mA, respectively. The threshold current is ~3.5 time lower than axial structure due to increase in active region. With increase in length, threshold current increases due to increase in non-uniform carrier injection.

4.2.2 Device fabrication

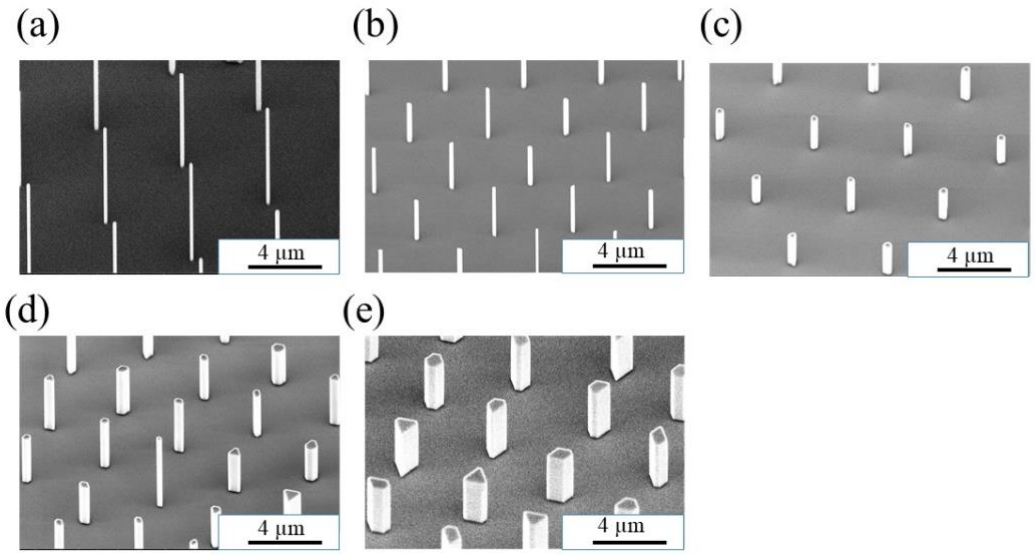

Figure 4-12 SEM images of the InP nanowire array after growth at 45° tilted view with V/III ratio of (a) 81, (b) 150, (c) 300, (d) 400 and (e) 500.

Owing to the reduction in array size, MOCVD growth was again optimised to achieve desired dimensions. Additionally, EBL parameters were revised to obtain minimum hole opening. In EBL, the dose was varied from 100 to 400 µJ/cm^2 and it was found that 275 µJ/cm^2 was required to obtain a hole of ~ 50 nm in a ~300 nm thick electron resist. As discussed in section 3.1.2, as the

dose increases, the pattern size increases. The minimum diameter of ~100 nm was obtained with 50 nm of designed diameter. Since lateral growth is required to obtain nanowires with a larger diameter than the hole opening, V/III ratio was varied from 80 to 500. Figure 4-12 shows that as V/III ratio increases, the diameter of the nanowires increases while their length decreases. Moreover, non-uniformity in the nanowires increases with higher V/III ratio. The rest of the growth parameters such as molar flow rates of trimethylindium, diethylzinc and temperature were the same as those used for the growth of axial structure. Time of growth was also varied to obtain the optimum height of 1-2 µm.

4.2.3 EL measurements

After MOCVD growth, the device was fabricated by depositing 20 nm of ITO and 10 nm of Au using sputter and an Au pad using e-beam evaporator near the array. To minimise heating, measurements were performed at 78 K and the current was pulsed with a pulse width of 0.5 µs and duty cycle of 1%. Figure 4-13 (a) shows the comparison of I-V characterises at 78 K. Deviation in the I-V behaviour confirms non-ideal contacts. However, current levels in the fabricated devices are significantly higher than the axial devices indicating significant reduction in the series resistance. Figure 4-13 (b) shows the EL characteristics of the device where light output increases with injection current. Similar to the axial structure, 2 peaks are observed at low current levels which start merging at higher injected currents due to heating. Moreover, significant red shift in the EL spectra also confirms excessive heating. An additional shoulder peak corresponds to ZB InP is observed at higher current levels [172]. This suggests that at higher currents, some carriers start recombining inside the substrate underneath the wires. Figure 4-13(c) confirms that emission is from the nanowires. After 140 mA, the device was burnt. The current passing through each nanowire is ~1.4 mA which is close to the threshold however, recombination inside the substrate

and excessive heat reduces the gain generated. Moreover, non-uniform light output in Figure 4-13(c) confirms the non-uniform resistance inside the array. Nevertheless, these measurements suggest that radial structure outperforms axial structure in terms of reducing lasing threshold, reducing series resistance and allowing more current to pass through the device before degradation.

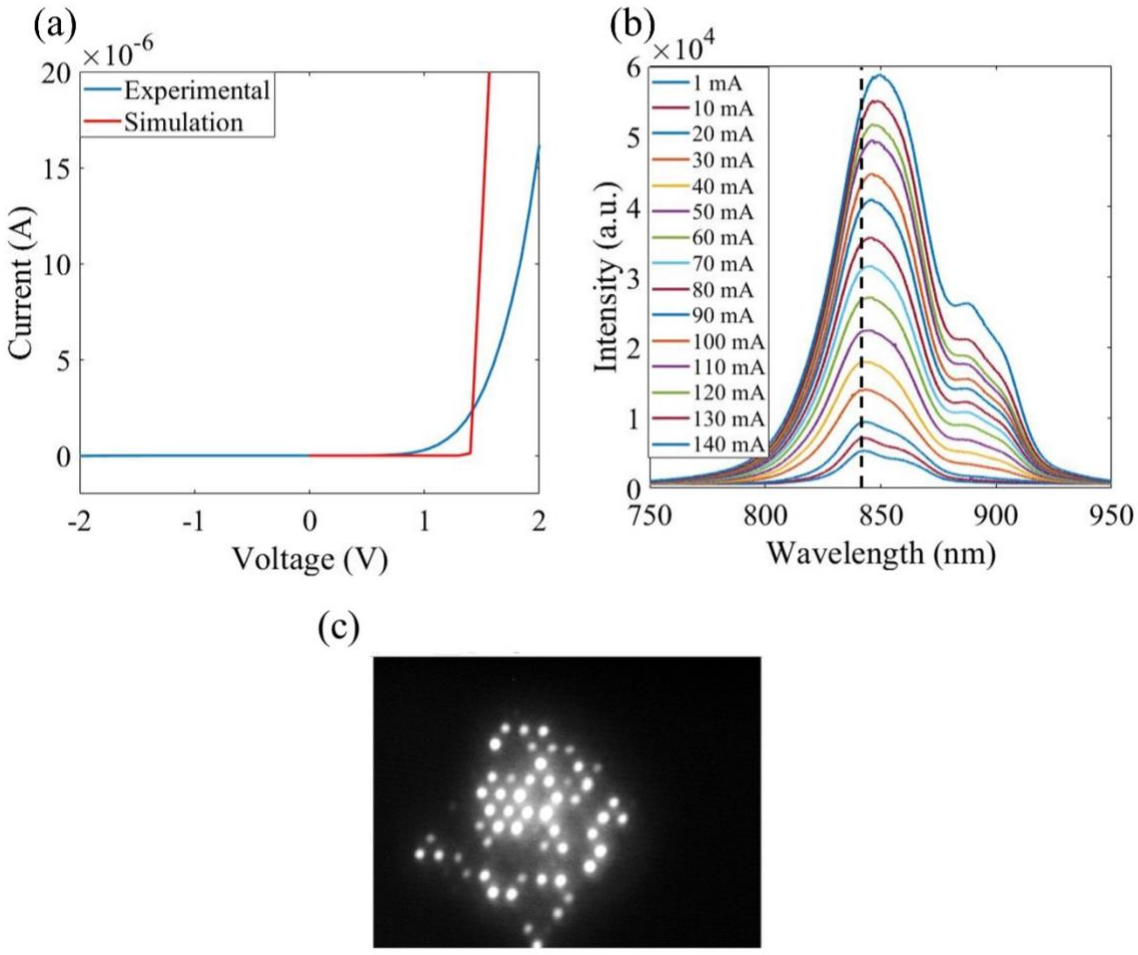

Figure 4-13 At 78 K (a) Comparison of simulated and measured I-V characteristics. (b) EL spectra of radial nanowire device at different current injection levels where, black dash line represents peak position at 840 nm. (c) Optical images of the emission from the 10 x 10 nanowire array at 100 mA.

To achieve lasing, a possible solution is to reduce the lasing threshold further either by decreasing the free carrier absorption or increasing gain. To decrease free carrier absorption, one feasible solution is to use TCOs as both contact and doped layer. This will also help in reducing contact

resistance, as it is easier to achieve higher doping concentration in TCOs as compared to p and n doped InP. Incorporation of quantum wells inside the nanowire can help in enhancing gain by quantum confinement. However, quantum well structures require a lot of optimisations due to facet evolution process, as InGaAs quantum wells prefer a ZB structure whereas InP nanowire has a WZ structure [93, 96, 173]. Additionally, different contributions from axial and radial quantum wells will further complicate the system. So, we decided to investigate the effect of various TCOs.

4.3 Conclusions

In conclusion, in this chapter we simulated the lasing behaviour in InP nanowires and observed that higher doping concentration is required to achieve low threshold lasing in axial structures. However, experimentally, the nanowires were burnt before reaching threshold. The potential reasons for degradation of device were high contact resistance, low doping concentration, metal absorption and excessive heating. To reduce heating related issues, measurements were performed at 78 K. Significant improvement in the light output was observed however, lasing could not be obtained as the nanowires were burnt at ~ 85 μA whereas the minimum simulated lasing threshold was ~ 2.5 mA. This indicates that to achieve lasing, threshold needs to be reduced. To reduce threshold, radial InP nanowires were investigated. Radial devices showed remarkable improvement in reduction of series resistance however, they struggled with shifting of recombination region inside the substrate as well as excessive heating and therefore, lasing was not achieved. The potential solutions for further improvement in the devices are to either incorporate quantum wells or use radial nanowire-TCOs structure. Quantum well generates significant higher gain due to confinement of carriers whereas TCOs reduces metal absorption and free carrier absorption and radial structure increases the active region.

Chapter 5. Core-shell p-InP/n-ZnO nanowire devices

In this chapter, we carry out in-depth studies about formation of p-n junction at p-InP/n-ZnO interface and realise LEDs from it. Following this, we simulate ZnO/InP radial structure to reduce lasing threshold. We also attempt to demonstrate laser from p-InP/n-ZnO interface and study the potential challenges. Finally, we investigate flexible LEDs and study their temperature dependent characteristics.

5.1 Introduction

ZnO is intrinsically n-type TCO. The origin of n-type conductivity in ZnO is attributed to oxygen vacancies, zinc interstitials and unintentional hydrogen doping [174, 175]. Hydrogen which is also considered as dominant donor comes from ALD precursors such as diethyl zinc and H_2O as well as water vapour present inside the chamber. Another advantage is thin ZnO layer acts as a passivation layer for InP nanowires, exhibit excellent chemical stability and biocompatibility [176-178].

Owing to these properties, several devices have been investigated using ZnO. ZnO/GaN heterojunction LEDs in UV regime has been area of interest to many researchers since the advent of TCOs. There are various reports of planar and nanowire UV LEDs using n-type ZnO grown on p-GaN [179-183]. However, these nanowire LEDs are not core-shell type but features ZnO nanowires grown on GaN substrate/thin layer. Growing ZnO nanowires on GaN is a cumbersome and complex process and the devices are either unstable and/or highly inefficient [184-186]. InP and GaAs based planar and nanowire solar cells have also been demonstrated using ZnO as an electron selective contact [187-189]. There are few examples of GaAs and InP based planar structures LEDs

[190-192]. Getting higher extraction efficiency with these planar devices is always challenging and this leads to the development of nanowire LEDs which can overcome this issue owing to their one-dimensional geometry with large surface area, leading to more efficient light emission and effective current spreading [99, 193-195]. Still, there are no reports on InP/ZnO nanowire LEDs.

5.2 Experimental methods

Fabrication of our on-substrate LED device can be divided into two sections: SAE of nanowires by MOCVD and device fabrication. Figure 5-1(a) shows the p-InP nanowires grown by SAE-MOCVD technique [22]. Process of preparing SAE template has already been discussed in the section 3.2.

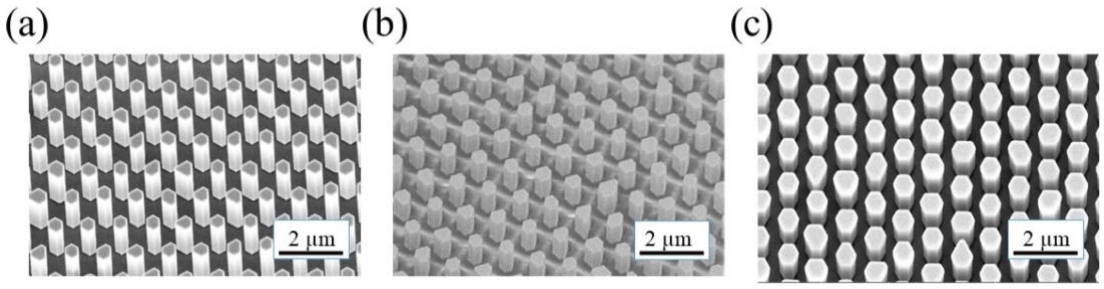

Figure 5-1 SEM images of the InP nanowire array after growth and during the device fabrication process at 15° tilted view. (a) As-grown nanowire array. (b) After SU-8 etching with ICP-RIE. (c) After ZnO, ITO and Au deposition.

To grow nanowires, SAE template on p-InP substrate with 300 nm openings and 1 µm pitch over a 100 µm x 100 µm area was used for growth by MOCVD at a base pressure of 100 mbar with H_2 as carrier gas at a total flow rate of 14.5 l/min. Trimethylindium and phosphine were used as precursors with a molar flow rate of 6.07×10^{-6} and 4.91×10^{-4} mol/ min, respectively for 15 mins at 730°C. For p-doping, diethylzinc with molar flow of 8.63×10^{-6} mol/min was used. SEM was carried out to image the nanowire arrays after growth and during the LED fabrication process, as shown in Fig. 5-1. Based on the SEM measurements, the average length of the nanowires is 3 µm

with an average diameter of 400 nm. Device fabrication process has also been described in detail in section 3.3.2.

To characterise the electrical and optical properties, both EL and PL measurements were performed using a home built μ-PL system. To investigate the junction properties, EBIC measurements were performed on the on-substrate device with a beam current of 0.17 nA and an accelerating voltage of 2 kV. For this purpose, after SAE growth, 120 nm of ZnO was deposited using ALD on nanowires with a diameter of ~500 nm. ICP-RIE etching was performed to expose the top of the nanowires, so that the cross-section from the top could be seen clearly under the microscope. Finally, a thin layer of SU-8 was spin-coated to avoid shorting and ICP etching was used to expose the tips of the embedded nanowires. To power the nanowire array device, the substrate and thus the nanowire core was electrically contacted with the FIB stage and the ZnO shell was contacted by a nano-manipulator inside the FIB chamber.

5.3 Study of p-InP/n-ZnO junction properties

First, we measured the I-V characteristics of heterojunction ZnO-InP nanowire LEDs fabricated on the InP substrate. Figure 5-2(a) shows the rectifying behaviour typical of an LED with a turn-on voltage of around 4 V and series resistance of around 88.9 Ω. To calculate the turn-on voltage and series resistance, I-V curve at higher voltages was extrapolated as a straight line (black dashed line in Figure 5-2 (a)). The x-intercept gives the turn-on voltage and the slope of line provides the series resistance. To gain a deeper understanding of the I-V characteristics, ln (I) vs V plot was plotted in the forward bias, in Figure 5-2(b). Current in a diode is given by [196].

$$I = I_s\left(e^{\frac{qV}{nkT}} - 1\right) \qquad 5.1$$

where I_s = reverse saturation current

q = charge on an electron (1.6 x 10 $^{-19}$ C)

n = ideality factor

k = Boltzmann's constant (1.380649×10^{-23} J·K^{-1})

T = temperature (300 K)

For sufficiently large bias, eq. (5.1) can be written as:

$$I = I_s \left(e^{\frac{qV}{nkT}}\right) \quad 5.2$$

Taking natural log on both sides:

$$\ln(I) = \ln(I_s) + \frac{q}{nkT}V \quad 5.3$$

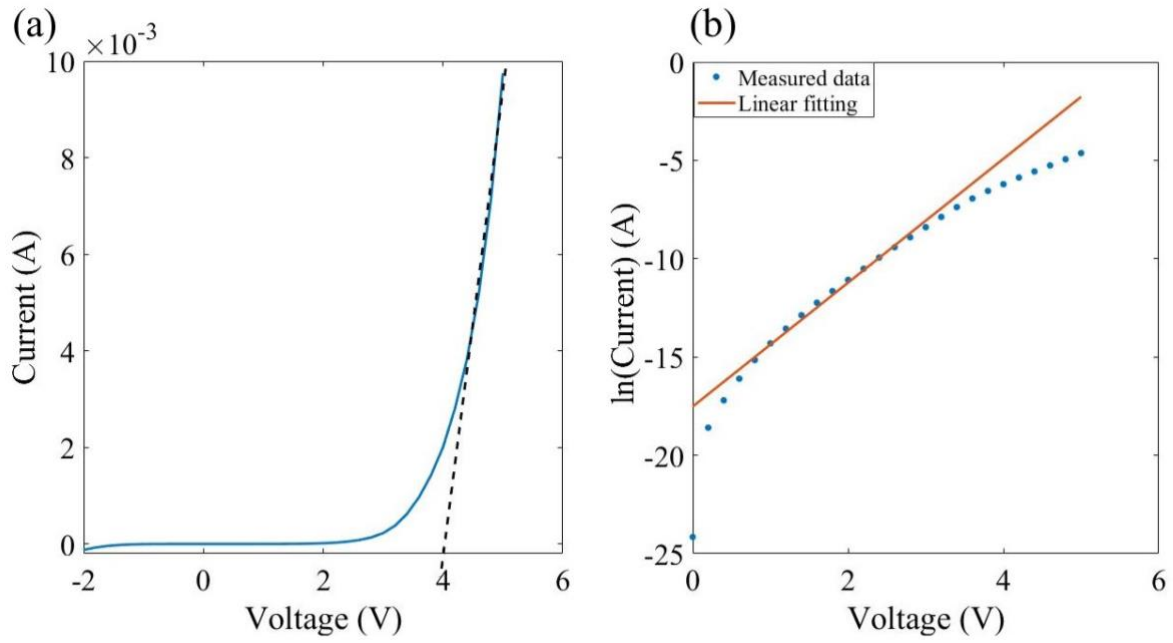

Figure 5-2 (a) I-V characteristics of the device at room temperature. (b) Plot of ln (I) vs V to calculate ideality factor of the device.

By plotting ln(I) vs V, the reverse saturation current and ideality factor can be obtained from the y-intercept and slope, respectively. By linear fitting the curve in Figure 5-2(b) with eq. (5.3), a reverse saturation current of 24.6 nA and an ideality factor of 12.2 are obtained. Here, an ideality factor larger than 2 is consistent with previously reported InP nanowire LEDs (n = 7.3) and implies that the current is dominated by tunnelling [89, 90]. Another reason for the high ideality factor may be due to the formation of a native oxide layer at the InP/ZnO interface [176].

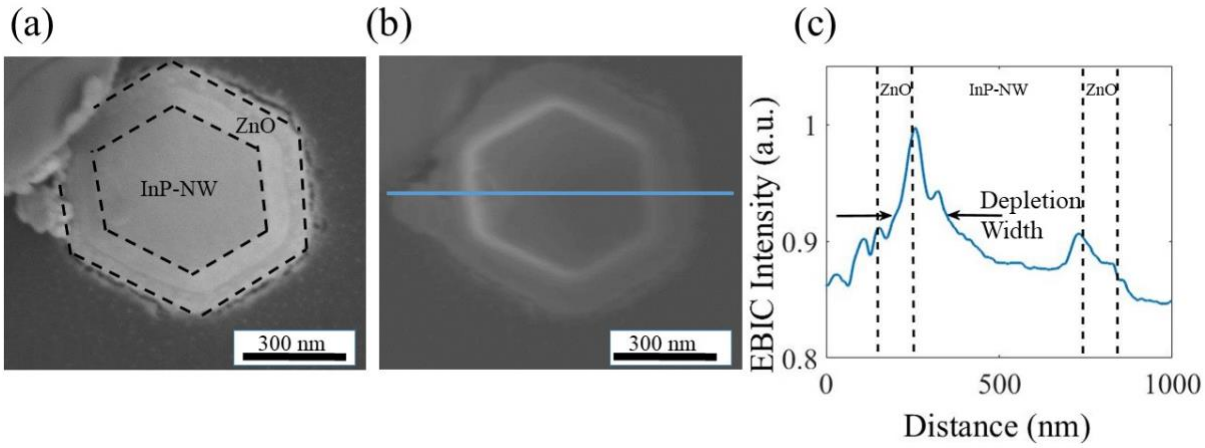

Figure 5-3 (a) SEM image of a single nanowire from the fabricated LED array. At the top left corner is the contact probe which makes good contact with the ZnO shell. (b) EBIC signal acquired under an accelerating voltage of 10 kV corresponding to the SEM image in (a). (c) EBIC scan profile across the nanowire, indicated by the blue solid line.

The property of the p-InP/n-ZnO heterojunction was investigated using EBIC measurement of a single nanowire device. Figure 5-3(a) shows the cross-sectional SEM image of the nanowire, with a clearly visible contrast of the InP nanowire core and ZnO shell. Figure 5-3(b) displays the corresponding EBIC signal measured under an accelerating voltage of 2 kV and 0.17 nA current. From Figure 5-3(b), a bright ring can be observed at the nanowire-ZnO interface, which can be attributed to the depletion region where the highest EBIC current is produced under 0 V bias. The EBIC intensity profile is plotted across the diameter of the nanowire as shown in Figure 5-3(c).

The depletion width is approximately 138 nm when measured at the 1/e of maximum intensity value. Using the depletion width we estimated that the p-doping level in the nanowire to be 6.75 x 10^{16} cm^{-3} which is consistent with previously reported values[104]. To calculate the carrier concentration of ZnO, a planar 30 nm film of n-ZnO (N_D) deposited under the same conditions on a glass substrate. Then, carrier concentration was calculated to be 2 x 10^{19} cm^{-3} using a combination of Drude and Cody-Lorentz model by ellipsometry and is consistent with the reported values in the literature [197]. The calculation of depletion width proceeds as follows [196]:

$$X_p = \sqrt{\frac{2\varepsilon_n\varepsilon_p N_D(V_{bi}-V)}{qN_A(\varepsilon_p N_A+\varepsilon_n N_D)}} \quad 5.4$$

$$X_n = \sqrt{\frac{2\varepsilon_n\varepsilon_p N_A(V_{bi}-V)}{qN_D(\varepsilon_p N_A+\varepsilon_n N_D)}} \quad 5.5$$

$$X = X_p + X_n \quad 5.6$$

$$V_{bi} = \frac{(\emptyset_p-\emptyset_n)}{q} \quad 5.7$$

where, X, X_p, X_n = total depletion width, depletion width in the p and n regions, respectively.

N_A = 6.75 x 10 [16] cm^{-3}

N_D =2 x 10 [19] cm^{-3}

$Ø_p$ = 4.65 eV [198]

$Ø_n$ = 3.7 eV [199]

ε_p = $12.35\varepsilon_0$ [200]

ε_p = $10.4\varepsilon_0$ [201]

V = 0, (unbiased EBIC)

Using the above-mentioned equations, a depletion width of 138.85 nm is derived, consistent with the value calculated from the EBIC results.

It is noticed that the EBIC profile is asymmetric, extending more into p-doped nanowire. This confirms that the depletion region is primarily formed in the nanowire where a majority of recombination occurs in this region. The possible reason for the non-symmetric profile at both the junctions could be a small angle tilt or non-uniform ICP-RIE etching of ZnO shell which is evident from the SEM image (Figure 5-3(a)).

5.4 EL properties of p-InP/n-ZnO

5.4.1 Room temperature EL properties

Figure 5-4(a) shows the EL spectra from the nanowire array LEDs on substrate with increasing forward current injection level at room temperature. The EL signal is detectable at an injection current of 1 mA, showing a peak at 870 nm with a shoulder at around 920 nm. To have deeper insight of heating, the room temperature EL spectrum measured at 5 mA is plotted in Figure 5-4(b), in comparison with their PL spectrum. Both spectra display same peak at 870 nm, confirming that Joule heating is kept to a minimum in our device even at continuous current injection. In the PL spectrum, the appearance of only one peak at 870 nm confirms that nanowires have a pure WZ structure. It has previously been reported that for the above mentioned growth conditions, the nanowires have a pure WZ phase irrespective of Zn doping concentration [104]. However, in the EL spectrum, a shoulder at higher wavelength is observed.

To investigate the origin of different peaks, Lorentz curve fitting was performed (Figure 5-4(c)). It is found that there are three peaks with majority contribution from the peak at 1.42 eV which corresponds to the fundamental bandgap of WZ InP nanowires [167, 202]. The peak at higher energy

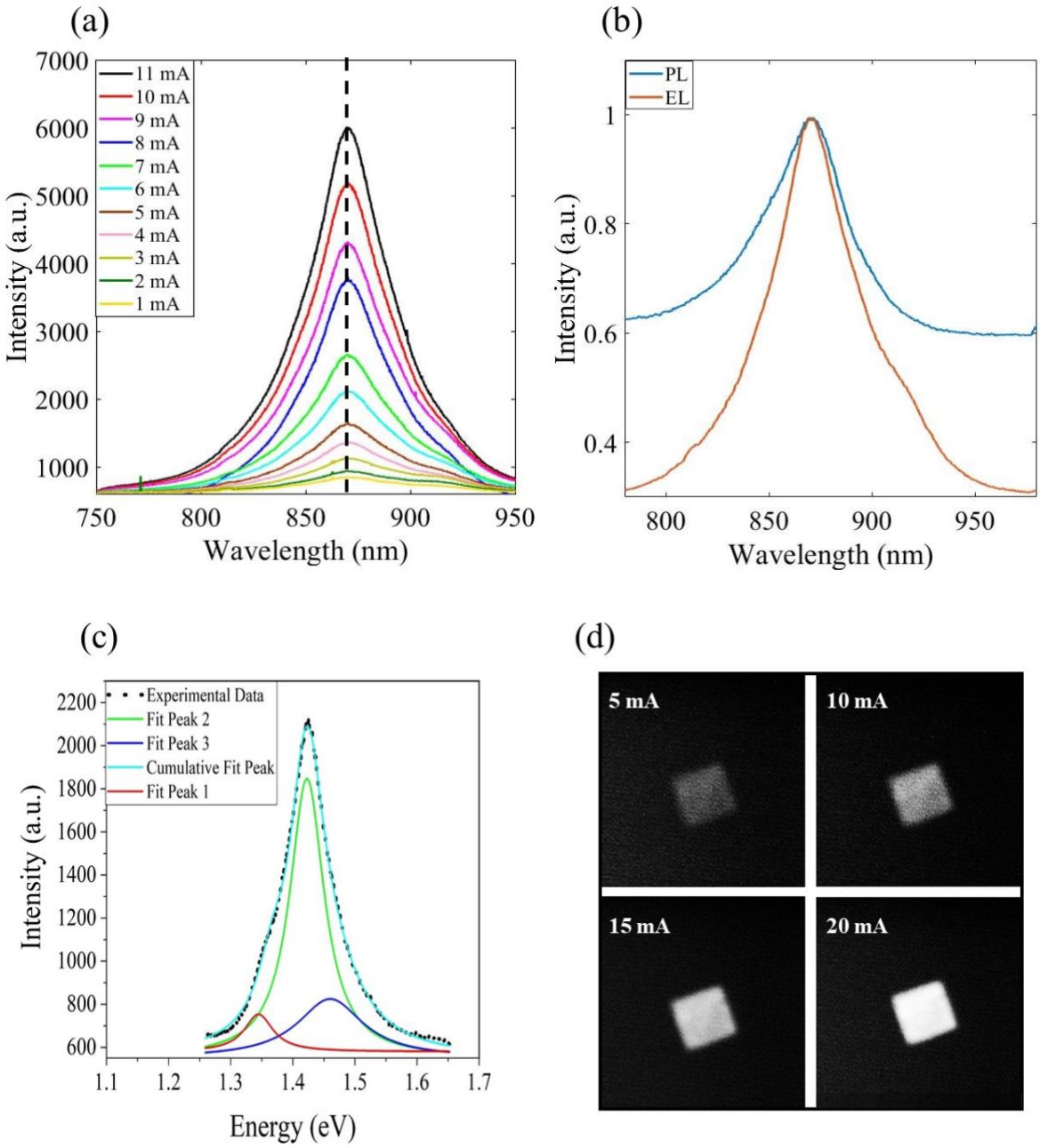

Figure 5-4 Room temperature EL spectra at different current injection levels. The black dashed line indicates the peak of the spectra at 870 nm. (b) PL spectrum at 17 μW excitation power and EL spectrum at 5 mA current. (c) Lorentz curve fitting of the EL spectrum measured at 5 mA at room temperature. (d) Optical images of the emission at room temperature from the 100 x 100 μm^2 array at different current injection levels.

of 1.46 eV is due to the light hole and heavy hole splitting in WZ structures [203]. A. Zilli et al.

reported that this peak becomes dominant at temperatures above 150 K due to thermal population of higher energy states [167]. The energy difference between these two peaks has been reported to be around 40 meV, consistent with our value of 37.8 meV [167, 203, 204]. We attributed the peak at the lowest energy of 1.34 eV to the recombination occurring at ZB InP substrate [202]. The existence of this peak confirms that some carriers are recombining in the substrate. At high injection current, EL intensity increases but the peak position slightly red-shifted to longer wavelength due to Joule heating. Figure 5-4(d) shows the optical microscopy image of the nanowire LED array captured by an infrared camera with 10x lens. It is clearly evident that light is emitted from the nanowires and with the increase of current injection, the emission intensity becomes more uniform across the entire array.

5.4.2 Temperature dependent EL properties

To investigate the temperature dependent characteristics of the device, I-V characteristics were studied from room temperature to 78 K from -1 to 1 V. As shown in Figure 5-5(a), as the temperature decreases, the current in the forward bias decreases. Following this, EL was conducted under an injection current of 5 mA from room temperature to 78 K and shown in Figure 5-5(b). The linewidth decreases with decreasing temperature and the spectra are blue-shifted, as a result of increased bandgap with decrease of temperature [167]. Interestingly, at ~238 K, we observed another peak in the EL spectra, which becomes more prominent at lower temperatures. Figure 5-5(c) shows the LED behaviour at 78 K as a function of increasing injection current. To understand the origin of this peak, Lorentz fitting was performed at 78 K (Figure 5-5(d)) and 3 peaks were observed. The highest energy peak at 1.48 eV corresponds to the bandgap of nanowires which is also known as the A exciton peak in WZ semiconductor. We attribute the lower energy peak at 1.44 eV to radiative recombination from the conduction band to Zn acceptor in the nanowires. We

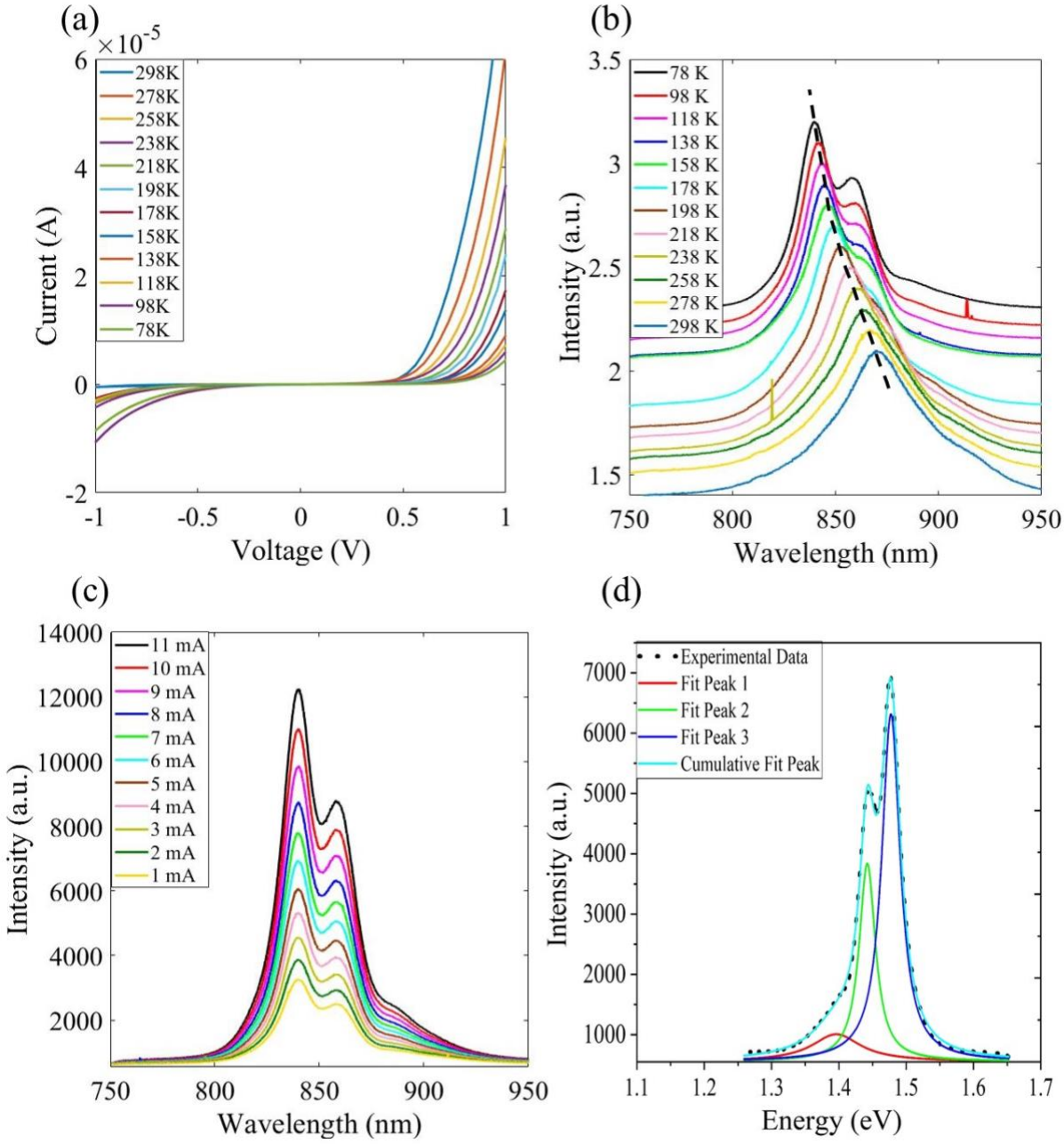

Figure 5-5 (a) Temperature dependent I-V characteristics of the device. (b) Temperature dependent EL spectra of the device at 5 mA current where black dashed line indicates the peak position. (c) EL spectra at 78 K at different current injection levels. (d) Lorentz curve fitting of the EL spectrum measured at 5 mA at 78 K.

calculated the activation energy of Zn acceptor level for doping concentration of 6.75 x 10^{16} cm^{-3} obtained from EBIC measurements using the formula given by K. Hansen et al [205].

$$E_A = E_0 - a(N_A^-)^{-\frac{1}{3}} \quad 5.8$$

where E_0 is the ionisation energy (51 meV) and a = 3.9 x 10^{-5} meV cm. This gives the activation energy of 35.1 meV which is same as the energy difference between these peaks confirming that the lower energy peak is related to Zn acceptor levels. Previously, defect related peak in pure wurtzite InP nanowires has been observed by various groups [38, 167, 206, 207]. The lowest energy peak at 1.40 eV is due to recombination at the substrate. The difference between this peak and the highest energy peak is around 80 meV which is consistent with the energy difference of WZ and ZB InP nanowires [202].

After confirming good optical and electrical properties without any proper design of p-InP/n-ZnO diode, simulations were performed to obtain optimum design to achieve low threshold lasing.

5.5 Electrically pumped nanowire laser

5.5.1 Simulations

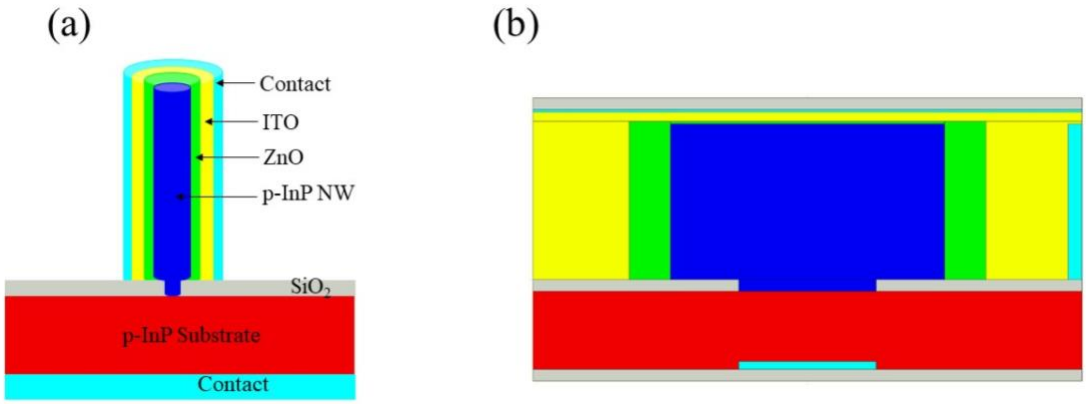

Figure 5-6 (a) Schematic diagram of core shell InP-ZnO nanowire (b) LaserMOD CAD layout (not to the scale).

Figure 5-6 shows the schematic diagram of the device modelled for lasing as well as CAD interface. Again, for better convergence, additional SiO_2 layer was used at the top and the bottom. Detailed steps of doing simulation are given in section 4.4.1. LaserMOD materials database does

not have ZnO material file so, to simulate n-ZnO/p-InP core shell structure, ZnO material was defined in the software. Five main parameters namely, bandgap, electron mobility, hole mobility, optical dielectric constant and static dielectric constant were taken from the literature to define the material. The bandgap as 3.08 eV, optical dielectric constant as 2.37 and static dielectric constant as 18.71 were used for calculations [208]. The electron and hole mobilities of ZnO film were set to 50 $cm^2V^{-1}s^{-1}$ and 20 $cm^2V^{-1}s^{-1}$, respectively [209]. The diameter and length of the nanowire were varied from 200– 900 nm and 1 – 4 µm, respectively. The ZnO thickness was fixed at 30 nm with doping concentration of 2 x 10^{19} cm^{-3} (measured from ellipsometer). Carrier concentration of p-InP nanowire was fixed at 6.75 x 10^{16} cm^{-3} which was estimated from EBIC. To define the substrate, in-built material parameters in LaserMOD of InP was used as the substrate has a ZB configuration. The doping concentration (p-type) of substrate was assumed to be 2 x 10^{18} cm^{-3}. Finally, to decrease the series resistance of the system, 70 nm of conformal ITO layer was considered with doping concentration of 1 x 10^{20} cm^{-3}.

Once the CAD layout and material files were defined, 1D simulations were performed to determine the longitudinal mode supported in the cavity of different lengths. Figure 5-7 illustrates the overlap of the gain curve with longitudinal modes at room temperature at a carrier density of 5x10^{18} cm^{-3}. Resonant wavelengths obtained for 1, 2, 3 and 4 µm long nanowire are 811.9, 851.4, 861.9 and 816.7 nm, respectively. For 3 and 4 µm long nanowires, two longitudinal modes align with the gain peak. Mode with higher transmission was taken for further calculations. Following this, 2D simulations were performed and nanowire diameter was varied from 200– 900 nm to obtain overlap of waveguide supported mode with the longitudinal mode. For mode calculation, *y min* was set to the bottom of the nanowire to study only the modes supported inside the nanowire

cavity. Full laser simulation was performed to determine the threshold condition for each cavity dimensions.

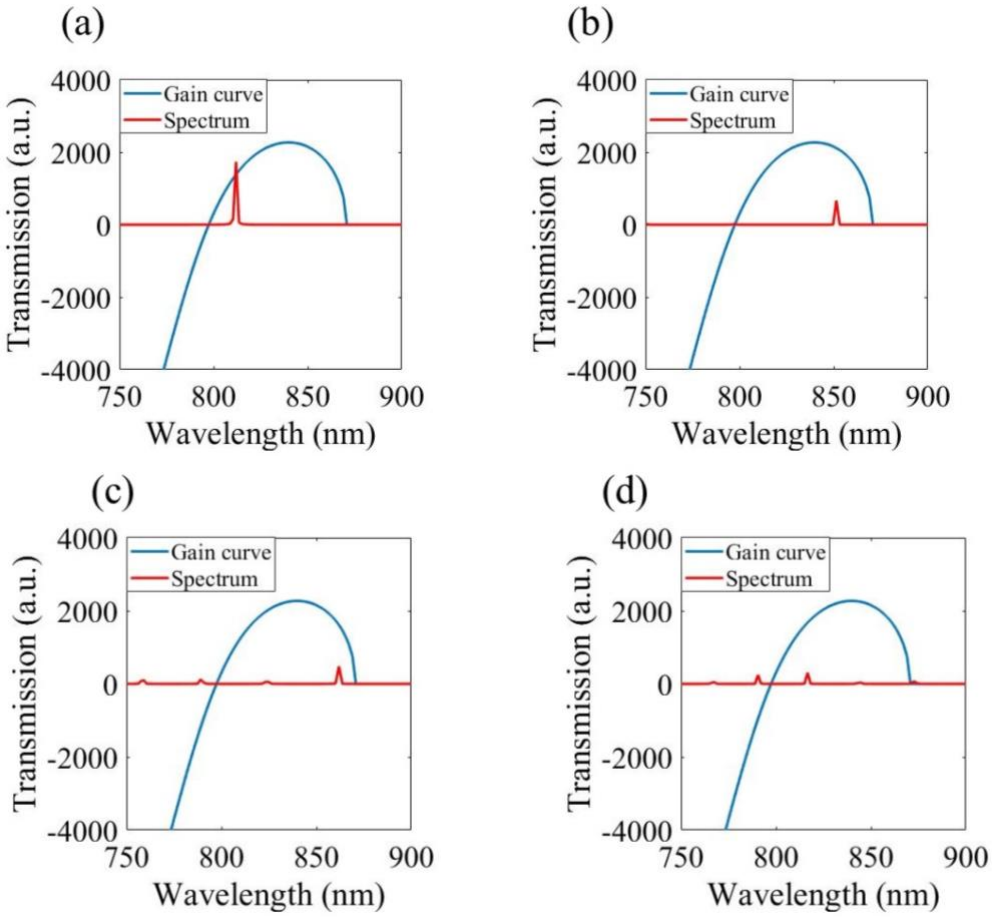

Figure 5-7 Overlap of gain curve at room temperature at a carrier density of $5x10^{18}$ cm^{-3} and modes supported in (a) 1 µm (b) 2 µm (c) 3 µm (d) 4 µm long InP/ ZnO core shell nanowires.

Fig. 5-8 shows the L-I curves for only those waveguide dimensions which showed lasing. Minimum threshold required for all cavity lengths corresponds to 200 nm diameter nanowires. The lowest threshold current of 0.26 mA for 1 µm long nanowire, 0.55 mA for 2 µm long nanowire, 0.83 mA for 3 µm nanowire and 1.07 mA for 4 µm nanowire were obtained. The threshold current increases with length as longer nanowire results in higher non-uniform current spreading from the bottom of the nanowire to the ZnO layer. Here, the advantage of incorporating TCOs is quite

evident as the threshold current required for lasing decreases by an order of magnitude simply by replacing InP homojunction with radial TCO-InP heterojunction.

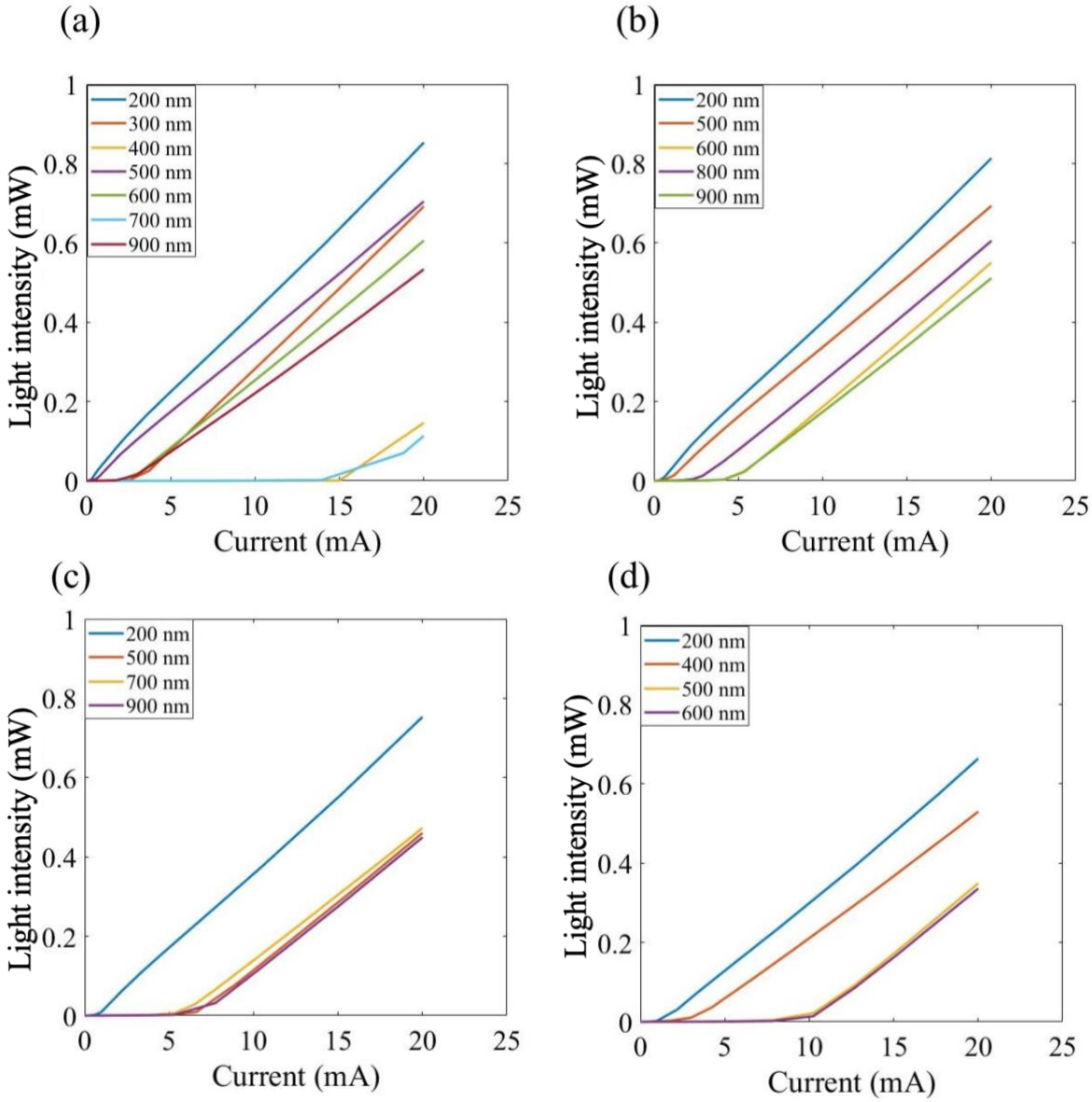

Figure 5-8 Room temperature L-I plots of n-ZnO/p-InP nanowire devices of various nanowire diameter with total length of (a) 1 µm (b) 2 µm (c) 3 µm and (d) 4 µm with different diameters showing lasing.

The minimum threshold current required per nanowire is 0.26 mA for 1 µm long nanowire with a diameter of 200 nm to achieve lasing. Furthermore, increasing nanowire length leads to non-uniform current injection which results in higher threshold current. Therefore, the optimised range

of length of nanowire was considered to be 1 – 2 µm with a diameter of 200 nm. The size of the array was reduced to 10x10 nanowires with a pitch of 5 µm. The array size was reduced so that higher current can be passed with our existing current source and the pitch was increased to avoid coupling among nanowires. Also, as discussed in section 5.4.1, when higher continuous current (~ 11 mA) was passed through the array device, a slight red shift in the EL curve was observed. To minimise heating in the device, the current was pulsed with a pulse width of 0.5 µs and duty cycle of 1%.

5.5.2 Fabrication of nanowire lasers

After MOCVD growth, the device was fabricated using simplified process by depositing 30 nm of ZnO, 70 nm of ITO and 10 nm of Au. Figure 5-9 shows the schematic diagram of the fabrication process.

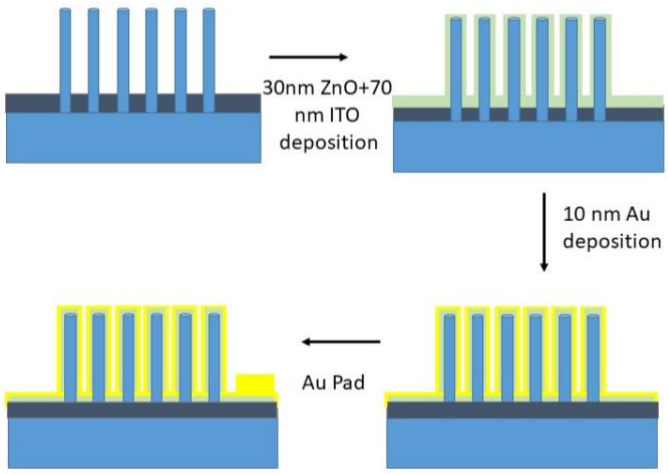

Figure 5-9 Schematic diagram of laser device fabrication process.

5.5.3 Room temperature EL measurements

EL measurements were carried out like the LED device except 50x lens was used instead of 10x lens to capture emitted light from individual nanowires. Figure 5-10 (a) represents EL spectra from

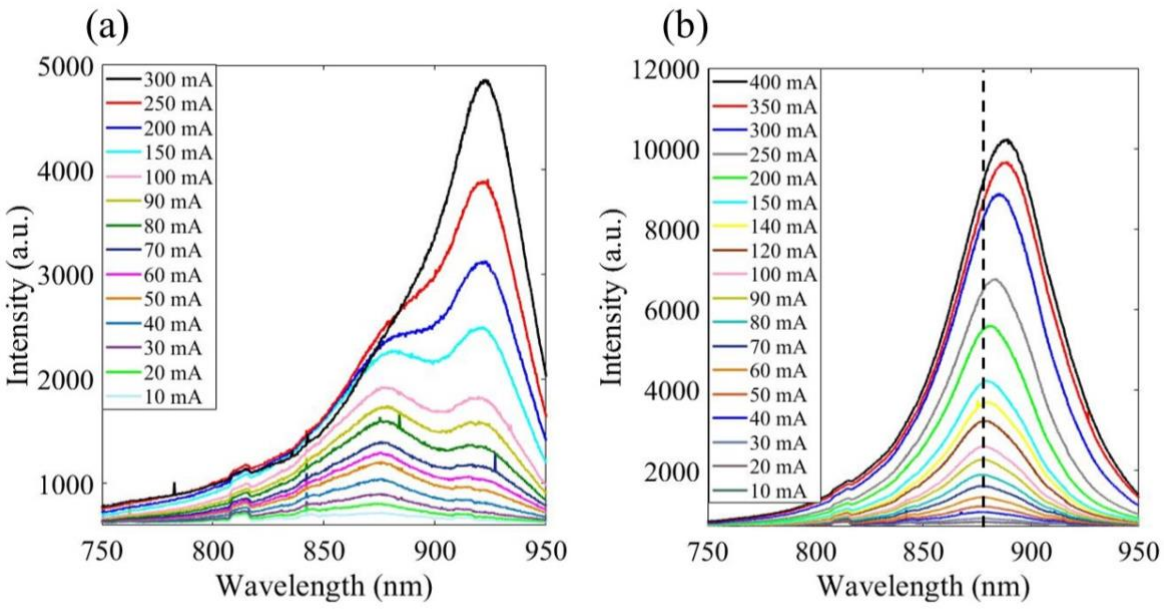

Figure 5-10 Room temperature EL spectra at different current injection levels of (a) a device fabricated without SU-8 and (b) a device fabricated with SU-8. The black dashed line indicates the peak of the spectra at 870 nm.

a single nanowire indicating that EL intensity increases with current injection. However, the device was burnt without reaching to lasing threshold after 300 mA which is ~ 3 mA per nanowire. The injected current is an order higher than simulated lasing threshold, indicating additional losses such as higher series resistance and carrier losses. At lower current injection levels, a single peak at 870 nm corresponding to the bandgap of WZ InP (nanowire) is observed [167, 202]. However, at higher current levels, additional peak at ~ 920 nm is detected. This peak corresponds to the bandgap of ZB InP (substrate) indicating that carrier recombination is occurring in the substrate [202]. With further increase in injected current, the ZB peak dominates over the WZ peak indicating most of the carriers recombine in the substrate. The reason behind this is the lower hole mobility as compared to electron mobility. The holes are injected from the bottom of a 350 µm-thick wafer. By the time they reach to the nanowires, the faster electrons coming from the 100 nm-thick (ZnO/ITO) film would have reached the substrate and recombination occurs within the substrate.

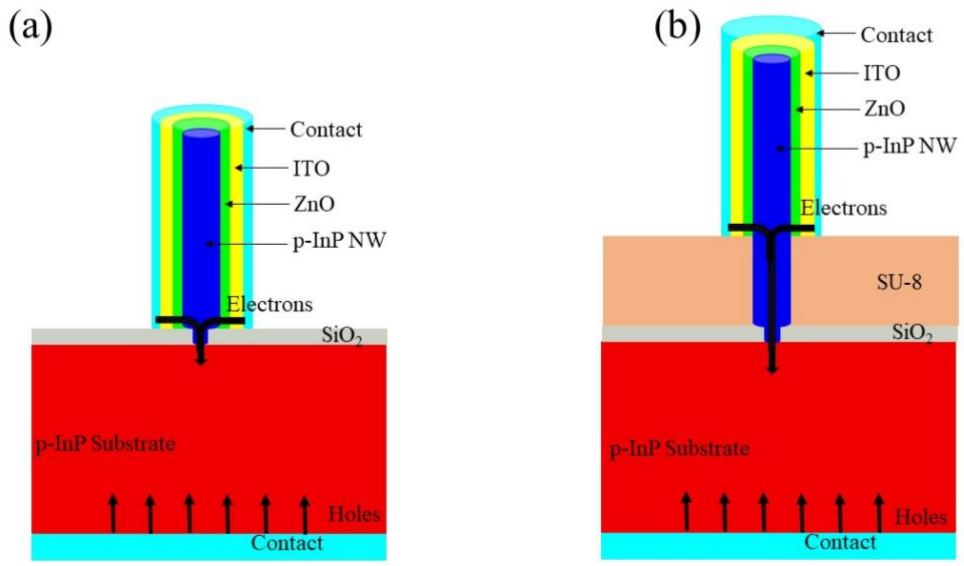

Figure 5-11 Schematic diagram of core shell InP-ZnO nanowire showing comparison of current injection path (a) without SU-8 (b) with SU-8 (not to the scale).

To mitigate this issue, another set of devices with 3-4 µm long nanowires were fabricated with ~ 2 µm thick SU-8 layer. It is evident from Figure 5-11, introduction of SU-8 layer increases electron path to the substrate. Figure 5-10 (b) represents EL spectra from a single nanowire in the array device. Again, the EL intensity increases with the increase in injected current but the device was burnt at ~ 400 mA current. The peak corresponding to the substrate is significantly lower than the previous case, indicating more recombination is now happening within the nanowires. However, at high injection current levels, a significant red shift in the EL spectra is observed, suggesting excessive heating in the device. This excess heat is detrimental to the device performance. To minimise heating effect, measurements were performed at 78 K.

5.5.4 78 K EL measurements

Figure 5-12 (a) displays the EL spectra of the 3-4 µm long nanowire device fabricated without SU-8. Similar to the room temperature measurements, with higher current levels, the peak from the

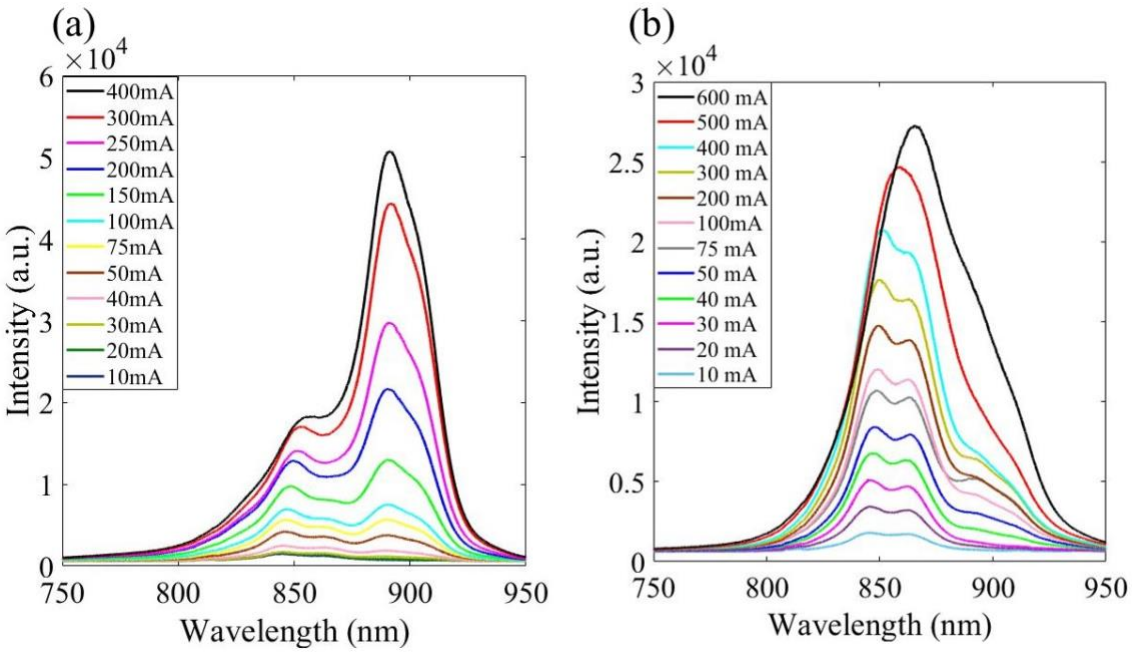

Figure 5-12 EL spectra at 78 K with different current injection levels of (a) a device fabricated without SU-8 and (b) a device fabricated with SU-8.

substrate starts to dominate, suggesting significant carrier recombination in the substrate. The results for the device fabricated with ~ 2 µm thick SU-8 layer is shown in Figure 5-12 (b). At a current injection level of ~ 50 mA, a shoulder due to the ZB InP can be observed indicating carrier recombination in the substrate. However, this effect is significantly lower as compared to the device without SU-8, since the n-type contact now is further away from the substrate thereby giving the chance for more electrons to recombine within the nanowire. At very high current levels, a large red shift is observed in the device indicating substantial heating in the device even at lower temperatures. With a current higher than 600 mA, the device was burnt.

To have deeper insight of degradation of device, SEM was performed. Figure 5-13 (a) shows the entire array after degradation of the device. It is evident that some wires are completely burnt whereas some are still present implying non-uniform current injection in individual nanowires. The potential reason could be different resistance due to slightly non-uniform growth or contact

formation. Figure 5-13 (b) is a magnified image at a burnt nanowire. It can be seen that the nanowire is burnt at the bottom suggesting excessive current crowding inside the part of nanowire grown with 100 nm diameter opening. To avoid this issue, a probable solution is to remove the substrate from the device. This will lead to carrier recombination only inside the nanowires.

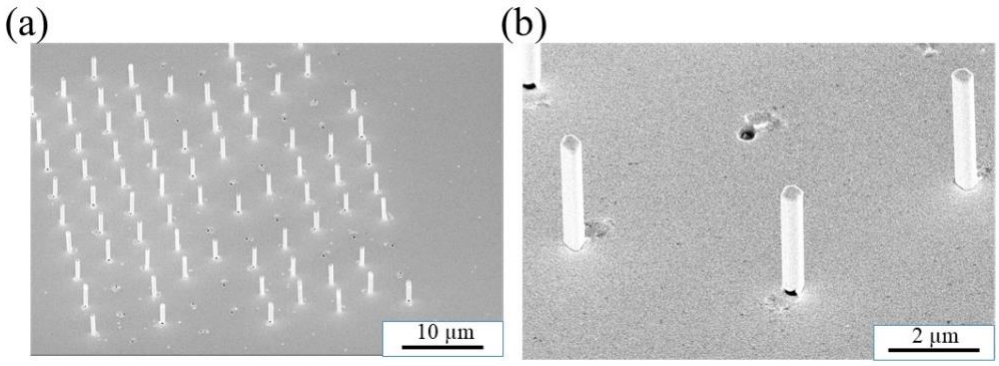

Figure 5-13 SEM images of device at a tilt of 45° (a) entire array, (b) magnified image.

5.6 Flexible LEDs

Flexible LEDs are gaining rapid popularity due to a plethora of applications such as flexible touch screens, flexible displays, sensors and wearables that make conformal contact with human skin for accurate measurements. Organic LEDs (OLED) are the most developed devices that are currently being used as flexible displays [210-213]. However, OLED technology has major drawbacks in terms of device lifetime, efficiency, brightness, and stability in humid conditions as compared to inorganic LEDs [214-216].

Mechanical peeling of nanowires embedded with PDMS has been investigated to make substrate-free LEDs [217, 218]. However, this technique has been only demonstrated on very long nanowires as thin PDMS layer is very difficult to handle [218]. Moreover, dry etching rate of PDMS is very slow and requires gases like CF_4 and O_2, which can damage the nanowires during the etching process [219]. On the other hand, SU-8 photoresist has excellent thermal properties, is easy to process and

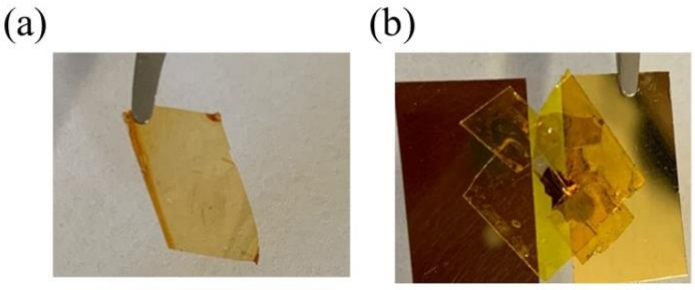

Figure 5-14 a) SU-8 lifted-off film from the substrate with embedded nanowire array (b) Final device with gold pad on acetate film on two sides that are used to connect the p and n regions of the nanowire array.

etch with precise control on its thickness. Thin SU-8 film can be easily handled, making it a good alternative to PDMS. However, SU-8 adheres very well to the substrate and is hard to mechanically peeled-off like PDMS. To overcome this problem, we report a simple solution where an SiO_2 film is used as a sacrificial layer for detaching nanowires embedded in SU-8 from the substrate. Fabrication process of flexible LEDs is described in section 3.3.3. Figure 5-14 shows the nanowire array lifted off in the polymer film and the final device.

5.6.1 LED characterization

The comparison between the I–V characteristics of the flexible device and on-substrate device in Figure 5-15(a) shows that the turn-on voltage for both devices is similar at ~ 3.5 V. However, there is a 'softer' turn-on voltage for the flexible device. The flexible LED is also slightly more resistive compared to the one on substrate, which might be due to poorer contact formed on the flexible device using silver adhesive paste.

To compare with the on-substrate nanowire LEDs, the PL characteristics of flexible LEDs were investigated. As shown in Figure 5-15(b), multiple, red-shifted and broader PL peaks are observed from the flexible device, in comparison to the on-substrate device. Furthermore, the peak of the PL spectra varies across the array, which is not observed for the on-substrate device. A possible

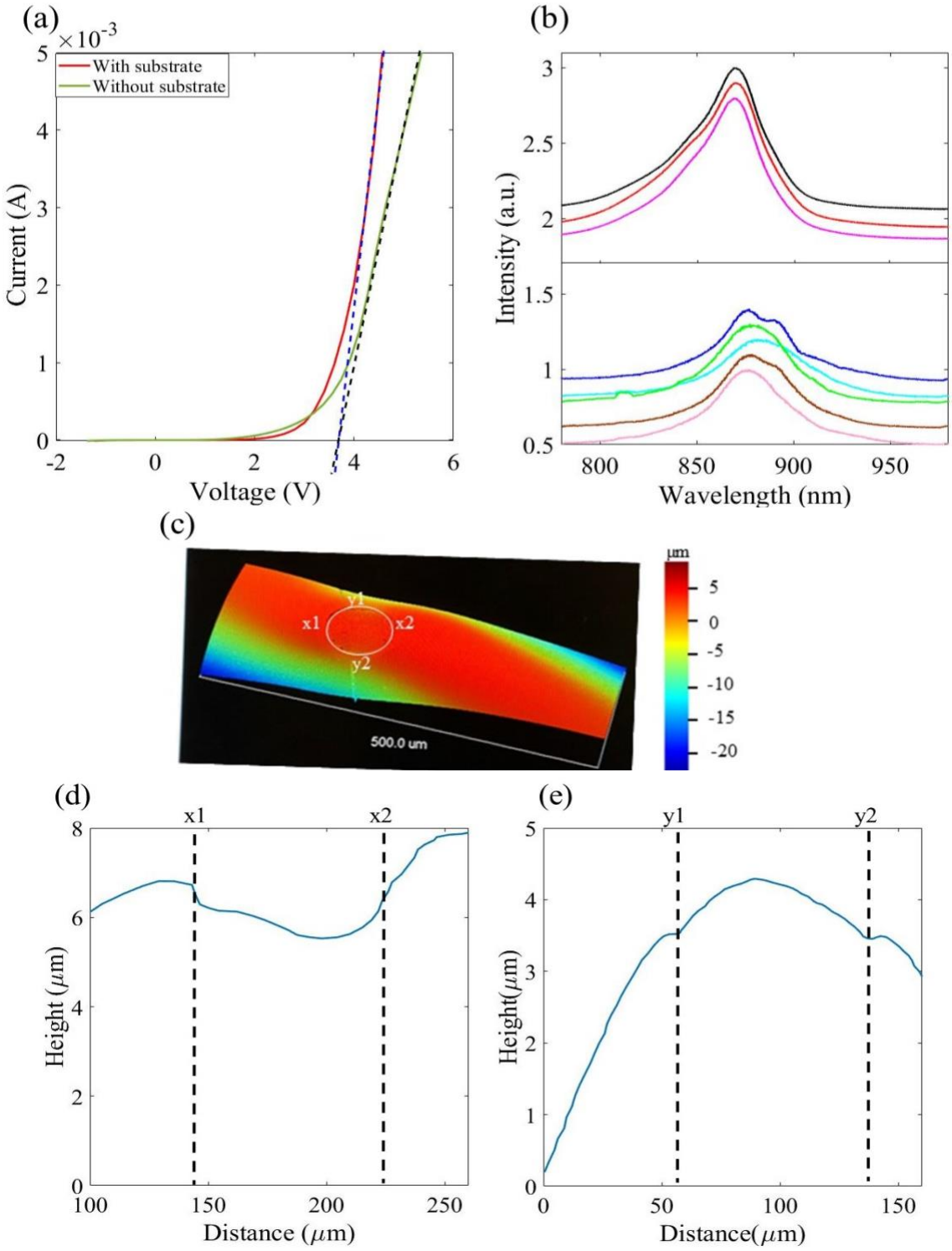

Figure 5-15 (a) I-V characteristics of the on-substrate and flexible devices. (b) Room temperature PL spectra at different positions on the array for on-substrate (top) and flexible device (bottom). (c) Surface profile of flexible LED captured from optical profilometer. The region where the nanowire array is located is indicated by the white circle. (d) Surface profile scan along points x1 to x2. (e) Surface profile scan along points y1 to y2.

explanation for these multiple peaks could be the effect of non-uniform strain on the nanowire array imposed by the SU-8 film or the acetate film [220-222]. We map the surface profile of the peeled SU-8 film after integration on the acetate sheet using an optical profilometer (Figure 5-15(c-e)) and observe that radius of curvature varies across the nanowire array. However, due to limitations around the measurement set up, we could not quantify the strain induced in the nanowire array. Furthermore, the intensity of the emission decreases significantly in comparison to the on-substrate device due to the wavy nature of the flexible device which leads to less light entering the detector.

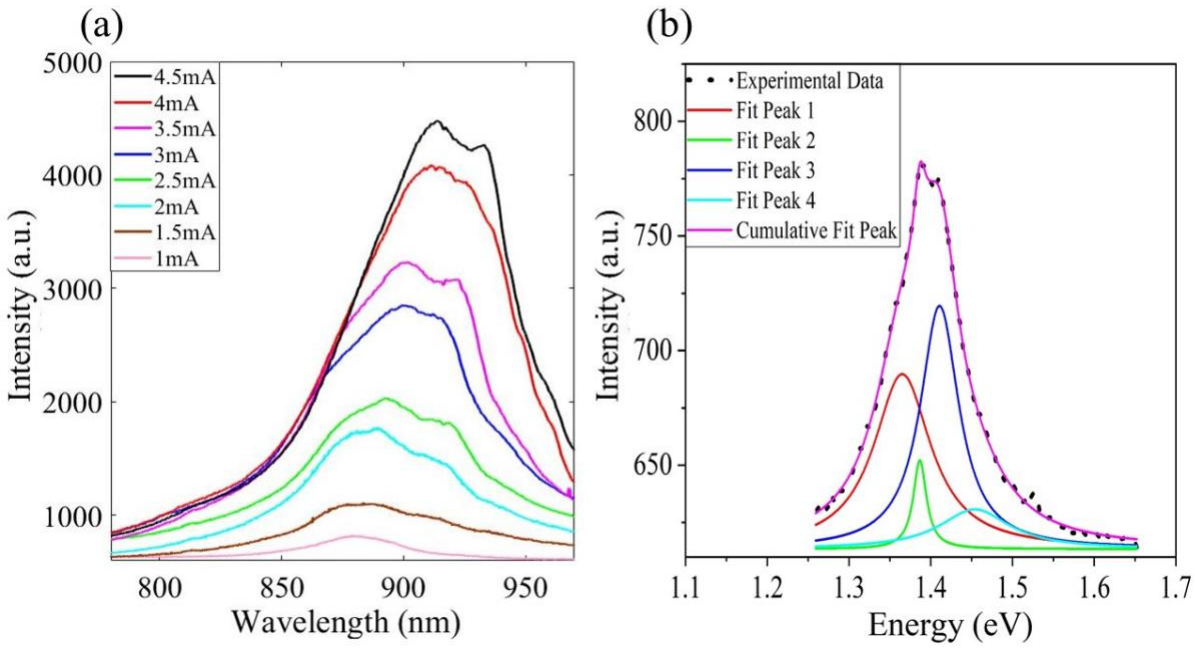

Figure 5-16 EL spectra from the flexible device at room temperature at different current injection levels. (b) Lorentz curve fitting of the EL spectrum measured at 1 mA at room temperature

Figure 5-16(a) shows that as the injection current increases, there is a significant red shift in the EL spectra due to Joule heating. In comparison, the on-substrate device does not show any significant shift in the emission wavelength (Figure 5-4(a)). This effect can be understood in terms of the InP substrate providing better heat dissipation in comparison to the transparent acetate film used for supporting the flexible device. We also fitted the EL spectrum obtained at 1 mA and found

that two additional peaks at the longer wavelengths (peak 1 and peak 2) in addition to the fundamental bandgap peak (peak 3) and transition from conduction band to light hole band (peak 4) (Figure 5-16(b)). The recombination from the conduction band to the heavy hole band and the light hole band is observed at 1.41 and 1.45 eV, respectively. Red shift of the spectrum suggests heating however, the energy difference remains around 40 meV. The possible reason for the two additional red-shifted peak might be strain related. Since radius of curvature varies across the nanowire array, it may induce non-uniform strain at different positions, similar to the report by G. Signorello et al. [221].

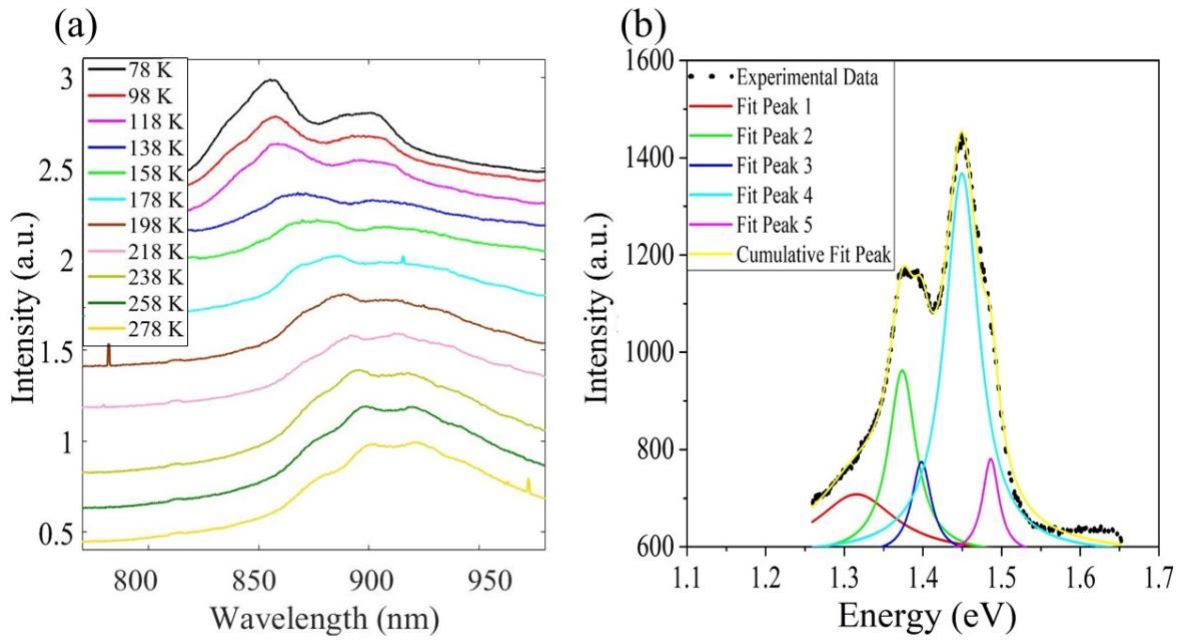

Figure 5-17 (a) Temperature dependent EL spectra at 1 mA current from the flexible LED. (b) Lorentz curve fitting of the EL spectrum measured at 1 mA at 78 K.

The temperature dependent behaviour of these peaks was studied by measuring the EL spectra at an injection current of 2 mA from room temperature to 78 K. As shown in Figure 5-17(a), the emission spectra are blue-shifted with decreasing temperature due to temperature dependence of bandgap. Moreover, slightly red-shifted, broader and multiple peaks are observed (Fig. 5-17(b))

as compared to on-substrate device which is possibly due to the combined effect of heating and strain induced by the SU-8 and/or acetate film on the nanowires due to thermal coefficient mismatch [220-222]. Moreover, a small peak at higher energy with a difference of ~ 40 meV indicates the splitting of heavy hole and light hole band confirming the temperature is higher than 150 K as this peak becomes dominant at temperatures above 150 K due to thermal population of higher energy states [167]. These measurements illustrate that substrate-free flexible device will confine recombination inside nanowire however, a proper heat sink is required to reduce excessive heating in order to achieve lasing from such devices.

5.7 Conclusions

In summary, we have demonstrated core-shell InP/ZnO heterojunction nanowire LED arrays and successfully fabricated flexible LEDs by embedding the nanowires in a thin SU-8 film, which is then peeled off from the InP substrate. We have also studied the temperature dependent behaviour of these LEDs and confirmed that EL spectra consists of three peaks at both room temperature and 78 K. The peaks related to band-to-band transition and recombination at the substrate are present across the temperature range, whereas the peak related to the transition from conduction band and light hole band quenches at low temperature; and Zn acceptor level peak became prominent at around 238 K. Our work provides a pathway for integrating LEDs on various substrates irrespective of their shape, lattice constants, chemical and mechanical properties. To achieve lasing, simulations were performed to get optimum dimensions and the number of wires were reduced to 100 nanowires, but due to excessive heating, higher series resistance and current crowding the device was burnt before reaching to lasing threshold. Additionally, substrate free devices were made to mitigate the recombination into the substrate. Future work will be carried out to further optimise the fabrication process and improve heat sinking (to minimise Joule

heating) to enhance the performance of the flexible device for a plethora of applications as low power and portable lasers.

Chapter 6. Core-shell p-InP/n-SnO_x nanowire devices

In this chapter, we investigate the electrical and optical properties of SnO_x layer deposited at different conditions and demonstrate that there is a trade-off between electrical conductivity and transparency. The advantages with SnO_x are that it is a low-cost material, and exhibits higher chemical stability as compared to ZnO and ITO. Subsequently, we investigate the performance of n-SnO_x/p-InP LEDs and study the effect of absorption and resistance on the device. After confirming good optical properties of the device, we simulate similar structures to get optimum dimensions for low threshold lasing and carry out experiments. Potential reasons for degradation of device are discussed.

6.1 Introduction

SnO_x is one of the extensively studied material among n-type TCOs owing to its application in various areas like flat panel displays, gas sensors, photovoltaic devices, solar cells, and transistors [223-227]. Other advantages of SnO_x are that it is a low-cost material, and exhibits higher chemical stability as compared to the commonly used TCOs of ZnO and ITO [228, 229]. These properties make SnO_x a potential candidate for future transparent electrodes for compound semiconductor based optoelectronic devices. SnO_x is, however, rarely in stoichiometric ratio due to oxygen vacancies. These oxygen vacancies lead to a provision of free electrons, which are present inside SnO_x to maintain charge neutrality and makes undoped SnO_x n-type [113].

Owing to various potential applications, many techniques to fabricate SnO_x thin films and nanostructures have been developed. Some of the commonly developed methods to deposit SnO_x

are chemical vapour deposition, pulsed laser deposition, sputtering, sol-gel process, and spray pyrolysis [230-234]. The properties of thin films depend significantly on the deposition techniques as well as process parameters. Out of the various techniques, magnetron sputtering is the most suited for industrial applications due to its higher deposition rate, better reproducibility and scalability [113, 233].

Some work has been reported for incorporating SnO_x film with InP [235-237]. Still, there are no report of InP/SnO_x nanowire device for light emitting properties. Moreover, progress in the field of using TCOs as both dopant and electrode layers for nanowire LEDs is also in nascent stage and only a few reports have been published [183, 238].

6.2 Experimental section

Table 6-1 Sputter deposition conditions for n-SnO_x study.

Target	Sn (99.9%)
Gases	Oxygen (5N), Argon (5N)
Power	100 W DC
Chamber Pressure	4 mTorr
Oxygen + Argon Flow	20 sccm
Oxygen Flow	2-10 sccm in steps of 2 sccm
Substrate Temperature	22°C

SnO_x films were deposited on Corning glass slides and silicon substrate. The silicon samples were used for thickness, refractive index and absorption coefficient measurements with ellipsometry. Corning glass samples were used for Hall-effect and UV-vis measurements. 99.9% pure Sn target was used as the source for Sn along with reactive oxygen gas to form SnO_x films. Argon was used as a sputtering gas. The purity of both gases was 5N. To obtain SnO_x films with different stoichiometry, the partial pressure of oxygen in the chamber was varied by changing its flow from 2 to 10 sccm in steps of 2 sccm. The total flow (O_2 + Ar) was kept constant at 20 sccm. Oxygen

percentage is defined as (O_2 flow/ (O_2 + Ar) flow) x 100. Chamber pressure was set to 4 mTorr and DC power of 100 W was applied to the Sn target. Depositions were done at room temperature. Table 6-1 summarises the SnO_x optimisation experiments. For the Hall Effect study, the van der Pauw method was used with Greek cross geometry to minimise the measurement error due to contact size and placement to less than 1% , with a = 2 mm and w = 1 mm ensuring that $a/w > 1.02$ where, a is the length and w is the width of each arm [149]. SnO_x film of ~2 µm thickness was deposited using a shadow mask to form a Greek cross geometry and contact pads of 10 nm Ti and 150 nm Au were deposited on four pads of this Greek cross using electron beam evaporation and a shadow mask. Following optimisation of SnO_x film, deposition on nanowires and LED fabrication were performed as discussed in section 3.3.2.

Optical properties of nanowire-LEDs were measured with micro-PL system using a 10x lens with numerical aperture of 0.3. To characterise electrical properties, I-V measurements, EL and Hall-effect measurements were performed. The output power from LEDs was measured using an integrating sphere connected to an optical multimeter (ILX Lightwave-Newport). Hall effect measurements were carried out in a magnetic field range from -0.24 to 0.24 T. Surface analysis was performed from XPS and UPS data.

6.3 Optical properties

Spectroscopic ellipsometry measurements were done on the sputter deposited SnO_x samples to determine the deposition rates and their optical properties such as refractive index and absorption coefficient in the spectral range of 200-1800 nm. Ellipsometry spectra, ψ and Δ were recorded at room temperature for three different angles of 55°, 65° and 75°. Here, ψ and Δ represent magnitude and phase of the change in polarisation of the light reflected from the sample, respectively. Ideally,

only one angle is required, but simultaneously fitting the data from three angles provide better accuracy of the computed parameters. The optical model consists of a semi-infinite Si wafer, with a homogenous and isotropic SnO_x layer on top followed by a Bruggeman-type effective medium approximation roughness layer composed of 50% SnO_x and 50% voids [239]. Ambient air medium was used on top of this roughness layer. Fitting of the measured data was performed using multiple Tauc-Lorentz/Gaussian optical oscillators in conjunction with least square regression analysis (built-in CompleteEase software) to obtain a unique fit. Tauc-Lorentz oscillator exhibited intraband absorption in the visible and UV region [240]. The absorption edge was cross-checked with UV-Vis-NIR measurements in a spectrophotometer for samples deposited on glass substrates. We found excellent agreement between the two.

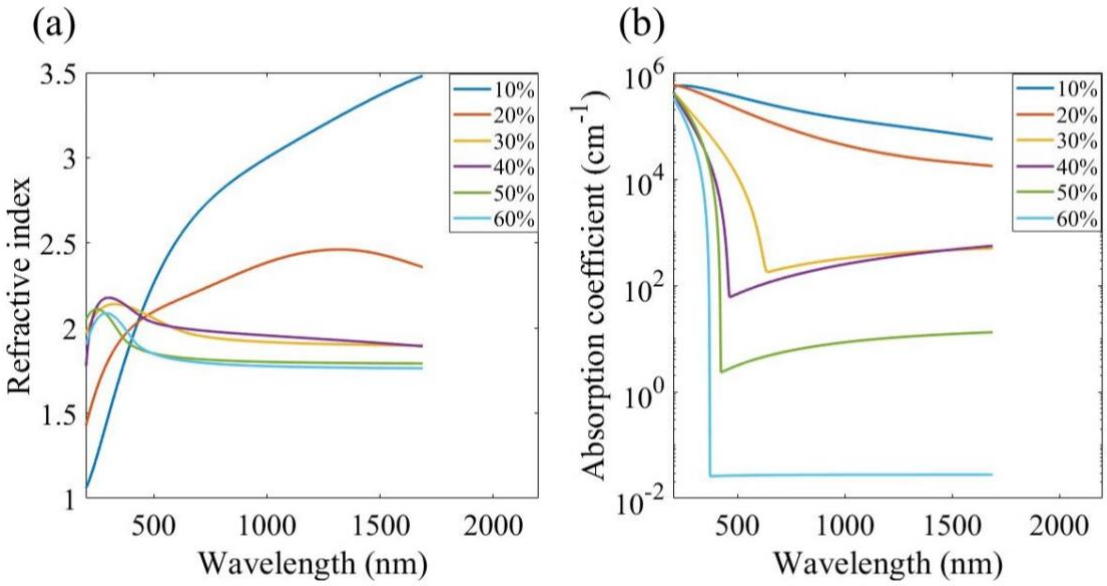

Figure 6-1 Comparison of SnO_x film deposited at various oxygen percentages. (a) Refractive index as a function of wavelength. (b) Absorption coefficient as a function of wavelength.

Various optical properties of the SnO_x films on Si wafers were compared using ellipsometer. Thickness of all the films were kept below 100 nm to obtain improved ellipsometer data fitting. Figure 6-1(a) shows the plot of refractive index as a function of wavelength for samples prepared

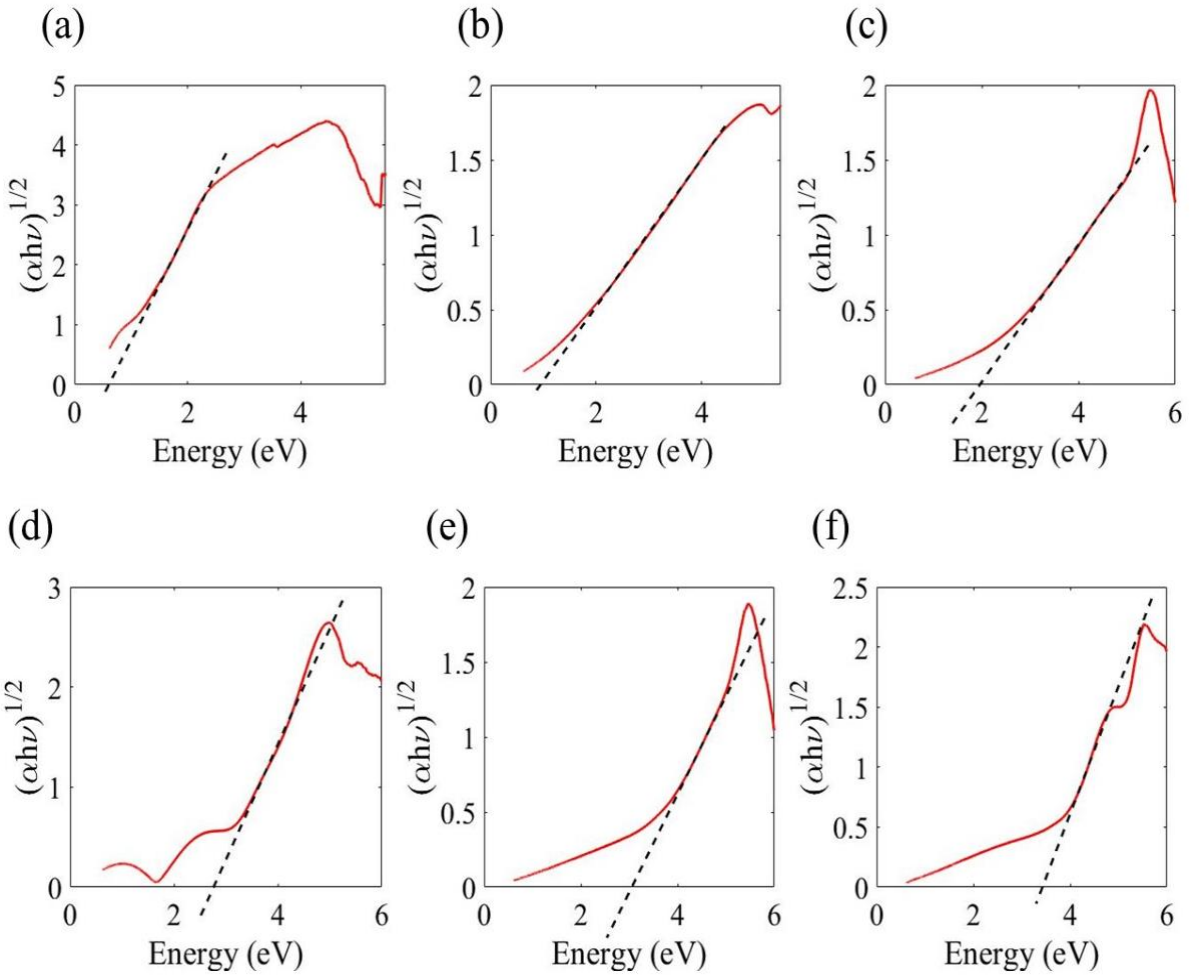

Figure 6-2 Tauc plot for SnO_x layer deposited with an oxygen percentage of (a) 10%, (b) 20%, (c) 30%, (d) 40%, (e) 50% and (f) 60%.

with different oxygen percentages. The trend of refractive index with wavelength for oxygen 10% and 20% is similar to that of metallic tin, indicating the film has more of a metallic characteristic [241]. This is also supported by their very high absorption coefficient (Figure 6-1 (b)). However, as the oxygen fraction increases, the film starts transitioning more towards metal oxide as both absorption coefficient and refractive index decrease, leading towards transparent electrode. Since our interest is only on transparent electrodes, the rest of the study is focused on films deposited with oxygen fraction of more than 20%.

To determine the optical bandgap, we measured the absorption of SnO_x deposited on glass substrates using UV-Vis-NIR spectrophotometer. Optical bandgap was determined from Tauc plot by extrapolating the linear region to the abscissa (Figure 6-2 (a-f)). Figure 6-3 shows that

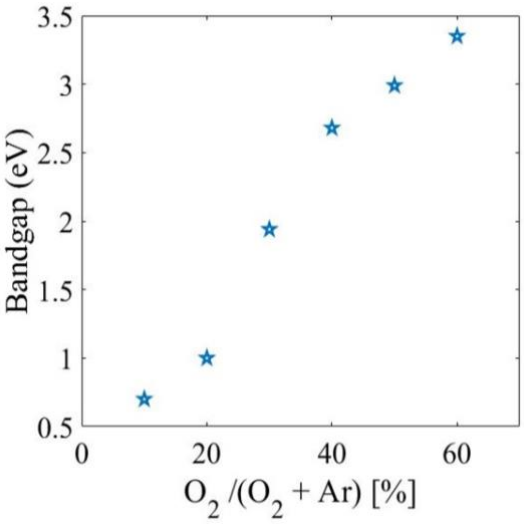

Figure 6-3 Bandgap of SnO_x film deposited at various oxygen percentages.

increasing the oxygen percentage leads to increasing the bandgap energy, indicating the transition towards SnO_2 [242]. Both SnO_2 and SnO have direct and indirect bandgap with energy levels lower for indirect bandgap [242-244]. Since the lowest energy band is indirect, we measured the indirect bandgap and considered it for band alignment with InP in later section.

6.4 Electrical properties

After studying the optical properties, the electrical transport properties were investigated by Hall-effect measurements. Figure 6-4 (a) shows the variation of resistivity as a function of oxygen percentage. It is evident that as the oxygen percentage increases, resistivity of the film increases. The lowest resistivity in the oxide phase is found for the sample with oxygen 40%, however with a higher absorption. Figure 6-4 (b) shows the carrier concentration as a function of oxygen percentage. For more than 20% oxygen, carrier concentrations of the order of 10^{13} cm^{-3} are obtained. Moreover, the mobility of all the films is below 15 $cm^2 V^{-1}s^{-1}$(Figure 6-4 (c)). In order to

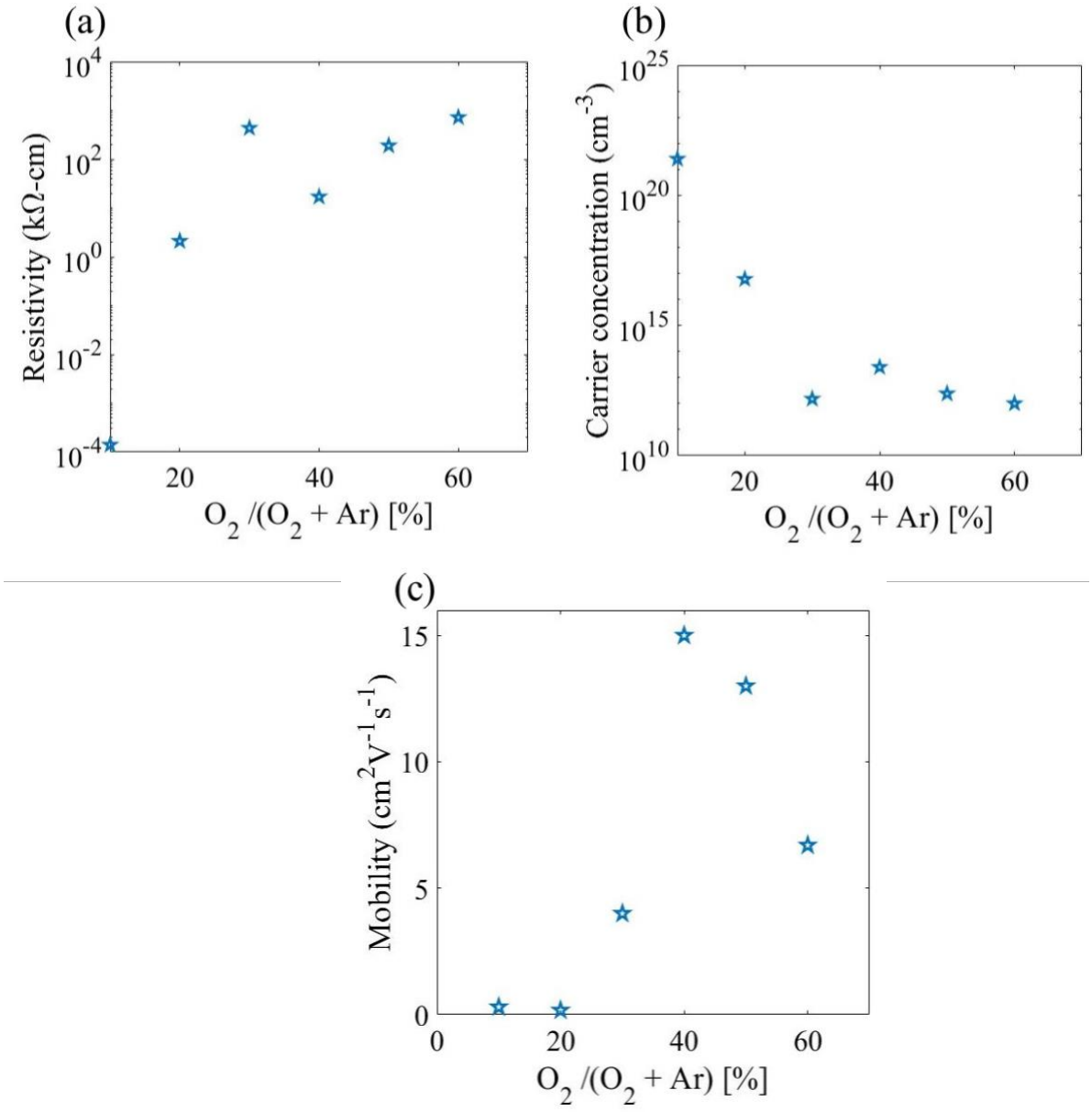

Figure 6-4 Electrical properties of SnO_x film deposited at various oxygen percentages: (a) resistivity, (b) carrier concentration and (c) mobility.

achieve the best outcome for device applications, low resistance and low absorption of the SnO_x layer is required. Our results show that there is a trade-off between resistance and transparency and hence, we investigated two deposition conditions in detail, one with oxygen 40% (higher absorption and lower resistance, Sample A) and another with oxygen 50% (lower absorption and higher resistance, Sample B).

6.5 Composition of SnO_x film

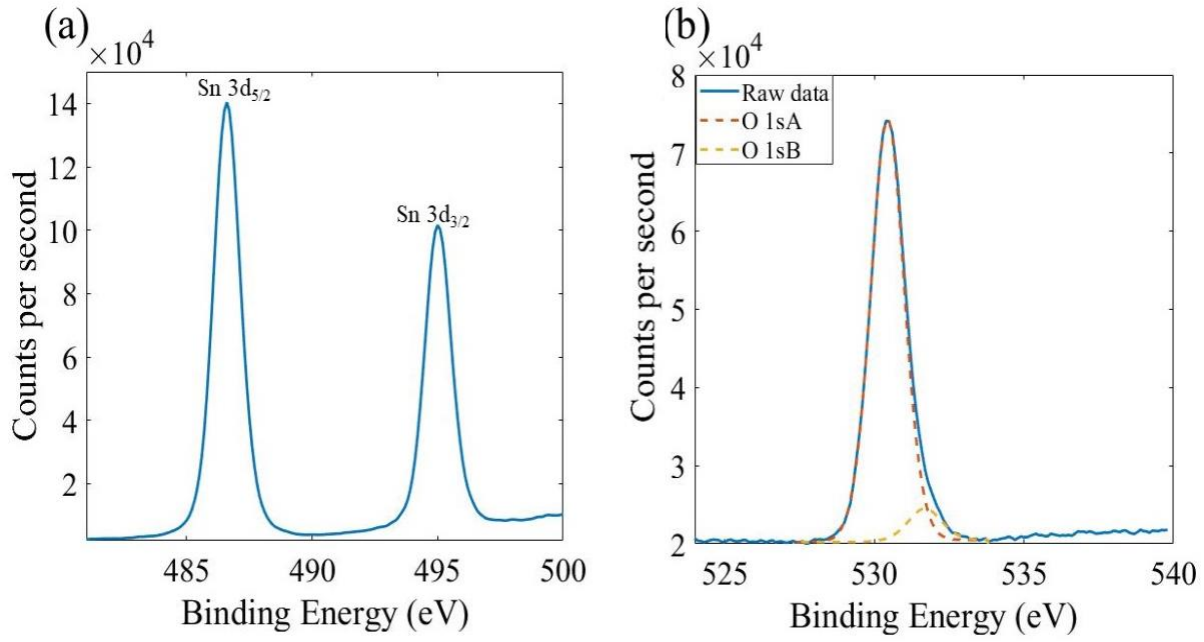

Figure 6-5 XPS spectra of SnO_x film in samples A and B in showing (a) Sn 3d core level and (b) O 1s core level.

For carrier injection purposes, it is important to have a deeper insight of compositional properties of SnO_x as well as the band alignment between InP and SnO_x at the interface. To investigate this, XPS measurements were performed which provides deeper insight about the SnO_x film. Figure 6-5 (a) shows the Sn 3d core level photoemission spectrum. The two peaks at 486.6 and 495 eV are due to spin-orbit splitting between Sn $3d_{5/2}$ and Sn $3d_{3/2}$ and the difference between these two peaks is 8.4 eV, which is in good agreement with the reported value [245]. Moreover, a single peak at 486.6 eV confirms that Sn is present only in the +4 state [246]. From Figure 6-5(b), it is evident that the O 1s spectrum of the SnO_x sample could be fitted reasonably well with two peaks at 530.4 and 531.7 eV. These two peaks have been reported to be due to the lattice oxygen in the form of O-Sn^{4+} [246, 247] and chemisorbed species of oxygen [246, 248], respectively.

6.6 Study of p-InP/n-SnO_x junction properties

6.6.1 Band alignment at p-InP/SnO_x interface

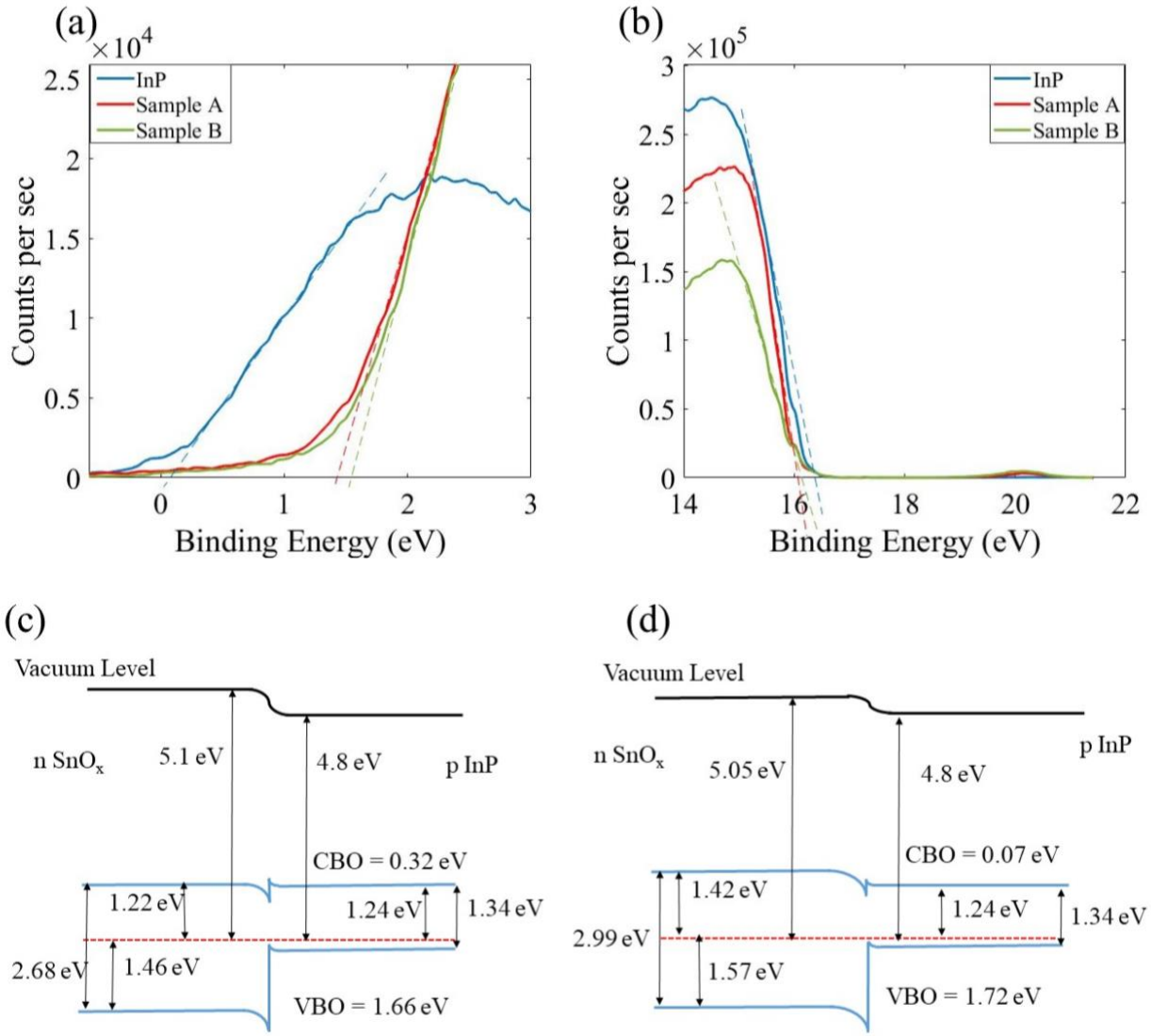

Figure 6-6 UPS spectra of SnO_x films and InP wafer showing (a) the VBM with the Fermi level at zero binding energy and (b) the secondary electron cut-off. Band alignment of SnO_x and InP for (c) sample A and (d) sample B, where the red dashed line represents the Fermi level at equilibrium.

To study the band alignment, UPS was carried out on a sample comprising of a 30 nm SnO_x deposited on p+ InP wafer. It has higher doping concentration than the nanowires and a ZB crystal phase whereas the nanowires have a WZ structure. This may lead to slight variation in band

alignment, however it is expected to be very small and not cause a considerable difference in device performance as the difference in the bandgap energy of ZB (bulk) and WZ (nanowire) phases is very small. A silver sample was used as reference and the Fermi levels for all the samples were calibrated and corrected at 0 eV. The valence band maximum (VBM) is estimated by extrapolating the UPS spectrum and it is found to have a value of 1.46 and 1.57 eV in samples A and B, respectively (Figure 6-6(a)). The work function is taken as the difference in the energy of the ultraviolet source (He-I line, 21.2 eV) and secondary electron cut-off (SECO). Figure 6-6 (b) indicates the secondary electron cut-off energy for both samples A and B and the work function obtained for both the samples are 5.1 and 5.05 eV, respectively. These results are consistent with the literature that work function decreases as the oxygen fraction increases in SnO_x film, with the reported work function of SnO_2 to be 4.84 eV and SnO to be 5.2 eV [249]. Similar analysis has been carried out on InP wafer and a VBM value of 0.1 eV and work function of 4.8 eV are obtained. The reported work function of n-InP is 4.65 eV at a carrier concentration of $6x10^{15}$ cm^{-3}, hence for p-doped InP with carrier concentration of $2x10^{18}$ cm^{-3}, the value of 4.8 eV is reasonable [198]. On the basis of these results, we draw the band diagram of the SnO_x-InP heterostructure, shown in Figure 6-6(c) and Figure 6-6(d) for samples A and B, respectively. The results reflect that in both the cases, reasonably large valence band offset (VBO) is observed. This indicates that SnO_x can act as a hole blocking layer leading to confinement of holes at the junction. On the contrary, very low conduction band offset (CBO) can cause a considerable electrons overflow. However, CBO in sample A is ~ 5 times higher than sample B whereas the VBO values are of similar order. Hence, this can improve the performance of sample A by reducing electron overflow without compromising hole confinement.

6.6.2 I-V characteristics

To characterise the electrical properties of SnO_x-InP nanowire LEDs, I-V behaviour was studied for both the samples A and B. Figure 6-7 (a) shows a typical rectifying behaviour in both the cases confirming the formation of a p-n junction. To measure the turn-on voltage and series resistance, the I-V curves at higher voltages were extrapolated as a straight line. The point where the line intersects with the abscissa is turn-on voltage and the slope of the line is the inverse of series resistance. Extrapolation of the curves is displayed in Figure 6-7 (a). A 'softer' turn-on voltage for sample B is observed as compared to sample A. The turn on voltage for sample A is observed at 2.8 V whereas sample B has slightly higher turn on voltage of 3.36 V. Moreover, sample B has slightly more series resistance (~760 Ω) compared to sample A (~ 440 Ω) which is due to lower carrier concentration in the SnO_x film. As compared to an ideal p-n junction, slightly higher series resistance and turn-on voltage in both the cases is observed due to the formation of oxide layer at the interface of InP while sputtering SnO_x. Indeed, the oxidation of InP at the interface has been confirmed by XPS. Figure 6-7(b) indicates the difference in the P 2p core level spectra at the interface of SnO_x-InP and bulk InP. Additional peak at 133.3 eV confirms the oxidation of InP at the interface [250].

6.7 EL measurements for LEDs

6.7.1 Room temperature EL measurements

Following I-V measurements at room temperature, EL measurements were carried out on both the nanowire array devices. To confirm that SnO_x –InP nanowire array works as an LED, EL spectra were measured at different current injection levels at room temperature. It is found that the EL intensity increases with input current (Figure 6-8 (a)). Moreover, a shoulder peak at higher energy is detected in addition to the peak corresponding to the bandgap of WZ InP. To quantify the

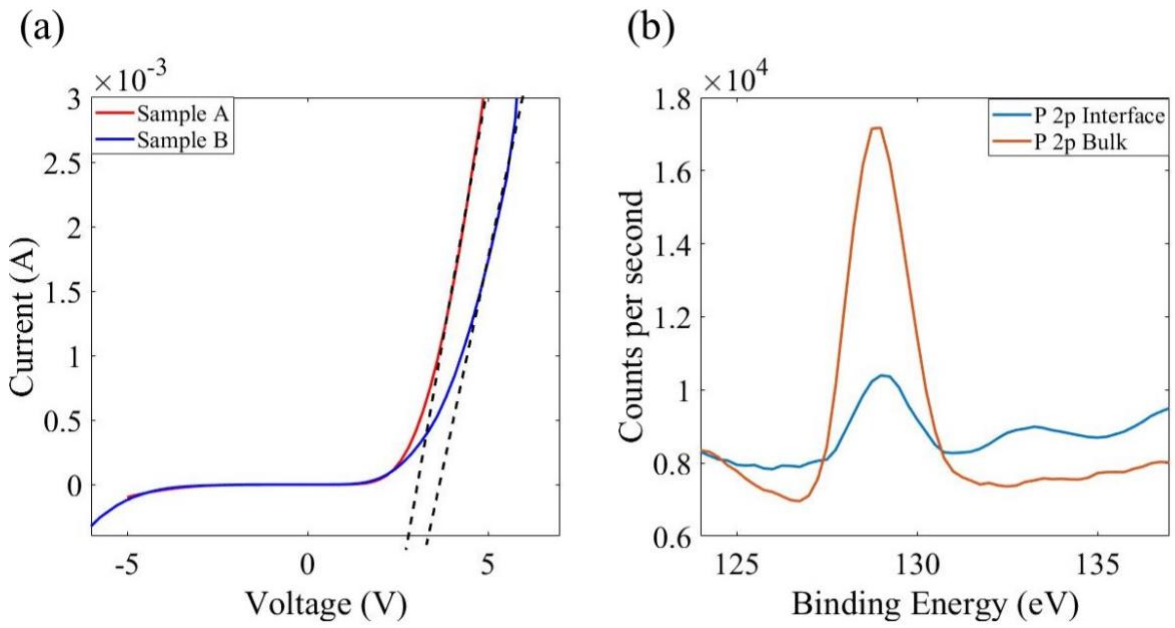

Figure 6-7 (a) Comparison of I-V characteristics of nanowire device at room temperature. (b) XPS spectra of P-2p in bulk and at the interface of SnO_x-InP

difference in light output from both samples, the optical power from LEDs was measured using an integrating sphere in which total emitted power is collected in all the directions. These measurements only provide a qualitative comparison as the integrating sphere was not suitable for our LED measurement setup. Figure 6-8(b) shows the output power from both samples. It is evident that sample A outperforms sample B as the output power is higher at all injection current levels. Our results thus far indicate that there is a fine balance between absorption and resistance for the device. Figure 6-8(c) shows the optical microscopy image of the nanowire LED array captured by an infrared camera with 10x lens. It is clearly evident that light is emitted from the nanowires and with the increase of current injection, the emission intensity becomes more uniform across the entire array.

6.7.2 Temperature dependent EL measurements

To gain further insight into the behaviour of these LEDs, temperature dependent EL spectra from room temperature to 78 K at 5 mA were measured. Similar but quite complex temperature

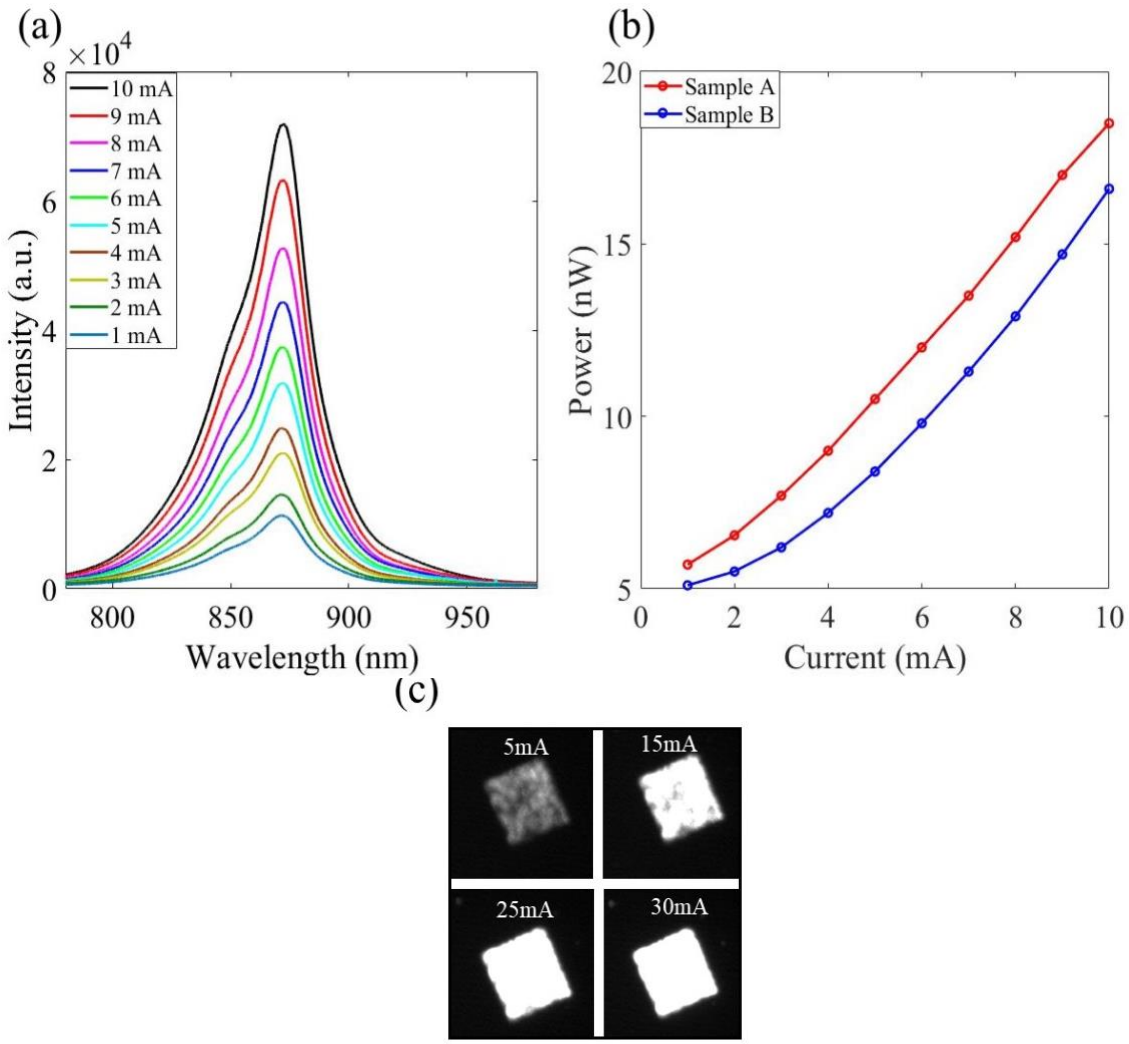

Figure 6-8 (a) Room temperature EL spectra at different current injection levels (Sample A). (b) Comparison of power output of samples A and B as a function of injection current. (c) Optical images of the emission at room temperature from the 100 x 100 μm^2 array at different current injection levels (Sample A).

dependent behaviour is obtained for both the devices where multiple peaks emerge with temperature (Figure 6-9(a)). To understand the origin of these peaks, temperature dependent EL-spectra are deconvoluted from Figure 6-9(b) and the peak shift values for each peak are plotted with temperature (Figure 6-9(b)). The blue shifted spectra clearly indicates that as temperature decreases, the bandgap of InP increases as expected from the temperature dependence of bandgap[167].

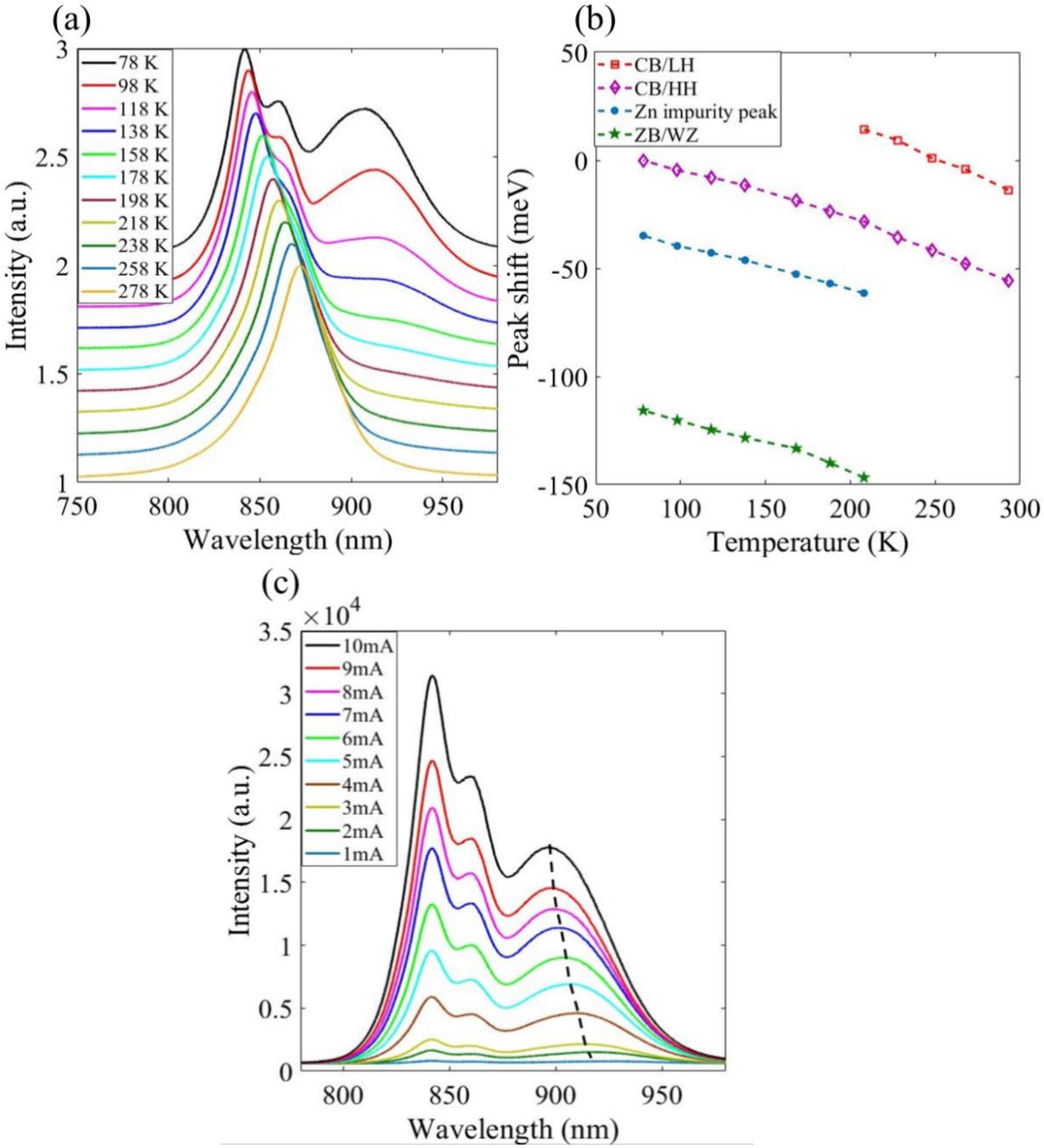

Figure 6-9 (a) Temperature dependent EL spectra at 5 mA injection current. (b) Peak shift as a function of temperature for different peaks of the EL spectra. (c) EL spectra at 78 K at different current injection levels where the black dashed line indicates the blue shift in the peak position of ZB/WZ interface peak.

Figure 6-9(b) depicts that at temperatures around 208 K, the EL spectrum exhibits 4 peaks due to contributions of different energy bands. The peak at highest energy is due to the transition from

conduction band (CB) to the light hole (LH) valence band, as a result of LH and heavy hole (HH) splitting in WZ structures [203]. This peak becomes dominant at temperatures above 150 K due to thermal population of higher energy states [167]. The energy difference between this peak and CB/HH peak remains ~40 meV, irrespective of temperature, which is consistent with the reported values [167, 203, 204]. The second highest energy peak (CB/HH), corresponds to the bandgap of free-exciton of WZ InP nanowires, in which recombination usually occurs between an electron at Γ_7^C point and a hole at Γ_9^V point of the Brillouin zone [251]. The lower energy peak (labelled as Zn impurity peak) is considered to be due to Zn related from p-doped InP nanowires. The energy difference between this peak and CB/HH peak remains around 34 meV which is consistent with reported values of Zn activation energy for low doping levels [205]. The lowest energy peak (ZB/WZ), is related to type II transition from ZB to WZ interface between the nanowires and substrate [252]. To confirm the origin of the lowest energy peak, EL spectra at different current levels were measured at 78 K. It can be seen in Figure 6-9(c) that the position of this peak is at ~920 nm at 1 mA of current injection, which is consistent with reported values [252]. Moreover, as the injected current increases, a blue shift in the peak is observed similar to that reported by Su *et al.* confirming this peak originates from the interface of nanowire (WZ) and InP substrate (ZB) [252]. Another possibility of this peak could be the mixed phase structure in the nanowires. However, we rule out this case here as it has previously been reported that for the above mentioned growth conditions, the nanowires have a pure WZ phase [104]. Multiple peaks in the LED are indication of many recombination centres in the device. After confirming excellent light output properties, optimum dimensions were found out to achieve low threshold lasing.

6.8 Electrically injected nanowire lasers

6.8.1 Simulations

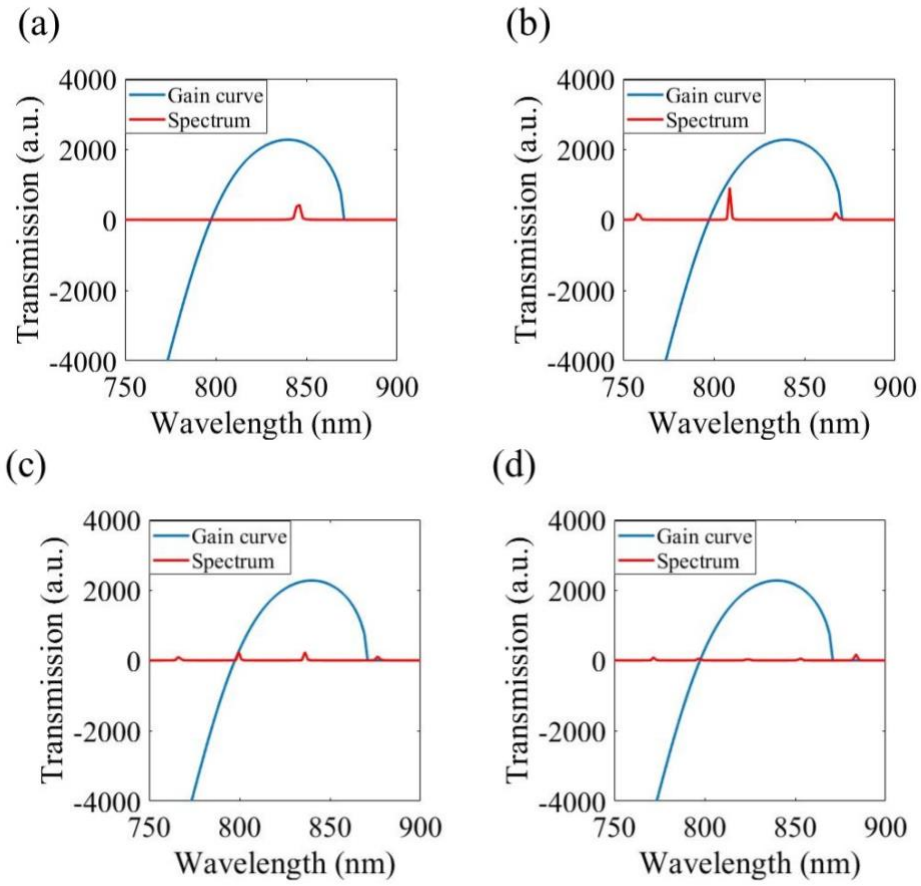

Figure 6-10 Overlap of gain curve at room temperature at a carrier density of $5x10^{18}$ cm^{-3} and modes supported in (a) 1 µm (b) 2 µm (c) 3 µm (d) 4 µm long InP/ SnO_x core shell nanowires.

To perform simulations, SnO_x material was defined. Bandgap of 3.6 eV [253], optical dielectric constant of 4 [254] and static dielectric constant of 9 [255] were chosen. The electron mobility of SnO_x film was measured from Hall-effect measurement system and taken as 15 $cm^2V^{-1}s^{-1}$ and hole mobility was considered $1/5^{th}$ of electron mobility according to the effective mass ratio of holes and electrons [256, 257]. CAD design for n-SnO_x/p-InP core shell nanowire is similar to n-ZnO/p-InP. The only difference is instead of 30 nm of ZnO film, 30 nm of SnO_x film was used with doping

concentration of $5x10^{12}$ cm^{-3}. 1-D simulation of n-SnO_x/p-InP cavity indicates that the resonant

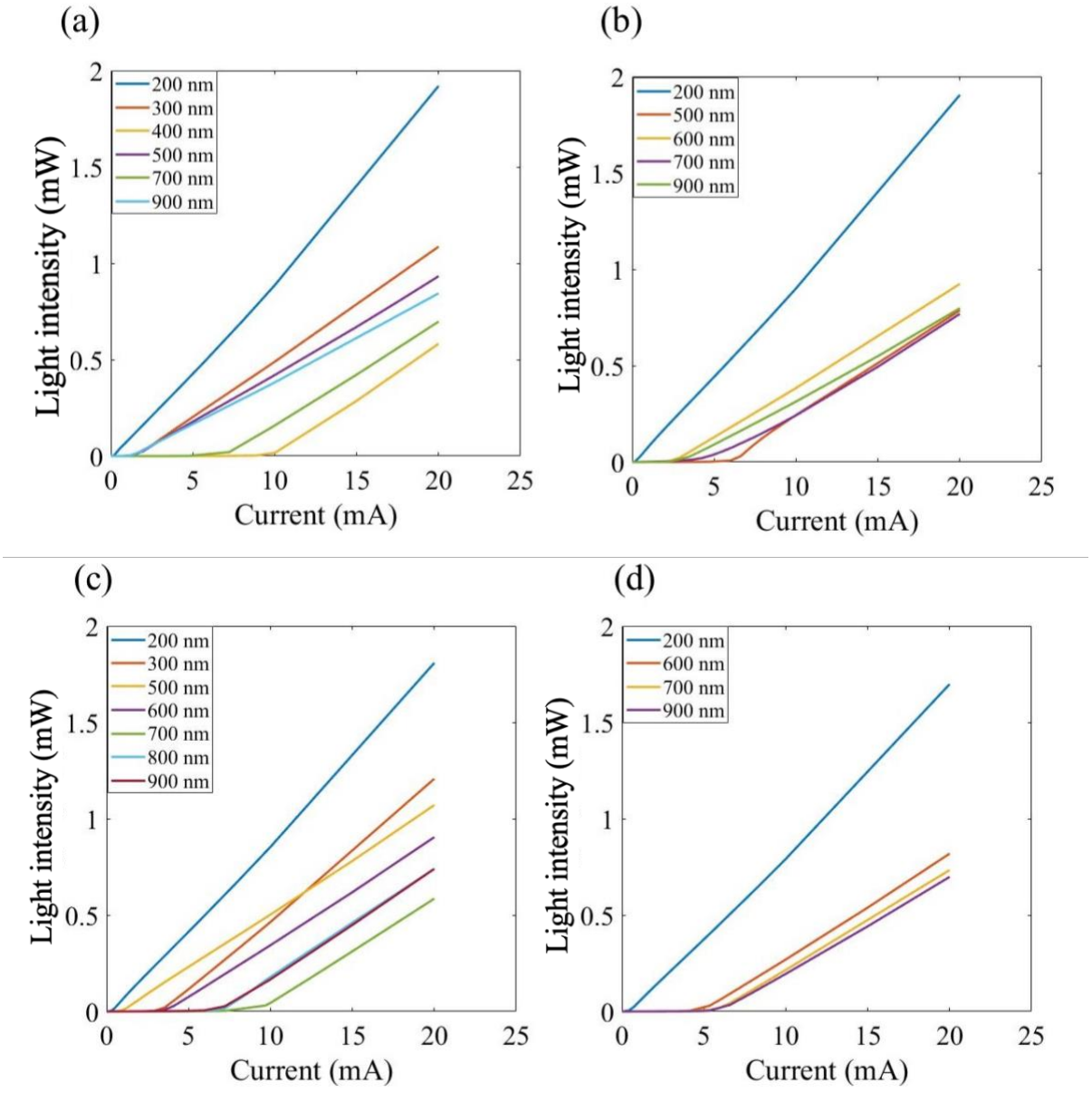

Figure 6-11 Room temperature L-I plots of n-SnO_x/p-InP nanowire devices of various nanowire diameter with total length of (a) 1 µm (b) 2 µm (c) 3 µm and (d) 4 µm with different diameters showing lasing.

wavelength is 846.3 nm for 1 µm long nanowire, 808.8 nm for 2 µm long nanowire, 836.2 nm for 3 µm long nanowire and 853.1 nm for 4 µm long nanowire (Figure 6-10).

The 2D simulation results are displayed in Figure 6-11. Similar to n-ZnO/p-InP cavity, the lowest current threshold is obtained for 200 nm of diameter irrespective of nanowire length. The minimum threshold current obtained for 1, 2, 3 and 4 µm long nanowire are 0.16, 0.18, 0.31 and 0.46 mA, respectively. The minimum threshold current required to achieve lasing increases with nanowire length due to increase in non-uniform current injection. Moreover, with very low doping concentration of SnO_x film, lasing could still be achieved. This happens due to high n-doping concentration of ITO layer. Therefore, the optimised range of length of nanowire was considered to be 1 – 2 µm with a diameter of 200 nm.

6.8.2 Experiments

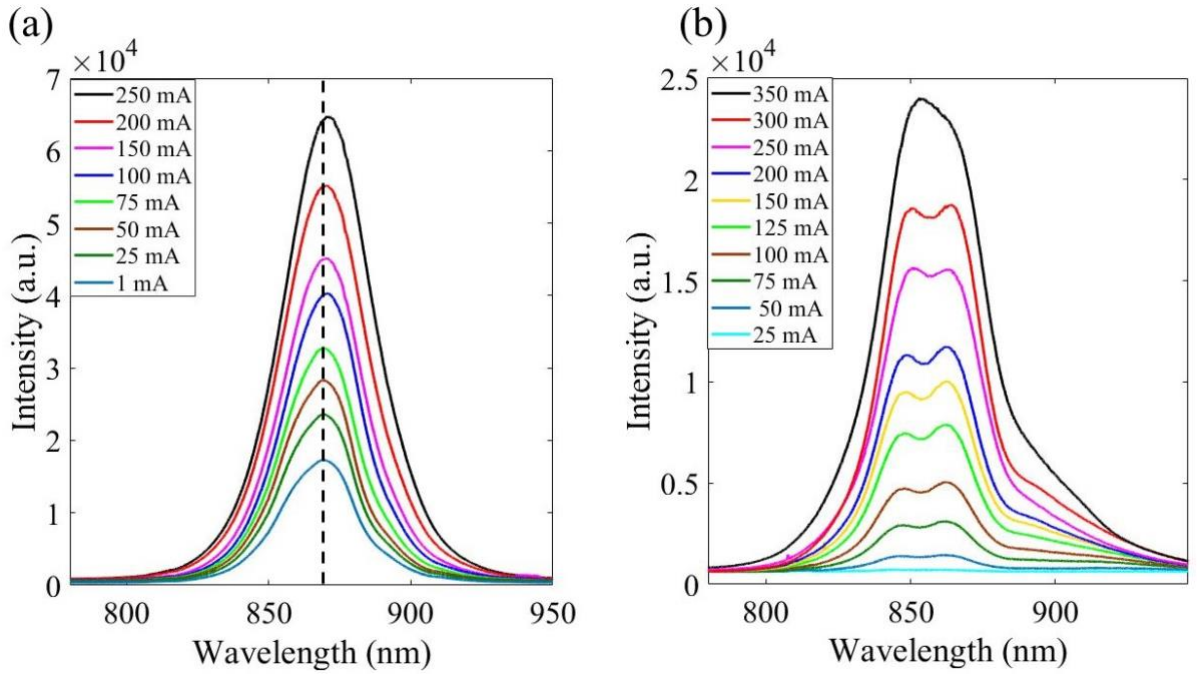

Figure 6-12 EL spectra from single nanowire at different current injection levels at (a) room temperature and (b) 78 K. The black dashed line in (a) indicates wavelength position at 870 nm.

Nanowires were grown using the same optimised parameters as described in 4.2.2. The size of the array was reduced to 10 x 10 nanowires with a pitch of 5 µm and pulsed current was passed with

pulse width of 0.5 µs and duty cycle of 1%. Also, to reduce recombination into the wafer, a 2 µm thick SU-8 was left after ICP etching.

Figure 6-12 (a) shows the EL spectra recorded from a single nanowire. It is evident that majority of recombination is occurring inside the nanowire as the peak position of EL curve is at 870 nm which corresponds to the fundamental bandgap of InP nanowires [167]. However, red shift in the EL spectra at higher injection current is a clear sign of heating in the device. To minimise heating, measurements were performed at 78 K. Figure 6-12(b) displays the EL spectra measured at 78K. Similar to the LED measurements, three peaks were obtained at lower injection currents. At higher current levels, a peak from the substrate becomes prominent indicating the some recombination are occurring inside the substrate. After 350 mA of current (3.5 mA per nanowire), the device was burnt. The value of current is significantly higher than the minimum threshold obtained from the simulations. The deviation in the simulations and experiments could be due to excessive heating, higher series resistance and some carriers recombining inside the substrate due to lower hole mobility. Additionally, multiple recombination sites reduce the gain generated for the mode corresponds to the fundamental bandgap of the nanowires.

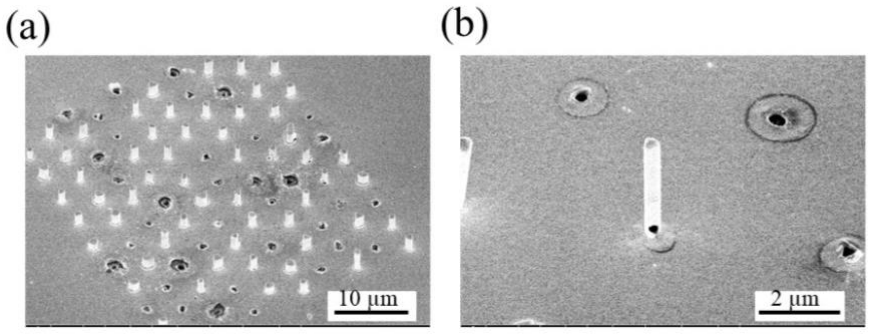

Figure 6-13 SEM images of the InP nanowire array device after degradation at 45° tilted view. (a) Entire array and (b) magnified image showing the burnt out nanowires.

To understand the degradation of device, SEM analysis was carried out. Figure 6-13(a) shows an image of the device after degradation. Some nanowires are completely burnt whereas some are still present indicating the non-uniformity in the wires. Figure 6-13(b) indicates the nanowires are burnt at the bottom suggesting the excessive carriers crowding. Further optimisation in the design of lasers is expected to reduce excessive heating, carriers crowding, shift of recombination region and provide a sharp emission profile, so that peak gain can be increased substantially, which can then pave a way towards electrically injected nanowire lasers.

6.9 Conclusions

In summary, we have studied the electrical and optical properties of sputter deposited SnO_x layer as a function of oxygen percentage and observed that there is a trade-off between absorption and resistance. To understand n-SnO_x/p-InP junction formation, we studied the band alignment at the interface and found that SnO_x acts as hole blocking layer. We have also demonstrated core-shell p-InP/n-SnO_x heterojunction nanowire LED arrays at different deposition conditions to understand the trade-off between absorption and series resistance. In terms of output power, sample A (higher absorption and lower resistance) was better than sample B (lower absorption and higher resistance). The potential reasons are better confinement of electrons at the junction due to higher CBO, efficient current injection and lower resistance which leads to less heat generation. This also provides evidence that some compromise of the absorption for lowering the device resistance can lead to an effective working device.

To have a deeper understanding of recombination mechanism of these LEDs, we performed temperature dependent behaviour of these LEDs and showed that 4 peaks could be resolved from the EL spectrum at ~208 K. These peaks originate from CB/LH, CB/HH, CB/Zn-dopant energy level and ZB/WZ transitions. The first peak quenches when the temperature is less than 208 K

whereas, the last two peaks become prominent with decreasing temperature. The second peak is related to the fundamental bandgap; hence it is observed in all the measurements, irrespective of temperature. The device was burnt when high current was passed through it to achieve lasing. Further optimisation in the design is required to reduce recombination inside the substrate, multiple recombination centres, excessive heating and current crowding.

Chapter 7. Core-shell n-InP/p-$Sn_xNi_yO_z$ nanowire emitters

In this chapter, we explore thin films of $Sn_xNi_yO_z$ as a p-type layer for n-InP nanowires to minimise the recombination inside the substrate. First, electrical and optical properties of $Sn_xNi_yO_z$ layer as a function of oxygen fraction and temperature are studied. Subsequently, we investigate the stability and the performance of p- $Sn_xNi_yO_z$ /n-InP nanowire LEDs. After confirming good optical properties of the device, we perform both numerical and experimental lasing measurements and discuss potential reasons for degradation of the device.

7.1 Introduction

To date, the TCOs used for commercial purposes are predominantly n-type and extensive investigation is ongoing to develop p-type TCOs that are reliable for practical applications. The significantly poorer performance of p-type TCOs in comparison to their n-type counterparts is due to their electronic configuration. The interaction between metal ns orbitals and oxygen 2p orbitals causes charge disparity leading to spatially disperse ns orbitals and highly localised oxygen 2p orbitals [258-260]. This results in smaller effective mass of electrons as compared to holes which leads to higher mobility and better transport of electrons [260]. Therefore, high performance p-type TCOs can be realised by reducing the localisation of oxygen 2p orbitals.

To reduce localisation, hybridisation of O 2p orbitals and closed-shell Cu $3d^{10}$ orbitals has been proposed since they have comparable energy levels and are expected to overlap [259]. However, most of the copper-based oxides such as CuO, Cu_2O and $CuAlO_2$ exhibit decent electron mobility but poor hole density [116, 261]. Furthermore, they are either deposited or annealed at very high

temperatures which is not suitable for most applications. SnO demonstrates high carrier concentration but struggles with stability [116, 261]. SnO has metastable phase and is stable only up to 300 °C [262, 263]. NiO is stable and shows decent carrier concentration, however, minor absorption due to low oscillator strength d–d interband transitions causes lower transparency in the visible range [264]. In this paper, we explore thin films of an alloy oxide of Sn and Ni ($Sn_xNi_yO_z$) to overcome these shortcomings. So far, its application in lithium storage, electrochemical and electro-catalytic properties, gas sensing and photo-catalytic properties have been studied [265-270]. Nevertheless, the use of these films in optoelectronics devices is nascent.

Combining p- $Sn_xNi_yO_z$ with III-V semiconductors has potential in a vast range of optoelectronic applications. High dopant concentration is required to form good Ohmic contact but results in free carrier absorption and Auger recombination that decrease device performance [168-170, 271]. In general, free carrier absorption from p-dopants is higher than n-dopants [169]. Therefore, replacing the p-doped layer with conformal TCOs layer over an n-type nanowire can mitigate free carrier absorption as well as simplify extensive optimisation process during nanowire growth.

7.2 Experimental section

Sn and Ni targets with 99% purity were used in a sputter coater system, coupled with reactive oxygen gas to obtain $Sn_xNi_yO_z$ films. Argon was used as the sputtering gas at a constant flow of 20 sccm. Sn target was powered with 120 W RF source while 90 W of DC power was applied to Ni target for all the experiments. The O_2/Ar percentage was varied from 10% to 25% while the temperature was varied from room temperature to 250^{o}C. All depositions for optimisation study were done on Corning glass and heavily doped n-InP substrates. Glass substrates were used for bandgap, absorption and Hall-effect measurements while InP substrates were used for computing thickness and refractive index using ellipsometer. For ellipsometer measurements, films were

deposited for 5 mins such that thickness of all the films were below 100 nm for better fitting. Details of ellipsometer fitting has been described in section 6.3. Van-der-Pauw Hall-effect measurements were carried out on ~2 µm thick $Sn_xNi_yO_z$ films as described in section 6.2. Energy dispersive X-Ray spectroscopy (EDX) was performed using an EDAX detector in FEI Helios 600 Nanolab FIB to estimate the composition of $Sn_xNi_yO_z$ films.

For fabricating the LEDs, n-doped InP nanowires were epitaxially grown on heavily n-doped InP substrates using SAE with SiO_2 mask with openings of 300 nm diameter, 1 µm pitch and array size of 100 x100 μm^2. At a base pressure of 100 mbar, trimethylindium with flow rate of 6.07×10^{-6} mol/min and phosphine with flow rate of 4.91×10^{-4} mol/min were introduced into the reaction chamber using H_2 as a carrier gas. For n-doping, silane with flow rate of 3.08×10^{-7} mol/min was introduced into the chamber. Growth was performed at 730°C for 15 mins. The nanowires were 3.5 µm long with an average diameter of 400 nm as shown in Figure 7-1(a). Figure 7-1(b) illustrates the device fabrication process for the LEDs, which have been described in detail in section 3.3.2.

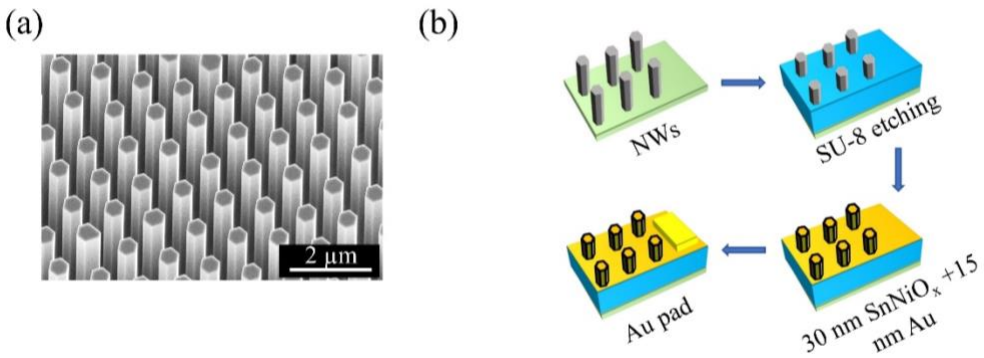

Figure 7-1 (a) SEM image of the InP nanowire array grown by SAE-MOCVD technique at 30° tilted view. (b) Schematic diagram of the LED fabrication process.

Bandgap and absorption coefficient of $Sn_xNi_yO_z$ films were measured by UV-Vis-NIR spectrophotometer. To study electrical properties of the film, Hall-effect measurements were

performed in a magnetic field range of -10 to 10 kG. Elemental and surface analysis of $Sn_xNi_yO_z$ films were carried out using XPS and UPS. EL of the nanowire LEDs was measured by μ-PL system. A 10x lens (numerical aperture of 0.3) was used for all the measurements. The I−V measurements were carried out using a source/measurement unit.

7.3 Oxygen dependent optical and electrical properties

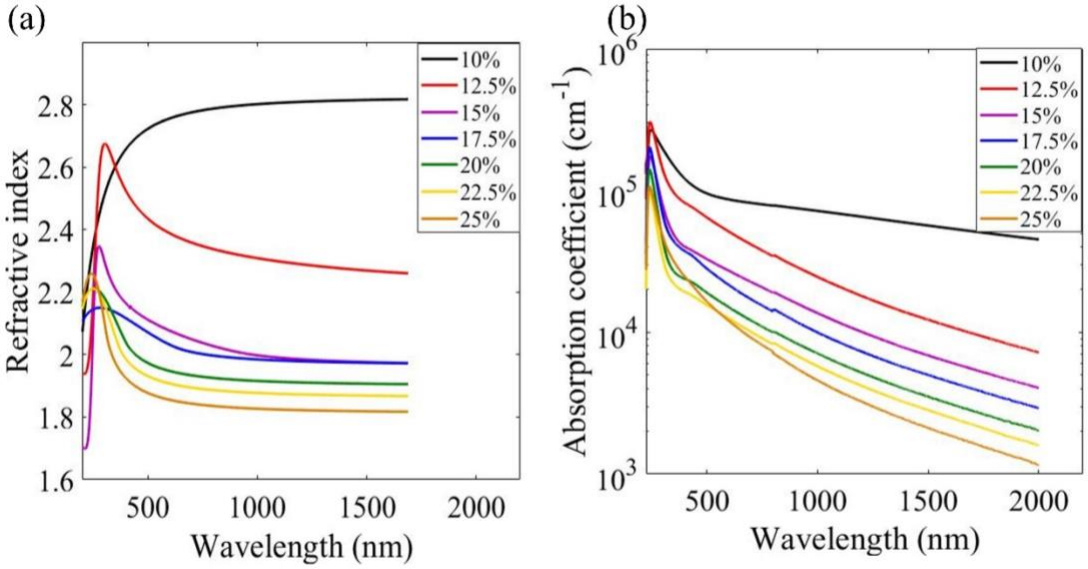

Figure 7-2 Comparison of $Sn_xNi_yO_z$ films deposited at various O_2/Ar percentages. (a) Refractive index as a function of wavelength. (b) Absorption coefficient as a function of wavelength.

To study the effect of oxygen partial pressure during deposition on $Sn_xNi_yO_z$ films, refractive index was computed as a function of O_2/Ar percentage for the thin film deposited on InP wafers. Figure 7-2(a) shows the plot of refractive index as a function of wavelength. The trend of refractive index for 10% O_2/Ar is different than the rest of the films. Monotonic increase in the refractive index indicates that film has more metallic characteristics than oxide. This is also evident from higher absorption coefficient (Figure 7-2(b)). However, as the oxygen percentage increases, both refractive index and absorption coefficient decreases, indicating film is transitioning towards a metal oxide layer. To confirm this, we performed EDX measurements to determine the

composition of $Sn_xNi_yO_z$ films. Table 7-1 indicates that with increasing oxygen partial pressure, both the concentration of Ni and Sn decreases monotonically. However, the change in Sn is higher than that of Ni. Further, the oxygen content increases from 33.8% to 60.2%. These results, therefore confirm that the film is transitioning towards oxides with increasing O_2/Ar percentage.

Table 7-1 EDX analysis of $Sn_xNi_yO_z$ films deposited at room temperature.

O_2/Ar percentage	Sn atomic %	Ni atomic %	Oxygen atomic %
10	42.8	23.4	33.8
12.5	34.6	22.9	42.5
15	29.4	22.5	48.1
17.5	25.9	21.7	52.4
20	24.0	20.5	55.5
22.5	21.8	19.8	58.4
25	20.6	19.2	60.2

To determine the optical bandgap, thin films were deposited on glass substrates. By extrapolating the linear region of the Tauc plot to the x-axis, the bandgap was deduced (Figure 7-3 (a-g)). Figure 7-3 (h) shows the variation of bandgap with O_2/Ar percentage. A sharp rise in the bandgap from the 10% to 12.5% samples further supports the metallic characteristics of the 10% film. As oxygen fraction increases, the bandgap increases which also supports the oxide nature of the film. Our results are consistent with literature where an increase in the bandgap of both NiO_x and SnO_x with increasing oxygen fraction has been reported [242, 272]. The fundamental bandgap of both SnO and SnO_2 is indirect [243, 244]. Moreover, NiO_x also exhibits indirect bandgap, therefore, we consider indirect bandgap of $Sn_xNi_yO_z$ film and use it for band alignment analyses with InP in later section[273].

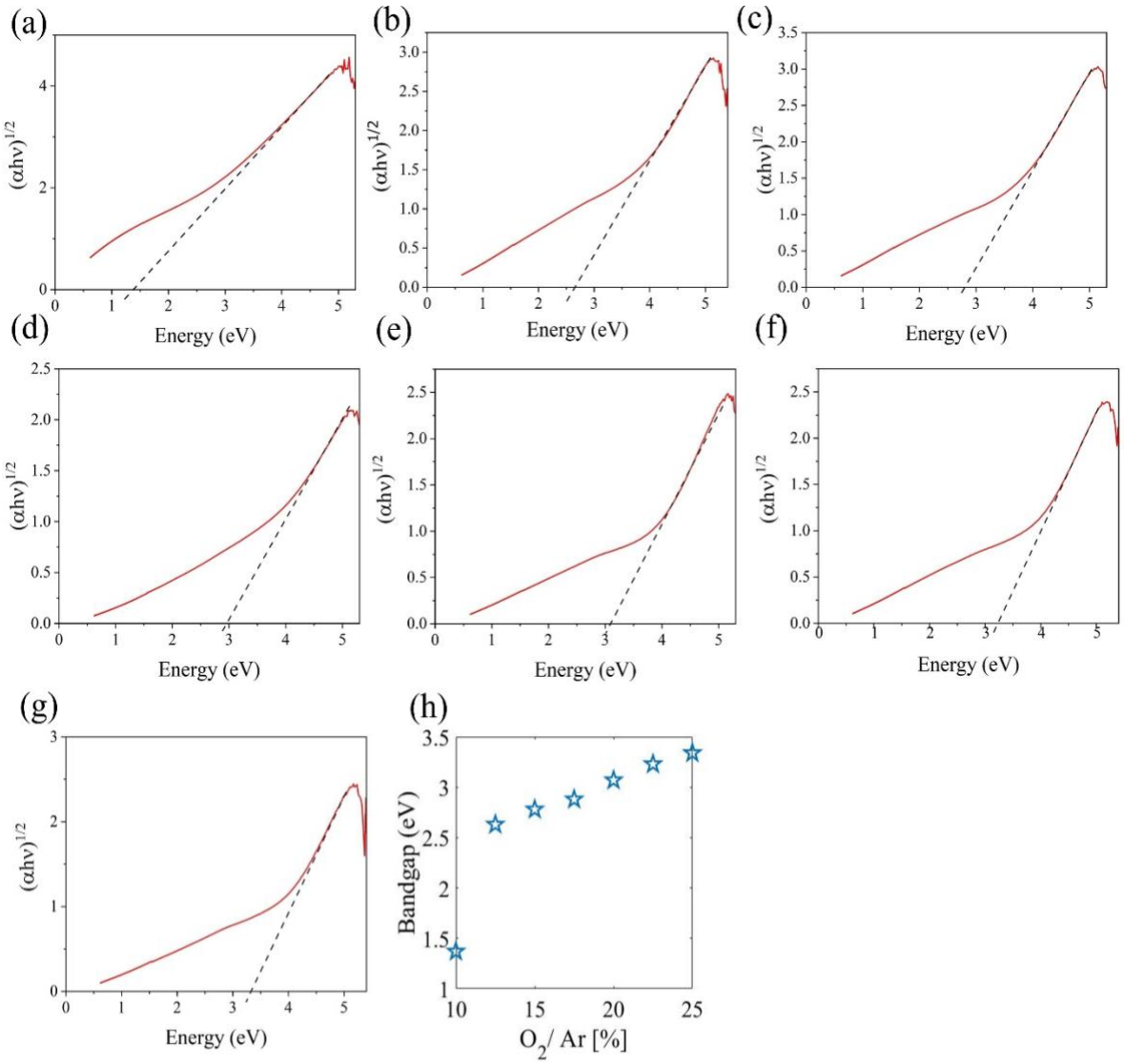

Figure 7-3 Tauc plot for $Sn_xNi_yO_z$ layer deposited at room temperature with O_2/Ar percentage of (a) 10% (b) 12.5% (c) 15% (d) 17.5% (e) 20% (f) 22.5% (g) 25%. (h) Bandgap of the $Sn_xNi_yO_z$ layer vs O_2/Ar percentage derived from Tauc plot.

After studying the optical properties, Hall-effect measurements were performed to investigate the electrical transport properties. Our results show that with increasing O_2/Ar percentage the film transition from n-type to p-type. Figure 7-4(a) shows the carrier concentration as a function of O_2/Ar percentage. Initially, films exhibit n-type characteristics. NiO is p-type irrespective of deposition condition [272]. However, when metallic tin dominates, the film behaves as n-type [274].

The presence of metallic characteristics is also supported by higher refractive index values in Figure 7-2(a). As O_2/Ar percentage increases, n-type conductivity decreases due to decrease in metallic elements which is evident from EDX results and finally the film exhibits p-type behaviour. The p-type behaviour is attributed to the formation of SnO, which is p-type in nature. Stability of

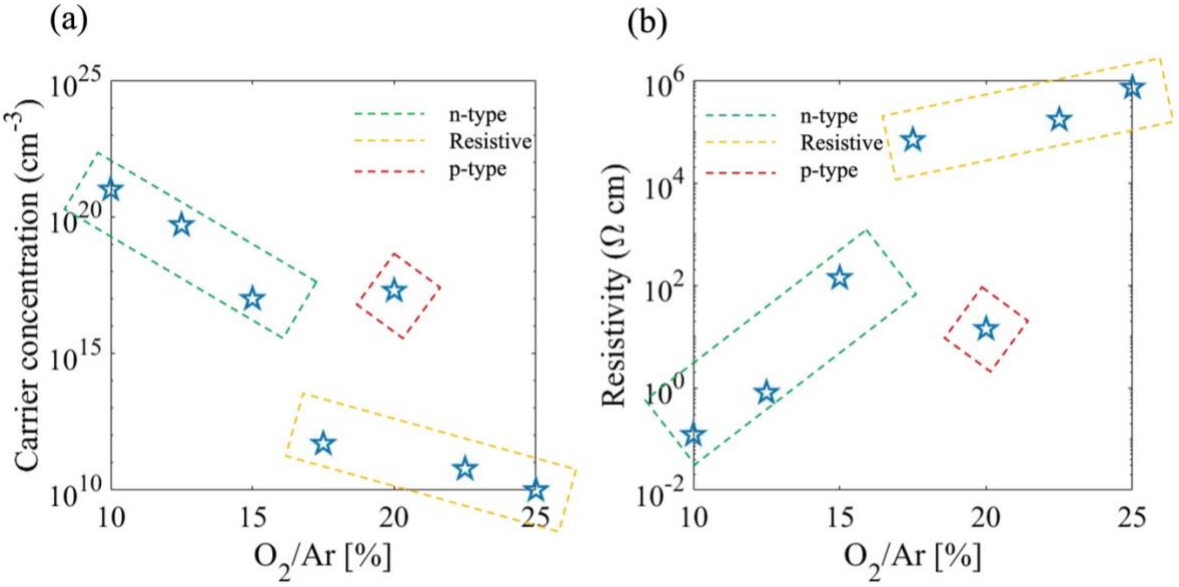

Figure 7-4 Comparison of $Sn_xNi_yO_z$ films deposited at room temperature with different O_2/Ar % (a) Carrier concentration and (b) Resistivity. The green, red and yellow rectangles indicate n-type, p-type and highly resistive behaviour of the films, respectively.

SnO phase is reported in very narrow oxygen range which is consistent with our results [275]. Further increase in the oxygen leads to SnO_2 phase which is n-type and therefore, the p-type conductivity decreases [274, 275] and the film becomes resistive. Figure 7-4(b) shows the variation of resistivity as a function of O_2/Ar percentage.

7.4 Temperature dependent optical and electrical properties

Following the study of the effect of O_2/Ar percentage, both optical and electrical transport properties were studied as a function of deposition temperature for the p-type film (O_2/Ar = 20%). Figure 7-5(a) shows the variation of refractive index as a function of wavelength for the films

deposited at different temperatures. Our results indicate that refractive index decreases with the increase in temperature and the films become more transparent (Figure 7-5(b)). However, the

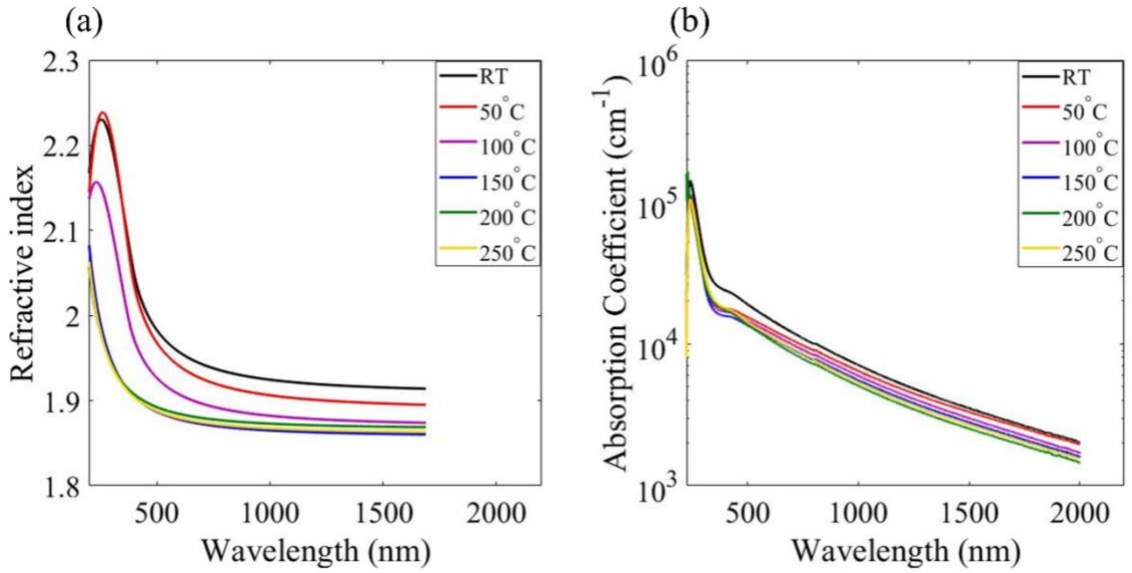

Figure 7-5 Comparison of $Sn_xNi_yO_z$ films deposited with 20% O_2/Ar at different deposition temperatures. (a) Refractive index as a function of wavelength. (b) Absorption coefficient as a function of wavelength.

change in both refractive index and absorption coefficient is relatively small which is due to minimal change in composition (Table 7-2).

Table 7-2 EDX analysis of $Sn_xNi_yO_z$ film deposited at 20% O_2/Ar percentage at different deposition temperatures.

Deposition Temperature (°C)	Sn atomic %	Ni atomic %	Oxygen atomic %
RT	24.0	20.5	55.5
50	23.9	20.1	56
100	23.5	19.7	56.8
150	22.3	19.5	58.2
200	20.7	19.2	60.1
250	19.4	19.1	61.5

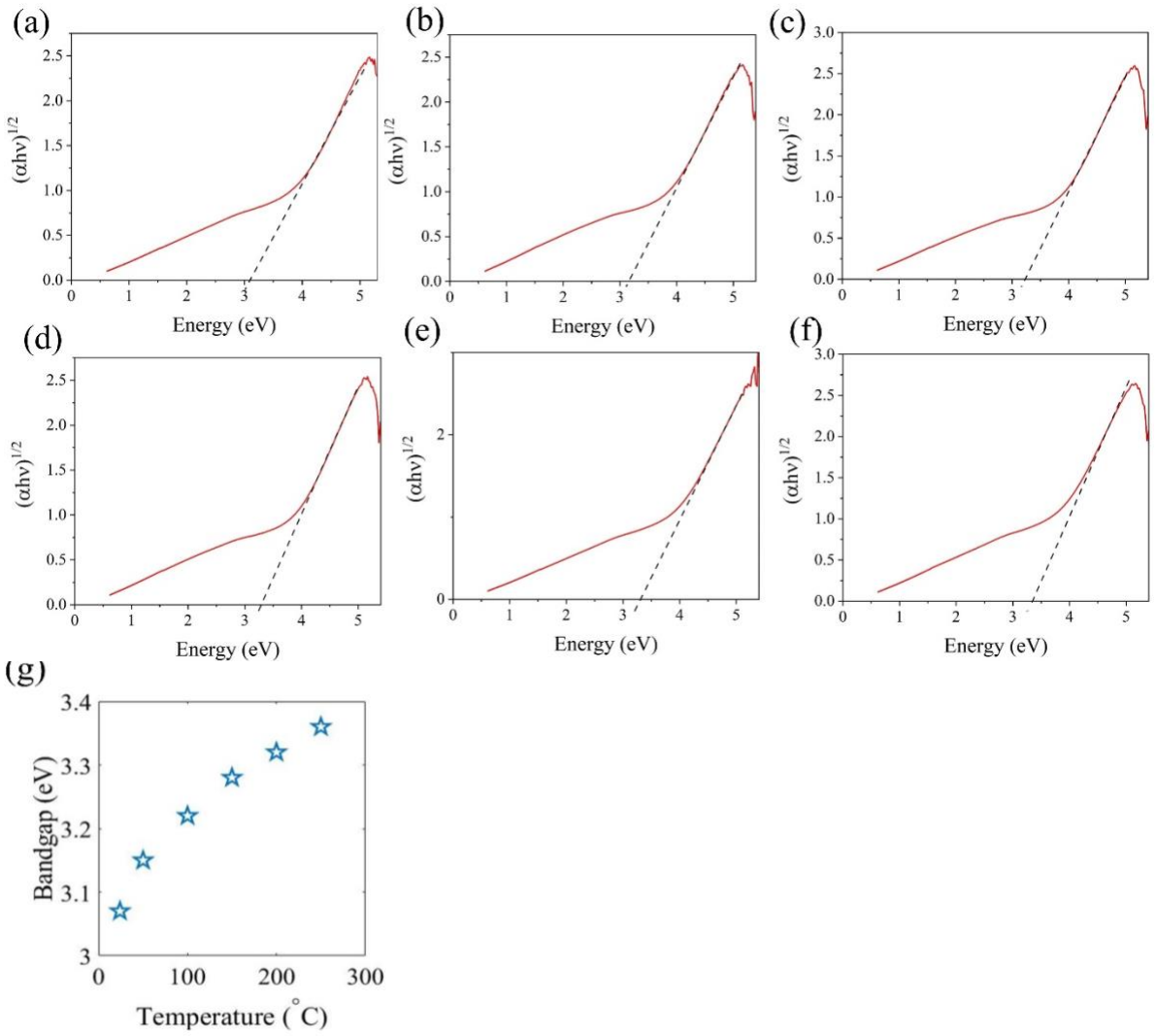

Figure 7-6 Tauc plot for $Sn_xNi_yO_z$ layer deposited with 20% O_2/Ar at the deposition temperature of (a) room temperature (b) 50°C (c) 100°C (d) 150°C (e) 200°C (f) 250°C. (g) Bandgap of the $Sn_xNi_yO_z$ layer vs deposition temperature derived from Tauc plot.

The optical bandgap was determined by extrapolating the linear region of the Tauc plot to the x-axis (Figure 7-6(a-f)). Figure 7-6(g) shows that the optical bandgap increases with the increase in deposition temperature. We attribute this to the transition of SnO towards SnO_2 as the change in NiO_x composition with temperature is quite small [272]. This argument is also supported by a decrease in the refractive index and absorption coefficient [276]. However, the bandgap of NiO_x decreases with an increase in deposition temperature [272]. Monotonic increase of the bandgap

suggests SnO_2 phase is becoming more dominant because the bandgap of SnO_2 is larger than that of SnO [242].

Figure 7-7(a) shows the variation of carrier concentration with deposition temperature. It is evident that as the deposition temperature increases, carrier concentration decreases implying that holes are being compensated by electrons and the film is transitioning towards an insulator. This transition can also be justified by the formation of SnO_2 because it is intrinsically n-type [277]. Moreover, this also supports the dominance of the SnO_2 phase since NiO_x exhibit p-type conductivity with same order of carrier concentration at different deposition temperatures [272]. Figure 7-7(b) depicts the variation of resistivity with deposition temperature. Thus, the film deposited at room temperature with 20% O_2/Ar demonstrates the best p-type behavior with an average carrier concentration of 2.04 x 10^{17} cm^{-3}, average resistivity of 14.01 Ωcm and average

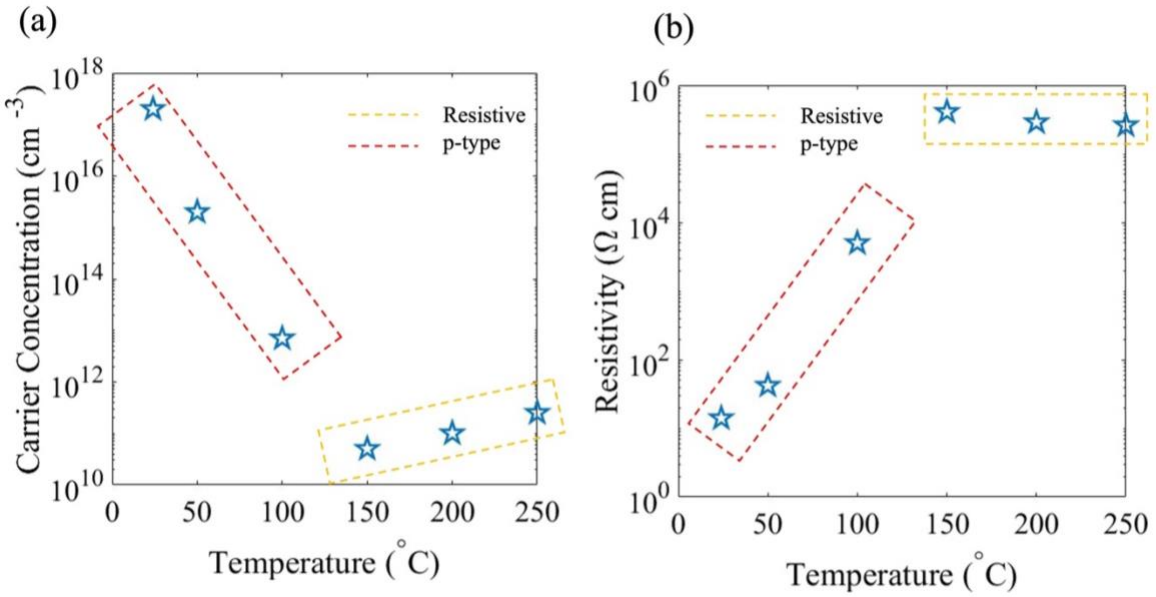

Figure 7-7 Comparison of $Sn_xNi_yO_z$ films deposited with 20% O_2/Ar at different deposition temperatures. (a) Carrier concentration and (b) Resistivity. The red and yellow rectangles indicate p-type and highly resistive behaviour of the films, respectively.

Hall mobility of 7.7 $cm^2V^{-1}s^{-1}$. The standard deviation was calculated using 10 data points and

values of 9 x 10^{16} cm^{-3}, 0.011 Ωcm and 2.4 $cm^2V^{-1}s^{-1}$ was observed for carrier concentration, resistivity and Hall mobility, respectively. An ideal TCO should have low resistance and high transparency but there is always a trade-off between both. Films deposited at room temperature with 20% O_2/Ar show lower absorption with highest p-type conductivity, hence it meets the criteria of a p-type TCO. The rest of the study in the sections below focuses on this film.

7.5 Composition of $Sn_xNi_yO_z$ film

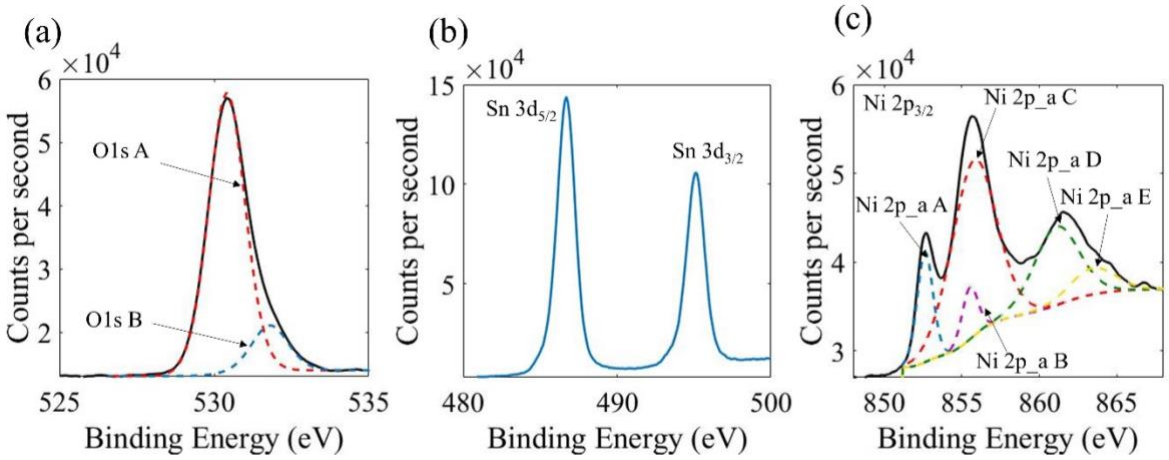

Figure 7-8 XPS spectra of $Sn_xNi_yO_z$ film with 20% O_2/Ar deposited at room temperature: (a) O 1s core level (b) Sn 3d core level and (c) Ni 2p core level.

To gain some chemical information about the film, elemental mapping was carried out using XPS. Figure 7-8 (a) shows the O 1s core level photoemission spectrum. The spectrum is deconvoluted and fitted reasonably well with two peaks centred at 530.4 and 531.9 eV. The first peak (O 1s_A) corresponds to the lattice oxygen and the second peak (O 1s_B) is the characteristic of OH^- in the form of $Ni(OH)_2$ [246, 278, 279]. Figure 7-8 (b) shows the Sn 3d core level photoemission spectrum. The two peaks obtained at 486.6 and 495 eV are due to spin-orbit splitting between Sn $3d_{5/2}$ and Sn $3d_{3/2}$, respectively [245]. The difference between these two peaks is 8.4 eV, which is consistent with the literature [245]. A complex spectrum for Ni is shown is Figure 7-8(c), where it can be fitted

with five peaks. The first peak (Ni 2p_a A) positioned at 852.6 eV is the characteristic peak of metallic Ni^0 [278]. The presence of metallic Ni results in a lower resistivity of the film. The second peak at 855.5 eV (Ni 2p_a B) corresponds to the +3 state of Ni [280]. The third peak (Ni 2p_a C) at 855.8 eV is characteristic peak of Ni^{+2} in the form of $Ni(OH)_2$ with a satellite peak at 861.0 eV (Ni 2p_a D) [279]. Significantly the high intensity of this peak suggests that greater proportion of Ni is bonded with hydroxyl group which could come from the presence of water vapour inside the sputter chamber and exposure to ambient after deposition. The last peak (Ni 2p_a E) at 863.4 eV is also satellite peak of Ni $2p_{3/2}$ [281]. Table 7-3 summarises the atomic fraction on the various peaks obtained from the film. From the values in Table 7-3, we estimate the stoichiometry of $Sn_xNi_yO_z$ film, where x, y and z are 1.4, 1 and 3.7, respectively.

Table 7-3 Summary showing the various XPS peaks and the respectively atomic percentage.

Name	Peak BE (eV)	Atomic %
O1s A	530.4	52.4
O1s B	531.9	8.5
Sn3d5	486.6	22.5
Ni2p_a A	852.6	1.9
Ni2p_a B	855.5	0.9
Ni2p_a C	855.8	8.6
Ni2p_a D	861.0	3.9
Ni2p_a E	863.4	1.3

7.6 Study of n-InP/p-$Sn_xNi_yO_z$ junction properties

7.6.1 Band alignment at n-InP/p-$Sn_xNi_yO_z$ interface

For carrier injection purposes, a deeper insight of the band alignment between n-InP nanowire and p- $Sn_xNi_yO_z$ is required. To study this, UPS analysis was performed on 30 nm of p- $Sn_xNi_yO_z$ film

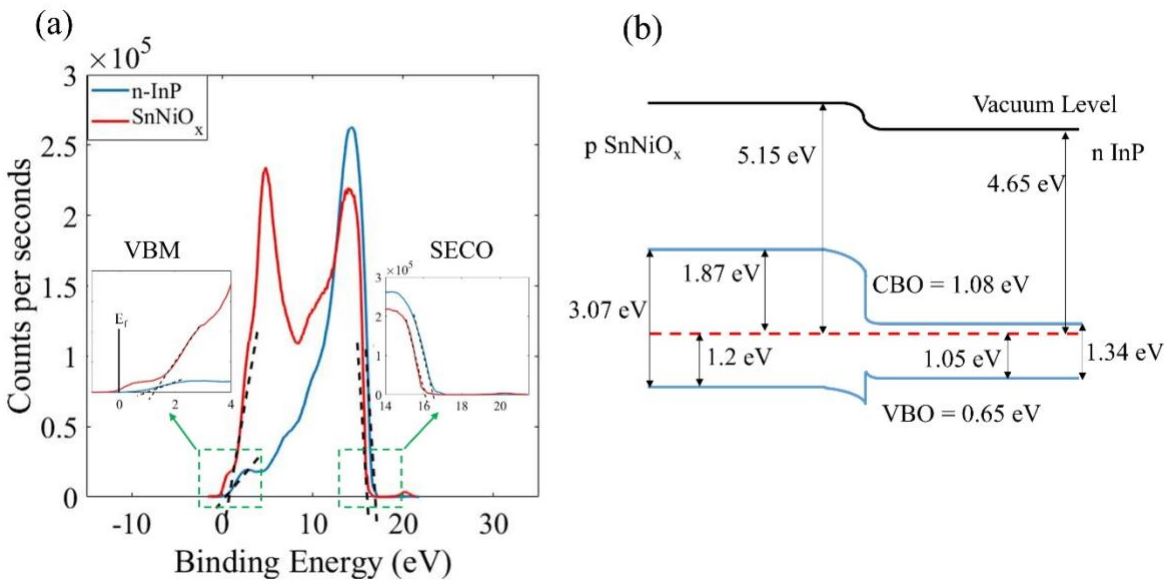

Figure 7-9 (a) UPS spectra of $Sn_xNi_yO_z$ film and InP wafer showing the VBM (left inset) and the SECO (right inset). (b) Band alignment of p- $Sn_xNi_yO_z$ and n+ InP, where the red dashed line represents Fermi level at equilibrium.

deposited on n+ InP wafer. The doping level of InP is $2x10^{18}$ cm^{-3} with a bandgap of 1.34 eV as bulk InP has a ZB crystal phase [202]. Since InP nanowires have WZ configuration (bandgap = 1.42 eV) and slightly lower doping concentration, this will result in a slight deviation in band diagram as compared to the actual working device [202]. Figure 7-9(a) shows the UPS spectra for both n-InP and p- $Sn_xNi_yO_z$. The Fermi level was calibrated and corrected at 0 eV using a silver sample as reference. VBM for both n-InP and p-$Sn_xNi_yO_z$ is approximated by extrapolating the leading edge of UPS spectra to the x–axis. VBM of 1.2 and 1.05 eV are determined for $Sn_xNi_yO_z$ and InP, respectively. Subsequently, work function is estimated as the difference in the energy of the ultraviolet source (He-I line, 21.2 eV) and secondary electron cut-off (SECO). We obtain the work function of InP ~ 4.65 eV which is consistent with the reported value [198]. Work function of 5.15 eV is extracted for $Sn_xNi_yO_z$ which is in the range of its individual components, where the work function of NiO is ~ 5.3 eV, SnO_2 is ~4.84 eV and SnO is ~ 5.2 eV [249, 282]. Using these values, we construct the band diagram of the $Sn_xNi_yO_z$/InP heterostructure, shown in Figure 7-9(b). The

results reflect that sufficiently large CBO (1.08 eV) can act as barrier for highly mobile electrons. This would lead to efficient recombination inside InP nanowires.

7.6.2 I-V characteristics

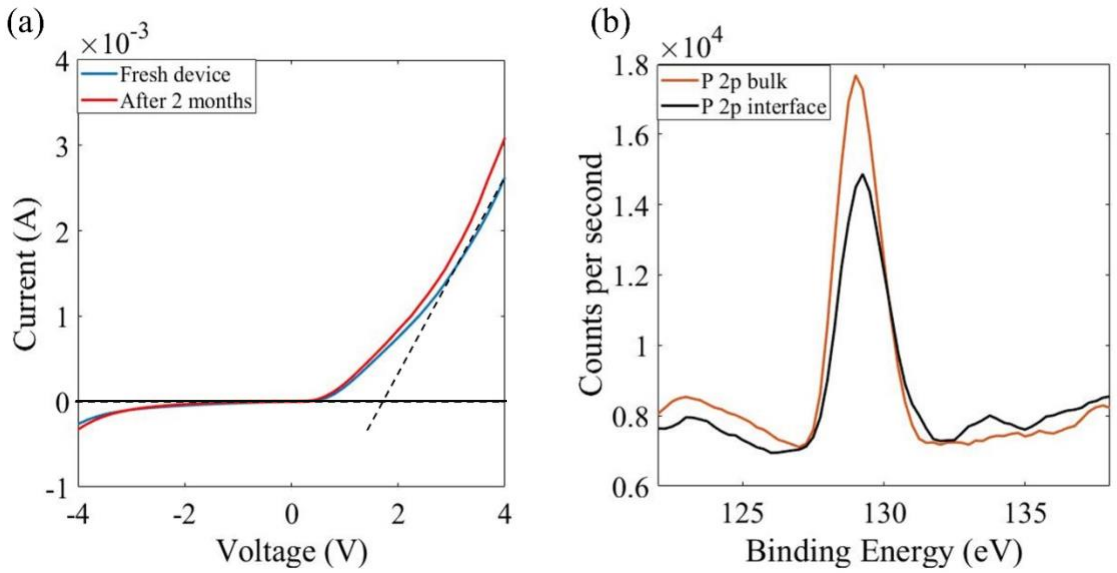

Figure 7-10 Comparison of I-V characteristics of a fresh device and after storing for two months at room temperature. The black dashed line is an extrapolation of the I-V curve to determine the turn-on voltage. (b) XPS spectra of P-2p in bulk and at the interface of $Sn_xNi_yO_z$-InP.

Electrical characteristics of the n-InP/p- $Sn_xNi_yO_z$ nanowire LEDs were studied by measuring I-V behaviour from -4 to 4 V. Figure 7-10(a) shows a rectifying behaviour typical of an LED with a turn-on voltage of around 1.76 V and series resistance of 880 Ω. However, the turn-on voltage is softer as compared to normal p-n junction diode. The higher series resistance is due to a slightly lower carrier concentration (2.04×10^{17} cm^{-3}) of the p-doped film. Furthermore, oxidation of InP nanowires while depositing $Sn_xNi_yO_z$ can also contribute to higher series resistance. Oxidation of InP nanowires during sputter deposition is supported by XPS data (Figure 7-10 (b)). Also, further optimisation is required to increase carrier concentration in $Sn_xNi_yO_z$ film. It can be achieved either

by adding dopants or varying Ni and Sn fraction by changing power of their targets while sputtering. This will improve device performance by reducing series resistance.

Long-term stability of a working device is a desirable property, particularly with p-type TCOs which are not known for their long-term stability. To confirm the stability of the device, after all the measurements, device was kept in atmospheric environment without any special treatment for two months and I-V characteristics were measured again. Similar I-V behaviour of the device after 2 months confirms the robustness of the p-type TCO and device (Figure 7-10(a)).

7.7 EL measurements for LEDs

Figure 7-11(a) shows the EL spectra from the nanowire array LED with increasing forward current injection level at room temperature. The array size of 100 μm x 100 μm consisting of ~11500 nanowires was injected. However, EL intensity was measured from a 10x lens with NA of 0.3 which captured ~1500 nanowires. The EL signal is detectable at an injection current of 1 mA with a peak at 872 nm. This wavelength corresponds to the fundamental bandgap of InP WZ structure at room temperature [202]. It is evident from Figure 7-11(a) that with increasing input current, EL intensity increases, thereby confirming the n-InP/p- $Sn_xNi_yO_z$ nanowires operating as an LED. However, at higher injection current levels, a slight red shift in the EL spectra is observed which indicates Joule heating in the device, potentially due to high series resistance. Therefore, reducing series resistance will enhance light output properties of the LEDs.

To have deeper insight into these LEDs, a systematic temperature dependent study is performed. EL is measured at an injection current of 2 mA from room temperature to 78 K (Figure 7-11(b)). As temperature decreases, a blue shift in the EL spectra is observed due to temperature dependence of the bandgap [252]. At the temperature of 98 K, a shoulder at ~920 nm can be observed. To

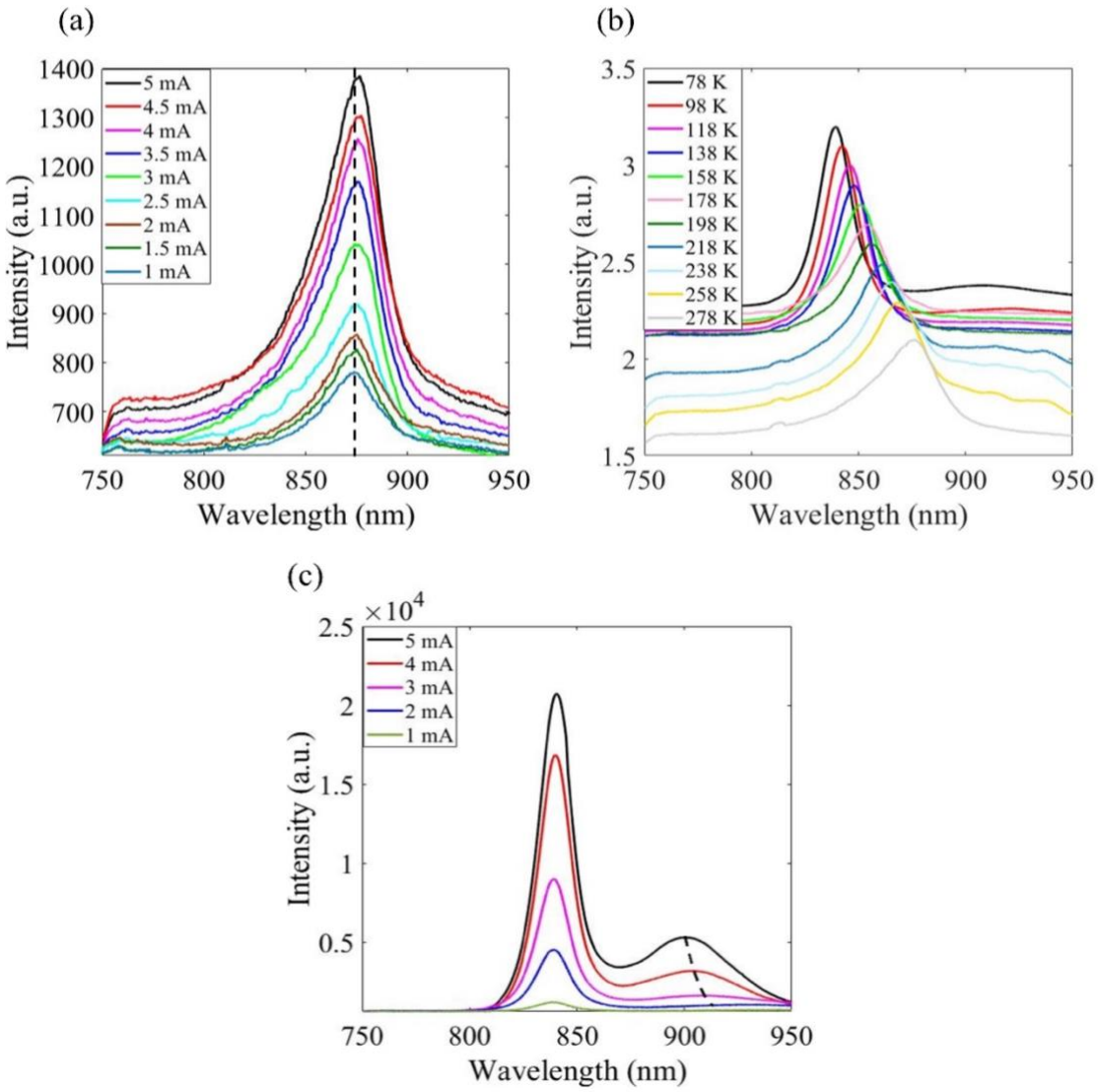

Figure 7-11 (a) Room temperature EL spectra at different current injection levels. The black dashed line indicates the peak of the spectrum at 872 nm. (b) Temperature dependent EL spectrum of the device at 2 mA current. (c) EL spectra at 78 K at different current injection levels where the black dashed line indicates the blue shift in the peak position of ZB/WZ interface peak.

investigate the origin of this peak, EL spectra at 78 K at various injection levels are measured. Figure 7-11(c) shows that the increase in injection current results in a blue shift of the shoulder. Similar blue shifted peak at ~920 nm has been reported due to type II transition from ZB to WZ interface [252]. We therefore attribute this peak to the recombination at the interface of InP nanowires

(WZ) and n+ InP substrate (ZB). Another possibility could be the mixed crystal phase present inside the nanowires. However, at the growth conditions used here, the nanowires have a pure WZ phase as has been reported [104]. Furthermore, the peak corresponding to the fundamental bandgap of InP has significantly higher intensity than ZB/WZ recombination indicating the majority of recombination occurs inside the nanowires.

To understand the effect of dopants on the LED properties, we compared EL spectra from heavily n-doped and undoped InP nanowire devices. Unintentionally doped InP nanowires typically result in a lightly n-type doping of the order of 5.5 x 10^{16} cm^{-3} due to donor surface states [283]. Figure 7-

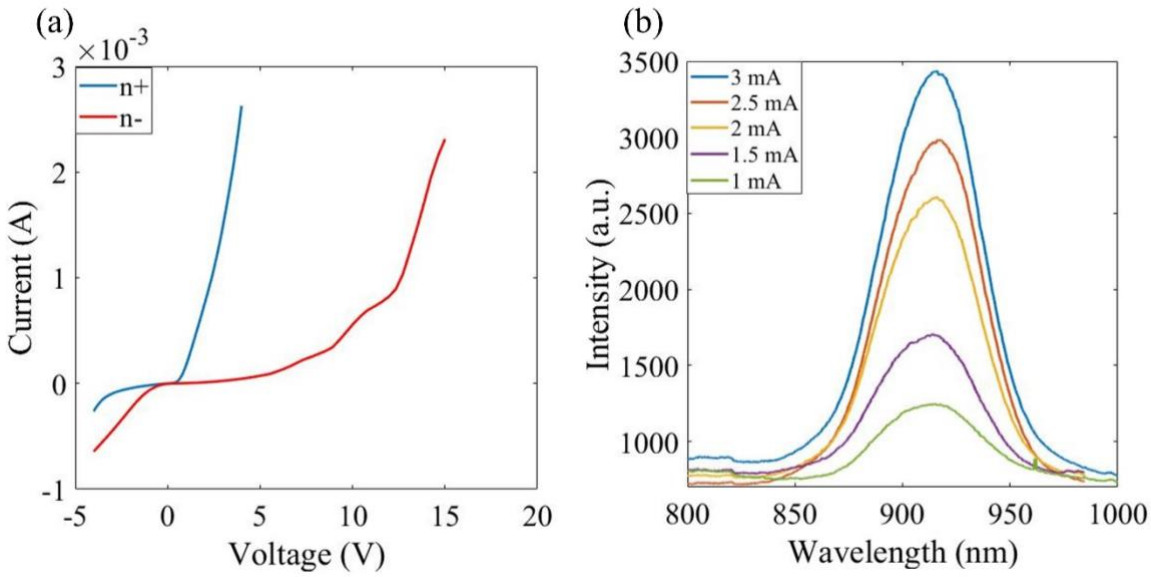

Figure 7-12 (a) Comparison of I-V characteristics of a heavily doped (n+) and undoped (n-) nanowire device. (b) Room temperature EL spectra at different current injection levels from the undoped nanowire device.

12 (a) shows the comparison of I-V characteristics at room temperature where very high series resistance is observed for the undoped nanowires. It is evident that a heavily doped layer is required to form a good p-n junction. However, light output from the undoped nanowires is higher than the n-doped nanowires indicating strong absorption due to free carriers (Figure 7-12 (b)). Peak position ~915 nm indicates significant heating in undoped nanowire devices. The reason for

excessive heating is significantly higher series resistance. For lasing, we need both higher light output and lower resistance therefore, we decided to study i-InP/n+InP nanowires with $Sn_xNi_yO_z$ as a p-doped layer.

7.8 Electrically injected nanowire lasers

7.8.1 Simulations

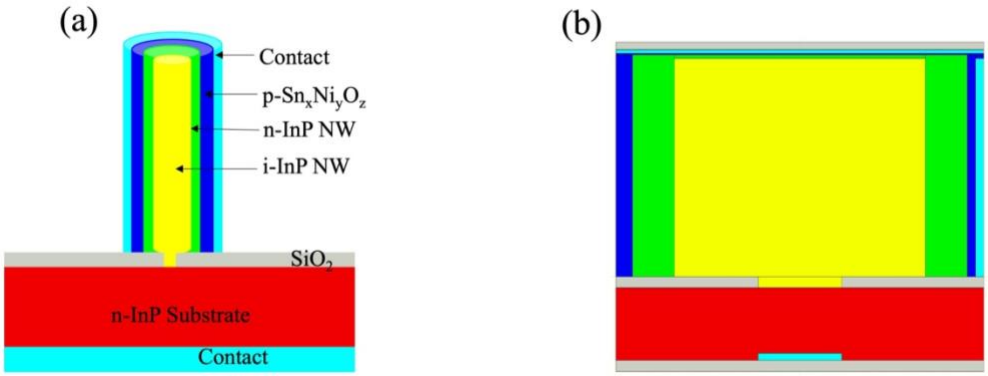

Figure 7-13 (a) Schematic diagram of i-InP/n+InP/p-$Sn_xNi_yO_z$ nanowire (b) LaserMOD CAD layout structure used for simulation (not to the scale)

Figure 7-13 displays the schematic diagram of i-InP/n+InP/p-$Sn_xNi_yO_z$ nanowire where 50 nm thick p-$Sn_xNi_yO_z$ layer was considered with doping concentration of 2.04×10^{17} cm^{-3}. Donor concentration of the 50 nm thick n-InP nanowire shell was taken as 1×10^{18} cm^{-3} as carrier concentration of this range has been reported at the same growth conditions [104]. The configuration of system was defined as WZ for the nanowire, ZB for the substrate with a doping level of 2×10^{18} cm^{-3}. Material parameters used for the simulations are assumed the same as n-SnO_x layer in the preceding chapter. Similar to pervious simulations, while calculating the modes in 2D, *y min* was set to the bottom of the nanowire to study only the modes supported inside the nanowire cavity. The rest of the steps were similar.

Figure 7-14 shows the longitudinal modes supported in a cavity of a specific length. By overlapping the modal spectrum with the gain profile, we can determine the possible longitudinal

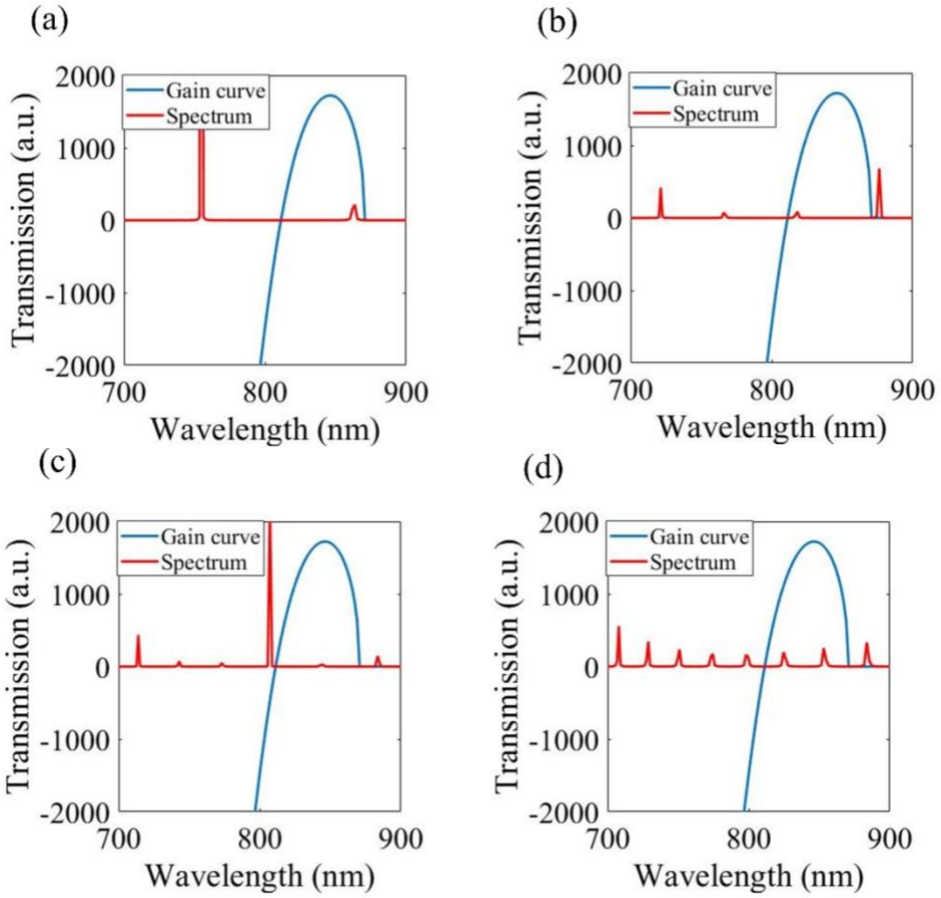

Figure 7-14 Overlap of gain curve at room temperature at a carrier density of $4x10^{18}$ cm^{-3} and modes supported in (a) 1 µm (b) 2 µm (c) 3 µm (d) 4 µm long i-InP/n+InP/p-$Sn_xNi_yO_z$ nanowires.

modes that can lase. Potential lasing wavelengths for 1, 2, 3 and 4 µm long cavity are 863.7, 818.2, 841 and 853.1 nm, respectively. For 4 µm long nanowires, the mode with higher lifetime was chosen.

Following this, full laser 2D simulations were performed where the diameter of the nanowire was varied from 200 – 900 nm. This provides more insight about whether transverse mode in a given waveguide overlaps with the desired longitudinal mode or not. Figure 7-15 shows the diameter

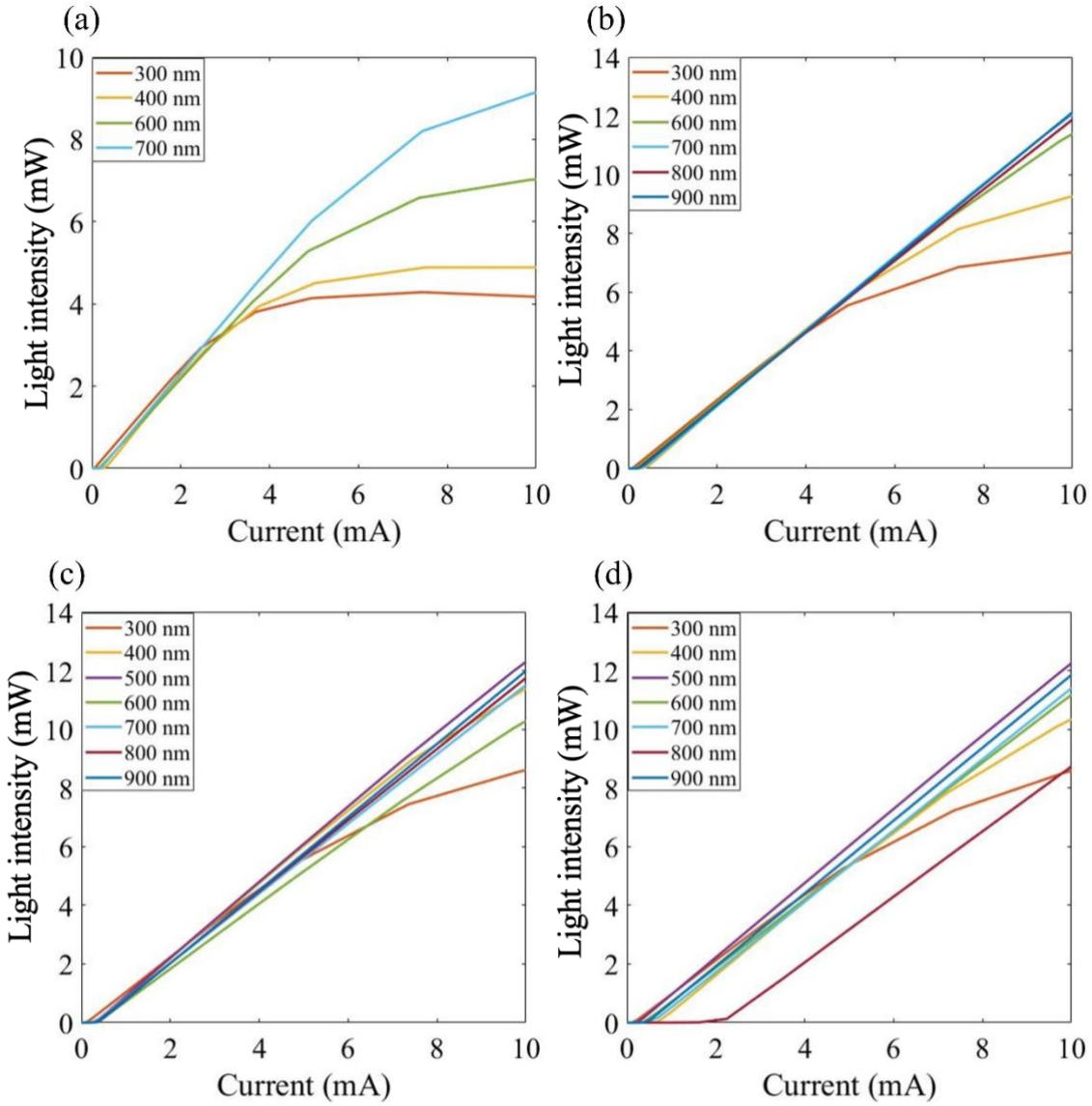

Figure 7-15 Room temperature L-I plots of i-InP/n+InP/p-$Sn_xNi_yO_z$ nanowire devices of various nanowire diameter with a length of (a) 1 µm (b) 2 µm (c) 3 µm and (d) 4 µm with different diameters showing lasing.

where good overlap is observed which leads to lasing in the structure. Minimum threshold is obtained for 300 nm diameter irrespective of the length of the cavity. The lowest threshold current for 1 µm long nanowire was obtained (0.06 mA). For 2, 3 and µm long nanowires, the minimum threshold currents required are 0.1, 0.15 and 0.2 mA, respectively. Significantly higher light output

than previous structure is obtained due to the lower mobility of holes than electrons. If holes are injected near the junction, then the probability of recombination in the active region is higher. In this configuration, holes are injected through the 50 nm thick p-doped $Sn_xNi_yO_z$ film (Figure 7-16 (a)), whereas in previous structures, holes are injected through the substrate that is 100's of microns thick (Figure 7-16 (b)).

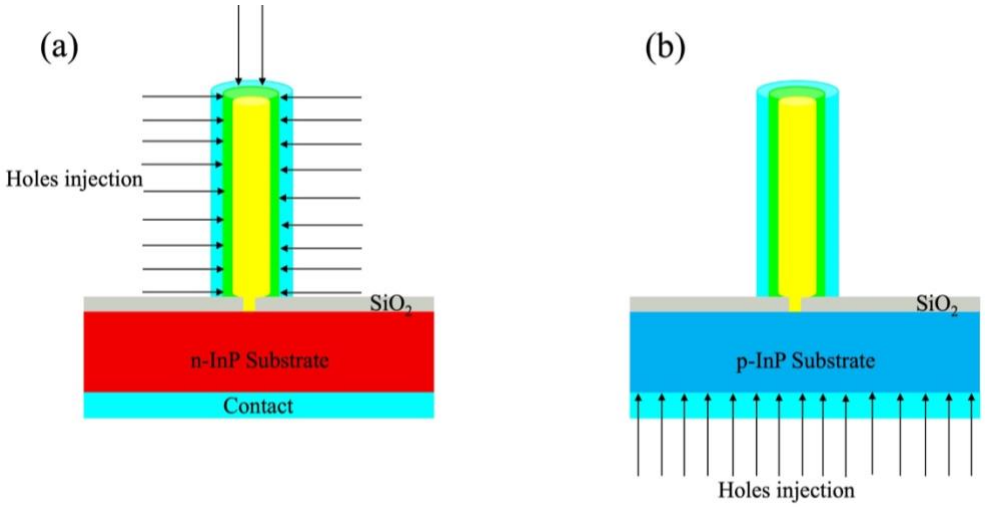

Figure 7-16 Comparison of holes injection in (a) the devices fabricated in this chapter on n-substrate. (b) the devices fabricated in the previous chapters on p-substrate.

7.8.2 Experiments

Nanowires were grown using the same optimised parameters except V/III ratio was increased to 150, nanowire growth time was reduced to 5 mins, size of the array was reduced to 10 x 10 nanowires with a pitch of 5 µm and hole opening in the SiO_2 mask was ~ 100 nm. Current injection with pulse width of 0.5 µs and duty cycle of 1% was used to minimise heating in the device. Also, to suppress recombination at the nanowire/substrate interface, a 2 µm thick SU-8 was left after ICP etching to cover most of the nanowires, except the top portion.

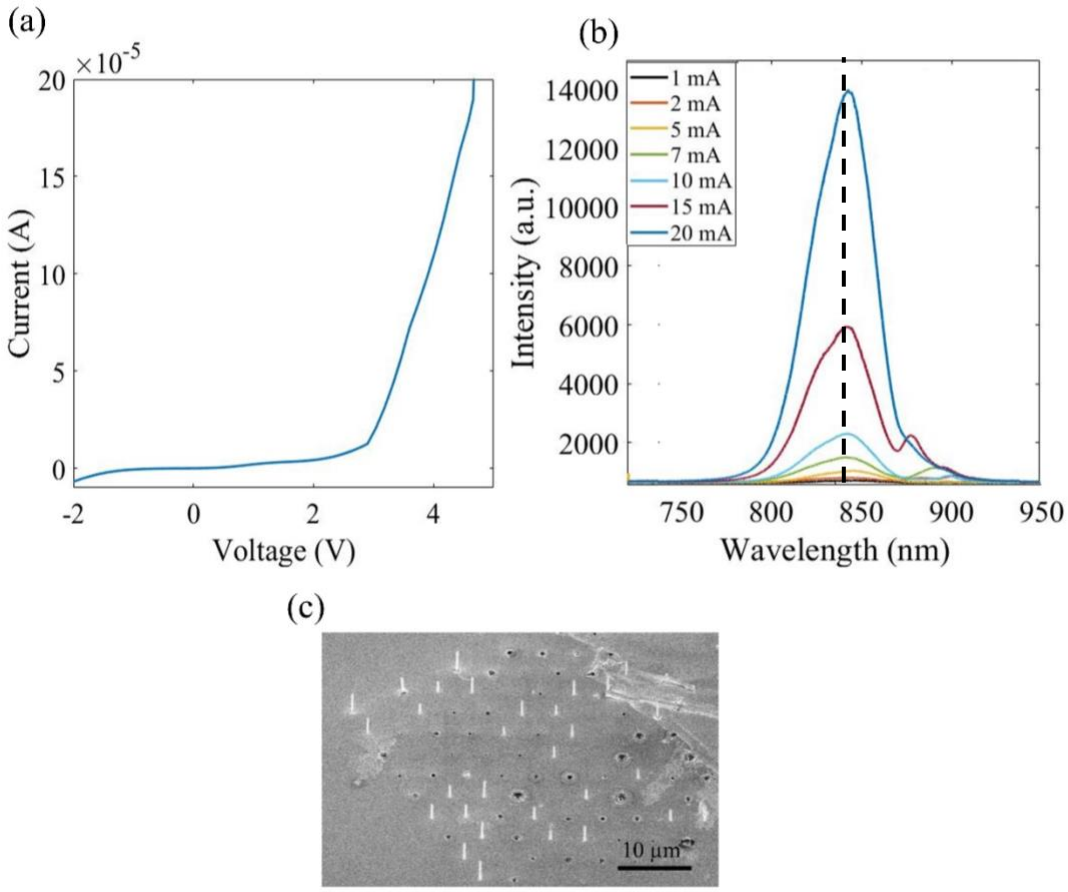

Figure 7-17 78 K (a) I-V characteristics (b) EL spectra at different current injection levels from i-InP/n+InP/p-$Sn_xNi_yO_z$ nanowire device where the black dash line represents peak position at 840 nm. (c) 45° tilted SEM image of the nanowire array LED after device failure.

Figure 7-17 (a) shows the I-V measurements at 78 K with typical rectifying behaviour. Lower series resistance and lower turn on voltage than undoped nanowire device confirm that a thin n-doped shell can improve the I-V properties significantly. Figure 7-17 (b) shows the EL spectra recorded from a single nanowire, although electrical injection is across the entire array. A dominant peak is observed at 840 nm with a shoulder appearing at ~920 nm with increasing injection current. Due to the significantly more intense 840 nm peak (i.e., from the WZ bandgap), it is evident that the majority of recombination is occurring inside the nanowire. The presence of a shoulder in the

spectrum confirms that some of the carriers are still recombining at the nanowire-substrate interface. Moreover, red shift in the EL spectra at higher injection current indicates the is still substantial heating in the device. After 20 mA of current (0.2 mA per nanowire), the device was burnt but this value is significantly higher than the minimum threshold obtained from simulations. The potential reasons behind the deviation in the simulations and experiments could be excessive heating due to lower p-doping concentration, higher series resistance and some carriers recombining inside the substrate. To understand the degradation of device, SEM analysis was carried out. Figure 7-17 (c) shows an image of the device after degradation which confirms previously described issues such as non-uniformity in the nanowires, excessive carrier crowding, heating and some carriers recombining at the nanowire-substrate interface. Further optimisation of p-doped layer is required to increase carrier concentration so that series resistance could be reduced. This will minimise heat generation in the device. Additionally, modification in the design of lasers is required to reduce carrier crowding and avoid recombination the nanowire-substrate interface region.

7.9 Conclusions

In summary, we investigated the optical and electrical properties of $Sn_xNi_yO_z$ as a function of oxygen fraction and deposition temperature. We observed a transition from n-type to p-type with increasing oxygen fraction primarily due to transition from metallic characteristics towards SnO. With increasing deposition temperature, p-type conductivity decreased which we attributed to the transition of SnO to SnO_2. The film deposited at room temperature with 20% O_2/Ar exhibited the highest p-type conductivity with a carrier concentration of 2.5 x 10^{17} cm^{-3}, resistivity of 14 Ωcm and Hall mobility of 8 $cm^2V^{-1}s^{-1}$. We also studied the band alignment at the p-$Sn_xNi_yO_z$/n-InP

interface, and found reasonably large CBO which enhanced the probability of recombination inside nanowires.

We demonstrated an LED with p-doped $Sn_xNi_yO_z$ deposited on n-InP nanowire arrays which was stable after 2 months. At 78 K, a shoulder in the emission spectrum due to ZB/WZ transition was observed (i.e., at nanowire-substrate interface). However, the majority of recombination occurred inside the nanowires. We also investigated lasing properties form i-InP/n+InP/p-$Sn_xNi_yO_z$ nanowire devices. However, device has failed before reaching lasing threshold. The slightly higher series resistance of the device indicates further optimisation in $Sn_xNi_yO_z$ is required to improve device performance. Nevertheless, our preliminary results show that $Sn_xNi_yO_z$ is a promising candidate as a p-type TCO for practical optoelectronics applications.

Chapter 8. Conclusions and Future Work

8.1 Conclusions

In this thesis, we investigated the various challenges to achieve electrically injected nanowire lasers. We designed, grew and fabricated several device structures to achieve lasing and also discussed the potential reasons impeding it. These structures include axial and radial InP nanowire homojunction, core-shell n-ZnO/p-InP nanowires, core-shell n-SnO_x/p-InP nanowires and core-shell p-$Sn_xNi_yO_z$/n-InP nanowires.

In Chapters 1 to 3, we presented the motivation of fabricating electrically injected nanowire lasers and reviewed the progress in the field. We also discussed challenges to achieve electrically pumped nanowire lasers and briefly introduced the experimental and numerical techniques used in this dissertation.

In Chapter 4, we investigated the basic structure of the nanowire F-P cavity using a p-i-n InP axial nanowire and found out that a minimum of ~ 3.2 mA current was required to achieve lasing for a nanowire with 500 nm diameter and 5 μm length. However, the nanowire device failed before reaching lasing threshold. Potential reasons of degradations were non ideal Ohmic contacts, high metal absorption, free carrier absorption, low gain, excessive heating and low doping concentration. To enhance gain, radial homojunction devices were investigated. Radial devices outperformed their axial counterparts in terms of both lower series resistance and ~3.5 times lower theoretical lasing threshold. However due to non-uniformity related to growth and device fabrication, shifting of recombination region into the nanowire-substrate interface and heating, lasing could not be achieved.

In Chapters 5-7, we investigated the use of transparent metal oxide to act as both the carrier injection and contact layer to the nanowire. Specifically, in Chapter 5 we demonstrated n-ZnO/p-InP core-shell nanowire array LEDs and investigated the junction properties using EBIC and I-V characterisation. After confirming good electrical and optical properties, we optimised the nanowire dimensions to achieve lasing. Our numerical results indicated ~4 times lower threshold current was possible in this design due to reduction in free carrier absorption and metal absorption as compared to homojunction InP devices. Experimentally however, due to heating, carrier crowding and lower hole mobility leading to the recombination at the nanowire-substrate interface, the device was burnt before reaching lasing threshold. To mitigate recombination inside the substrate, substrate free device was fabricated by lifting off nanowire arrays into an SU-8 film. However, excessive heating was observed due to low thermal conductivity of SU-8 film.

In Chapter 6, we investigated n-SnO_x/p-InP core-shell nanowire structure for lasing. SnO_x films sputter-deposited at different oxygen flow rates were first characterised for their optical and electrical properties. To understand the balance between absorption and resistance, we fabricated two different devices with n-SnO_x deposited at different oxygen flow rates; one with higher absorption and lower resistance (sample A) and the other with lower absorption and higher resistance (sample B). Sample A outperformed sample B in terms of light output. The potential reasons were better confinement of electrons at the junction due to higher CBO, efficient current injection and lower resistance indicating some compromise of the absorption for lowering the device resistance can lead to an effective working device. Following this, we numerically designed the optimum dimensions of the InP nanowires to obtain lasing. Experimentally however, lasing was not achieved as similar issues as the n-ZnO/p-InP device such as heating, carrier crowding and recombination at the nanowire-substrate interface continue to plague the design.

In Chapter 7, we develop a stable p-type transparent conducting oxide, $Sn_xNi_yO_z$ and studied the p-$Sn_xNi_yO_z$/n-InP core-shell nanowire structure for lasing. In particular we modified our device fabrication sequence to minimise recombination at the nanowire-substrate interface region. We first characterised the various optical and electrical properties of $Sn_xNi_yO_z$ as a function of oxygen flow rate and temperature used during sputter depositions. With the optimised deposition conditions to obtain low resistance and high transmission, we then investigated the core-shell nanowire array LED characteristics and found out that heavily doped nanowires were required to have good I-V characteristics. On the other hand, to achieve higher light output power, undoped nanowires were preferred. Subsequently, we design and fabricated i-InP/n+InP/p-$Sn_xNi_yO_z$ nanowire arrays for lasing. However, due to lower p-type doping concentration, excessive heating was observed and the device was burnt before reaching lasing threshold.

8.2 Future work

In this thesis, we successfully demonstrated various geometries to reduce lasing threshold. However, substantial work is required to achieve lasing from these structures. Based on the knowledge of our studies, we provide following recommendations.

8.2.1 Optimisation of design

As discussed, several challenges still persist to achieve electrically pumped lasing from nanowires. We believe that further optimisation of the laser geometry is required to address some of the challenges.

8.2.1.1 Mitigation of recombination inside the substrate

The bottom contact can be fabricated on top of SiO_2 layer, thereby, reducing possibility of recombination at the nanowire-substrate interface (Figure 8-1). Line-of-sight deposition

techniques such as e-beam/thermal evaporation can be used to deposit metals at the bottom of nanowire arrays. The challenges with this technique are mounting the sample exactly perpendicular to the source, as well as selecting a deposition tool that has large sample-source distance to make sure the metal flux is parallel to the nanowires. However, there will still be thin deposition on sides of nanowires, which can be removed by wet-etching, but controlling the etching time would be very crucial.

Another possibility is to increase both the hole opening and thickness of the SiO_2 mask. It will also address issues related to the excessive carrier crowding. For this, optimisation in the SAE process is required. Removing substrate from the device can also solve this challenge however, proper heat sinking is required.

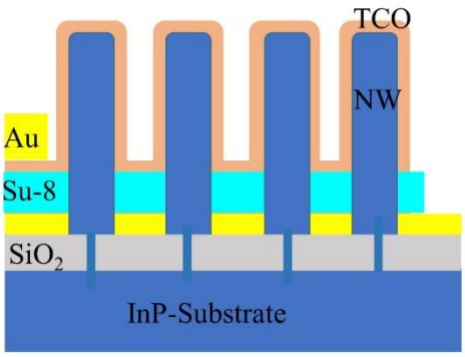

Figure 8-1 Schematic diagram of modified fabrication process for nanowire-TCO devices.

8.2.1.2 Further improvement of p-TCOs

Mobility of holes is significantly lower than the mobility of electrons therefore, the injection of holes in the vicinity of the junction will confine recombination inside the active region (nanowire). To inject holes, a good quality of p-TCO is required. An ideal TCO is one with low resistance and absorption. While it is possible to achieve both the properties in n-type TCOs, more work is still required in the development of good p-type TCOs. Possible options to achieve good quality p-

TCOs is include adding dopants into existing p-TCOs or look for another material system. In this thesis, we investigated $Sn_xNi_yO_z$ thin films as a function of oxygen fraction and temperature. For future studies, these films can be investigated as a function of Sn and Ni fraction to achieve desired performance.

8.2.2 Heat sinking

Excessive heat generation is the main reason for the degradation of the devices investigated in this dissertation. Future work should focus on mounting devices on a suitable heat-sink platform. Instead of using SU-8, high thermally conductive and electrically insulating material such as diamond coating can be used. Another way is to mount the SU-8-based flexible device onto a metal plate instead of an acetate film. Since metals have significantly higher thermal conductivity than acetate films and InP substrate, it may solve both heating issue and recombination inside the substrate

8.2.3 Incorporation of quantum wells and quantum dots

Optically pumped quantum well and quantum dot nanowire lasers have significantly lower lasing threshold than the homojunction lasers due to the quantum confinement of the carriers. This also reduces significant heating and allows to tune the emission wavelength by changing the composition or well width. However, as mentioned before, getting defect free and homogenous quantum wells inside the nanowire structure requires a lot of growth optimisation. Moreover, the non-uniform differential efficiency trend was also observed in nanowires due to mode profile as a function of diameter. Therefore, we recommend to optimise the position of quantum wells/dots inside the nanowire geometry such that all the recombination occurs in the active region. This may pave a way towards low threshold and tunable electrically injected nanowire lasers for wide range of applications.

In conclusion, electrically injected nanowire lasers are a key element for various applications and despite several attempts, further optimisations are required to achieve F-P cavity lasers from III-V semiconductor nanowires. This thesis addresses some of the key challenges however, other issues such as excessive heating, non-uniform current injection and recombination at the nanowire-substrate interface need to be addressed to achieve lasing. We envisage that knowledge and understanding of several challenges identified in this thesis will advance the development of nanoscale lasers.

References

1. Wu, X.; Chen, Q.; Xu, P.; Chen, Y.-C.; Wu, B.; Coleman, R. M.; Tong, L.; Fan, X., Nanowire lasers as intracellular probes. *Nanoscale* **2018,** *10* (20), 9729-9735.
2. Patrizio, A., IDC: Expect 175 zettabytes of data worldwide by 2025. *Network world* Dec 3, 2018.
3. Packan, P. A., Pushing the Limits. *Science* **1999,** *285* (5436), 2079-2081.
4. Miller, D. A. B., Device Requirements for Optical Interconnects to Silicon Chips. *Proceedings of the IEEE* **2009,** *97* (7), 1166-1185.
5. Ning, C. Z., Semiconductor nanolasers. *physica status solidi (b)* **2010,** *247* (4), 774-788.
6. Maslov, A. V.; Ning, C. Z., Reflection of guided modes in a semiconductor nanowire laser. *Applied Physics Letters* **2003,** *83* (6), 1237-1239.
7. Hill, M. T.; Gather, M. C., Advances in small lasers. *Nature Photonics* **2014,** *8* (12), 908-918.
8. Coldren, L. A.; Corzine, S. W.; Mashanovitch, M. L., *Diode lasers and photonic integrated circuits*. John Wiley & Sons: 2012; Vol. 218.
9. Huang, M. H.; Mao, S.; Feick, H.; Yan, H.; Wu, Y.; Kind, H.; Weber, E.; Russo, R.; Yang, P., Room-Temperature Ultraviolet Nanowire Nanolasers. *Science* **2001,** *292* (5523), 1897-1899.
10. Johnson, J. C.; Choi, H.-J.; Knutsen, K. P.; Schaller, R. D.; Yang, P.; Saykally, R. J., Single gallium nitride nanowire lasers. *Nature materials* **2002,** *1* (2), 106-110.
11. Duan, X.; Huang, Y.; Agarwal, R.; Lieber, C. M., Single-nanowire electrically driven lasers. *Nature* **2003,** *421* (6920), 241-245.
12. Chu, S.; Wang, G.; Zhou, W.; Lin, Y.; Chernyak, L.; Zhao, J.; Kong, J.; Li, L.; Ren, J.; Liu, J., Electrically pumped waveguide lasing from ZnO nanowires. *Nature Nanotechnology* **2011,** *6* (8), 506-510.
13. Gradečak, S.; Qian, F.; Li, Y.; Park, H.-G.; Lieber, C. M., GaN nanowire lasers with low lasing thresholds. *Applied Physics Letters* **2005,** *87* (17), 173111.
14. Chin, A. H.; Vaddiraju, S.; Maslov, A. V.; Ning, C. Z.; Sunkara, M. K.; Meyyappan, M., Near-infrared semiconductor subwavelength-wire lasers. *Applied Physics Letters* **2006,** *88* (16), 163115.
15. Hua, B.; Motohisa, J.; Kobayashi, Y.; Hara, S.; Fukui, T., Single GaAs/GaAsP Coaxial Core−Shell Nanowire Lasers. *Nano Letters* **2009,** *9* (1), 112-116.
16. Zhang, Y.; Saxena, D.; Aagesen, M.; Liu, H., Toward electrically driven semiconductor nanowire lasers. *Nanotechnology* **2019,** *30* (19), 192002.
17. Zimmler, M. A.; Capasso, F.; Müller, S.; Ronning, C., Optically pumped nanowire lasers: invited review. *Semiconductor Science and Technology* **2010,** *25* (2), 024001.
18. Mayer, B.; Rudolph, D.; Schnell, J.; Morkötter, S.; Winnerl, J.; Treu, J.; Müller, K.; Bracher, G.; Abstreiter, G.; Koblmüller, G.; Finley, J. J., Lasing from individual GaAs-AlGaAs core-shell nanowires up to room temperature. *Nature Communications* **2013,** *4* (1), 2931.
19. Saxena, D.; Mokkapati, S.; Parkinson, P.; Jiang, N.; Gao, Q.; Tan, H. H.; Jagadish, C., Optically pumped room-temperature GaAs nanowire lasers. *Nature Photonics* **2013,** *7* (12), 963-968.
20. Azimi, Z.; Gagrani, N.; Qu, J.; Lem, O. L. C.; Mokkapati, S.; Cairney, J. M.; Zheng, R.; Tan, H. H.; Jagadish, C.; Wong-Leung, J., Understanding the role of facets and twin defects in the optical performance of GaAs nanowires for laser applications. *Nanoscale Horizons* **2021,** *6* (7), 559-567.
21. Joyce, H. J.; Docherty, C. J.; Gao, Q.; Tan, H. H.; Jagadish, C.; Lloyd-Hughes, J.; Herz, L. M.; Johnston, M. B., Electronic properties of GaAs, InAs and InP nanowires studied by terahertz spectroscopy. *Nanotechnology* **2013,** *24* (21), 214006.

22. Gao, Q.; Saxena, D.; Wang, F.; Fu, L.; Mokkapati, S.; Guo, Y.; Li, L.; Wong-Leung, J.; Caroff, P.; Tan, H. H.; Jagadish, C., Selective-Area Epitaxy of Pure Wurtzite InP Nanowires: High Quantum Efficiency and Room-Temperature Lasing. *Nano Letters* **2014,** *14* (9), 5206-5211.
23. Tatebayashi, J.; Kako, S.; Ho, J.; Ota, Y.; Iwamoto, S.; Arakawa, Y., Room-temperature lasing in a single nanowire with quantum dots. *Nature Photonics* **2015,** *9* (8), 501-505.
24. Saxena, D.; Jiang, N.; Yuan, X.; Mokkapati, S.; Guo, Y.; Tan, H. H.; Jagadish, C., Design and Room-Temperature Operation of GaAs/AlGaAs Multiple Quantum Well Nanowire Lasers. *Nano Letters* **2016,** *16* (8), 5080-5086.
25. Stettner, T.; Zimmermann, P.; Loitsch, B.; Döblinger, M.; Regler, A.; Mayer, B.; Winnerl, J.; Matich, S.; Riedl, H.; Kaniber, M.; Abstreiter, G.; Koblmüller, G.; Finley, J. J., Coaxial GaAs-AlGaAs core-multishell nanowire lasers with epitaxial gain control. *Applied Physics Letters* **2016,** *108* (1), 011108.
26. Yan, X.; Wei, W.; Tang, F.; Wang, X.; Li, L.; Zhang, X.; Ren, X., Low-threshold room-temperature AlGaAs/GaAs nanowire/single-quantum-well heterostructure laser. *Applied Physics Letters* **2017,** *110* (6), 061104.
27. Zhang, X.; Yi, R.; Gagrani, N.; Li, Z.; Zhang, F.; Gan, X.; Yao, X.; Yuan, X.; Wang, N.; Zhao, J.; Chen, P.; Lu, W.; Fu, L.; Tan, H. H.; Jagadish, C., Ultralow Threshold, Single-Mode InGaAs/GaAs Multiquantum Disk Nanowire Lasers. *ACS Nano* **2021,** *15* (5), 9126-9133.
28. Zhang, G.; Takiguchi, M.; Tateno, K.; Tawara, T.; Notomi, M.; Gotoh, H., Telecom-band lasing in single InP/InAs heterostructure nanowires at room temperature. *Science Advances* **2019,** *5* (2), eaat8896.
29. Ho, J.; Tatebayashi, J.; Sergent, S.; Fong, C. F.; Iwamoto, S.; Arakawa, Y., Low-Threshold near-Infrared GaAs–AlGaAs Core–Shell Nanowire Plasmon Laser. *ACS Photonics* **2015,** *2* (1), 165-171.
30. Mayer, B.; Janker, L.; Rudolph, D.; Loitsch, B.; Kostenbader, T.; Abstreiter, G.; Koblmüller, G.; Finley, J. J., Continuous wave lasing from individual GaAs-AlGaAs core-shell nanowires. *Applied Physics Letters* **2016,** *108* (7), 071107.
31. Burgess, T.; Saxena, D.; Mokkapati, S.; Li, Z.; Hall, C. R.; Davis, J. A.; Wang, Y.; Smith, L. M.; Fu, L.; Caroff, P.; Tan, H. H.; Jagadish, C., Doping-enhanced radiative efficiency enables lasing in unpassivated GaAs nanowires. *Nature Communications* **2016,** *7* (1), 11927.
32. Xu, W.-Z.; Ren, F.-F.; Jevtics, D.; Hurtado, A.; Li, L.; Gao, Q.; Ye, J.; Wang, F.; Guilhabert, B.; Fu, L.; Lu, H.; Zhang, R.; Tan, H. H.; Dawson, M. D.; Jagadish, C., Vertically Emitting Indium Phosphide Nanowire Lasers. *Nano Letters* **2018,** *18* (6), 3414-3420.
33. Scofield, A. C.; Kim, S.-H.; Shapiro, J. N.; Lin, A.; Liang, B.; Scherer, A.; Huffaker, D. L., Bottom-up Photonic Crystal Lasers. *Nano Letters* **2011,** *11* (12), 5387-5390.
34. Takiguchi, M.; Yokoo, A.; Nozaki, K.; Birowosuto, M. D.; Tateno, K.; Zhang, G.; Kuramochi, E.; Shinya, A.; Notomi, M., Continuous-wave operation and 10-Gb/s direct modulation of InAsP/InP sub-wavelength nanowire laser on silicon photonic crystal. *APL Photonics* **2017,** *2* (4), 046106.
35. Yokoo, A.; Takiguchi, M.; Birowosuto, M. D.; Tateno, K.; Zhang, G.; Kuramochi, E.; Shinya, A.; Taniyama, H.; Notomi, M., Subwavelength Nanowire Lasers on a Silicon Photonic Crystal Operating at Telecom Wavelengths. *ACS Photonics* **2017,** *4* (2), 355-362.
36. Chen, R.; Tran, T.-T. D.; Ng, K. W.; Ko, W. S.; Chuang, L. C.; Sedgwick, F. G.; Chang-Hasnain, C., Nanolasers grown on silicon. *Nature Photonics* **2011,** *5* (3), 170-175.
37. Sun, H.; Ren, F.; Ng, K. W.; Tran, T.-T. D.; Li, K.; Chang-Hasnain, C. J., Nanopillar Lasers Directly Grown on Silicon with Heterostructure Surface Passivation. *ACS Nano* **2014,** *8* (7), 6833-6839.
38. Li, K.; Sun, H.; Ren, F.; Ng, K. W.; Tran, T.-T. D.; Chen, R.; Chang-Hasnain, C. J., Tailoring the Optical Characteristics of Microsized InP Nanoneedles Directly Grown on Silicon. *Nano Letters* **2014,** *14* (1), 183-190.
39. Tran, T. T. D.; Chen, R.; Ng, K. W.; Ko, W. S.; Lu, F.; Chang-Hasnain, C. J., Three-dimensional whispering gallery modes in InGaAs nanoneedle lasers on silicon. *Applied Physics Letters* **2014,** *105* (11), 111105.

40. Lu, F.; Bhattacharya, I.; Sun, H.; Tran, T.-T. D.; Ng, K. W.; Malheiros-Silveira, G. N.; Chang-Hasnain, C., Nanopillar quantum well lasers directly grown on silicon and emitting at silicon-transparent wavelengths. *Optica* **2017,** *4* (7), 717-723.
41. Schuster, F.; Kapraun, J.; Malheiros-Silveira, G. N.; Deshpande, S.; Chang-Hasnain, C. J., Site-Controlled Growth of Monolithic InGaAs/InP Quantum Well Nanopillar Lasers on Silicon. *Nano Letters* **2017,** *17* (4), 2697-2702.
42. Wang, Z.; Tian, B.; Paladugu, M.; Pantouvaki, M.; Le Thomas, N.; Merckling, C.; Guo, W.; Dekoster, J.; Van Campenhout, J.; Absil, P.; Van Thourhout, D., Polytypic InP Nanolaser Monolithically Integrated on (001) Silicon. *Nano Letters* **2013,** *13* (11), 5063-5069.
43. Tian, B.; Wang, Z.; Pantouvaki, M.; Guo, W.; Campenhout, J. V.; Clement, M.; Thourhout, D. V. In *InP nanowire lasers epitaxially grown on (001) silicon 'V-groove' templates*, 26th International Conference on Indium Phosphide and Related Materials (IPRM), 11-15 May 2014; 2014; pp 1-2.
44. Nomura, M.; Iwamoto, S.; Watanabe, K.; Kumagai, N.; Nakata, Y.; Ishida, S.; Arakawa, Y., Room temperature continuous-wave lasing in photonic crystal nanocavity. *Opt. Express* **2006,** *14* (13), 6308-6315.
45. Kim, H.; Lee, W.-J.; Farrell, A. C.; Balgarkashi, A.; Huffaker, D. L., Telecom-Wavelength Bottom-up Nanobeam Lasers on Silicon-on-Insulator. *Nano Letters* **2017,** *17* (9), 5244-5250.
46. Kim, H.; Lee, W.-J.; Farrell, A. C.; Morales, J. S. D.; Senanayake, P.; Prikhodko, S. V.; Ochalski, T. J.; Huffaker, D. L., Monolithic InGaAs Nanowire Array Lasers on Silicon-on-Insulator Operating at Room Temperature. *Nano Letters* **2017,** *17* (6), 3465-3470.
47. Lee, W.-J.; Kim, H.; You, J.-B.; Huffaker, D. L., Ultracompact bottom-up photonic crystal lasers on silicon-on-insulator. *Scientific Reports* **2017,** *7* (1), 9543.
48. Kim, H.; Lee, W.-J.; Chang, T.-Y.; Huffaker, D. L., Room-Temperature InGaAs Nanowire Array Band-Edge Lasers on Patterned Silicon-on-Insulator Platforms. *physica status solidi (RRL) – Rapid Research Letters* **2019,** *13* (3), 1800489.
49. Mayer, B.; Janker, L.; Loitsch, B.; Treu, J.; Kostenbader, T.; Lichtmannecker, S.; Reichert, T.; Morkötter, S.; Kaniber, M.; Abstreiter, G.; Gies, C.; Koblmüller, G.; Finley, J. J., Monolithically Integrated High-β Nanowire Lasers on Silicon. *Nano Letters* **2016,** *16* (1), 152-156.
50. Ma, X.; Pan, J.; Chen, P.; Li, D.; Zhang, H.; Yang, Y.; Yang, D., Room temperature electrically pumped ultraviolet random lasing from ZnO nanorod arrays on Si. *Opt. Express* **2009,** *17* (16), 14426-14433.
51. Liu, C. Y.; Xu, H. Y.; Ma, J. G.; Li, X. H.; Zhang, X. T.; Liu, Y. C.; Mu, R., Electrically pumped near-ultraviolet lasing from ZnO/MgO core/shell nanowires. *Applied Physics Letters* **2011,** *99* (6), 063115.
52. Liu, X.-Y.; Shan, C.-X.; Wang, S.-P.; Zhang, Z.-Z.; Shen, D.-Z., Electrically pumped random lasers fabricated from ZnO nanowire arrays. *Nanoscale* **2012,** *4* (9), 2843-2846.
53. Huang, J.; Chu, S.; Kong, J.; Zhang, L.; Schwarz, C. M.; Wang, G.; Chernyak, L.; Chen, Z.; Liu, J., ZnO p–n Homojunction Random Laser Diode Based on Nitrogen-Doped p-type Nanowires. *Advanced Optical Materials* **2013,** *1* (2), 179-185.
54. Bashar, S. B.; Suja, M.; Shi, W.; Liu, J., Enhanced random lasing from distributed Bragg reflector assisted Au-ZnO nanowire Schottky diode. *Applied Physics Letters* **2016,** *109* (19), 192101.
55. Gao, F.; Morshed, M. M.; Bashar, S. B.; Zheng, Y.; Shi, Y.; Liu, J., Electrically pumped random lasing based on an Au–ZnO nanowire Schottky junction. *Nanoscale* **2015,** *7* (21), 9505-9509.
56. Que, M.-L.; Wang, X.-D.; Peng, Y.-Y.; Pan, C.-F., Flexible electrically pumped random lasing from ZnO nanowires based on metal–insulator–semiconductor structure. *Chinese Physics B* **2017,** *26* (6), 067301.
57. Bashar, S. B.; Suja, M.; Morshed, M.; Gao, F.; Liu, J., An Sb-doped p-type ZnO nanowire based random laser diode. *Nanotechnology* **2016,** *27* (6), 065204.

58. Frost, T.; Jahangir, S.; Stark, E.; Deshpande, S.; Hazari, A.; Zhao, C.; Ooi, B. S.; Bhattacharya, P., Monolithic Electrically Injected Nanowire Array Edge-Emitting Laser on (001) Silicon. *Nano Letters* **2014,** *14* (8), 4535-4541.
59. Hazari, A.; Aiello, A.; Ng, T.-K.; Ooi, B. S.; Bhattacharya, P., III-nitride disk-in-nanowire 1.2 μm monolithic diode laser on (001)silicon. *Applied Physics Letters* **2015,** *107* (19), 191107.
60. Jahangir, S.; Frost, T.; Hazari, A.; Yan, L.; Stark, E.; LaMountain, T.; Millunchick, J. M.; Ooi, B. S.; Bhattacharya, P., Small signal modulation characteristics of red-emitting (λ = 610 nm) III-nitride nanowire array lasers on (001) silicon. *Applied Physics Letters* **2015,** *106* (7), 071108.
61. Banerjee, D.; Takhar, K.; Sankaranarayanan, S.; Upadhyay, P.; Ruia, R.; Chouksey, S.; Khachariya, D.; Ganguly, S.; Saha, D., Electrically injected ultra-low threshold room temperature InGaN/GaN-based lateral triangular nanowire laser. *Applied Physics Letters* **2015,** *107* (10), 101108.
62. Li, K. H.; Liu, X.; Wang, Q.; Zhao, S.; Mi, Z., Ultralow-threshold electrically injected AlGaN nanowire ultraviolet lasers on Si operating at low temperature. *Nature Nanotechnology* **2015,** *10* (2), 140-144.
63. Zhao, S.; Liu, X.; Woo, S. Y.; Kang, J.; Botton, G. A.; Mi, Z., An electrically injected AlGaN nanowire laser operating in the ultraviolet-C band. *Applied Physics Letters* **2015,** *107* (4), 043101.
64. Zhao, S.; Woo, S. Y.; Bugnet, M.; Liu, X.; Kang, J.; Botton, G. A.; Mi, Z., Three-Dimensional Quantum Confinement of Charge Carriers in Self-Organized AlGaN Nanowires: A Viable Route to Electrically Injected Deep Ultraviolet Lasers. *Nano Letters* **2015,** *15* (12), 7801-7807.
65. Mi, Z.; Zhao, S.; Woo, S. Y.; Bugnet, M.; Djavid, M.; Liu, X.; Kang, J.; Kong, X.; Ji, W.; Guo, H.; Liu, Z.; Botton, G. A., Molecular beam epitaxial growth and characterization of Al(Ga)N nanowire deep ultraviolet light emitting diodes and lasers. *Journal of Physics D: Applied Physics* **2016,** *49* (36), 364006.
66. Zhao, S.; Liu, X.; Wu, Y.; Mi, Z., An electrically pumped 239 nm AlGaN nanowire laser operating at room temperature. *Applied Physics Letters* **2016,** *109* (19), 191106.
67. Ding, K.; Ning, C. Z., Fabrication challenges of electrical injection metallic cavity semiconductor nanolasers. *Semiconductor Science and Technology* **2013,** *28* (12), 124002.
68. Hill, M. T.; Oei, Y.-S.; Smalbrugge, B.; Zhu, Y.; de Vries, T.; van Veldhoven, P. J.; van Otten, F. W. M.; Eijkemans, T. J.; Turkiewicz, J. P.; de Waardt, H.; Geluk, E. J.; Kwon, S.-H.; Lee, Y.-H.; Nötzel, R.; Smit, M. K., Lasing in metallic-coated nanocavities. *Nature Photonics* **2007,** *1* (10), 589-594.
69. Ding, K.; Ning, C. Z., Metallic subwavelength-cavity semiconductor nanolasers. *Light: Science & Applications* **2012,** *1* (7), e20-e20.
70. Ding, K.; Hill, M. T.; Liu, Z. C.; Yin, L. J.; van Veldhoven, P. J.; Ning, C. Z., Record performance of electrical injection sub-wavelength metallic-cavity semiconductor lasers at room temperature. *Opt. Express* **2013,** *21* (4), 4728-4733.
71. Gu, Q.; Shane, J.; Vallini, F.; Wingad, B.; Smalley, J. S. T.; Frateschi, N. C.; Fainman, Y., Amorphous Al2O3 Shield for Thermal Management in Electrically Pumped Metallo-Dielectric Nanolasers. *IEEE Journal of Quantum Electronics* **2014,** *50* (7), 499-509.
72. Dolores-Calzadilla, V.; Romeira, B.; Pagliano, F.; Birindelli, S.; Higuera-Rodriguez, A.; van Veldhoven, P. J.; Smit, M. K.; Fiore, A.; Heiss, D., Waveguide-coupled nanopillar metal-cavity light-emitting diodes on silicon. *Nature Communications* **2017,** *8* (1), 14323.
73. Fang, C.; Vallini, F.; Amili, A. E.; Smalley, J. S. T.; Fainman, Y., Low Resistance Tunnel Junctions for Efficient Electrically Pumped Nanolasers. *IEEE Journal of Selected Topics in Quantum Electronics* **2017,** *23* (6), 1-6.
74. Fang, C.-Y.; Pan, S. H.; Vallini, F.; Tukiainen, A.; Lyytikäinen, J.; Nylund, G.; Kanté, B.; Guina, M.; El Amili, A.; Fainman, Y., Lasing action in low-resistance nanolasers based on tunnel junctions. *Opt. Lett.* **2019,** *44* (15), 3669-3672.

75. Fang, C.; Vallini, F.; Amili, A. E.; Tukiainen, A.; Lyytikäinen, J.; Guina, M.; Fainman, Y. In *Development of Efficient Electrically Pumped Nanolasers based on InAlGaAs Tunnel Junction*, 2018 Conference on Lasers and Electro-Optics (CLEO), 13-18 May 2018; 2018; pp 1-2.
76. Ding, K.; Liu, Z. C.; Yin, L. J.; Hill, M. T.; Marell, M. J. H.; van Veldhoven, P. J.; Nöetzel, R.; Ning, C. Z., Room-temperature continuous wave lasing in deep-subwavelength metallic cavities under electrical injection. *Physical Review B* **2012,** *85* (4), 041301.
77. Haraguchi, K.; Katsuyama, T.; Hiruma, K.; Ogawa, K., GaAs p-n junction formed in quantum wire crystals. *Applied Physics Letters* **1992,** *60* (6), 745-747.
78. Haraguchi, K.; Katsuyama, T.; Hiruma, K., Polarization dependence of light emitted from GaAs p-n junctions in quantum wire crystals. *Journal of Applied Physics* **1994,** *75* (8), 4220-4225.
79. Lysov, A.; Offer, M.; Gutsche, C.; Regolin, I.; Topaloglu, S.; Geller, M.; Prost, W.; Tegude, F. J., Optical properties of heavily doped GaAs nanowires and electroluminescent nanowire structures. *Nanotechnology* **2011,** *22* (8), 085702.
80. Gutsche, C.; Lysov, A.; Braam, D.; Regolin, I.; Keller, G.; Li, Z.-A.; Geller, M.; Spasova, M.; Prost, W.; Tegude, F.-J., n-GaAs/InGaP/p-GaAs Core-Multishell Nanowire Diodes for Efficient Light-to-Current Conversion. *Advanced Functional Materials* **2012,** *22* (5), 929-936.
81. Svensson, C. P. T.; Mårtensson, T.; Trägårdh, J.; Larsson, C.; Rask, M.; Hessman, D.; Samuelson, L.; Ohlsson, J., Monolithic GaAs/InGaP nanowire light emitting diodes on silicon. *Nanotechnology* **2008,** *19* (30), 305201.
82. Chuang, L. C.; Sedgwick, F. G.; Chen, R.; Ko, W. S.; Moewe, M.; Ng, K. W.; Tran, T.-T. D.; Chang-Hasnain, C., GaAs-Based Nanoneedle Light Emitting Diode and Avalanche Photodiode Monolithically Integrated on a Silicon Substrate. *Nano Letters* **2011,** *11* (2), 385-390.
83. Herranz, J.; Corfdir, P.; Luna, E.; Jahn, U.; Lewis, R. B.; Schrottke, L.; Lähnemann, J.; Tahraoui, A.; Trampert, A.; Brandt, O.; Geelhaar, L., Coaxial GaAs/(In,Ga)As Dot-in-a-Well Nanowire Heterostructures for Electrically Driven Infrared Light Generation on Si in the Telecommunication O Band. *ACS Applied Nano Materials* **2020,** *3* (1), 165-174.
84. Dimakis, E.; Jahn, U.; Ramsteiner, M.; Tahraoui, A.; Grandal, J.; Kong, X.; Marquardt, O.; Trampert, A.; Riechert, H.; Geelhaar, L., Coaxial Multishell (In,Ga)As/GaAs Nanowires for Near-Infrared Emission on Si Substrates. *Nano Letters* **2014,** *14* (5), 2604-2609.
85. Tomioka, K.; Motohisa, J.; Hara, S.; Hiruma, K.; Fukui, T., GaAs/AlGaAs Core Multishell Nanowire-Based Light-Emitting Diodes on Si. *Nano Letters* **2010,** *10* (5), 1639-1644.
86. Romeira, B.; Borme, J.; Fonseca, H.; Gaspar, J.; Nieder, J. B., Efficient light extraction in subwavelength GaAs/AlGaAs nanopillars for nanoscale light-emitting devices. *Opt. Express* **2020,** *28* (22), 32302-32315.
87. Gudiksen, M. S.; Lauhon, L. J.; Wang, J.; Smith, D. C.; Lieber, C. M., Growth of nanowire superlattice structures for nanoscale photonics and electronics. *Nature* **2002,** *415* (6872), 617-620.
88. Duan, X.; Huang, Y.; Cui, Y.; Wang, J.; Lieber, C. M., Indium phosphide nanowires as building blocks for nanoscale electronic and optoelectronic devices. *Nature* **2001,** *409* (6816), 66-69.
89. Motohisa, J.; Kameda, H.; Sasaki, M.; Tomioka, K., Characterization of nanowire light-emitting diodes grown by selective-area metal-organic vapor-phase epitaxy. *Nanotechnology* **2019,** *30* (13), 134002.
90. Maeda, S.; Tomioka, K.; Hara, S.; Motohisa, J., Fabrication and Characterization of InP Nanowire Light-Emitting Diodes. *Japanese Journal of Applied Physics* **2012,** *51* (2), 02BN03.
91. Borgström, M. T.; Norberg, E.; Wickert, P.; Nilsson, H. A.; Trägårdh, J.; Dick, K. A.; Statkute, G.; Ramvall, P.; Deppert, K.; Samuelson, L., Precursor evaluation forin situInP nanowire doping. *Nanotechnology* **2008,** *19* (44), 445602.
92. Motohisa, J.; Kohashi, Y.; Maeda, S., Far-Field Emission Patterns of Nanowire Light-Emitting Diodes. *Nano Letters* **2014,** *14* (6), 3653-3660.

93. Akamatsu, T.; Tomioka, K.; Motohisa, J., Demonstration of InP/InAsP/InP axial heterostructure nanowire array vertical LEDs. *Nanotechnology* **2020,** *31* (39), 394003.
94. Zhang, G.; Gnatek, D.; Takiguchi, M.; Xu, X.; Tateno, K.; Sasaki, S.; Tawara, T.; Gotoh, H., Nanowire-based telecom-band light-emitting diodes with efficient light extraction. *Japanese Journal of Applied Physics* **2020,** *59* (10), 105003.
95. Deshpande, S.; Bhattacharya, I.; Malheiros-Silveira, G.; Ng, K. W.; Schuster, F.; Mantei, W.; Cook, K.; Chang-Hasnain, C., Ultracompact Position-Controlled InP Nanopillar LEDs on Silicon with Bright Electroluminescence at Telecommunication Wavelengths. *ACS Photonics* **2017,** *4* (3), 695-702.
96. Yang, I.; Kim, S.; Niihori, M.; Alabadla, A.; Li, Z.; Li, L.; Lockrey, M. N.; Choi, D.-Y.; Aharonovich, I.; Wong-Leung, J.; Tan, H. H.; Jagadish, C.; Fu, L., Highly uniform InGaAs/InP quantum well nanowire array-based light emitting diodes. *Nano Energy* **2020,** *71*, 104576.
97. Yang, I.; Li, Z.; Wong-Leung, J.; Zhu, Y.; Li, Z.; Gagrani, N.; Li, L.; Lockrey, M. N.; Nguyen, H.; Lu, Y.; Tan, H. H.; Jagadish, C.; Fu, L., Multiwavelength Single Nanowire InGaAs/InP Quantum Well Light-Emitting Diodes. *Nano Letters* **2019,** *19* (6), 3821-3829.
98. Takiguchi, M.; Zhang, G.; Sasaki, S.; Nozaki, K.; Chen, E.; Tateno, K.; Tawara, T.; Shinya, A.; Gotoh, H.; Notomi, M., Direct modulation of a single InP/InAs nanowire light-emitting diode. *Applied Physics Letters* **2018,** *112* (25), 251106.
99. Minot, E. D.; Kelkensberg, F.; van Kouwen, M.; van Dam, J. A.; Kouwenhoven, L. P.; Zwiller, V.; Borgström, M. T.; Wunnicke, O.; Verheijen, M. A.; Bakkers, E. P. A. M., Single Quantum Dot Nanowire LEDs. *Nano Letters* **2007,** *7* (2), 367-371.
100. Kivisaari, P.; Berg, A.; Karimi, M.; Storm, K.; Limpert, S.; Oksanen, J.; Samuelson, L.; Pettersson, H.; Borgström, M. T., Optimization of Current Injection in AlGaInP Core–Shell Nanowire Light-Emitting Diodes. *Nano Letters* **2017,** *17* (6), 3599-3606.
101. Hussain, L.; Karimi, M.; Berg, A.; Jain, V.; Borgström, M. T.; Gustafsson, A.; Samuelson, L.; Pettersson, H., Defect-induced infrared electroluminescence from radial GaInP/AlGaInP quantum well nanowire array light- emitting diodes. *Nanotechnology* **2017,** *28* (48), 485205.
102. Koren, E.; Hyun, J. K.; Givan, U.; Hemesath, E. R.; Lauhon, L. J.; Rosenwaks, Y., Obtaining Uniform Dopant Distributions in VLS-Grown Si Nanowires. *Nano Letters* **2011,** *11* (1), 183-187.
103. Gutsche, C.; Lysov, A.; Regolin, I.; Blekker, K.; Prost, W.; Tegude, F.-J., n-Type Doping of Vapor–Liquid–Solid Grown GaAs Nanowires. *Nanoscale Res Lett* **2010,** *6* (1), 65.
104. Gao, Q.; Li, Z.; Li, L.; Vora, K.; Li, Z.; Alabadla, A.; Wang, F.; Guo, Y.; Peng, K.; Wenas, Y. C.; Mokkapati, S.; Karouta, F.; Tan, H. H.; Jagadish, C.; Fu, L., Axial p-n junction design and characterization for InP nanowire array solar cells. *Progress in Photovoltaics: Research and Applications* **2019,** *27* (3), 237-244.
105. Li, Z.; Yang, I.; Li, L.; Gao, Q.; Chong, J. S.; Li, Z.; Lockrey, M. N.; Tan, H. H.; Jagadish, C.; Fu, L., Reducing Zn diffusion in single axial junction InP nanowire solar cells for improved performance. *Progress in Natural Science: Materials International* **2018,** *28* (2), 178-182.
106. Mingo, N.; Broido, D. A., Lattice Thermal Conductivity Crossovers in Semiconductor Nanowires. *Physical Review Letters* **2004,** *93* (24), 246106.
107. Carrete, J.; Longo, R. C.; Varela, L. M.; Rino, J. P.; Gallego, L. J., Molecular-dynamics prediction of the thermal conductivity of thin InP nanowires: Similarities to Si. *Physical Review B* **2009,** *80* (15), 155408.
108. Li, D.; Wu, Y.; Kim, P.; Shi, L.; Yang, P.; Majumdar, A., Thermal conductivity of individual silicon nanowires. *Applied Physics Letters* **2003,** *83* (14), 2934-2936.
109. Vukajlovic-Plestina, J.; Kim, W.; Ghisalberti, L.; Varnavides, G.; Tütüncuoglu, G.; Potts, H.; Friedl, M.; Güniat, L.; Carter, W. C.; Dubrovskii, V. G.; Fontcuberta i Morral, A., Fundamental aspects to localize self-catalyzed III-V nanowires on silicon. *Nature Communications* **2019,** *10* (1), 869.
110. Dubrovskii, V. G.; Xu, T.; Álvarez, A. D.; Plissard, S. R.; Caroff, P.; Glas, F.; Grandidier, B., Self-Equilibration of the Diameter of Ga-Catalyzed GaAs Nanowires. *Nano Letters* **2015,** *15* (8), 5580-5584.

111. Granqvist, C. G.; Hultåker, A., Transparent and conducting ITO films: new developments and applications. *Thin Solid Films* **2002,** *411* (1), 1-5.
112. Ingram, B. J.; Gonzalez, G. B.; Kammler, D. R.; Bertoni, M. I.; Mason, T. O., Chemical and Structural Factors Governing Transparent Conductivity in Oxides. *Journal of Electroceramics* **2004,** *13* (1), 167-175.
113. Kim, S. E.-K.; Oliver, M., Structural, electrical, and optical properties of reactively sputtered SnO2 thin films. *Metals and Materials International* **2010,** *16* (3), 441-446.
114. Dixon, S. C.; Scanlon, D. O.; Carmalt, C. J.; Parkin, I. P., n-Type doped transparent conducting binary oxides: an overview. *Journal of Materials Chemistry C* **2016,** *4* (29), 6946-6961.
115. Minami, T., Transparent conducting oxide semiconductors for transparent electrodes. *Semiconductor Science and Technology* **2005,** *20* (4), S35-S44.
116. Fleischer, K.; Norton, E.; Mullarkey, D.; Caffrey, D.; Shvets, I. V., Quantifying the Performance of P-Type Transparent Conducting Oxides by Experimental Methods. *Materials* **2017,** *10* (9), 1019.
117. Scanlon, D. O.; Watson, G. W., On the possibility of p-type SnO2. *Journal of Materials Chemistry* **2012,** *22* (48), 25236-25245.
118. Kawazoe, H.; Yasukawa, M.; Hyodo, H.; Kurita, M.; Yanagi, H.; Hosono, H., P-type electrical conduction in transparent thin films of CuAlO 2. *Nature* **1997,** *389* (6654), 939-942.
119. Zhang, K. H. L.; Xi, K.; Blamire, M. G.; Egdell, R. G., P-type transparent conducting oxides. *Journal of Physics: Condensed Matter* **2016,** *28* (38), 383002.
120. Lucovsky, G., Preparation of device-quality SiO2 thin films by remote plasma-enhanced chemical vapour deposition (PECVD): Applications in metal-oxide-semiconductor (MOS) devices. *Advanced Materials for Optics and Electronics* **1996,** *6* (2), 55-72.
121. Gupta, K.; Jain, N. K.; Laubscher, R., Advanced gear manufacturing and finishing: classical and modern processes. **2017**.
122. Rai-Choudhury, P., *Handbook of microlithography, micromachining, and microfabrication: microlithography*. SPIE press: 1997; Vol. 1.
123. Pala, N.; Karabiyik, M., Electron Beam Lithography (EBL). In *Encyclopedia of Nanotechnology*, Bhushan, B., Ed. Springer Netherlands: Dordrecht, 2016; pp 1033-1057.
124. Pimpin, A.; Srituravanich, W., Review on micro-and nanolithography techniques and their applications. *Engineering Journal* **2012,** *16* (1), 37-56.
125. Chang, T. H. P., Proximity effect in electron-beam lithography. *Journal of Vacuum Science and Technology* **1975,** *12* (6), 1271-1275.
126. Pfirrmann, S.; Kirchner, R.; Lohse, O.; Guzenko, V.; Voigt, A.; Harder, I.; Kolander, A.; Schift, H.; Grützner, G., *mr-PosEBR: a novel positive tone resist for high resolution electron beam lithography and 3D surface patterning*. SPIE: 2016; Vol. 9779.
127. Stringfellow, G. B., *Organometallic vapor-phase epitaxy: theory and practice*. Elsevier: 1999.
128. Ritter, D.; Heinecke, H., Evaluation of cracking efficiency of As and P precursors. *Journal of Crystal Growth* **1997,** *170* (1), 149-154.
129. Chen, Q.; Dapkus, P., On the thermal decomposition of trimethylgallium—A molecular beam sampling mass spectroscopy study. *Journal of the Electrochemical Society* **1991,** *138* (9), 2821.
130. Sakai, S.; Yamamoto, S.-i.; Umeno, M., MOCVD Growth of InP Using Plasma Pre-Cracking. *Japanese Journal of Applied Physics* **1986,** *25* (Part 1, No. 8), 1156-1160.
131. Huff, M., Recent Advances in Reactive Ion Etching and Applications of High-Aspect-Ratio Microfabrication. *Micromachines* **2021,** *12* (8), 991.
132. Hess, D. W.; Reinhard, K. A., 6 - Plasma Stripping, Cleaning, and Surface Conditioning. In *Handbook of Silicon Wafer Cleaning Technology (Second Edition)*, Reinhardt, K. A.; Kern, W., Eds. William Andrew Publishing: Norwich, NY, 2008; pp 355-427.
133. Goyal, A.; Hood, V.; Tadigadapa, S., High speed anisotropic etching of Pyrex® for microsystems applications. *Journal of Non-Crystalline Solids* **2006,** *352* (6), 657-663.

134. Ganjian, M.; Modaresifar, K.; Zhang, H.; Hagedoorn, P.-L.; Fratila-Apachitei, L. E.; Zadpoor, A. A., Reactive ion etching for fabrication of biofunctional titanium nanostructures. *Scientific Reports* **2019,** *9* (1), 18815.
135. Gili, V. F. All-dielectric nonlinear nanophotonics. Université Sorbonne Paris Cité, 2018.
136. Rasmussen, K. H.; Keller, S. S.; Jensen, F.; Jorgensen, A. M.; Hansen, O., SU-8 etching in inductively coupled oxygen plasma. *Microelectron. Eng.* **2013,** *112* (C), 35–40.
137. Tiwari, A., *Handbook of antimicrobial coatings*. Elsevier: 2017.
138. Hashmi, S., *Comprehensive materials processing*. Newnes: 2014.
139. Johnson, R. W.; Hultqvist, A.; Bent, S. F., A brief review of atomic layer deposition: from fundamentals to applications. *Materials Today* **2014,** *17* (5), 236-246.
140. Leskelä, M.; Ritala, M., Atomic Layer Deposition Chemistry: Recent Developments and Future Challenges. *Angewandte Chemie International Edition* **2003,** *42* (45), 5548-5554.
141. Awan, T.; Bashir, A.; Tehseen, A.; Orders, T. E., Chemistry of Nanomaterials. **2004**.
142. Goldstein, J. I.; Newbury, D. E.; Michael, J. R.; Ritchie, N. W.; Scott, J. H. J.; Joy, D. C., *Scanning electron microscopy and X-ray microanalysis*. Springer: 2017.
143. contributors, W. Scanning electron microscope. https://en.wikipedia.org/w/index.php?title=Scanning_electron_microscope&oldid=1042875111.
144. Fox, M., Optical properties of solids. American Association of Physics Teachers: 2002.
145. Saxena, D. Design and Characterisation of III-V Semiconductor Nanowire Lasers. Ph.D., The Australian National University (Australia), 2017.
146. Zhou, R.; Yu, M.; Tweddle, D.; Hamer, P.; Chen, D.; Hallam, B.; Ciesla, A.; Altermatt, P. P.; Wilshaw, P. R.; Bonilla, R. S., Understanding and optimizing EBIC pn-junction characterization from modeling insights. *Journal of Applied Physics* **2020,** *127* (2), 024502.
147. Van der Heide, P., *X-ray photoelectron spectroscopy: an introduction to principles and practices*. John Wiley & Sons: 2011.
148. Paun, M.-A.; Sallese, J.-M.; Kayal, M., Hall effect sensors design, integration and behavior analysis. *Journal of Sensor and Actuator Networks* **2013,** *2* (1), 85-97.
149. David, J. M.; Buehler, M. G., A numerical analysis of various cross sheet resistor test structures. *Solid-State Electronics* **1977,** *20* (6), 539-543.
150. Fujiwara, H., *Spectroscopic ellipsometry: principles and applications*. John Wiley & Sons: 2007.
151. Janicek, P.; Putri, M.; Kim, K. H.; Lee, H. J.; Bouska, M.; Šlang, S.; Lee, H. Y., Spectroscopic Ellipsometry Characterization of As-Deposited and Annealed Non-Stoichiometric Indium Zinc Tin Oxide Thin Film. *Materials* **2021,** *14* (3), 578.
152. Nolen, J. R.; Runnerstrom, E. L.; Kelley, K. P.; Luk, T. S.; Folland, T. G.; Cleri, A.; Maria, J.-P.; Caldwell, J. D., Ultraviolet to far-infrared dielectric function of n-doped cadmium oxide thin films. *Physical Review Materials* **2020,** *4* (2), 025202.
153. Fujiwara, H.; Collins, R. W., *Spectroscopic ellipsometry for photovoltaics*. Springer: 2018; Vol. 1.
154. Mouton, A.; Sundararaman, C.; Lafontaine, H.; Poulin, S.; Currie, J., Etching of InP by H3PO4, H2O2 solutions. *Japanese journal of applied physics* **1990,** *29* (10R), 1912.
155. Yang, I., Selective-Area Epitaxial Growth of InGaAs/InP Quantum Well Nanowires for Light Emitting Device Applications. **2019**.
156. Dhaka, V.; Perros, A.; Naureen, S.; Shahid, N.; Jiang, H.; Kakko, J.-P.; Haggren, T.; Kauppinen, E.; Srinivasan, A.; Lipsanen, H., Protective capping and surface passivation of III-V nanowires by atomic layer deposition. *AIP Advances* **2016,** *6* (1), 015016.
157. Todeschini, M.; Bastos da Silva Fanta, A.; Jensen, F.; Wagner, J. B.; Han, A., Influence of Ti and Cr Adhesion Layers on Ultrathin Au Films. *ACS Applied Materials & Interfaces* **2017,** *9* (42), 37374-37385.
158. Zhang, Y.; Zhang, X.; Fang, J.; Jiang, S.; Zhang, Y.; Gu, D.; Nelson, R. D.; LaRue, J. C. In *Application of SU-8 as the insulator toward a novel planar microelectrode array for extracellular neural recording*,

2010 IEEE 5th International Conference on Nano/Micro Engineered and Molecular Systems, 20-23 Jan. 2010; 2010; pp 395-398.
159. Sainiemi, L.; Franssila, S., Mask material effects in cryogenic deep reactive ion etching. *Journal of Vacuum Science & Technology B: Microelectronics and Nanometer Structures Processing, Measurement, and Phenomena* **2007,** *25* (3), 801-807.
160. LaBianca, N.; Gelorme, J., *High-aspect-ratio resist for thick-film applications*. SPIE: 1995; Vol. 2438.
161. Ceyssens, F.; Puers, B., SU-8 photoresist. **2012**.
162. Inan, U. S.; Marshall, R. A., *Numerical electromagnetics: the FDTD method*. Cambridge University Press: 2011.
163. contributors, W. Finite-difference time-domain method. https://en.wikipedia.org/w/index.php?title=Finite-difference_time-domain_method&oldid=1038661340.
164. Lumerical, A. MODE - Finite Difference Eigenmode (FDE) solver introduction. https://support.lumerical.com/hc/en-us/articles/360034917233-MODE-Finite-Difference-Eigenmode-FDE-solver-introduction.
165. Grupen, M.; Hess, K., Simulation of carrier transport and nonlinearities in quantum-well laser diodes. *IEEE Journal of Quantum Electronics* **1998,** *34* (1), 120-140.
166. Henneghien, A.-L.; Gayral, B.; Désières, Y.; Gérard, J.-M., Simulation of waveguiding and emitting properties of semiconductor nanowires with hexagonal or circular sections. *J. Opt. Soc. Am. B* **2009,** *26* (12), 2396-2403.
167. Zilli, A.; De Luca, M.; Tedeschi, D.; Fonseka, H. A.; Miriametro, A.; Tan, H. H.; Jagadish, C.; Capizzi, M.; Polimeni, A., Temperature Dependence of Interband Transitions in Wurtzite InP Nanowires. *ACS Nano* **2015,** *9* (4), 4277-4287.
168. Shen, T. C.; Gao, G. B.; Morkoç, H., Recent developments in ohmic contacts for III–V compound semiconductors. *Journal of Vacuum Science & Technology B: Microelectronics and Nanometer Structures Processing, Measurement, and Phenomena* **1992,** *10* (5), 2113-2132.
169. Burkhard, H.; Dinges, H. W.; Kuphal, E., Optical properties of In1−xGaxP1−yAsy, InP, GaAs, and GaP determined by ellipsometry. *Journal of Applied Physics* **1982,** *53* (1), 655-662.
170. Semyonov, O.; Subashiev, A.; Chen, Z.; Luryi, S., Radiation efficiency of heavily doped bulk n-InP semiconductor. *Journal of Applied Physics* **2010,** *108* (1), 013101.
171. Johnson, P. B.; Christy, R. W., Optical Constants of the Noble Metals. *Physical Review B* **1972,** *6* (12), 4370-4379.
172. Mishra, A.; Titova, L. V.; Hoang, T. B.; Jackson, H. E.; Smith, L. M.; Yarrison-Rice, J. M.; Kim, Y.; Joyce, H. J.; Gao, Q.; Tan, H. H.; Jagadish, C., Polarization and temperature dependence of photoluminescence from zincblende and wurtzite InP nanowires. *Applied Physics Letters* **2007,** *91* (26), 263104.
173. Yang, I.; Zhang, X.; Zheng, C.; Gao, Q.; Li, Z.; Li, L.; Lockrey, M. N.; Nguyen, H.; Caroff, P.; Etheridge, J.; Tan, H. H.; Jagadish, C.; Wong-Leung, J.; Fu, L., Radial Growth Evolution of InGaAs/InP Multi-Quantum-Well Nanowires Grown by Selective-Area Metal Organic Vapor-Phase Epitaxy. *ACS Nano* **2018,** *12* (10), 10374-10382.
174. Van de Walle, C. G., Hydrogen as a Cause of Doping in Zinc Oxide. *Physical Review Letters* **2000,** *85* (5), 1012-1015.
175. Guziewicz, E.; Krajewski, T. A.; Przezdziecka, E.; Korona, K. P.; Czechowski, N.; Klopotowski, L.; Terziyska, P., Zinc Oxide Grown by Atomic Layer Deposition: From Heavily n-Type to p-Type Material. *physica status solidi (b)* **2020,** *257* (2), 1900472.
176. Raj, V.; dos Santos, T. S.; Rougieux, F.; Vora, K.; Lysevych, M.; Fu, L.; Mokkapati, S.; Tan, H. H.; Jagadish, C., Indium phosphide based solar cell using ultra-thin ZnO as an electron selective layer. *Journal of Physics D: Applied Physics* **2018,** *51* (39), 395301.

177. Sharma, D. K.; Shukla, S.; Sharma, K. K.; Kumar, V., A review on ZnO: Fundamental properties and applications. *Materials Today: Proceedings* **2020**.
178. Janotti, A.; Van de Walle, C. G., Fundamentals of zinc oxide as a semiconductor. *Reports on Progress in Physics* **2009,** *72* (12), 126501.
179. Alivov, Y. I.; Nostrand, J. E. V.; Look, D. C.; Chukichev, M. V.; Ataev, B. M., Observation of 430 nm electroluminescence from ZnO/GaN heterojunction light-emitting diodes. *Applied Physics Letters* **2003,** *83* (14), 2943-2945.
180. Yang, L.; Wang, Y.; Xu, H.; Liu, W.; Zhang, C.; Wang, C.; Wang, Z.; Ma, J.; Liu, Y., Color-Tunable ZnO/GaN Heterojunction LEDs Achieved by Coupling with Ag Nanowire Surface Plasmons. *ACS Applied Materials & Interfaces* **2018,** *10* (18), 15812-15819.
181. Jeong, S.; Oh, S. K.; Ryou, J.-H.; Ahn, K.-S.; Song, K. M.; Kim, H., Monolithic Inorganic ZnO/GaN Semiconductors Heterojunction White Light-Emitting Diodes. *ACS Applied Materials & Interfaces* **2018,** *10* (4), 3761-3768.
182. Peng, Y.; Que, M.; Lee, H. E.; Bao, R.; Wang, X.; Lu, J.; Yuan, Z.; Li, X.; Tao, J.; Sun, J.; Zhai, J.; Lee, K. J.; Pan, C., Achieving high-resolution pressure mapping via flexible GaN/ ZnO nanowire LEDs array by piezo-phototronic effect. *Nano Energy* **2019,** *58*, 633-640.
183. Lupan, O.; Pauporté, T.; Viana, B., Low-Voltage UV-Electroluminescence from ZnO-Nanowire Array/p-GaN Light-Emitting Diodes. *Advanced Materials* **2010,** *22* (30), 3298-3302.
184. Zhang, X.-M.; Lu, M.-Y.; Zhang, Y.; Chen, L.-J.; Wang, Z. L., Fabrication of a High-Brightness Blue-Light-Emitting Diode Using a ZnO-Nanowire Array Grown on p-GaN Thin Film. *Advanced Materials* **2009,** *21* (27), 2767-2770.
185. Ng, A. M. C.; Xi, Y. Y.; Hsu, Y. F.; Djurišić, A. B.; Chan, W. K.; Gwo, S.; Tam, H. L.; Cheah, K. W.; Fong, P. W. K.; Lui, H. F.; Surya, C., GaN/ZnO nanorod light emitting diodes with different emission spectra. *Nanotechnology* **2009,** *20* (44), 445201.
186. Lee, S.-D.; Kim, Y.-S.; Yi, M.-S.; Choi, J.-Y.; Kim, S.-W., Morphology Control and Electroluminescence of ZnO Nanorod/GaN Heterojunctions Prepared Using Aqueous Solution. *The Journal of Physical Chemistry C* **2009,** *113* (20), 8954-8958.
187. Pande, K. P.; Manikopoulos, C. N., ZnO・p-InP heterojunction solar cells. *Solar Cells* **1981,** *4* (2), 147-152.
188. Ocak, Y. S.; Kulakci, M.; Turan, R.; Kilicoglu, T.; Gullu, O., Analysis of electrical and photoelectrical properties of ZnO/p-InP heterojunction. *Journal of Alloys and Compounds* **2011,** *509* (23), 6631-6634.
189. Caban, P.; Pietruszka, R.; Kopalko, K.; Witkowski, B. S.; Gwozdz, K.; Placzek-Popko, E.; Godlewski, M., ZnO/GaAs heterojunction solar cells fabricated by the ALD method. *Optik* **2018,** *157*, 743-749.
190. Köç, P.; Tekmen, S.; Baltakesmez, A.; Tüzemen, S.; Meral, K.; Onganer, Y., Stimulated electroluminescence emission from n-ZnO/p-GaAs:Zn heterojunctions fabricated by electro-deposition. *AIP Advances* **2013,** *3* (12), 122107.
191. Karatum, O.; Jalali, H. B.; Sadeghi, S.; Melikov, R.; Srivastava, S. B.; Nizamoglu, S., Light-Emitting Devices Based on Type-II InP/ZnO Quantum Dots. *ACS Photonics* **2019,** *6* (4), 939-946.
192. Eren, G. O.; Sadeghi, S.; Bahmani Jalali, H.; Ritter, M.; Han, M.; Baylam, I.; Melikov, R.; Onal, A.; Oz, F.; Sahin, M.; Ow-Yang, C. W.; Sennaroglu, A.; Lechner, R. T.; Nizamoglu, S., Cadmium-Free and Efficient Type-II InP/ZnO/ZnS Quantum Dots and Their Application for LEDs. *ACS Applied Materials & Interfaces* **2021,** *13* (27), 32022-32030.
193. Jin, S. X.; Li, J.; Li, J. Z.; Lin, J. Y.; Jiang, H. X., GaN microdisk light emitting diodes. *Applied Physics Letters* **2000,** *76* (5), 631-633.
194. Jin, S. X.; Li, J.; Lin, J. Y.; Jiang, H. X., InGaN/GaN quantum well interconnected microdisk light emitting diodes. *Applied Physics Letters* **2000,** *77* (20), 3236-3238.
195. Dai, L.; Zhang, B.; Lin, J. Y.; Jiang, H. X., Comparison of optical transitions in InGaN quantum well structures and microdisks. *Journal of Applied Physics* **2001,** *89* (9), 4951-4954.

196. SZE, S. M., p-n Junctions. In *Semiconductor Devices Physics and Technology*, 2 ed.; John Wiley & Son: 2001.
197. Guziewicz, E.; Godlewski, M.; Krajewski, T.; Wachnicki, Ł.; Szczepanik, A.; Kopalko, K.; Wójcik-Głodowska, A.; Przeździecka, E.; Paszkowicz, W.; Łusakowska, E.; Kruszewski, P.; Huby, N.; Tallarida, G.; Ferrari, S., ZnO grown by atomic layer deposition: A material for transparent electronics and organic heterojunctions. *Journal of Applied Physics* **2009,** *105* (12), 122413.
198. Fischer, T. E., Photoelectric Emission and Work Function of InP. *Physical Review* **1966,** *142* (2), 519-523.
199. Sharma, A.; Untch, M.; Quinton, J. S.; Berger, R.; Andersson, G.; Lewis, D. A., Nanoscale heterogeniety and workfunction variations in ZnO thin films. *Applied Surface Science* **2016,** *363*, 516-521.
200. Hilsum, C.; Fray, S.; Smith, C., The optical frequencies and dielectric constants of InP. *Solid State Communications* **1969,** *7* (15), 1057-1059.
201. Langton, N. H.; Matthews, D., The dielectric constant of zinc oxide over a range of frequencies. *British Journal of Applied Physics* **1958,** *9* (11), 453-456.
202. Yong, C. K.; Wong-Leung, J.; Joyce, H. J.; Lloyd-Hughes, J.; Gao, Q.; Tan, H. H.; Jagadish, C.; Johnston, M. B.; Herz, L. M., Direct observation of charge-carrier heating at WZ-ZB InP nanowire heterojunctions. *Nano Lett* **2013,** *13* (9), 4280-7.
203. Perera, S.; Pemasiri, K.; Fickenscher, M. A.; Jackson, H. E.; Smith, L. M.; Yarrison-Rice, J.; Paiman, S.; Gao, Q.; Tan, H. H.; Jagadish, C., Probing valence band structure in wurtzite InP nanowires using excitation spectroscopy. *Applied Physics Letters* **2010,** *97* (2), 023106.
204. Tuin, G. L.; Borgström, M. T.; Trägårdh, J.; Ek, M.; Wallenberg, L. R.; Samuelson, L.; Pistol, M.-E., Valence band splitting in wurtzite InP nanowires observed by photoluminescence and photoluminescence excitation spectroscopy. *Nano Research* **2011,** *4* (2), 159-163.
205. Hansen, K.; Peiner, E.; Schlachetzki, A.; Von Ortenberg, M., Dopant activation energy and hole effective mass in heavily Zn-Doped InP. *Journal of Electronic Materials* **1994,** *23* (9), 935-941.
206. Vu, T. T. T.; Zehender, T.; Verheijen, M. A.; Plissard, S. R.; Immink, G. W. G.; Haverkort, J. E. M.; Bakkers, E. P. A. M., High optical quality single crystal phase wurtzite and zincblende InP nanowires. *Nanotechnology* **2013,** *24* (11), 115705.
207. De Luca, M.; Polimeni, A.; Fonseka, H. A.; Meaney, A. J.; Christianen, P. C. M.; Maan, J. C.; Paiman, S.; Tan, H. H.; Mura, F.; Jagadish, C.; Capizzi, M., Magneto-Optical Properties of Wurtzite-Phase InP Nanowires. *Nano Letters* **2014,** *14* (8), 4250-4256.
208. Iqbal, J.; Jilani, A.; Ziaul Hassan, P. M.; Rafique, S.; Jafer, R.; Alghamdi, A. A., ALD grown nanostructured ZnO thin films: Effect of substrate temperature on thickness and energy band gap. *Journal of King Saud University - Science* **2016,** *28* (4), 347-354.
209. Niemegeers, A.; Burgelman, M.; Herberholz, R.; Rau, U.; Hariskos, D.; Schock, H.-W., Model for electronic transport in Cu(In,Ga)Se2 solar cells. *Progress in Photovoltaics: Research and Applications* **1998,** *6* (6), 407-421.
210. Sasabe, H.; Kido, J., Development of high performance OLEDs for general lighting. *Journal of Materials Chemistry C* **2013,** *1* (9), 1699-1707.
211. Brütting, W.; Frischeisen, J.; Schmidt, T. D.; Scholz, B. J.; Mayr, C., Device efficiency of organic light-emitting diodes: Progress by improved light outcoupling. *physica status solidi (a)* **2013,** *210* (1), 44-65.
212. Sekitani, T.; Nakajima, H.; Maeda, H.; Fukushima, T.; Aida, T.; Hata, K.; Someya, T., Stretchable active-matrix organic light-emitting diode display using printable elastic conductors. *Nat Mater* **2009,** *8* (6), 494-9.
213. Thejokalyani, N.; Dhoble, S. J., Novel approaches for energy efficient solid state lighting by RGB organic light emitting diodes – A review. *Renewable and Sustainable Energy Reviews* **2014,** *32*, 448-467.

214. Gaul, D. A.; Rees Jr., W. S., True Blue Inorganic Optoelectronic Devices. *Advanced Materials* **2000,** *12* (13), 935-946.
215. Ponce, F. A.; Bour, D. P., Nitride-based semiconductors for blue and green light-emitting devices. *Nature* **1997,** *386* (6623), 351-359.
216. Aziz, H.; Popovic, Z. D.; Hu, N. X.; Hor, A. M.; Xu, G., Degradation mechanism of small molecule-based organic light-emitting devices. *Science* **1999,** *283* (5409), 1900-2.
217. Dai, X.; Messanvi, A.; Zhang, H.; Durand, C.; Eymery, J.; Bougerol, C.; Julien, F. H.; Tchernycheva, M., Flexible Light-Emitting Diodes Based on Vertical Nitride Nanowires. *Nano Letters* **2015,** *15* (10), 6958-6964.
218. Neplokh, V.; Messanvi, A.; Zhang, H.; Julien, F. H.; Babichev, A.; Eymery, J.; Durand, C.; Tchernycheva, M., Substrate-Free InGaN/GaN Nanowire Light-Emitting Diodes. *Nanoscale Research Letters* **2015,** *10* (1), 447.
219. Garra, J.; Long, T.; Currie, J.; Schneider, T.; White, R.; Paranjape, M., Dry etching of polydimethylsiloxane for microfluidic systems. *Journal of Vacuum Science & Technology A* **2002,** *20* (3), 975-982.
220. González, J. C.; da Silva, M. I. N.; Lozano, X. S.; Zanchet, D.; Ugarte, D.; Ribeiro, E.; Gutiérrez, H. R.; Cotta, M. A., Structural and Optical Characterization of Strained Free-Standing InP Nanowires. *Journal of Nanoscience and Nanotechnology* **2006,** *6* (7), 2182-2186.
221. Signorello, G.; Karg, S.; Björk, M. T.; Gotsmann, B.; Riel, H., Tuning the Light Emission from GaAs Nanowires over 290 meV with Uniaxial Strain. *Nano Letters* **2013,** *13* (3), 917-924.
222. Anufriev, R.; Chauvin, N.; Khmissi, H.; Naji, K.; Gendry, M.; Bru-Chevallier, C., Impact of substrate-induced strain and surface effects on the optical properties of InP nanowires. *Applied Physics Letters* **2012,** *101* (7), 072101.
223. Das, S.; Jayaraman, V., SnO2: A comprehensive review on structures and gas sensors. *Progress in Materials Science* **2014,** *66*, 112-255.
224. Kim, H.; Kushto, G. P.; Auyeung, R. C. Y.; Piqué, A., Optimization of F-doped SnO2 electrodes for organic photovoltaic devices. *Applied Physics A* **2008,** *93* (2), 521-526.
225. Murugadoss, G.; Kanda, H.; Tanaka, S.; Nishino, H.; Ito, S.; Imahori, H.; Umeyama, T., An efficient electron transport material of tin oxide for planar structure perovskite solar cells. *Journal of Power Sources* **2016,** *307*, 891-897.
226. D.M, P.; Mannam, R.; Rao, M. S. R.; DasGupta, N., Effect of annealing ambient on SnO2 thin film transistors. *Applied Surface Science* **2017,** *418*, 414-417.
227. Isono, T.; Fukuda, T.; Nakagawa, K.; Usui, R.; Satoh, R.; Morinaga, E.; Mihara, Y., Highly conductive SnO2 thin films for flat-panel displays. *Journal of the Society for Information Display* **2007,** *15* (2), 161-166.
228. Minami, T., Transparent and conductive multicomponent oxide films prepared by magnetron sputtering. *Journal of Vacuum Science & Technology A* **1999,** *17* (4), 1765-1772.
229. Ding, X.; Fang, F.; Jiang, J., Electrical and optical properties of N-doped SnO2 thin films prepared by magnetron sputtering. *Surface and Coatings Technology* **2013,** *231*, 67-70.
230. Jeong, J.; Choi, S. P.; Hong, K. J.; Park, J. S.; Song, H. J., Structural and optical properties of SnO2 thin films deposited by using CVD techniques. *Journal of the Korean Physical Society* **2006,** *48* (5), 960-963.
231. Kim, H.; Piqué, A., Transparent conducting Sb-doped SnO2 thin films grown by pulsed-laser deposition. *Applied Physics Letters* **2004,** *84* (2), 218-220.
232. Bouras, K.; Rehspringer, J. L.; Schmerber, G.; Rinnert, H.; Colis, S.; Ferblantier, G.; Balestrieri, M.; Ihiawakrim, D.; Dinia, A.; Slaoui, A., Optical and structural properties of Nd doped SnO2 powder fabricated by the sol–gel method. *Journal of Materials Chemistry C* **2014,** *2* (39), 8235-8243.

233. Leng, D.; Wu, L.; Jiang, H.; Zhao, Y.; Zhang, J.; Li, W.; Feng, L., Preparation and Properties of SnO₂ Film Deposited by Magnetron Sputtering. *International Journal of Photoenergy* **2012,** *2012*, 235971.
234. Udayakumar, R.; Khanaa, V.; Saravanan, T., Synthesis and structural characterization of thin films of SnO 2 prepared by spray pyrolysis technique. *Indian Journal of Science and Technology* **2013,** *6* (S6), 4754-4757.
235. Kim, T. W.; Lee, D. U.; Lee, J. H.; Yoon, Y. S., Surface and microstructural properties of SnO2 thin films grown on p-InP (100) substrates at low temperature. *Solid State Communications* **2000,** *115* (9), 503-507.
236. Kim, T. W.; Lee, D. U.; Jung, M.; Lee, J. H.; Choo, D. C.; Cho, J. W.; Seo, K. Y.; Yoon, Y. S., Dependence of the structural, the electrical, and the optical properties on the Ar/O2 flow-rate ratios for SnO2 thin films grown on p-InP (1 0 0) substrates at low temperature. *Applied Surface Science* **2001,** *182* (1), 69-76.
237. Pande, K. P.; Hsu, Y. S.; Roberts, G. G., Electronic processes in SnO2- (n-type) InP heterojunctions. *Journal of Applied Physics* **1980,** *51* (3), 1650-1654.
238. Kim, Y. C.; Lee, S. J.; Myoung, J.-M., Enhanced Light Extraction from p-Si Nanowires/n-IGZO Heterojunction LED by Using Oxide–Metal–Oxide Structured Transparent Electrodes. *The Journal of Physical Chemistry C* **2017,** *121* (12), 6788-6795.
239. Srinivas, G.; Vankar, V. D., Microstructural studies of molybdenum silicide thin films by spectroscopic ellipsometry. *Materials Letters* **1997,** *30* (1), 35-40.
240. Jr., G. E. J.; Modine, F. A., Parameterization of the optical functions of amorphous materials in the interband region. *Applied Physics Letters* **1996,** *69* (3), 371-373.
241. Golovashkin, A.; Motulevich, G., Optical and electrical properties of tin. *Sov. Phys. JETP* **1964,** *19* (2), 310-317.
242. Geurts, J.; Rau, S.; Richter, W.; Schmitte, F., SnO films and their oxidation to SnO2: Raman scattering, IR reflectivity and X-ray diffraction studies. *Thin solid films* **1984,** *121* (3), 217-225.
243. Ogo, Y.; Hiramatsu, H.; Nomura, K.; Yanagi, H.; Kamiya, T.; Hirano, M.; Hosono, H., p-channel thin-film transistor using p-type oxide semiconductor, SnO. *Applied Physics Letters* **2008,** *93* (3), 032113.
244. Arlinghaus, F., Energy bands in stannic oxide (SnO2). *Journal of Physics and Chemistry of solids* **1974,** *35* (8), 931-935.
245. Themlin, J.-M.; Chtaïb, M.; Henrard, L.; Lambin, P.; Darville, J.; Gilles, J.-M., Characterization of tin oxides by x-ray-photoemission spectroscopy. *Physical Review B* **1992,** *46* (4), 2460-2466.
246. Szuber, J.; Czempik, G.; Larciprete, R.; Koziej, D.; Adamowicz, B., XPS study of the L-CVD deposited SnO2 thin films exposed to oxygen and hydrogen. *Thin Solid Films* **2001,** *391* (2), 198-203.
247. Wu, Q.-H.; Song, J.; Kang, J.; Dong, Q.-F.; Wu, S.-T.; Sun, S.-G., Nano-particle thin films of tin oxides. *Materials Letters* **2007,** *61* (17), 3679-3684.
248. Kolmakov, A.; Potluri, S.; Barinov, A.; Menteş, T. O.; Gregoratti, L.; Niño, M. A.; Locatelli, A.; Kiskinova, M., Spectromicroscopy for Addressing the Surface and Electron Transport Properties of Individual 1-D Nanostructures and Their Networks. *ACS Nano* **2008,** *2* (10), 1993-2000.
249. Doh, W. H.; Jeong, W.; Lee, H.; Park, J.; Park, J. Y., Work function engineering of SnO single crystal microplates with thermal annealing. *Nanotechnology* **2016,** *27* (33), 335603.
250. Peisert, H.; Streubel, P.; Chassé, T.; Szargan, R., Chemical stability of (NH4)2S-passivated InP(001) surfaces – investigations by XPS and XPD. *Fresenius' Journal of Analytical Chemistry* **1997,** *358* (1), 201-203.
251. Birman, J. L., Some Selection Rules for Band-Band Transitions in Wurtzite Structure. *Physical Review* **1959,** *114* (6), 1490-1492.
252. Su, Z.; Wang, N.; Tan, H. H.; Jagadish, C., 2D Carrier Localization at the Wurtzite-Zincblende Interface in Novel Layered InP Nanomembranes. *ACS Photonics* **2021,** *8* (6), 1735-1745.

253. Zhou, W.; Liu, Y.; Yang, Y.; Wu, P., Band Gap Engineering of SnO2 by Epitaxial Strain: Experimental and Theoretical Investigations. *The Journal of Physical Chemistry C* **2014,** *118* (12), 6448-6453.
254. Summitt, R.; Borrelli, N. F., Infrared absorption in single crystal stannic oxide. *Journal of Physics and Chemistry of Solids* **1965,** *26* (5), 921-925.
255. Daal, H. J. v., The Static Dielectric Constant of SnO2. *Journal of Applied Physics* **1968,** *39* (9), 4467-4469.
256. Zervos, M.; Othonos, A.; Tsokkou, D.; Kioseoglou, J.; Pavlidou, E.; Komninou, P., Structural properties of SnO2 nanowires and the effect of donor like defects on its charge distribution. *physica status solidi (a)* **2013,** *210* (1), 226-229.
257. Ghodsi, F. E.; Mazloom, J., Optical, electrical and morphological properties of p-type Mn-doped SnO2 nanostructured thin films prepared by sol–gel process. *Applied Physics A* **2012,** *108* (3), 693-700.
258. Hautier, G.; Miglio, A.; Ceder, G.; Rignanese, G.-M.; Gonze, X., Identification and design principles of low hole effective mass p-type transparent conducting oxides. *Nature Communications* **2013,** *4* (1), 2292.
259. Kawazoe, H.; Yasukawa, M.; Hyodo, H.; Kurita, M.; Yanagi, H.; Hosono, H., P-type electrical conduction in transparent thin films of CuAlO2. *Nature* **1997,** *389* (6654), 939-942.
260. He, H., 2 - Metal oxide semiconductors and conductors. In *Solution Processed Metal Oxide Thin Films for Electronic Applications*, Cui, Z.; Korotcenkov, G., Eds. Elsevier: 2020; pp 7-30.
261. Wang, Z.; Nayak, P. K.; Caraveo-Frescas, J. A.; Alshareef, H. N., Recent Developments in p-Type Oxide Semiconductor Materials and Devices. *Advanced Materials* **2016,** *28* (20), 3831-3892.
262. Platteeuw, J.; Meyer, G., The system tin+ oxygen. *Transactions of the Faraday Society* **1956,** *52*, 1066-1073.
263. Giefers, H.; Porsch, F.; Wortmann, G., Kinetics of the disproportionation of SnO. *Solid State Ionics* **2005,** *176* (1), 199-207.
264. Irwin, M. D.; Buchholz, D. B.; Hains, A. W.; Chang, R. P. H.; Marks, T. J., p-Type semiconducting nickel oxide as an efficiency-enhancing anode interfacial layer in polymer bulk-heterojunction solar cells. *Proceedings of the National Academy of Sciences* **2008,** *105* (8), 2783-2787.
265. Liang, J.; Lu, Y.; Liu, Y.; Liu, X.; Gong, M.; Deng, S.; Yang, H.; Liu, P.; Wang, D., Oxides overlayer confined Ni3Sn2 alloy enable enhanced lithium storage performance. *Journal of Power Sources* **2019,** *441*, 227185.
266. Tong, W.; Wang, Y.; Bian, Y.; Wang, A.; Han, N.; Chen, Y., Sensitive Cross-Linked SnO2:NiO Networks for MEMS Compatible Ethanol Gas Sensors. *Nanoscale Research Letters* **2020,** *15* (1), 35.
267. Yang, H.; Tao, Q.; Zhang, X.; Tang, A.; Ouyang, J., Solid-state synthesis and electrochemical property of SnO2/NiO nanomaterials. *Journal of Alloys and Compounds* **2008,** *459* (1), 98-102.
268. Gopi, S.; Al-Mohaimeed, A. M.; Elshikh, M. S.; Yun, K., Facile fabrication of bifunctional SnO–NiO heteromixture for efficient electrocatalytic urea and water oxidation in urea-rich waste water. *Environmental Research* **2021,** *201*, 111589.
269. Alshehri, M.; Al-Marzouki, F.; Alshehrie, A.; Hafez, M., Synthesis, characterization and band alignment characteristics of NiO/SnO2 bulk heterojunction nanoarchitecture for promising photocatalysis applications. *Journal of Alloys and Compounds* **2018,** *757*, 161-168.
270. Kaur, M.; Dadhich, B. K.; Singh, R.; KailasaGanapathi; Bagwaiya, T.; Bhattacharya, S.; Debnath, A. K.; Muthe, K. P.; Gadkari, S. C., RF sputtered SnO2: NiO thin films as sub-ppm H2S sensor operable at room temperature. *Sensors and Actuators B: Chemical* **2017,** *242*, 389-403.
271. Walukiewicz, W.; Lagowski, J.; Jastrzebski, L.; Rava, P.; Lichtensteiger, M.; Gatos, C. H.; Gatos, H. C., Electron mobility and free-carrier absorption in InP; determination of the compensation ratio. *Journal of Applied Physics* **1980,** *51* (5), 2659-2668.
272. Cheemadan, S.; Santhosh Kumar, M. C., Effect of substrate temperature and oxygen partial pressure on RF sputtered NiO thin films. *Materials Research Express* **2018,** *5* (4), 046401.

273. Koffyberg, F. P.; Benko, F. A., p-Type NiO as a Photoelectrolysis Cathode. *Journal of The Electrochemical Society* **1981,** *128* (11), 2476-2479.
274. Caraveo-Frescas, J. A.; Nayak, P. K.; Al-Jawhari, H. A.; Granato, D. B.; Schwingenschlögl, U.; Alshareef, H. N., Record Mobility in Transparent p-Type Tin Monoxide Films and Devices by Phase Engineering. *ACS Nano* **2013,** *7* (6), 5160-5167.
275. Barros, R.; Saji, K. J.; Waerenborgh, J. C.; Barquinha, P.; Pereira, L.; Carlos, E.; Martins, R.; Fortunato, E., Role of Structure and Composition on the Performances of P-Type Tin Oxide Thin-Film Transistors Processed at Low-Temperatures. *Nanomaterials* **2019,** *9* (3), 320.
276. Isidorsson, J.; Granqvist, C. G.; von Rottkay, K.; Rubin, M., Ellipsometry on sputter-deposited tin oxide films: optical constants versus stoichiometry, hydrogen content, and amount of electrochemically intercalated lithium. *Appl. Opt.* **1998,** *37* (31), 7334-7341.
277. Jarzebski, Z. M.; Marton, J. P., Physical Properties of SnO2 Materials: II . Electrical Properties. *Journal of The Electrochemical Society* **1976,** *123* (9), 299C-310C.
278. Marchetti, L.; Miserque, F.; Perrin, S.; Pijolat, M., XPS study of Ni-base alloys oxide films formed in primary conditions of pressurized water reactor. *Surface and Interface Analysis* **2015,** *47* (5), 632-642.
279. Legrand, D. L.; Nesbitt, H. W.; Bancroft, G. M., X-ray photoelectron spectroscopic study of a pristine millerite (NiS) surface and the effect of air and water oxidation. *American Mineralogist* **1998,** *83* (11-12_Part_1), 1256-1265.
280. Islam, M. B.; Yanagida, M.; Shirai, Y.; Nabetani, Y.; Miyano, K., NiOx Hole Transport Layer for Perovskite Solar Cells with Improved Stability and Reproducibility. *ACS Omega* **2017,** *2* (5), 2291-2299.
281. Kwon, Y. H.; Chun, S. H.; Han, J.-H.; Cho, H. K., Correlation between electrical properties and point defects in NiO thin films. *Metals and Materials International* **2012,** *18* (6), 1003-1007.
282. Yip, H.-L.; Jen, A. K. Y., Recent advances in solution-processed interfacial materials for efficient and stable polymer solar cells. *Energy & Environmental Science* **2012,** *5* (3), 5994-6011.
283. Joyce, H. J.; Wong-Leung, J.; Yong, C.-K.; Docherty, C. J.; Paiman, S.; Gao, Q.; Tan, H. H.; Jagadish, C.; Lloyd-Hughes, J.; Herz, L. M.; Johnston, M. B., Ultralow Surface Recombination Velocity in InP Nanowires Probed by Terahertz Spectroscopy. *Nano Letters* **2012,** *12* (10), 5325-5330.